

NOAA Technical Memorandum OAR ARL-259



CLIMATOGRAPHY OF THE IDAHO NATIONAL LABORATORY 3rd EDITION

K.L. Clawson
R.M. Eckman
N.F. Hukari
J.D. Rich
N.R. Ricks

Field Research Laboratory
Idaho Falls, Idaho

Air Resources Laboratory
Silver Spring, Maryland
December 2007

NOAA Technical Memorandum OAR ARL-259

CLIMATOGRAPHY OF THE IDAHO NATIONAL LABORATORY 3rd EDITION

K.L. Clawson
R.M. Eckman
N.F. Hukari
J.D. Rich
N.R. Ricks

Field Research Laboratory
Idaho Falls, Idaho

Air Resources Laboratory
Silver Spring, Maryland
December 2007



**UNITED STATES
DEPARTMENT OF COMMERCE**

**Carlos M. Gutierrez
Secretary**

**NATIONAL OCEANIC AND
ATMOSPHERIC ADMINISTRATION**

**VADM Conrad C. Lautenbacher, Jr.
Under Secretary for Oceans
and Atmosphere/Administrator**

**Office of Oceanic and
Atmospheric Research**

**Dr. Richard Spinrad
Assistant Administrator**

NOTICE

This report was prepared as an account of work sponsored by an agency of the United States Government. Neither the United States Government nor any agency thereof, or any of their employees, makes any warranty, expressed or implied, or assumes any legal liability or responsibility for any third party's use, or the results of such use, of any information, apparatus, product, or process disclosed in this report, or represents that its use by such third party would not infringe on privately owned rights. Mention of a commercial company or product does not constitute an endorsement by NOAA/OAR. Use of information from this publication concerning proprietary products or tests of such products for publicity or advertising is not authorized.

PREFACE

This Climatology is a product of the Field Research Division (FRD) of the Air Resources Laboratory (ARL). The ARL belongs to the National Oceanic and Atmospheric Administration's (NOAA) Office of Oceanic and Atmospheric Research (OAR). NOAA is a federal agency focused on the condition of the oceans and the atmosphere. It plays several distinct roles within the U.S. Department of Commerce:

A Supplier of Environmental Information Products. One of the most important resources in our society is information. NOAA supplies information to its customers that pertains to the state of the oceans and the atmosphere. This is clearly manifest in the production of weather warnings and forecasts through the National Weather Service, but NOAA's information products extend to climate, ecosystems and commerce as well.

A Provider of Environmental Stewardship Services. NOAA is also the steward of national coastal and marine environments. In coordination with federal, state, local, tribal and international authorities, NOAA manages the use of these environments, regulating fisheries and marine sanctuaries as well as protecting threatened and endangered marine species.

A Leader in Applied Scientific Research. NOAA is a trusted source of accurate and objective scientific information in four particular areas of national and global importance:

Ecosystems: Ensure the sustainable use of resources and balance competing uses of coastal and marine ecosystems, recognizing both their human and natural components.

Climate: Understand changes in climate, including the El Niño phenomenon, to ensure that we can plan and respond properly.

Weather & Water: Provide data and forecasts for weather and water cycle events, including storms, droughts, and floods.

Commerce & Transportation: Provide weather, climate, and ecosystem information to make sure individual and commercial transportation is safe, efficient and environmentally sound.

NOAA'S VISION

“An informed society that uses a comprehensive understanding of the role of the oceans, coasts and atmosphere in the global ecosystem to make the best social and economic decisions.”

NOAA's MISSION

“To understand and predict changes in the Earth's environment and conserve and manage coastal and marine resources to meet our nation's economic, social and environmental needs.”

ARL's MISSION

Within the broad science mission of NOAA, ARL conducts research on processes that relate to air quality and climate, concentrating on the transport, dispersion, transformation, and removal of trace gases and aerosols, their climatic and ecological influences, and exchange between the atmosphere and biological and non-biological surfaces. The time frame of interest ranges from minutes and hours to that of the global climate. Research in all of these areas involves physical and numerical studies, leading to the development of improved atmospheric models. ARL provides scientific and technical advice to elements of NOAA and other government agencies on atmospheric science, environmental problems, emergency assistance (Homeland Security), and climate change.

FRD's MISSION

The primary goal of FRD within the ARL mission is to advance the state of knowledge of the transport, dispersion, and removal of materials in the atmosphere. It places particular emphasis on the development of innovative measurement technologies and also on field experiments that use nontoxic tracers. The division works closely with other federal agencies, including the U.S. Departments of Energy, Defense, and Homeland Security. More locally, it works with several state and local-governmental entities, including the State of Idaho and the Shoshone Bannock Tribes.

NOAA'S 200th ANNIVERSARY

This year (2007), the National Oceanic and Atmospheric Administration (NOAA) is celebrating 200 years of science and service to the nation. From the establishment of the Survey of the Coast in 1807 by Thomas Jefferson to the formation of the Weather Bureau and the Commission of Fish and Fisheries in the 1870's, much of America's scientific heritage is rooted in NOAA. NOAA is dedicated to enhancing economic security and national safety through the prediction and research of weather and climate-related events and information service delivery for transportation, and by providing environmental stewardship of the nation's coastal and marine resources. Through the emerging Global Earth Observation System of Systems (GEOSS), NOAA is working with its federal partners, more than 60 countries and the European Commission to develop a global monitoring network that is as integrated as the planet it observes, predicts, and protects. In this bicentennial year of celebration, it is fitting that a climatology of the Idaho National Laboratory and of southeastern Idaho should be published using meteorological data obtained from the NOAA/INL Mesonet, a system contributing to the GEOSS vision.

HISTORICAL CONTENT

Numerous research and climatological reports have been published about the INL by ARLFRD or the various agency names under which this office has operated. Several preliminary reports were prepared in the late 1940's that described the expected climatology of the National Reactor Testing Station, as the INL was then called. The first series of reports using meteorological data acquired on-site was published during the time period 1958 to 1960 (IDO-12003, IDO-12004, and IDO-12015). A major addition to that original body of climatological literature was the first edition (1966) of the *Climatology of the National Reactor Testing Station* (IDO-12048). Each of these reports were written primarily to: 1) provide engineers, health physicists, scientists, and other researchers with a source of meteorological information pertinent to designing, locating, and operating nuclear reactors and support facilities, and 2) provide insight into the atmospheric aspects of health physics.

In December 1989, the first edition of the INL climatology was updated (*Climatology of the Idaho National Engineering Laboratory*, 2nd Edition, DOE/ID-12118) to include full 30-year normalized data, including averages and extreme values for most of the climatic parameters used in engineering design. It also included an updated treatment of atmospheric transport and dispersion from INL sources. The 2nd Edition reflected most notably the considerable strides in the state-of-the-science of atmospheric transport and dispersion that occurred in the 1970's and 1980's. Much of this progress was based on field validation of numerical models, some of which occurred at the INL.

By 1993, a telemetered weather observation network that reported not only winds and temperature, but also precipitation, atmospheric moisture, barometric pressure, and solar radiation was fully operational. This system provided continuous five-minute data for these parameters within each of the three climatic zones identified at INL: CFA (Central Facilities Area, southwest INL), SMC (Specific Manufacturing Capability, north end of INL), and MFC (Materials and Fuels Complex, southeast INL). Additionally, a radar wind profiler and acoustic sounding system (RASS), installed in 1992, has provided continuous upper air wind and temperature data throughout the atmospheric mixing layer. Over 10 years of quality-controlled data are now available from each of these systems for sources throughout the INL. Using these data, this third edition of the INL climatology builds significantly on the material found in its predecessors. Historical data summaries for now-discontinued monitoring locations have not been included in this edition, but are available from ARLFRD.

UNITS OF MEASURE

It is general NOAA policy to express all units of measure using the protocols established in the International System of Units [Système Internationale (SI)]. However, this document is intended not only for the scientifically oriented reader, but also for general public consumption. Therefore, following the prevailing local custom, SI convention is not strictly followed in this publication. Instead, the U.S. customary system, or American system, is used for such measures as distance and temperature. SI units are invoked only when they are commonly used in the United States.

TABLE OF CONTENTS

	<u>Page</u>
NOTICE.....	ii
PREFACE.	iii
NOAA’S VISION.	iii
NOAA’s MISSION.	iv
ARL’s MISSION.	iv
FRD’s MISSION.	iv
NOAA’s 200 th ANNIVERSARY.....	iv
HISTORICAL CONTENT.	v
UNITS OF MEASURE.	vi
TABLE OF CONTENTS.....	vii
LIST OF FIGURES.	xi
LIST OF TABLES.....	xix
INTRODUCTION.	1
HISTORICAL DEVELOPMENT.	1
CONTENTS.....	2
AREA PHYSIOGRAPHIC DESCRIPTION.....	3
METEOROLOGICAL DATA SOURCES.	7
NOAA INL MESONET.....	7
CFA THERMOSCREEN.....	13
RADAR WIND PROFILER AND RASS.....	15
ENERGY FLUX STATION.	16
DATA ACQUISITION HISTORY.	16
DATA QUALITY CONTROL.	17
REQUESTING HISTORICAL DATA.	17
GENERAL CLIMATOLOGY OF THE ESRP.	21
SPECIFIC CLIMATOLOGY.....	23
WIND.....	23
On-site Surface Wind Characteristics.	24
On-site Wind Averages and Maximums.	33
Regional Near-Surface Wind Flow Patterns.	36

Wind Trends..	36
Terrain Influences.	36
Atmospheric Stability Influences..	37
Mesonet Wind Field Clusters..	37
Wind Pattern 1..	38
Wind Pattern 2..	41
Wind Pattern 3..	43
Wind Pattern 4..	45
Wind Pattern 5..	47
Wind Pattern 6..	49
Wind Pattern 7..	51
Wind Pattern 8..	53
Occurrence of Wind Patterns by Season.	55
Winds Aloft.	61
Radar Profiler..	61
RASS.	61
Mean Winds and Persistence.	64
Surface Wind Channeling Mechanisms in the Snake River Plain..	64
AIR TEMPERATURE..	70
Daily Surface Air Temperature Ranges..	70
Surface Air Temperature Means and Extremes..	71
Temporal and Spatial Variability of Surface Air Temperature Means and Extremes	71
.....	71
Specific Surface Air Temperatures.	74
Heat Index.	75
Wind Chill.	76
Warm Season Duration.	76
Near-Surface Freeze/Thaw Cycles..	78
Degree Days Based on Surface Air Temperatures..	79
Upper Air Temperatures.	81
Profile Characteristics Above 250 ft. AGL	84
Soil Temperatures.	85
PRECIPITATION.	86
General Characteristics.	86
Design Storm and Return Periods.	89
Precipitation Characteristics Based on MESONET Five-Minute Data.	90
Snow.	93
ATMOSPHERIC MOISTURE.	96
Wet Bulb Temperature	97
Relative Humidity	98
Dew Point Temperature..	99
Mixing Ratio.	99
ATMOSPHERIC PRESSURE..	101

Station Pressure.	101
Air Density	101
SOLAR AND TERRESTRIAL RADIATION.	102
Sunrise and Sunset Times	102
Solar Radiation..	103
SURFACE ENERGY FLUX..	106
Soil Temperature.	106
Net Radiation.	107
Surface Soil Heat Flux	108
SPECIAL PHENOMENA	109
Dew.	109
Thunderstorms.	109
Lightning.	110
Hail..	114
Airborne Dust and Sand..	114
Dust Devils..	114
Blowing Snow	114
Icing.	115
Tornadoes..	115
RANGE FIRES.	117
ATMOSPHERIC TRANSPORT AND DIFFUSION.	121
THE ATMOSPHERIC BOUNDARY LAYER..	121
ATMOSPHERIC STABILITY.	123
TRANSPORT and DIFFUSION MODELING.	124
Gaussian Plume Model.	125
Gaussian Puff Model.	126
Lagrangian Particle Models.	127
Turbulence Estimation.	129
PROCESSES AFFECTING TRANSPORT AND DIFFUSION..	132
Effects of Source Configuration.	132
Removal Processes..	133
CLIMATOLOGICAL DISPERSION PATTERNS..	134
ACKNOWLEDGMENTS.	137
REFERENCES.	139
APPENDIX A: SURFACE AIR TEMPERATURE AVERAGES AND EXTREMES.....	A-1
APPENDIX B: PRECIPITATION AVERAGES AND EXTREMES.	B-1
APPENDIX C: NOAA INL MESONET WIND ROSES.	C-1

APPENDIX D: BLACKFOOT AND HAMER TOWER RELOCATION COMPARISON. .	D-1
BLACKFOOT.	D-1
Temperature.	D-1
Winds.	D-1
HAMER.	D-6
Temperature.	D-6
Winds.	D-6
SUMMARY.	D-6
 APPENDIX E: NOAA INL WEATHER CENTER.	 E-1
 APPENDIX F: NOAA/INL MESONET INSTRUMENTATION.	 F-1
INSTRUMENT SPECIFICATIONS	F-4

LIST OF FIGURES

	<u>Page</u>
Figure 1. INL location on Eastern Snake River Plain, Idaho.	3
Figure 2. ESRP terrain features at the INL..	4
Figure 3. The three distinct INL microclimate zones of the INL.....	5
Figure 4. On-site NOAA INL Mesonet stations as of December 2007.....	11
Figure 5. Off-site NOAA INL Mesonet stations as of December 2007.....	12
Figure 6. Example NOAA INL Mesonet station layout, with the addition of the community monitoring station kiosk (foreground) on the Idaho Falls Greenbelt near John’s Hole Bridge and Forebay.....	13
Figure 7. CFA thermoscreen is the longest and most complete set of temperature and precipitation data set at the INL	14
Figure 8. Radar wind profiler and RASS located near Grid 3, just north of INTEC.....	15
Figure 9. Day (top), night (middle), and all hours (bottom) wind roses for the 10 m (33 ft.) level at Grid 3..	26
Figure 10. Day (top), night (middle), and all hours (bottom) wind roses for the 61 m (200 ft.) level at Grid 3..	27
Figure 11. Day (top), night (middle), and all hours (bottom) wind roses for the 10 m (33 ft.) level at SMC..	28
Figure 12. Day (top), night (middle), and all hours (bottom) wind roses for the 46 m (150 ft.) level at SMC.....	29
Figure 13. Day (top), night (middle), and all hours (bottom) wind roses for the 10 m (33 ft.) level at MFC..	31
Figure 14. Day (top), night (middle), and all hours (bottom) wind roses for the 76 m (250 ft.) level at MFC.....	32
Figure 15. Wind pattern 1 wind vectors – low wind speed drainage flow from the northeast.. .	39

Figure 16. Temporal occurrence of wind pattern 1 - low wind speed drainage flow from the northeast..	40
Figure 17. Persistence of wind pattern 1 - low wind speed drainage flow from the northeast..	40
Figure 18. Wind vectors for wind pattern 2 – light winds and variable direction..	41
Figure 19. Temporal occurrence of wind pattern 2 – light winds and variable direction..	42
Figure 20. Persistence of wind pattern 2 – light winds and variable direction..	42
Figure 21. Wind vectors for wind pattern 3 – moderate upslope flow..	43
Figure 22. Temporal occurrence of wind pattern 3 – moderate upslope flow..	44
Figure 23. Persistence of wind pattern 3 – moderate upslope flow..	44
Figure 24. Wind vectors for wind pattern 4 – moderate synoptic effects and decreasing upslope flow after sunset..	45
Figure 25. Temporal occurrence of wind pattern 4 – moderate synoptic effects and decreasing upslope flow after sunset..	46
Figure 26. Persistence of wind pattern 4 – moderate synoptic effects and decreasing upslope flow after sunset..	46
Figure 27. Wind vectors for wind pattern 5 – well developed upslope flow..	47
Figure 28. Temporal occurrence of wind pattern 5 – well developed upslope flow..	48
Figure 29. Persistence of wind pattern 5 – well developed upslope flow..	48
Figure 30. Wind vectors for wind pattern 6 – down-canyon drainage flow aided by synoptic features..	49
Figure 31. Temporal occurrence of wind pattern 6 – down-canyon drainage flow aided by synoptic features..	50
Figure 32. Persistence of wind pattern 6 – down-canyon drainage flow aided by synoptic features..	50
Figure 33. Wind vectors for wind pattern 7 – strong synoptic effects yield SW winds...	51

Figure 34. Temporal occurrence of wind pattern 7 – strong synoptic effects yield SW winds. .	52
Figure 35. Persistence of wind pattern 7 – strong synoptic effects yield SW winds.....	52
Figure 36. Wind vectors for wind pattern 8 – strong synoptic effects yield NNE winds..	53
Figure 37. Temporal occurrence of wind pattern 8 – strong synoptic effects yield NNE winds.	54
Figure 38. Persistence of wind pattern 8 – strong synoptic effects yield NNE winds.....	54
Figure 39. Typical wind pattern occurrence during January..	55
Figure 40. Typical wind pattern occurrence during February..	55
Figure 41. Typical wind pattern occurrence during March..	56
Figure 42. Typical wind pattern occurrence during April..	56
Figure 43. Typical wind pattern occurrence during May.....	57
Figure 44. Typical wind pattern occurrence during June.....	57
Figure 45. Typical wind pattern occurrence during July..	58
Figure 46. Typical wind pattern occurrence during August.....	58
Figure 47. Typical wind pattern occurrence during September.....	59
Figure 48. Typical wind pattern occurrence during October.....	59
Figure 49. Typical wind pattern occurrence during November.....	60
Figure 50. Typical wind pattern occurrence during December..	60
Figure 51. Radar (Mode 2) data availability (%) as a function of time and height..	62
Figure 52. Radar (Mode 2) scalar wind speed (m s^{-1}) as a function of time and height..	62
Figure 53. Radar (Mode 2) vector wind speed (m s^{-1}) as a function of time and height..	63
Figure 54. RASS data availability (%) as a function of time and height.....	63
Figure 55. RASS virtual temperature (C) as a function of time and height.....	64

Figure 56. Radar (Mode 2) persistence (%) as a function of time and height.. 65

Figure 57. Expected relationship of surface winds within the Snake River Plain to winds aloft for different channeling mechanisms.. 67

Figure 58. Wind roses at the GRI tower 10 m level for night and daytime periods.. 68

Figure 59. Wind roses at the BLU tower for night and daytime periods.. 68

Figure 60. Frequency Diagram: GRI Tower 10 m Wind Direction vs Radar Profiler 1,577 m Wind Direction. (Rectangle sizes are scaled according to relative frequency of the GRI winds within 5° bins along the x axis).. 70

Figure 61. CFA 30-year average daily maximum and minimum air temperature from 1976 to 2005. 73

Figure 62. Average time of onset and dissipation of the nocturnal inversion as a function of time of year.. 83

Figure 63. Idaho Falls 46W (CFA) precipitation amount versus return years.. 90

Figure 64. Monthly traces of maximum daytime, average daytime, 24-hour, and nocturnal total daily net radiation.. 108

Figure 65. Lightning strike 5-year average density for period January 2000 through December 2004. 111

Figure 66. Lightning strike density across the INL during 2001.. 112

Figure 67. Lightning strike density across the INL during 2004.. 113

Figure 68. Tornado sightings in the ESRP according to National Climatic Data Base from 1950 through 2005. Each sighting is indicated by the strength (F0-blue dot, F1-green dot, and F2-red dot) and direction (arrow). 117

Figure 69. Wildland fire areas at INL from 1994 through 2007.. 119

Figure 70. Five-minute air temperature spike from July 1, 1994 range fire at DEA and BAS.. 120

Figure 71. Schematic diagram of ABL structure in fair weather.. 122

Figure 72. Plots of versus downwind distance as obtained by Markee (1963) for the five Pasquill stability classes.. 130

Figure 73. Contours of the 95th percentile TIC derived from hourly MDIFF model runs spanning the period from April 1993 to December 2001. The TIC values are normalized by the total mass Q of material released. The release points are (a) INTEC, (b) RWMC, (c) SMC, and (d) RTC.. 135

Figure 74. Contours of the 95th percentile TIC for (a) INTEC and (b) RTC using a larger model domain extending to about 60 km from the release points. As in Fig. 72, the TIC values are normalized by the total mass Q of material released... 136

Figure C-1. Day (top), night (middle), and all hours (bottom) wind roses for the 2 meter level at ABE... C-2

Figure C-2. Day (top), night (middle), and all hours (bottom) wind roses for the 15 meter level at ABE... C-3

Figure C-3. Day (top), night (middle), and all hours (bottom) wind roses for the 15 meter level at ARC.. C-4

Figure C-4. Day (top), night (middle), and all hours (bottom) wind roses for the 15 meter level at ATO.. C-5

Figure C-5. Day (top), night (middle), and all hours (bottom) wind roses for the 15 meter level at BAS... C-6

Figure C-6. Day (top), night (middle), and all hours (bottom) wind roses for the 15 meter level at BIG.. C-7

Figure C-7. Day (top), night (middle), and all hours (bottom) wind roses for the 15 meter level at BLK... C-8

Figure C-8. Day (top), night (middle), and all hours (bottom) wind roses for the 15 meter level at BLU... C-9

Figure C-9. Day (top), night (middle), and all hours (bottom) wind roses for the 15 meter level at CFA... C-10

Figure C-10. Day (top), night (middle), and all hours (bottom) wind roses for the 15 meter level at CIT.. C-11

Figure C-11. Day (top), night (middle), and all hours (bottom) wind roses for the 15 meter level at CRA.. C-12

Figure C-12. Day (top), night (middle), and all hours (bottom) wind roses for the 15 meter level at DEA.. . . . C-13

Figure C-13. Day (top), night (middle), and all hours (bottom) wind roses for the 15 meter level at DUB.. . . . C-14

Figure C-14. Day (top), night (middle), and all hours (bottom) wind roses for the 15 meter level at FOR... . . . C-15

Figure C-15. Day (top), night (middle), and all hours (bottom) wind roses for the 10 meter level at Grid 3.. . . . C-16

Figure C-16. Day (top), night (middle), and all hours (bottom) wind roses for the 61 meter level at Grid 3.. . . . C-17

Figure C-17. Day (top), night (middle), and all hours (bottom) wind roses for the 15 meter level at HAM... . . . C-18

Figure C-18. Day (top), night (middle), and all hours (bottom) wind roses for the 15 meter level at HOW... . . . C-19

Figure C-19. Day (top), night (middle), and all hours (bottom) wind roses for the 15 meter level at IDA.. . . . C-20

Figure C-20. Day (top), night (middle), and all hours (bottom) wind roses for the 2 meter level at KET... . . . C-21

Figure C-21. Day (top), night (middle), and all hours (bottom) wind roses for the 15 meter level at KET... . . . C-22

Figure C-22. Day (top), night (middle), and all hours (bottom) wind roses for the 15 meter level at LOS... . . . C-23

Figure C-23. Day (top), night (middle), and all hours (bottom) wind roses for the 10 meter level at MFC.. . . . C-24

Figure C-24. Day (top), night (middle), and all hours (bottom) wind roses for the 76 meter level at MFC.. . . . C-25

Figure C-25. Day (top), night (middle), and all hours (bottom) wind roses for the 15 meter level at MIN... . . . C-26

Figure C-26. Day (top), night (middle), and all hours (bottom) wind roses for the 2 meter level at MON..... C-27

Figure C-27. Day (top), night (middle), and all hours (bottom) wind roses for the 15 meter level at MON..... C-28

Figure C-28. Day (top), night (middle), and all hours (bottom) wind roses for the 15 meter level at NRF..... C-29

Figure C-29. Day (top), night (middle), and all hours (bottom) wind roses for the 15 meter level at RIC.. C-30

Figure C-30. Day (top), night (middle), and all hours (bottom) wind roses for the 15 meter level at ROB.. C-31

Figure C-31. Day (top), night (middle), and all hours (bottom) wind roses for the 15 meter level at ROV.. C-32

Figure C-32. Day (top), night (middle), and all hours (bottom) wind roses for the 15 meter level at RWM... C-33

Figure C-33. Day (top), night (middle), and all hours (bottom) wind roses for the 15 meter level at RXB.. C-34

Figure C-34. Day (top), night (middle), and all hours (bottom) wind roses for the 15 meter level at SAN... C-35

Figure C-35. Day (top), night (middle), and all hours (bottom) wind roses for the 10 meter level a SMC..... C-36

Figure C-36. Day (top), night (middle), and all hours (bottom) wind roses for the 46 meter level at SMC.. C-37

Figure C-37. Day (top), night (middle), and all hours (bottom) wind roses for the 15 meter level at SUG..... C-38

Figure C-38. Day (top), night (middle), and all hours (bottom) wind roses for the 6 meter level at SUM.. C-39

Figure C-39. Day (top), night (middle), and all hours (bottom) wind roses for the 15 meter level at TAB..... C-40

Figure C-40. Day (top), night (middle), and all hours (bottom) wind roses for the 15 meter level at TER.....	C-41
Figure C-41. Day (top), night (middle), and all hours (bottom) wind roses for the 15 meter level at TRA.....	C-42
Figure D-1. Average temperatures by hour and month of the old Blackfoot Mesonet station from 22 August 2001 through 26 May 2003....	D-3
Figure D-2. Average temperatures by hour and month of the new Blackfoot Mesonet station from 22 August 2001 through 26 May 2003....	D-3
Figure D-3. Temperature difference (multiplied by 10) between the new and old Blackfoot Mesonet station between 22 August 2001 and 26 May 2003.....	D-4
Figure D-4. Wind rose for the old Blackfoot Mesonet station from 23 August 2001 through 26 May 2003..	D-5
Figure D-5. Wind rose for the new Blackfoot Mesonet station from 23 August 2001 through 26 May 2003..	D-5
Figure D-6. Average temperatures by hour and month of the old Hamer Mesonet station from 1 April 1993 through 27 September 1999..	D-7
Figure D-7. Average temperatures by hour and month of the new Hamer Mesonet station from 22 January 2000 through 31 October 2007..	D-7
Figure D-8. Temperature difference (multiplied by 10) between the new and old Hamer Mesonet station..	D-8
Figure D-9. Wind rose for the old Hamer Mesonet station from 1 April 1993 through 27 September 1999..	D-9
Figure D-10. Wind rose for the new Hamer Mesonet station from 22 January 2000 through 31 October 2007.....	D-9
Figure E-1. Snapshot of the new NOAA INL Weather Center web page.....	E-1
Figure F-1. Example NOAA INL Mesonet station layout, with the addition of the community monitoring station kiosk (foreground) on the Idaho Falls Greenbelt at the John’s Hole Bridge and Forebay.	F-1

LIST OF TABLES

	<u>Page</u>
Table 1. NOAA INL Mesonet stations located inside the INL as of December 2007.....	8
Table 2. NOAA INL Mesonet stations outside the INL as of December 2007.....	9
Table 3. Changes to the INL Mesonet stations since the 2 nd Edition Climatology was published.	19
Table 4. Compilation of National Climatic Data Center (NCDC) temperature and precipitation records for observation stations on and surrounding the INL from the years 1981-1985. N/A indicates that the data is not available for a given station. Normals are average data from the 30 year period of 1951-1980..	22
Table 5. Monthly mean wind speed (mph) values for three NOAA INL Mesonet tower stations.	34
Table 6. Monthly peak ^a wind speed (mph) values for three NOAA INL Mesonet tower stations.	35
Table 7. Wind speed means and extremes for 10 meter tower level at station GRI..	35
Table 8. Average and maximum daily air temperature ranges summarized by month for CFA	.71
Table 9. Daily air temperature extremes summarized by month for CFA.	72
Table 10. Monthly and annual air temperature averages and extreme averages for CFA.....	72
Table 11. Monthly and annual average number of days (%) when the maximum daily air temperature was at or below 32° F and at or above 90° F at CFA.....	74
Table 12. Monthly and annual average number of days (%) when the minimum daily air temperature was at or below 32° F at CFA.....	75
Table 13. Average number of days per year in each heat index category and average number of days of heat days a year.....	76
Table 14. Dates of the last minimum air temperature of 24°, 28°, and 32° F in the spring, the first fall occurrence of these temperatures, and number of days between those dates for CFA.....	77
Table 15. Monthly and annual summary of daily freeze/thaw cycles for CFA ^a ..	79

Table 16. Monthly and annual average and extreme heating degree days (HDD) for CFA.	80
Table 17. Monthly and annual average and extreme cooling degree days (CDD) for CFA ^a	81
Table 18. Average onset and dissipation times of inversion and lapse air temperature profiles together with intensity values for CFA ^a	82
Table 19. Average total monthly and annual precipitation (water equivalent) for CFA ^a	87
Table 20. Ten greatest daily precipitation totals from CFA.	87
Table 21. Monthly and annual average number of days (%) on which precipitation was recorded at CFA.	88
Table 22. Longest periods at CFA without measurable (0.01 in. or greater) daily precipitation..	88
Table 23. Twenty greatest precipitation events ^a with longest duration from station GRI ^b	91
Table 24. Greatest precipitation amounts (inches) during selected periods at GRI.	92
Table 25. Average number of monthly precipitation events ^a at GRI.	93
Table 26. Monthly and annual snowfall totals and monthly and daily extreme totals for CFA..	94
Table 27. Ten greatest daily snowfall totals at CFA..	94
Table 28. Monthly and annual average number of days (%) and extreme number of days with snowfall amounts, of equal to or greater than 0.1, 1.0, and 3.0 in. for CFA.	95
Table 29. Monthly and annual average snow depths on the ground and extreme snow depths for CFA.	95
Table 30. Longest periods at CFA with continuous snow cover of 1.0 inch or greater.	96
Table 31. Monthly and annual averages and extremes of hourly wet bulb temperatures for station CFA.	97
Table 32. Monthly and annual averages of daily maximum and minimum wet bulb temperatures for station CFA.	98
Table 33. Monthly and annual relative humidity averages and extremes for CFA.	99

Table A-12. CFA daily surface air temperature extremes for November..... A-15

Table A-13. CFA daily surface air temperature extremes for December..... A-16

Table B-1. CFA daily precipitation averages..... B-1

Table B-2. CFA daily precipitation extremes for January..... B-3

Table B-3. CFA daily precipitation extremes for February..... B-4

Table B-4. CFA daily precipitation extremes for March. B-5

Table B-5. CFA daily precipitation extremes for April. B-6

Table B-6. CFA daily precipitation extremes for May.. B-7

Table B-7. CFA daily precipitation extremes for June.. B-8

Table B-8. CFA daily precipitation extremes for July..... B-9

Table B-9. CFA daily precipitation extremes for August..... B-10

Table B-10. CFA daily precipitation extremes for September.. B-11

Table B-11. CFA daily precipitation extremes for October..... B-12

Table B-12. CFA daily precipitation extremes for November..... B-13

Table B-13. CFA daily precipitation extremes for December..... B-14

INTRODUCTION

HISTORICAL DEVELOPMENT

This climatography is the most recent in a series of publications that are designed to provide meteorological statistics to support design engineering, facility operations, and operational safety at of the Department of Energy's (DOE's) Idaho National Laboratory (INL) and the Idaho Completion Project (ICP).

The INL was originally created under the Atomic Energy Commission (AEC) and was called the National Reactor Testing Station (NRTS). In 1949, the U. S. Weather Bureau, by agreement with the Reactor Development Division of the AEC, established a Weather Bureau Research Station as part of the Special Projects Section with a complete complement of meteorologists and technicians at the NRTS. The initial objective was to describe the meteorology and climatology of the NRTS with the focus on protecting the health and safety of site workers and nearby residents. The office provided a full range of hourly and daily climatological observations, including balloon soundings, which were transmitted to the U.S. Weather Bureau (and later the National Weather Service (NWS)) observations network.

After 15 years of operation, the first complete climatography of the area was published (Yanskey et al., 1966). It was based on an assemblage of four previous reports (DeMarrais, 1958a and 1958b; DeMarrais and Islitzer, 1960; and Johnson and Dickson, 1962. At that time, regular observation functions related solely to synoptic forecasting were reduced to allow for more intense research on atmospheric transport and diffusion. Basic meteorological observations

of the renamed Idaho National Engineering Laboratory (INEL) were continued, however, in order to satisfy DOE requirements.

In 1989, a second edition of the INL climatography was issued to integrate new information acquired since the publication of the first edition. The period of record that had been developed by that time provided full 30-year normalized climatological values for all important atmospheric parameters. The Second Edition Climatography (Clawson et al., 1989) supported the broad research mission of the Idaho National Engineering and Environmental Laboratory (INEEL). Building upon the atmospheric dispersion climatology of the first edition, it also included summaries of wind transport trajectories for sources near Central Facilities Area (CFA).

The Second Edition Climatography proved to be the single most popular publication of the Air Resources Laboratory Field Research Division (ARLFRD) with both on-site users and the general public. Today ARLFRD continues to furnish forecast and emergency support to DOE while reporting only basic climatological parameters to the National Climatic Data Center (NCDC).

In this most-recent edition, the majority of Mesonet data is updated through 2006 with some additional information updated through 2007. The order of topical presentation found in both the first and second editions are preserved. In addition to climatological parameters updated, the current INL climatography includes new insights on winds and temperatures aloft derived from remote sensing systems, channeled wind flows, statistical wind trajectory groupings, and precipitation return periods. Data are

presented in the context of three distinct local micro-climatic regimes (INL north-end, INL southwest, and INL southeast) that have emerged in recent assessments. It is anticipated that this most recent INL climatology will continue to be useful to planners and operations staff who support the most recent INL and ICP mission directives of revitalized nuclear reactor research and completion of the legacy cleanup.

CONTENTS

Chapter 2 provides a description of the topographical setting of the INL, and describes three INL local climate zones to provide a context for discussion of meteorological variables. Chapter 3 summarizes the data sources used for the climatology, including the mesoscale meteorological station network (mesonet), the use of historical thermoscreen parameters from CFA, the radar wind profiler with radio-acoustic sounding system (RASS), and the atmospheric sensible heat flux station. Chapter 4 discusses the general INL

climatology in the context of its topographical setting and geophysical setting. Chapter 5 comprises the specific climatology data for winds (including wind trajectories and cluster analyses), temperatures, precipitation, atmospheric moisture, solar/terrestrial radiation, atmospheric pressure, and special phenomena, including range fires. Chapter 6 presents updated information on atmospheric transport and diffusion.

Some information can best be presented in the independent format of the appendices. Appendix A presents climatological temperature means and extremes. Appendix B provides historical precipitation data including snow fall and snow depth information. Appendix C presents wind roses for the complete set of the NOAA INL Mesonet stations. Appendix D provides a data comparison of two Mesonet towers that were recently relocated. Appendix E explains the new NOAA/INL Weather Center web site, and Appendix F gives the NOAA/INL Mesonet instrument specifications.

AREA PHYSIOGRAPHIC DESCRIPTION

The climatology of the INL cannot be fully understood without knowledge of the topography and some of the geological features of the site itself and the surrounding area. The INL is located along the western edge of the Eastern Snake River Plain (ESRP) in southeastern Idaho (Fig. 1).

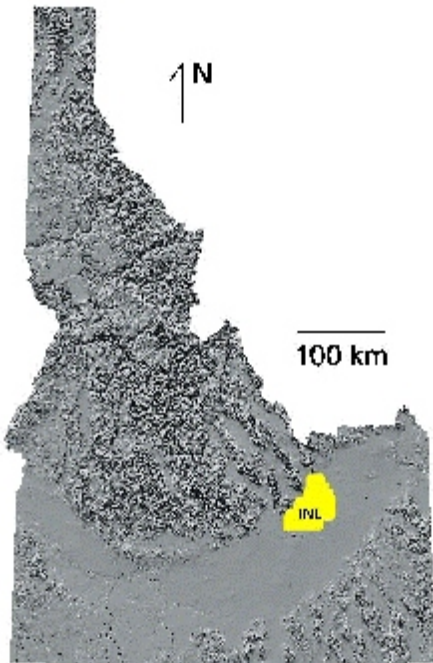


Figure 1. INL Location on Eastern Snake River Plain, Idaho.

The ESRP is the segment of the Snake River Plain that extends from Twin Falls, Idaho, to the Yellowstone Plateau as shown in Fig. 1. Lying at the foot of the Lost River, Lemhi and Bitterroot-Centennial Mountain Ranges, the INL occupies a 2,305 square kilometer (890 square mile) area. The mountains rise to approximately 3,354 m (11,000 ft.) above mean sea level (msl).

The general orientation of the ESRP is northeast to southwest. Long, deep mountain valleys bordering the INL immediately to the northwest, however, are oriented in a northwest-southeast direction.

The general surface of the INL, like that of the entire Snake River Plain, is rolling grass and sagebrush steppe broken by occasional lava outcroppings. The average elevation of the INL is about 1,524 m (5,000 ft.) msl (Fig. 2). A broad, low, volcanic ridge extends from Craters of the Moon National Monument along the southern edge of the INL and northeastward through the eastern INL to the south and east of the Mud Lake area. Two buttes, located in the southeast corner of the INL, rise approximately 427 m and 488 m (1,400 and 1,600 ft.) above the surface of the valley floor. Just a few miles south of the INL is the Big Southern Butte. This butte has an elevation of 2,310 m (7,576 ft.) msl and is a major landmark.

Three streams enter the ESRP from the northwest and flow through the INL across alluvial fans into playas or sinks. Due to seepage, evaporation, and substantial upstream water diversion for irrigation, the streams in the INL are often dry during the warm months of the year.

The two principal surface materials at the INL, according to the U. S. Geological Survey (Nace et al., 1975) are loess and olivine basalt. Other surface materials are sand, black basalt, playa deposits, alluvial-fan deposits, slope wash and talus, and lakebed sediments with associated beach and bar deposits. Plant life consists primarily of sagebrush and various grasses.

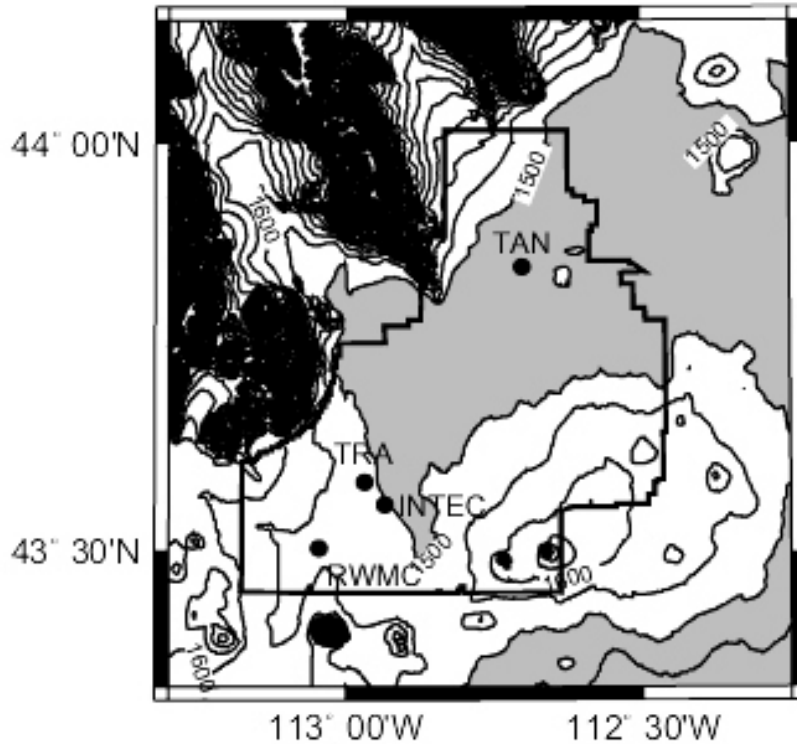


Figure 2. ESRP terrain features and valley floor elevations at the INL.

The physiographic features of the INL result in three distinct local-climatic zones, depicted in Fig. 3, that are apparent in the review of INL climatic data, and need to be considered when interpreting data for specific site assessments. The northwest INL (TAN southward to approximately NRF) is influenced by down-canyon winds and up-valley flows that originate in the southeast-to-northwest trending valleys that dominate the terrain northwest of the INL. The northwest INL is also influenced by rain-shadow effects of these mountains. The southwest INL (RTC, INTEC, CFA, WROC/PB, RWMC) is commonly influenced by shallow down-valley winds that are associated with the Big Lost

River channel from CFA to INTEC, as well as by strong pre-frontal southwesterly winds and frequent afternoon winds, also from the southwest, that result from the diurnal heating cycle. The southeast INL (MFC; EBR-II and TREAT) is isolated from the channeling flows that commonly affect the western portions of the site. In that area, temperatures, cloud cover, and surface winds are influenced by the subtle features of topography and higher elevation along the southern perimeter of the INL. The meteorological effects of these physiographic features will be clarified in later chapters as they relate to wind fields, transport and diffusion, air temperatures, and other atmospheric parameters.

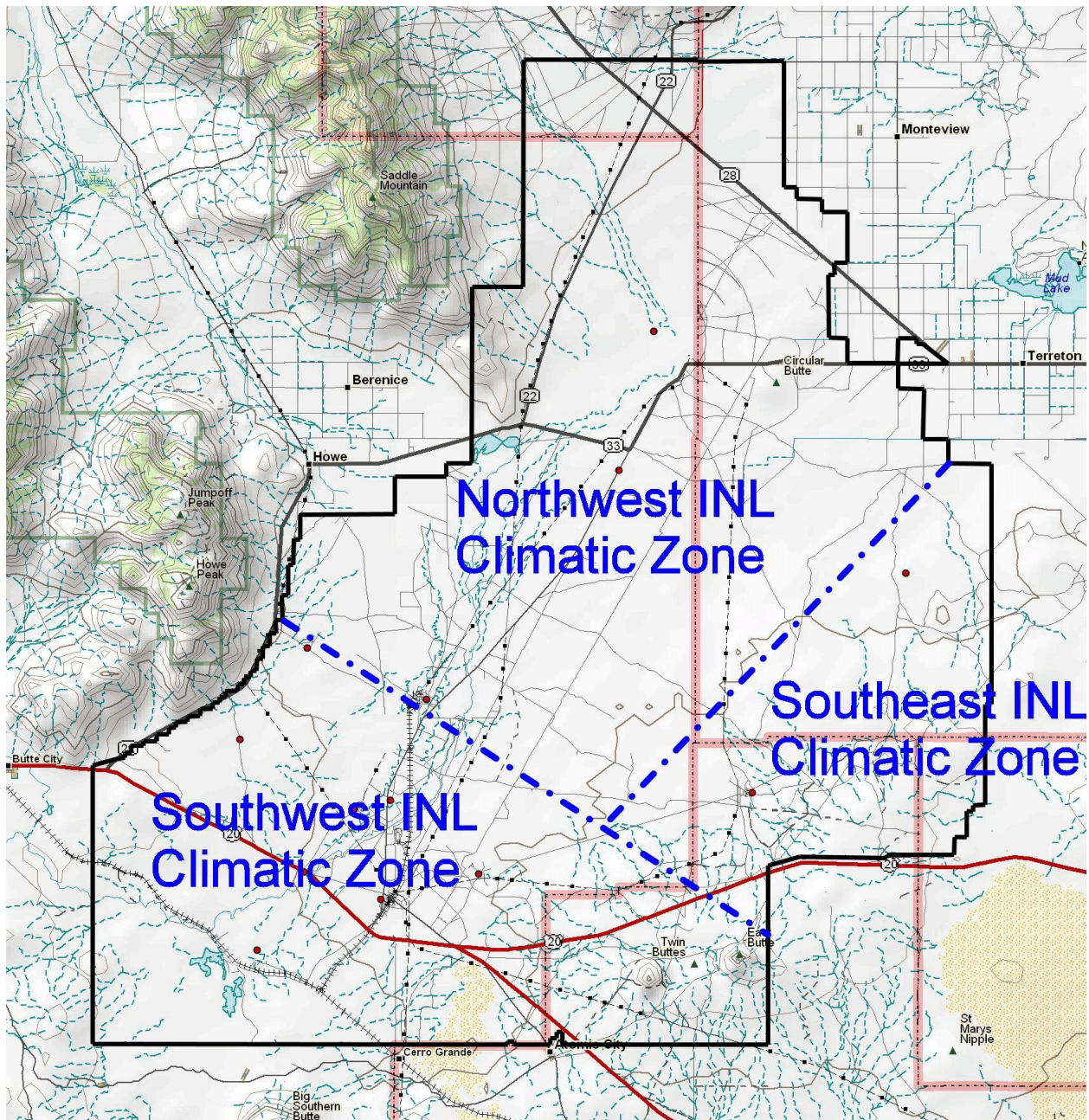


Figure 3. The three distinct INL local-climatic zones.

This page intentionally left blank.

METEOROLOGICAL DATA SOURCES

NOAA INL MESONET

The NOAA INL MESOscale meteorological monitoring NETWORK (Mesonet) began with a single station at the Central Facilities Area (CFA) in 1949. Between 1950-1970, six on-site and 16 off-site monitoring stations were added to form an expanded observational network. The number of meteorological monitoring stations continued to expand and change over the years in support of various projects and to gain a better understanding of the climatology of the INL and ESRP. The current configuration of the Mesonet meets the needs of INL planners, engineers, and operations personnel.

There were 35 meteorological observation stations in operation at the INL and surrounding area as of December 31, 2007. Thirteen of these were located within the boundaries of the INL (Table 1). The remaining stations are sited at key locations throughout the ESRP (Table 2) including several at schools and other places frequented by the public to enhance relations with the local communities. The station designator, location, elevation, and types of data being collected at each level on the tower are provided in the following tables.

Temperature and relative humidity are measured at all mesonet stations, at the conventional 2 m level. Wind measurements (speed and direction, gusts, and standard deviation of the wind direction) are currently made at all Mesonet stations, normally at 15m (50 ft.) above ground level.

Data is collected at each station by a datalogger and transmitted every 5-minutes by radio link back to the office. Data is also stored for a short time at each individual station and can be retrieved manually if the radio link breaks for an extended period of time. Most of the Mesonet data is recorded as averages or totals over a 5-minute period. The exceptions include the maximum and minimum temperature data that is measured as a 1-second average and wind gusts that originally measured a 1-second average but changed to a 3-second average to match the engineer standard in June 2006.

The locations of each tower comprising the Mesonet are depicted in Fig. 4 and Fig. 5 for on-site and off-site locations, respectively. A typical mesonet tower, representative of the configuration and instrument layout used throughout the array, is shown in Fig. 6.

Three on-site locations at Grid 3/INTEC (GRI), MFC, and SMC are designated as "primary" observation stations, and are more densely instrumented. Tall towers at these stations are equipped to measure winds and air temperatures up to 250 feet in addition to the measurements made at the mid and lower levels.

As shown in Tables 1 and 2, the Mesonet facilitates the collection of meteorological data throughout the INL region. Additional reported parameters include precipitation, atmospheric pressure, and solar radiation. All of these data are continuously being added to the INL climatological database and are available for customized analyses, as required.

Table 1. NOAA INL Mesonet stations located inside the INL as of December 2007.

Station ID	Station Name	Latitude (deg N)	Longitude (deg W)	Elevation		Bottom Level		Middle Level		Top Level		Other Data
				MSL (feet)		Data	Height	Data	Height	Data	Height	
690	CFA Building 690	43.532598	112.947757	4950		T,R	2m	W,t	15m	W,t	15m	P,S,B
BAS*	Base of Howe Peak	43.677557	113.006053	4900		T,R	2m	W,t	15m	W,t	15m	S,B
DEA*	Dead Man Canyon	43.624868	113.059840	5108		T,R	2m	W,t	15m	W,t	15m	S,B
	Materials and Fuels											
MFC	Complex	43.594138	112.651713	5143		T,R	2m	W,t	10m	W,t	10m	P,S,B
GRI	Grid 3/INTEC	43.589718	112.939855	4897		T,R	2m	W,t	10m	W,t	10m	P,S,B
	Specific Manufactur-											
SMC	ing Complex	43.859793	112.730253	4790		T,R	2m	W,t	10m	W,t	10m	P,S,B
LOS*	Lost River Rest Area	43.548538	113.008460	4983		T,R	2m	W,t	15m	W,t	15m	P,S,B
	Naval Reactor											
NRF	Facility	43.647887	112.911193	4847		T,R	2m	W,t	15m	W,t	15m	P,S,B
	Critical Infrastructure											
CIT	Test Range Complex	43.547477	112.869697	4910		T,R	2m	W,t	15m	W,t	15m	P,S,B
ROV	Rover	43.720590	112.529560	5008		T,R	2m	W,t	15m	W,t	15m	S,B
RWM	RWMC	43.503362	113.046030	5025		T,R	2m	W,t	15m	W,t	15m	P,S,B
SAN	Sand Dunes	43.779632	112.758165	4820		T,R	2m	W,t	15m	W,t	15m	P,S,B
	Reactor Technologies											
RTC	Complex	43.584612	112.968653	4937		T,R	2m	W,t	15m	W,t	15m	P,S,B

W: Wind (Mean Speed, Peak Speed, Mean Direction, Direction Standard Deviation)

T: Temperature (Mean Temperature, Maximum Temperature, Minimum Temperature)

t: Temperature (Mean Temperature)

R: Relative Humidity (Mean Relative Humidity)

P: Precipitation (Total Precipitation)

S: Solar Radiation (Mean Solar Radiation)

B: Barometric Pressure (Mean Pressure)

*: New station since 2nd Edition Climatology. (BAS and DEA started in April 1993, LOS started in April 1995.)

Table 2. NOAA INL Mesonet stations outside the INL as of December 2007.

Station ID	Station Name	Latitude (deg N)	Longitude (deg W)	Elevation MSL (feet)	Bottom Level		Middle Level		Top Level		Other Data
					Data	Height	Data	Height	Data	Height	
ABE	Aberdeen	42.954968	112.824550	4392	W,T,R	2m	W,t	15m			P,S,L
ARC	Arco	43.624522	113.297087	5290	T,R	2m	W,t	15m			P,S
ATO*	Atomic City	43.443700	112.812400	5058	T,R	2m	W,t	15m			P,S,B
	Big Southern										
BIG*	Butte (Base)	43.294095	113.181607	5200	T,R	2m	W,t	15m			
BLK	Blackfoot	43.189867	112.333300	4520	T,R	2m	W,t	15m			P,S,B
BLU	Blue Dome	44.074897	112.842082	5680	T,R	2m	W,t	15m			
	Craters of the										
CRA*	Moon	43.429115	113.538265	5996	T,R	2m	W,t	15m			B
DUB	Dubois	44.242393	112.201815	5465	T,R	2m	W,t	15m			P,S,B
FOR*	Fort Hall	43.019833	112.412068	4452	T,R	2m	W,t	15m			P,S,B
HAM	Hamer	44.007535	112.238845	4843	T,R	2m	W,t	15m			P,S
HOW	Howe	43.784113	112.977358	4815	T,R	2m	W,t	15m			

W: Wind (Mean Speed, Peak Speed, Mean Direction, Direction Standard Deviation)
T: Temperature (Mean Temperature, Maximum Temperature, Minimum Temperature)

t: Temperature (Mean Temperature)

R: Relative Humidity (Mean Relative Humidity)

P: Precipitation (Total Precipitation)

S: Solar Radiation (Mean Solar Radiation)

B: Barometric Pressure (Mean Pressure)

L: Soil Temperature (Mean Temperature)

*: New station since 2nd Edition Climatolgy. (ATO started in April 1995, BIG and CRA started in April 1993, and FOR started in March 1997).

Table 2 (Continued).

Station ID	Station Name	Latitude (deg N)	Longitude (deg W)	Elevation		Bottom Level Data	Bottom Level Height	Middle Level Data	Middle Level Height	Top Level Data	Top Level Height	Other Data
				MSL (feet)								
IDA	Idaho Falls	43.504078	112.050117	4709		T,R	2m	W,t	15m			P,S,B
KET	Kettle Butte	43.547555	112.326315	5190		W,T,R	2m	W,t	15m			P,S
MIN	Minidoka	42.804510	113.589783	4285		T,R	2m	W,t	15m			B
MON	Monteview	44.015378	112.535885	4797		W,T,R	2m	W,t	15m			P,S
RIC	Richfield	43.058408	114.134670	4315		T,R	2m	W,t	15m			P,S,B
ROB	Roberts	43.742210	112.125752	4760		T,R	2m	W,t	15m			P,S
RXB*	Rexburg	43.809483	111.800400	4870		T,R	2m	W,t	15m			P,S,B
SUG*	Sugar City	43.896578	111.737600	4895		T,R	2m	W,t	15m			B
SUM	Big Southern Butte (Summit)	43.396300	113.021800	7576		T,R	2m	W	6m			
TAB	Taber	43.318700	112.691875	4730		T,R	2m	W,t	15m			P,S
TER	Terreton	43.841650	112.418305	4792		T,R	2m	W,t	15m			P,S,B

W: Wind (Mean Speed, Peak Speed, Mean Direction, Direction Standard Deviation)

T: Temperature (Mean Temperature, Maximum Temperature, Minimum Temperature)

T: Temperature (Mean Temperature)

R: Relative Humidity (Mean Relative Humidity)

P: Precipitation (Total Precipitation)

S: Solar Radiation (Mean Solar Radiation)

B: Barometric Pressure (Mean Pressure)

*: New station since 2nd Edition Climatology. (RXB started in August 2001, SUG started in April 1993).

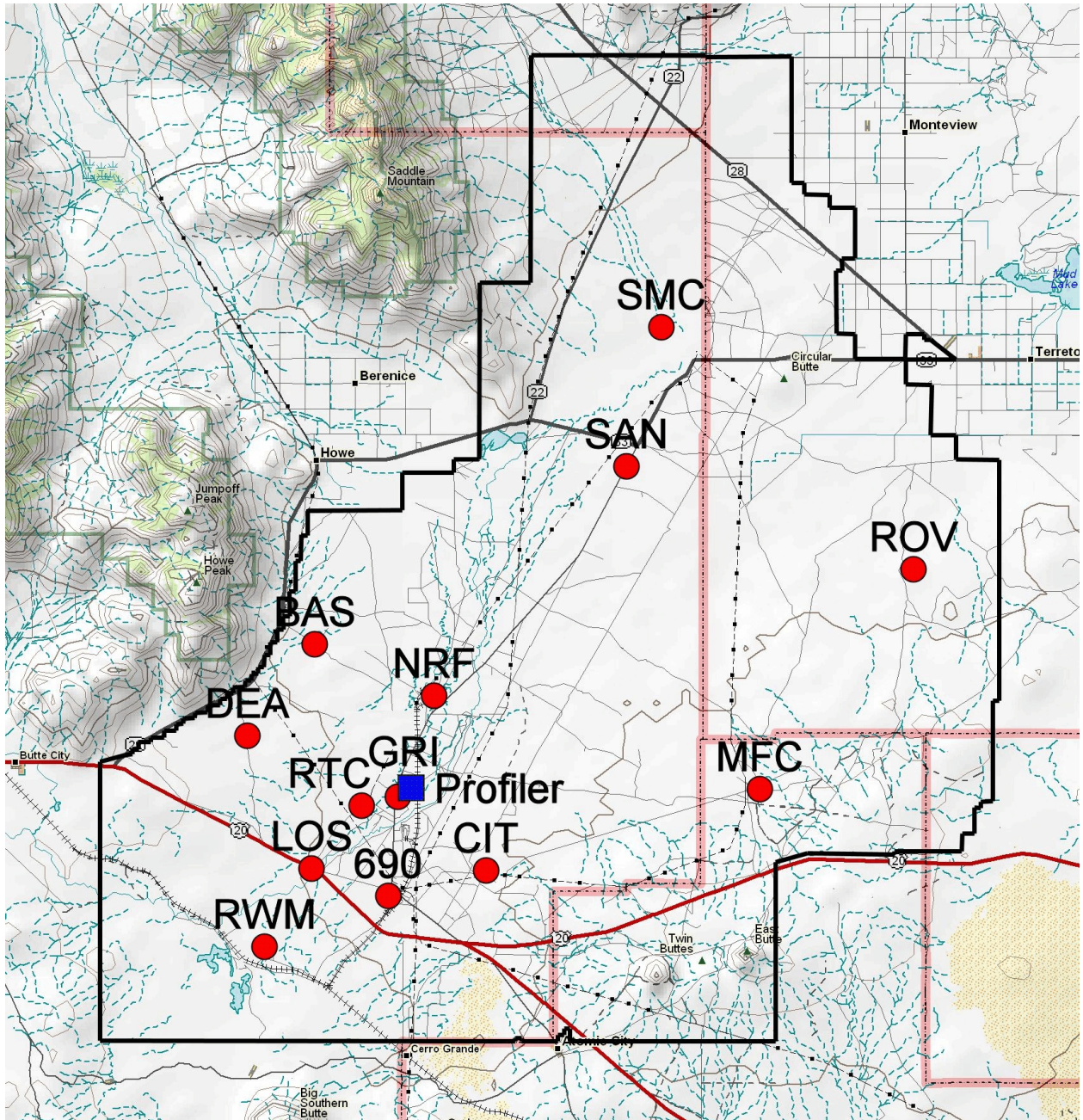


Figure 4. On-Site NOAA INL Mesonet stations as of December 2007.

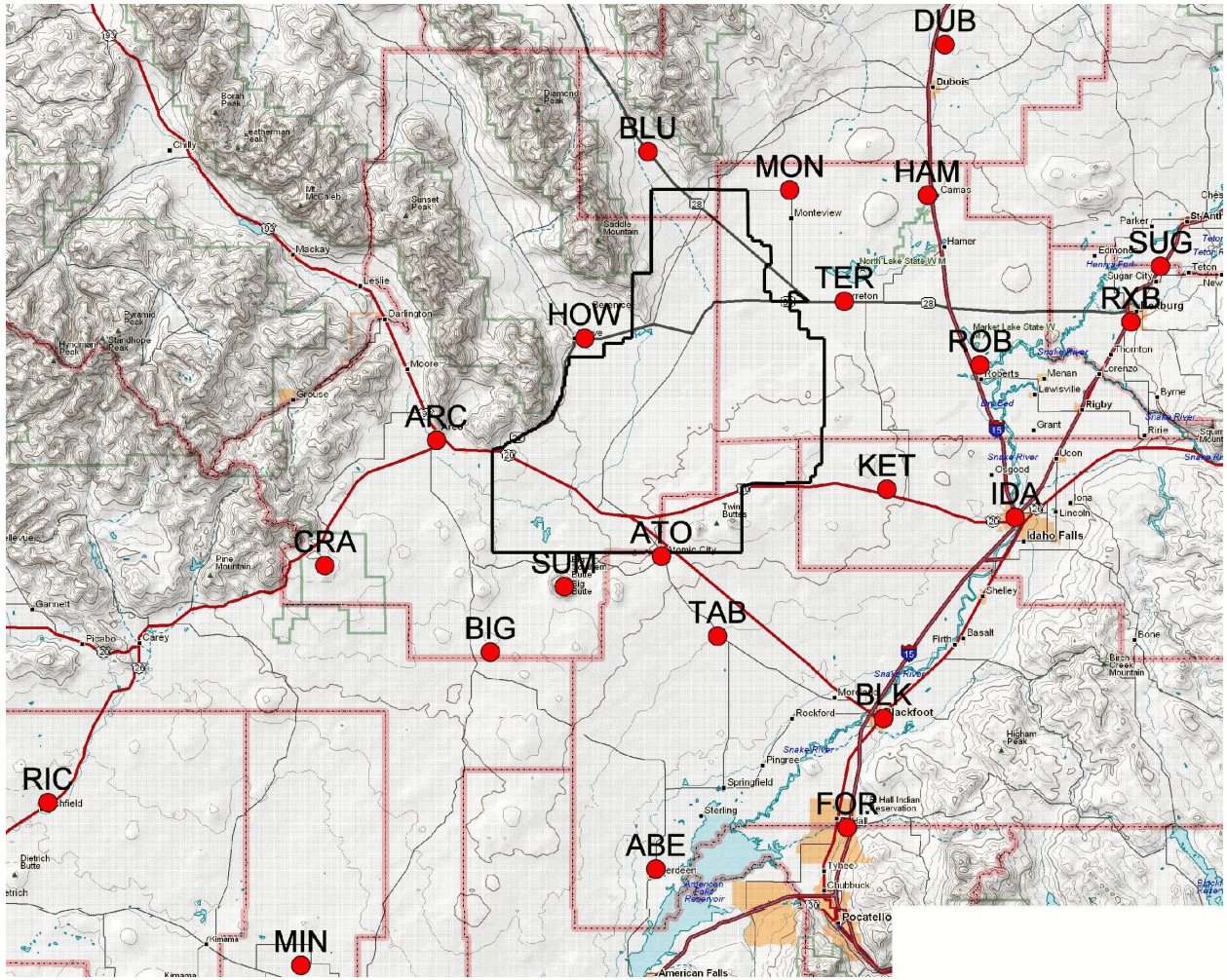


Figure 5. Off-Site NOAA INL Mesonet stations as of December 2007.



Figure 6. Example NOAA INL Mesonet station layout, Idaho Falls Greenbelt.

CFA THERMOSCREEN

The weather station at CFA, also established in 1950, was the first meteorological observation station established solely in support of the INL. The dataset is known as thermoscreen data because the

temperatures are recorded on a thermograph located inside a thermoscreen (also known as a Cotton Region Shelter) (Fig. 7). The thermoscreen station is different than a mesonet station in that the data set consists only of daily maximum and minimum temperatures, total precipitation, total snow-



Figure 7. CFA thermoscreen is the longest and most complete set of temperature and precipitation data set at the INL.

fall, and snow depth. Precipitation is collected in a range gauge about 15 feet away from the thermoscreen and manually measured weekly when the thermograph chart is changed. The graph is manually interpreted and the data are archived in the INL meteorological database. The total snowfall,

also recorded weekly, is estimated from the amount of precipitation recorded, temperatures at time of precipitation, and the INL weather camera. This dataset is what comprises the NWS cooperative observer station known as Idaho Falls 46W (or IDF 46W). The data from IDF 46W are also

included in the NOAA's National Climate Data Center database. This station has an uninterrupted record for air temperature and precipitation since its establishment, and continues to operate today.

RADAR WIND PROFILER AND RASS

In this edition, the climatology of upper winds and air temperature profiles have been derived from a radar wind profiler with Radar Acoustic Sounding System (RASS). The wind profiler measures the upper-level wind profiles and the RASS measures the upper-level temperature profiles. This system has operated continuously at a location near

INTEC (Fig.8) since 1994. In previous editions of this report, upper air data were derived from uninstrumented pilot balloons (PIBALs) taken at CFA and TAN, and from radiosonde soundings (RAWIN) taken at CFA. Because of the rapid ascent of the RAWIN, however, very limited resolution within the mixing layer was available. The radar wind profiler with RASS provides highly-resolved round-the-clock data for mixing layer characteristics above the sounding site that are much superior to the twice-per-day soundings that formed the previous upper air record. Researchers interested in INL upper tropospheric data above the ceiling capability of the RASS should refer to the balloon soundings



Figure 8. Radar wind profiler and RASS located near INTEC.

summaries in Section V of the 2nd Edition Climatology (Clawson et al., 1989).

The radar profiler has a vertical range of approximately 150 to 4,000 m with a vertical resolution of 60 to 100 m. Remotely-sensed measurements include horizontal wind speed (u) and direction (Θ), the standard deviation of the horizontal wind direction (σ_{Θ}), and vertical wind speed (w). In addition, the radar estimates the refractive index structure parameter (C_N^2). This value is a direct measurement of the turbulent intensity of humidity fluctuations in the atmospheric boundary layer and is useful for estimating the mixed layer height (z_i).

FLUX STATION

Since 1999, ARLFRD has operated a surface flux station that encompasses two individual towers at Grid 3 using instrumentation at the 2 m level. This flux station provides information on how the INL climate interacts with the global energy cycle. One tower measures the surface energy budget, the amount of energy gained or lost from the ground. The measurements include solar radiation, soil temperature, net radiation, soil moisture and soil heat flux. The second tower measures water vapor (H_2O) and carbon dioxide (CO_2) fluxes. These are major greenhouse gases that contribute to an offset in the global energy budget and warmer global temperatures. Data from this station also provide both energy and momentum fluxes. Climatology data from this station are also useful for estimating atmospheric stability, a standard input required by many dispersion models. A few of the measurements from the flux station are included in this report, however a more detailed summary of the global energy cycle including the CO_2 and H_2O fluxes, and the

surface energy budget may be summarized in a future addition of the climatology.

DATA ACQUISITION HISTORY

ARLFRD began collecting meteorological data with the installation of the first station at CFA in 1950. The collection of the data was done manually by a strip chart recording system. This original system was replaced and automated during the 1969-1970 time period with radio telemetry equipment.

The data collection of the monitoring stations in the 1970's and 1980's was an evolving and complex situation. The most complete description of the hardware and software collection of the Mesonet data during this time can be found in Ackermann and Johnson, 1989. A brief synopsis is provided below.

Several different computer systems were used to archive the data on strip chart recorders, printers, tape recorders, magnetic tapes, and optical drives over the two decades. Between 1978 and 1980, a new computer system began ingesting the data by modem. Data for emergency situations were available within 15 to 30 minutes which at the time was considered sufficient. In 1984, ARLFRD moved its offices into Idaho Falls and so the data had to be transmitted using analog transmitter/receiver pairs. In 1986 another new computer system came online that brought all of the data into a single place. Prior to this time, off-site and few non-essential meteorological stations were managed by DOE and eventual DOE contractor EG&G. Chart recorders continued to be used for forecasts and in support of emergency operations. Unfortunately up until this time the data acquisition still did not

allow for real-time emergency support or user interface for computer aided forecasting.

In 1993, a major upgrade of the Mesonet was undertaken to focus on the need for simultaneous quality-controlled data for the entire ESRP that could define atmospheric transport, as well as local subtleties in climate at each site area, and for real-time emergency support. A completely new digital data recording and telemetry system was developed at ARLFRD. This new system was called the Real-Time Monitoring System (RTMS). This system reported not only winds and temperature, but also precipitation, atmospheric moisture, and solar radiation. The RTMS provided continuous 5-minute data for these parameters within each of the three climate zones. Over 13 years of quality-controlled RTMS data are now available for stations throughout the INL and ESRP. Another minor upgrade to the RTMS was completed in 2004 with new telemetry hardware and data recording hardware. Data recoveries for the numerous meteorological parameters are generally in excess of 99% and make the RTMS a very reliable system.

The majority of the data used in this climatological report are based off of the RTMS from January 1994 through December 2006 or CFA thermograph data from January 1950 through December 2006. The dates selected for this report were based on the first and last full years of complete data for these systems. Using partial yearly data would skew the yearly averages.

In a few cases (e.g., soil temperatures), some climatological data in this report are carried over from historical measurements made at CFA, since an adequate period of record existed for these parameters, and

measurements for those parameters are not part of the current program.

DATA QUALITY CONTROL

The NOAA INL Mesonet has a detailed and comprehensive data quality assurance program. ARLFRD has adopted the standard DOE ANSI 3.11 meteorological guidelines for data quality control. To help follow these guidelines the quality assurance program uses an excellent software display of trended meteorological data which enhances the data quality evaluations and makes them more efficient. Every 5-minute period for every station is plotted for missing or spiked data. Data is also screened for electronic noise, non-working aspirators that effect temperature and relative humidity values, orientation errors in the wind direction, stalled wind sensors, rime icing in the winter that degrade wind speeds, and other erroneous values caused by maintenance, sprinklers, bird droppings, or any other small animal. Plotting the data allows the meteorologist to flag any of the problems in the database and if needed be fixed quickly by a technician.

REQUESTING HISTORICAL DATA

Researchers who require analyses of historical non-Mesonet climatological data must exercise care when working with older data. Some stations have been known by more than one name. Other stations have been relocated, discontinued, or combined. Stations have been moved because of private property owners selling the land, changing landscapes (such as new construction or better exposure to the weather), or for public relations such as a community monitoring station (CMS).

Nonetheless, relocation of stations, even over short distances, can have huge implications on the historical data. Appendix D compares two Mesonet stations (Blackfoot and Hamer) that were recently relocated. Large differences were often found between the new and old stations in both temperature and wind speed and direction data.

Table 3 lists all of the changes that have occurred to Mesonet stations since the 2nd Edition INL Climatology. Other problems

using historical data may arise because the data averaging was every 6 minutes compared to the current 5 minutes with the RTMS. Therefore, caution is advised when working with older data. Details on the nomenclature, capabilities and the period of record of the historical stations (including discontinued stations) are summarized in the 2nd Edition Climatology (Clawson et al., 1989.) Note: no stations have been discontinued or combined since the 2nd Edition Climatology.

Table 3. Changes to NOAA/INL Mesonet stations after publication of the 2nd Edition Climatology.

Station Name Changes				
<u>New ID</u>	<u>New Station Name</u>	<u>Old ID</u>	<u>Old Station Name</u>	<u>Date of Change</u>
<u>On-Site</u>				
ATR	Advanced Test Reactor Complex	RTC	Reactor Technology complex	Sep-08
		TRA	Test Reactor Area	Mar-06
CIT	Critical Infrastructure Test Range Complex	PBF	Power Burst Facility	Mar-06
GRI	Grid 3/INTEC	GRD3	Grid 3	Apr-93
MFC	Materials and Fuels Complex	ANL ^a	Argonne National Laboratory-West	Mar-06
RWM	Radioactive Waste Management Complex	RWMC	(unchanged)	Apr-93
SAN	San Dunes	DUN	(unchanged)	Apr-93
SMC	Special Manufacturing Capability	LOFT ^b	Loss of Fluid Test	Mar-06
<u>Off-Site</u>				
ABE	Aberdeen	ABN	(unchanged)	Apr-93
COX	Cox's Well	BIG	Big South Butte (Base)	Mar-06
		BSN		Apr-93
BLU	Blue Dome	BDM	(unchanged)	Apr-93
DUB	Dubois	DBS	(unchanged)	Apr-93
HAM	Hamer	HMR	(unchanged)	Apr-93
IDA	Idaho Falls	IDF	(unchanged)	Apr-93
KET	Kettle Butte	KTB	(unchanged)	Apr-93
MON	Montevieu	MTV	(unchanged)	Apr-93
RIC	Richfield	RCH	(unchanged)	Apr-93
ROB	Roberts	RBT	(unchanged)	Apr-93
TAB	Taber	TBR	(unchanged)	Apr-93
TER	Terreton	TRN	(unchanged)	Apr-93
Relocated Stations				
<u>Station</u>	<u>Old Lat.</u>	<u>Old Long.</u>	<u>Date moved</u>	<u>Description</u>
DUB	44.16890	112.22450	Apr-93	Moved as part of the RTMS upgrade.
KET	43.53430	112.31900	Apr-93	Moved as part of the RTMS upgrade.
MIN	42.83684	113.57388	Apr-93	Moved as part of the RTMS upgrade.
STA	43.97100	111.68300	Apr-93	Moved to SUG to have better weather exposure.
ABE	42.95497	112.82460	Jun-96	Moved because the property sold.
IDA	43.51130	112.05970	Jun-97	Moved to Idaho Falls Greenbelt to become a CMS ^a .
TER	43.81162	112.41410	Aug-97	Moved to become a CMS ^a .
RWM	43.50173	113.04020	Jun-98	Moved because building construction blocked wind flow.
HAM	43.96278	112.16670	Nov-99	Moved because development of linear sprinkling system.
LOS	43.54854	113.00846	Jun-07	Moved across parking lot to expand the rest area.
Discontinued Stations				
<u>Station</u>	<u>Old Lat.</u>	<u>Old Lon.</u>	<u>Date Discontinued</u>	<u>Description</u>
CFA	43.529	112.944	May-97	Moved because of safety issues with the tower.
BLA	43.25601	112.3971	May-03	BLA discontinued to allow BLK to become CMS ^c .

a. Station also known as EBR II-Experimental Breeder Reactor II.

b. Station also known as TAN - Test Area North.

c. Community Monitoring Station (CMS).

This page intentionally left blank.

GENERAL CLIMATOLOGY

The location of the INL in the ESRP, including altitude above sea level, latitude, and inter-mountain setting, affects the climate of the site. Moist air masses coming from the Pacific Ocean lose much of their moisture as they move over mountains between the Pacific coast and the ESRP. As a result, annual rainfall at the INL is light. The type of precipitation at the INL is dependant upon the season. In the summer, precipitation most often falls as rain showers or thunderstorms. In the spring and autumn rain showers, or periods of rain or snow may occur. Most precipitation during the winter comes as snow. Precipitation can occur in any month, but the heaviest accumulations are generally in the spring or early summer. Most intense rainfall is associated with thundershowers.

The ESRP is classified as an arid climate with overall light annual rainfall. The relatively dry air and infrequent low clouds permit intense solar heating of the surface during the day and rapid radiational cooling at night. These factors combine to give a large diurnal range of temperature near the ground.

The moderating influence of the Pacific Ocean produces a climate which is usually warmer in the winter and cooler in summer than is found at locations with similar latitudes in the more continental regions of the United States to the east of the Continental Divide. The Centennial and Beaverhead Mountain Ranges act as an effective barrier to

movement of most of the intensely cold winter air masses that pass to the south out of Canada toward the ESRP. Occasionally, however, cold air spills over the mountains and is trapped in the ESRP. The INL then experiences below normal temperatures for periods lasting usually a week to 10 days.

The orientation of the ESRP tends to channel surface winds along a southwest-northeast axis. This channeling is caused by several factors, most notably the steering of synoptic winds by the topography and the pressure of diurnal thermally driven circulations within the ESRP. Locations on the west side of INL often are affected by more local winds generated by the tributary valleys to the west of INL.

A summary of recent climatological data from 14 NCDC stations on and surrounding the INL (U. S. Department of Commerce, 1980-1985) is given in Table 3. The data have been compiled for a common time period (January 1981 through December 1985) to facilitate a climatological comparison of these sites. The data include average annual statistics for air temperature and precipitation. Normal annual air temperatures and precipitation levels, which are an average of the 30-year period of 1951-1980, are also provided where available. Data listed under the heading "Upper Snake River Plains Division", is an average of all NCDC stations in the ESRP, and represents the average regional climate.

Table 4. Compilation of National Climatic Data Center (NCDC) temperature and precipitation records for observation stations on and surrounding the INL from the years 1981-1985. N/A indicates that the data is not available for a given station. Normals are average data from the 30 year period of 1951-1980.

National Climatic Data Center ID	Elevation (ft. msl)	Absolute Maximum Temperature (deg F)	Absolute Minimum Temperature (deg F)	Annual Average Temperature (deg F)	Annual Average Cooling Degree Days (DGD/yr)	Annual Average Heating Degree Days (DGD/yr)	Absolute Maximum Daily Precip (in.)	Annual Average Snowfall (in)	Annual Average Precip (Normal) (in)
Aberdeen Exp. Station	4405	98	-38 ^a	42.9 ^a (44.8)	247 ^a (269)	7975 ^a (7633)	0.76 ^a	N/A	10.23 ^a (8.81)
Arco 3 SW	5328	97	-45 ^b	40.9 ^d	217 ^b (204)	7286 ^a (8613)	1.64 ^c	N/A	14.35 ^b
Blackfoot 2 SSW	4487	97	-24 ^b	43.6 ^d	409 ^d	6144 ^a	1.36	N/A	10.20 ^c (10.70)
Craters of the Moon	5897	95	-37	42.4 ^c	355 ^c	7751	2.00 ^c	121.9 ^a	17.71 ^a
Dubois Exp Station	5450	98	-25	42.4 (42.7)	335 (301)	8250 (8424)	1.25	50.9	16.05 (11.74)
Hamer 4 NW	4791	98	-46 ^a	38.7 ^d (42.5)	116 ^c (262)	8352 ^a (8441)	0.81 ^c	31.8	11.49 ^a (8.46)
Howe	4820	97 ^a	-38 ^a	43.0 ^c	244 ^c	7890	2.02 ^c	19.8	10.16 ^c (8.85)
Idaho Falls 2 ESE	4765	98 ^a	-34 ^b	45.5 ^c	393 ^b	7480 ^a	1.13 ^c	39.1 ^c	16.39 ^b
Idaho Falls FAA AP	4730	100	-38	42.8 (43.8)	309 (288)	8094 (7995)	0.97	43.5	12.89 (9.77)
Idaho Falls 46 W	4938	99	-47	40.7 (42.0)	272 (253)	8840 (8626)	1.51	28.3	10.31 (8.62)
Mimidoka 10 WNW	4290	105 ^c	-30 ^c	40.3 ^d	343 ^c	7551 ^c	1.95	N/A	10.73
Rexburg Ricks College	4290	97 ^a	-31 ^b	43.7 ^b	310 ^b	7948 (7443)	1.40 ^c	75.1	17.39 ^b
Richfield	4306	100	-28	44.4 (45.4)	369 (332)	7546 (8398)	1.36	39.5	14.51 (11.09)
St. Anthony 1 WNW	4950	95	-39	41.6 ^b (42.2)	104 ^b (146)	8297 ^a	1.14 ^b	N/A	14.50 ^a
Upper Snake River Plains	N/A	N/A	N/A	43.1 (43.9)	N/A	N/A (N/A)	N/A	N/A	14.62 (11.21)

- a. Data missing for all or part of 1 year.
- b. Data missing for all or part of 2 years.
- c. Data missing for all or part of 3 years.
- d. Data missing for all or part of 4 years.

SPECIFIC CLIMATOLOGY

This section presents climatological relationships for specific meteorological parameters, including winds, air temperature, precipitation, atmospheric moisture content, and atmospheric pressure. Winds provide the most important transport mechanism affecting site operations and potential off-site impacts; therefore, the wind regime on and around the INL has been monitored in detail for many years. Wind data comprise the largest portion of the INL climatological database. Air temperature reflects the thermal energy that drives many atmospheric processes and is related to atmospheric stability and turbulence. Air temperature has been monitored in detail for many years and comprises the second largest portion of the database. Both of these parameters are currently monitored at many locations both on and offsite (Tables 1 and 2).

Precipitation, atmospheric moisture, atmospheric pressure, and solar and terrestrial radiation also comprise a portion of the climatological database. These parameters are currently being measured at the INL. Other parameters which have been measured in the past, but for which observations have been discontinued include soil temperature and the state or condition of the ground. Other special atmospheric phenomena have been observed and are found in the climatological database. Descriptions and summaries of each of these types of data are found in the following sections.

WIND

Wind speed and direction (always recorded as the direction from which the wind is blowing) have been continuously monitored

at a large number of stations on and surrounding the INL since 1950. The network of wind stations supporting operational requirements at the INL has expanded considerably since the installation of the original six stations. The original stations were upgraded and new sites were established to form an expanded observational network using 50 ft. towers. There were 35 meteorological observation stations in operation at the INL and surrounding area as of December, 2007. Thirteen of these are located within the boundaries of the INL (Table 1) while the remainder are sited at key locations throughout the ESRP (Tables 2). Knowledge of the general wind flow patterns on the INL is based on these data records.

The wind pattern over the INL can, at times, be quite complex. The orientation of the bordering mountain ranges, as well as the general orientation of the INL, plays an important part in determining the wind regime. The INL is within the latitudes of prevailing westerly winds but these are normally channeled by the topography. This channeling usually produces a west-southwest or southwest wind. When the prevailing westerlies at the gradient level (at mountain-top levels approximately 1,524 m (5,000 ft.) above the surface) are strong, the winds channeled across the INL between the mountains become very strong. Some of the highest wind speeds at the INL are observed under these meteorological conditions. The greatest frequency of this wind is in the spring.

Local mountain and valley features exhibit a strong influence on the wind flow under other meteorological conditions as well.

When the winds above the gradient level are strong and from a northwesterly direction, channeling in the ESRP usually continues to produce southwesterly winds over most of the INL. At the mouth of Birch Creek however, the northwest to southeast orientation of this valley channels strong north - northwest winds into the SMC area. This "Birch Creek" wind may equal the strongest southwesterly winds recorded at other locations on the INL.

Drainage winds also contribute to the overall wind flow over the INL. On clear or partly cloudy nights with only high thin clouds, the valley experiences rapid surface radiational cooling. This results in a cooling of the air near the surface that causes the air to become stable and less turbulent. However, air along the slopes of the mountains cools at a faster rate than the air at the same elevation located aloft over the valley. Consequently, it becomes more dense and flows or sinks toward the valley floor, forming a down-slope wind. When this air reaches the valley, it still flows toward lower elevations and becomes a down-valley wind. Based on wind roses, the nocturnal down-valley flow is the second most frequent wind observed over the INL, and flows primarily out of the north-northeast.

A reverse flow, opposite in direction to that of the drainage wind, occurs during the daytime when the air along slopes is heated more rapidly than air at the same elevation over the valley. The air rises up the slopes as it becomes less dense. This results in both up-slope and up-valley winds. Up-valley winds are seldom detectable as a separate component of the wind until the synoptic pressure gradient becomes quite weak. Although the mountain and valley winds are predominantly "fair weather" phenomena, they can also occur under other sky cover conditions.

In addition to the local drainage winds, a somewhat stronger wind has been observed. It develops during an outbreak of cold air east of the Continental Divide during the winter and behaves in the same manner as the down-valley wind. If the cold air becomes deep enough, it spills over the Continental Divide and flows down across the INL. The result of this phenomenon is valley winds from the northeast.

Pressure gradient forces related to passing synoptic weather systems, as well as local storms, all affect the winds of the INL. These storms alter the local flow regime such that winds from any direction can be observed. The frequency of occurrence of these types of wind flow patterns is very small, however.

On-site Near-Surface Wind

The characteristics of the near-surface winds at the INL can best be described using a graphical display called a wind rose. Wind roses are graphs that display the frequency (in percentages) of the occurrence of winds from various direction sectors for selected speed classes. This is an effective method of showing joint wind speed and direction frequency distributions at a glance. The differences between stations, seasons, sensor levels, stability classes, etc., are easily seen.

The geography of the INL results in three general climatic zones (southwest including Grid 3 (GRI), CFA, CIT, RTC, and RWMC; northwest including NRF, TAN, and SMC; and the southeast, including MFC and TREAT). Tall towers are located within each of these areas (GRI, SMC, and MFC, respectively) to document climatic characteristics that are specific to each area.

Wind roses for GRI are illustrated in Figs. 9 and 10. The GRI tower is located approximately one mile north of INTEC on the east side Lincoln Boulevard, and is representative of wind flow patterns over the southwest INL. In this 3rd edition of the climatology, GRI replaces CFA as the source of tall tower data for this portion of the INL. GRI has the advantage of being sited close to the Lost River channel, where it is easily influenced by both general down-valley (northeast) breezes that develop during the night and by a shallow surface flow that moves down the Lost River Channel (from the southwest). The figures present all-stability, annual wind roses as a function of sensor height and time of day (day, night, and all hours). Data for GRI are obtained from the 10 m and 61 m levels. The GRI data lead to the following conclusions:

1. A distinct channeling effect of the wind is apparent. The directions with the highest percentages of occurrence are the west-southwest to southwest and north-northeast to northeast quadrants.
2. A very small percentage of the wind direction originates from the southeast and northwest quadrants.
3. Much higher wind speeds are observed during lapse conditions (usually daytime)

than during inversion (usually nighttime) conditions.

4. Higher wind speeds and therefore, a smaller frequency of calms (period of very low wind speeds), are observed at the 61 m level.
5. A higher frequency of calm periods occurs during the winter months while the lowest frequency of calm periods occurs during the spring months.
6. Nighttime wind directions are often different between the 10 m and 61 m levels due to the limited vertical mixing within the atmosphere during inversion (usually nighttime) conditions.

Wind roses for SMC are illustrated in Figs. 11 and 12. This tower is located immediately northeast of the historic Aircraft Nuclear Propulsion (ANP) hangar, and is representative of wind flow patterns over the northwest INL. It is the identical source of tall tower data used in the 2nd Edition Climatology (Clawson et al., 1989). The SMC tower is near the mouth of Birch Creek Valley, and is influenced by flows from that valley. The figures present all-stability, annual wind roses as a function of sensor height and time of day (day, night, and all hours). Data for SMC are obtained from the 10 and 46 m levels.

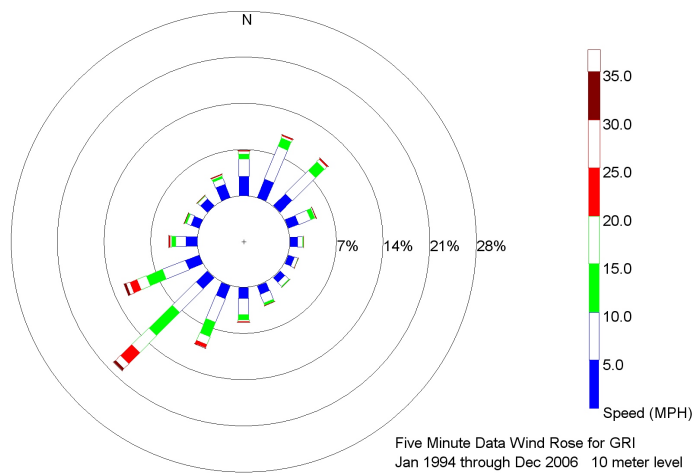
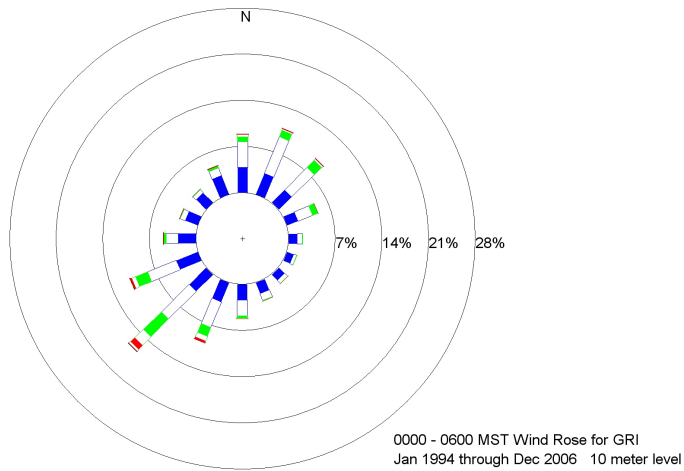
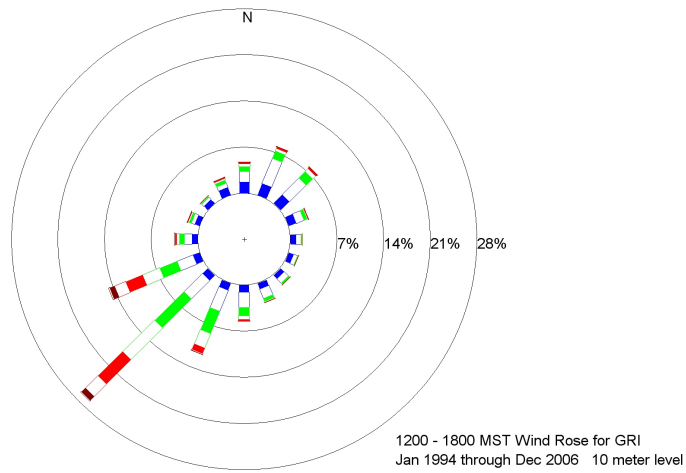


Figure 9. Day (top), night (middle), and all hours (bottom) wind roses for the 10 meter level at Grid 3.

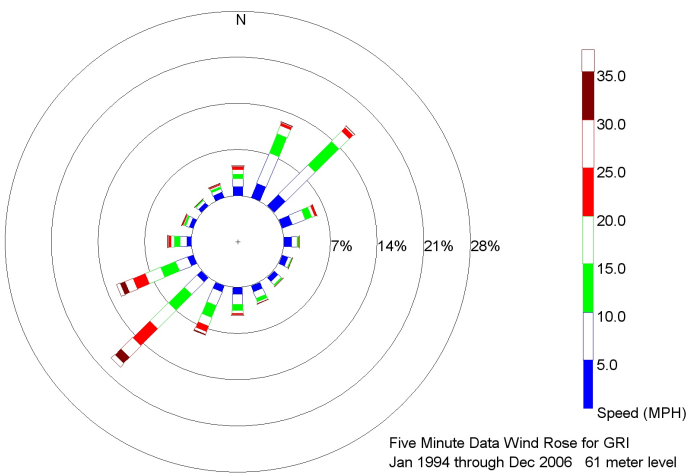
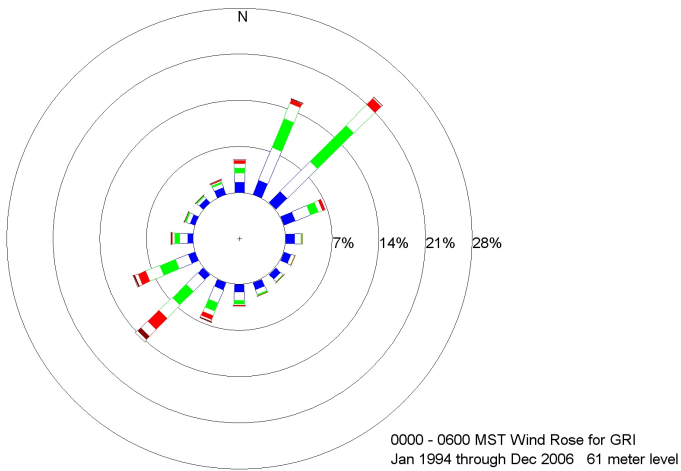
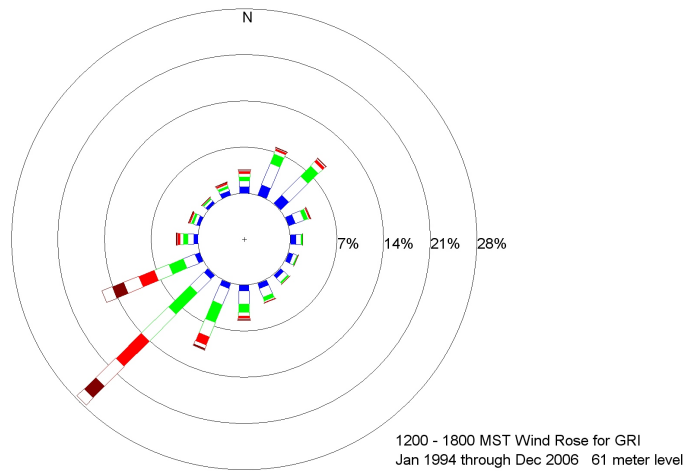


Figure 10. Day (top), night (middle), and all hours (bottom) wind roses for the 61 meter level at Grid 3.

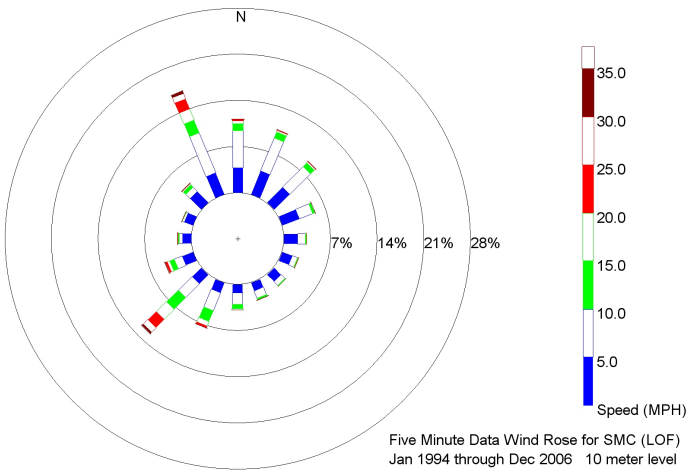
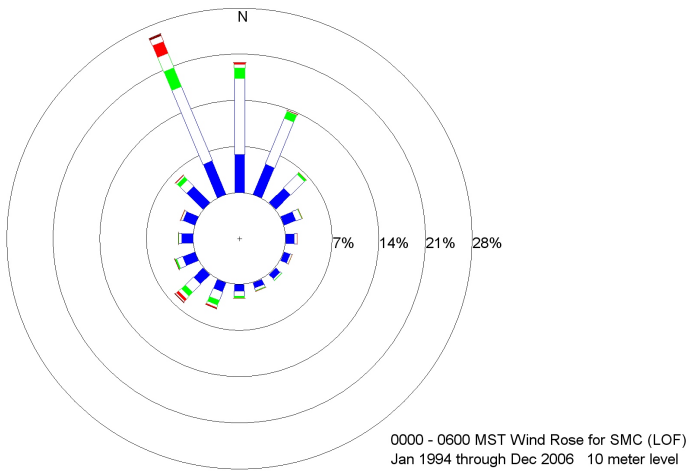
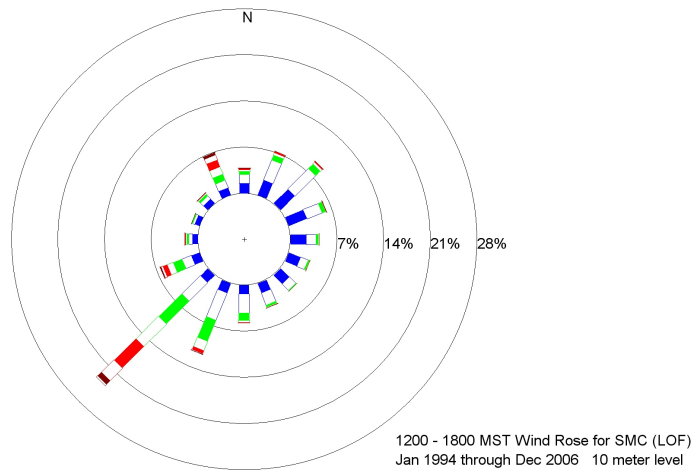


Figure 11. Day (top), night (middle), and all hours (bottom) wind roses for the 10 meter level at SMC.

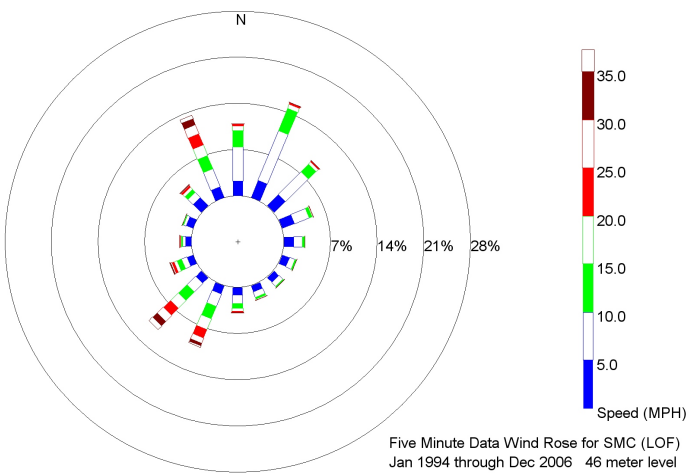
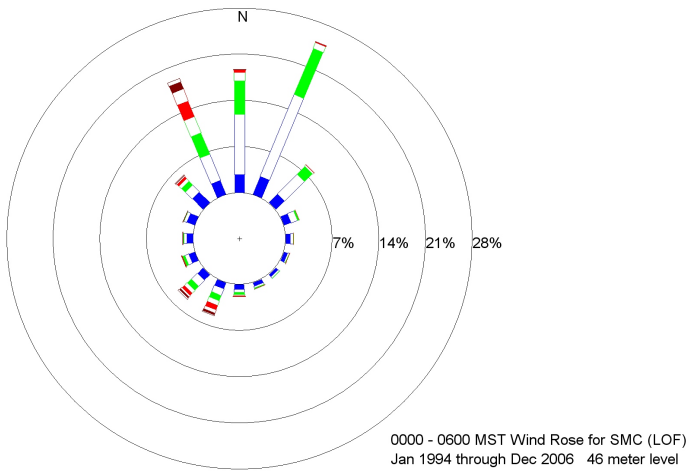
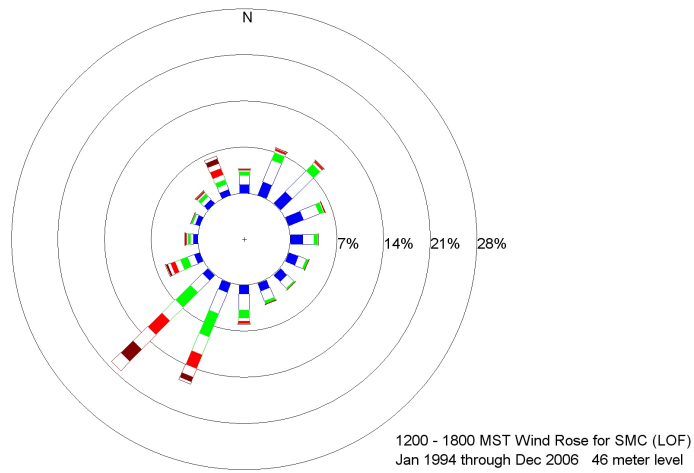


Figure 12. Day (top), night (middle), and all hours (bottom) wind roses for the 46 meter level at SMC.

The data from SMC lead to the following conclusions:

1. A distinct channeling effect of the wind is apparent. The directions with the highest percentages of occurrence are the south to southwest and northwest to northeast quadrants. The large northwest component at night indicates the strong influence of the Birch Creek drainage at SMC.
2. A very small percentage of the wind direction originates from the west and southeast quadrants.
3. Higher wind speeds are observed during lapse (daylight) conditions than during inversion (generally night time) conditions.
4. Higher wind speeds and hence, a smaller frequency of calms, are observed at the 46 m level, and large differences in directional distribution between the surface and elevated sensor levels are noted.
5. A greater diversity of wind direction is observed at SMC when compared to GRI.
6. A much higher frequency of calm periods occurs during the winter months, approximately 2.5 times as often as for any other season. The lowest frequency of calm periods occurs during the summer season (June-August).

Wind roses for the MFC area are illustrated in Figs. 13 and 14. This tower is

located on the southeast perimeter of the MFC complex, and is representative of wind flow patterns over the southeast INL. The figures present all-stability, annual wind roses as a function of sensor height and time of day (day, night, and all hours). Data for MFC are obtained from the 10 and 76 m levels.

The data from MFC lead to the following conclusions:

1. In most respects, daytime winds at MFC are similar to GRI.
2. At night, the 10 m MFC winds are more variable in direction than at GRI, and there is a higher frequency of easterly and southerly winds. These differences are likely associated with the high terrain that runs along the southeast corner of INL (Fig.2).
3. At MFC, a very small percentage of the wind directions originate from the northwest and southeast quadrants. MFC is missing NNW winds.
4. At night, MFC experiences upper level northwesterly winds to a greater extent than at GRI. This is a result of terrain shielding of NW winds at GRI.
5. At night, MFC experiences upper level southwesterly winds over a greater range in azimuths than at GRI. Southwesterly winds are not present at SMC at night.
6. Higher wind speeds and a smaller frequency of calms are observed at the 76 m level.

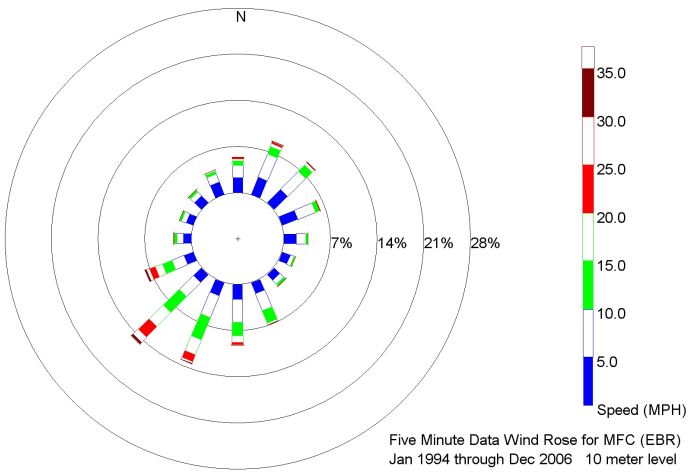
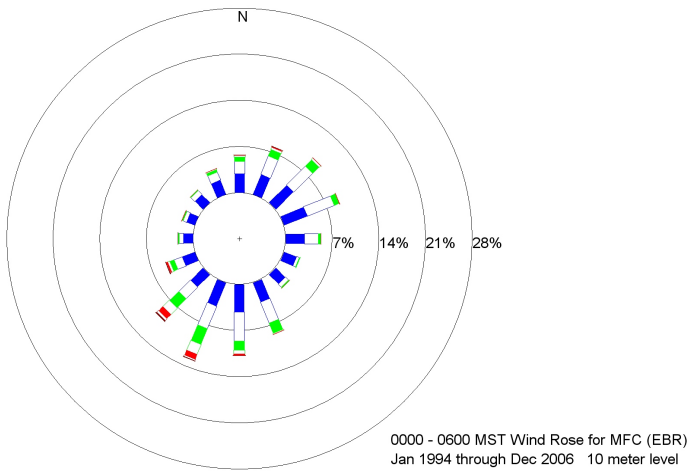
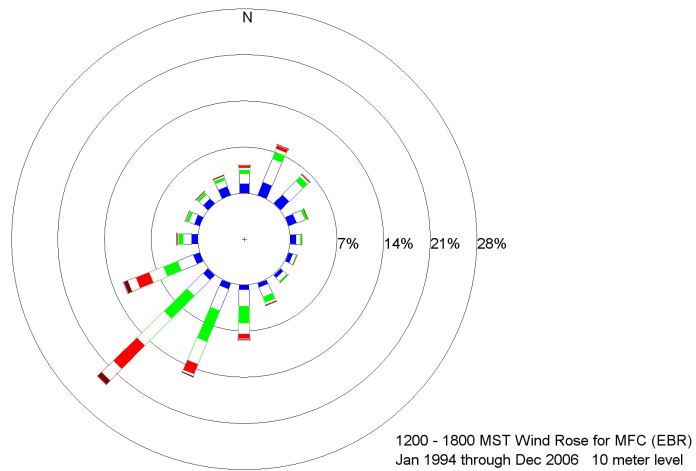


Figure 13. Day (top), night (middle), and all hours (bottom) wind roses for the 10 meter level at MFC.

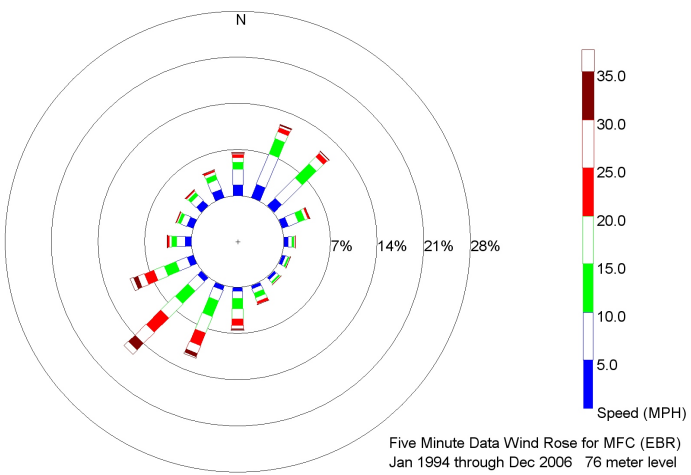
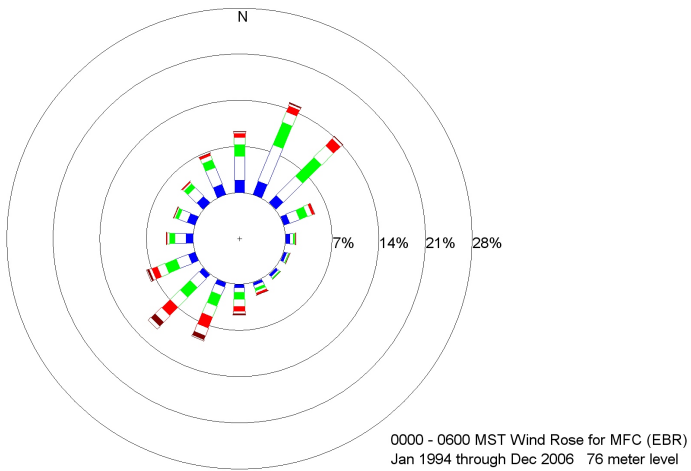
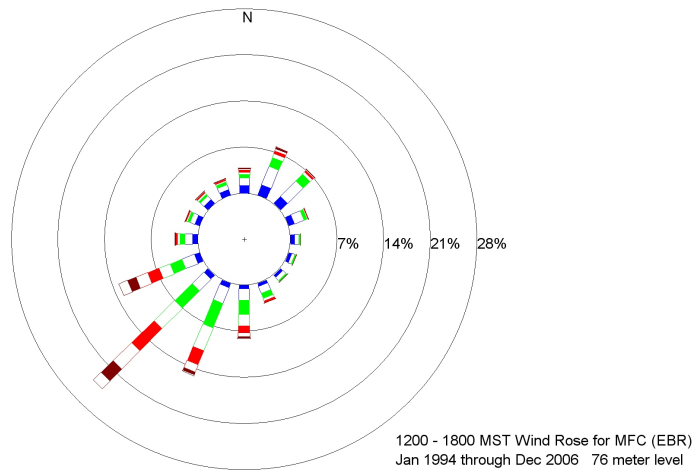


Figure 14. Day (top), night (middle), and all hours (bottom) wind roses for the 76 meter level at MFC.

A distinct diurnal trend is evident in the data from all three locations. There is a tendency for an increase in the frequency of winds from the northeast quadrant during the nighttime hours at GRI. The increase is not large, however, and is due to the lag of the diurnal shift of the wind direction after the temperature stability class has changed from lapse to inversion near sunset, and back sometime after sunrise. Thus, southwest winds can continue to blow for some hours after sunset. Conversely, the northeast winds associated with down-valley drainage conditions can continue to blow in the morning after the inversion has dissipated near the ground. There is also a tendency for shallow southwest drainage winds to occur at GRI (often less than 152 m (500 ft.) deep) due to the local sloping of the terrain from southwest to northeast.

The shift of wind direction with a change from lapse to inversion is much more pronounced at SMC than at GRI. This is evidenced by an increase in the percentage of northerly winds at night at SMC. The distribution indicates that, for a certain fraction of time, there exists an opposing wind direction between GRI and SMC. Winds from the southwest at GRI and from the northeast at SMC can be observed simultaneously. Predominant wind direction in the winter season at SMC is from the northeast, while at GRI it is from the southwest.

At GRI, multiple wind layers are frequently observed under nocturnal conditions. A shallow southwesterly surface flow follows the local Lost River Channel slope toward the northeast. This flow often lies below a layer of northeasterly winds at the height of the tower top which follows the northeast-to-southwest slope of the general

ESRP at GRI. This middle flow is often capped by a layer of upper level winds from the west or southwest that reflects synoptic-scale gradient winds above the atmospheric mixing layer.

On-site Wind Averages and Maximums

Monthly average wind speeds for the period January 1994 through December 2006, classified by month and observed at MFC, GRI, and SMC, are given in Table 5. The months with the highest average wind speeds at all three locations and at all tower levels are April, May, and June. The 10 m monthly mean speed values range from 10.0 to 11.0 mph in these months. The month with the lowest average wind speeds at all three locations and at all tower levels is January. The 10 m monthly mean speed values range from 5.7 to 7.5 mph in January.

Peak wind gusts between January 1994 and December 2006, classified by month and observed at MFC, GRI, and SMC, are given in Table 6. The measurement levels at both 10 m and at the tower top are noted. The maximum instantaneous gust recorded at GRI at the tower top (61 m) was 93.1 mph. The maximum gust at the tower top at SMC was 80.2 mph, and at MFC was 84.7 mph. Higher gusts almost always occur at greater heights on each of the towers, where the influence of surface friction is less and eddy sizes are larger. Each site, however, has instances where the maximum annual gust at the 10 m level does not occur in the same month as the maximum annual gust at the tower top. High wind gusts at the INL may result from either pressure gradients from large-scale systems or local thunderstorms. Most gusts from synoptic systems are channeled from the southwest. Gust directions from thunderstorms are recorded from a variety of directions since

they may form in varying locations and move in any direction. Gusts at the 10 m level that exceed speeds measured at the tower top are an artifact of separate gust events.

Both the monthly average and the maximum gust wind speeds at each of the stations are comparable when sensor height differences are considered. The relationship

between the monthly mean speed, the greatest hourly mean speed, and the greatest peak gust amplitude at the GRI 10 m level is listed in Table 7. The wind directions for all of the highest hourly speeds listed for GRI are from the west-southwest and southwest. This is not always true at SMC where strong winds are often channeled towards SMC from Birch Creek.

Table 5. Monthly mean wind speed (mph) values for three NOAA INL Mesonet tower stations.

	MFC		GRI		SMC	
	10M (MPH)	76M (MPH)	10M (MPH)	61M (MPH)	10M (MPH)	46M (MPH)
January	7.5	11.3	6.9	9.7	5.7	7.5
February	7.9	11.8	7.5	10.6	6.9	9.0
March	10.2	14.5	9.9	13.6	9.0	11.9
April	10.8	15.0	10.5	14.2	10.2	13.3
May	11.0	15.4	11.0	14.8	10.0	13.2
June	10.7	14.9	10.7	14.3	10.0	13.1
July	10.0	14.2	10.1	13.7	9.4	12.5
August	9.7	13.7	9.6	13.2	9.0	11.9
September	9.1	13.1	8.9	12.4	8.3	11.1
October	9.4	13.8	9.1	12.8	8.6	11.4
November	8.5	12.7	8.0	11.6	6.9	9.2
December	7.9	11.9	7.1	10.0	6.4	8.5
All	9.4	13.6	9.1	12.6	8.4	11.1

Note: Data period of records span January 1994 through December 2006.

Table 6. Monthly peak^a wind speed (mph) values for three NOAA INL Mesonet tower stations.

	MFC ^b		GRI ^b		SMC ^b	
	10M (MPH)	76M (MPH)	10M (MPH)	61M (MPH)	10M (MPH)	46M (MPH)
January	62.4	68.5	62.3	70.8	61.1	68.7
February	73.5	75.3	70.4	81.1	59.8	65.4
March	62.0	69.2	62.5	70.4	62.6	67.8
April	71.3	84.7	76.5	93.1	64.6	78.4
May	73.8	70.2	71.4	67.3	61.3	77.6
June	67.4	82.5	77.2	86.2	71.6	80.2
July	65.5	74.4	81.6	89.6	69.1	72.6
August	70.4	69.3	66.6	75.1	69.6	78.8
September	61.1	68.6	65.4	76.8	61.9	70.3
October	62.4	69.4	65.2	70.3	64.3	74.9
November	62.4	73.1	58.4	66.9	68.5	77.5
December	60.1	68.1	57.3	68.0	57.4	62.4
All	73.8	84.7	81.6	93.1	71.6	80.2

a. Mesonet peak winds are defined by 1-second gust duration, not the standard 3-second gust duration used by engineers.

b. Data period of record spans January 1994 through December 2006.

Table 7. Wind speed means and extremes for 10 meter tower level at station GRI.

	Monthly		Greatest Hourly Mean		Greatest Peak Gusts		
	Mean Speed (MPH)	Speed (MPH)	Direction (deg)	(16 th)	Speed (MPH)	Direction (deg)	(16 th)
January	7.1	36	221	SW	62	203	SSW
February	7.6	38	235	SW	70	255	WSW
March	9.8	43	243	WSW	63	237	WSW
April	10.5	43	235	SW	76	247	WSW
May	11.0	38	257	WSW	71	270	W
June	10.7	40	230	SW	77	223	SW
July	10.1	40	243	WSW	82	232	SW
August	9.6	38	230	SW	67	256	WSW
September	8.9	37	236	SW	65	240	WSW
October	9.1	43	230	SW	65	224	SW
November	8.1	39	243	WSW	58	226	SW
December	7.4	40	236	SW	57	238	WSW
ANNUAL	9.2	43	243	WSW	82	232	SW

Note: Data period of record spans from January 1994 through December 2006.

Regional Near-Surface Wind Flow Patterns

Annual, all-stability wind roses for three time periods -- day, night, and all hours -- are provided for all of the NOAA INL Mesonet stations in Appendix C. When reviewing the individual wind roses, a number of consistent trends become apparent as a result of terrain and atmospheric stability considerations.

Wind Trends

Regional winds are affected by bordering mountain ranges and by the orientation of the ESRP. The overall wind pattern can be complex, given a variety of terrain features having varying size and orientation.

The INL's latitude places it within the belt of prevailing westerly winds, which are normally channeled by the ESRP. These channeled winds can become strong when the gradient winds (at mountain-top levels approximately 1,524 m (5,000 ft.) above the surface) are strong. This phenomenon is most common during the springtime.

Mountains and valleys affect winds during many other meteorological conditions. For example, the Birch Creek Canyon causes strong northwest winds in the SMC area when winds aloft are strong and from the northwest. Wind speeds under these conditions may equal those of the strong southwest winds at other site locations.

Drainage winds contribute to overall wind flow at the INL. Radiational cooling near the surface during clear nights produces cold, dense air along the mountain slopes which sinks toward the valley floor (down-slope wind). The down-slope wind over the INL is generally from the north-northeast.

The reverse of the drainage wind occurs during daytime as heated (less dense) air rises along the mountain slopes. The up-valley wind is most evident during periods of weak surface pressure gradient. Stronger down-slope wind occasionally develops when cold air deepens east of the Continental Divide and spills down toward the INL.

Wind flows may be modified by passing synoptic-scale systems and by local storms.

Terrain Influences

The predominant southwest-northeast flow direction of the ESRP is evident in most of the wind roses. This predominance is a result of the orientation of the ESRP when convective heating couples the surface winds with the persistent westerly winds aloft. Prefrontal winds are also invariably southwesterly. Nocturnal drainage winds are from the northeast at most stations. The monitoring stations which exhibit these occurrences are Idaho Falls (IDA), Kettle Butte (KET), and Sugar City (SUG).

Subtle terrain features adjacent to individual stations considerably affect the overall southwest-northeast flow. These features modify the wind direction when a low wind speed prevails, particularly during inversion conditions. The Materials and Fuels Complex (MFC), Rover (ROV), and Terreton (TER) stations have broadened northwest-southeast components due to drainage winds moving northwest from elevated terrain located to the south and east of these stations. The CIT has an augmented southerly component that results from

slightly higher terrain located to the south. Both Hamer (HAM) and Dubois (DUB) have significant distributions of easterly winds caused by terrain blockage of the airflow at the north end of the INL.

Channeled canyon cold air drainage dominates the wind distributions at stations located at the boundaries of mountain valleys and the INL. Arco (ARC), Blue Dome (BLU), Montevieu (MON) and SMC (particularly the lower level) are dominated by this flow pattern. The Sand Dunes (SAN), the NRF, and ROV stations have augmented northwesterly winds that result from the influence of these canyon winds as they flow out onto the ESRP. The other monitoring stations not specifically enumerated above exhibit some or all of the main flow characteristics given in the preceding discussion.

Atmospheric Stability Influences

In neutral conditions, i.e. stability class D, winds at the upper and lower tower levels show very similar characteristics. No large wind shears are evident. Stability class D is common when the atmospheric thermal gradient is near adiabatic due to high wind speeds with strong mechanical turbulence or during heavy overcast conditions when the net radiation flux is very small. Under high wind conditions, the possibility of a large directional shear with height is minimized.

In stable conditions, i.e. stability classes E and F, the flow near the surface becomes decoupled from the winds aloft. Stability classes E and F indicate the presence of temperature inversions. Large shears in wind direction between the upper and lower levels are manifest under these conditions. Additionally, the surface wind exhibits a large

variability in direction (meander) during conditions of low wind speeds.

In unstable conditions, i.e. stability classes A, B, and C, winds at both the upper and lower levels are influenced by buoyant eddies which rise as air is warmed at the surface. Stability classes A through C are common when solar heating is strong. The buoyant eddies tend to broaden the directional distribution of low-speed winds which would otherwise exist, because they are somewhat randomly distributed spatially. This disruption is weakest at the upper level where, due to a reduction of frictional effects, the winds are stronger.

Mesonet Wind Field Clusters

Wind roses depict wind conditions at the station without regard to wind stagnation or changes in wind direction and speed with time. Recent numerical analyses (see unpublished FRD manuscript Carter et al., 2008: "Identifying Natural Clusters in Eastern Idaho Wind Fields") have made it possible to improve on the qualitative wind trajectory discussion that appeared in the 2nd Edition Climatology (Clawson et al., 1989) by using a more rigorous numerical cluster analysis technique that identifies and quantifies the occurrence of preferential wind fields. The "k-means" cluster analysis technique that was used in the following assessment identifies a relatively small number of wind fields (eight) that can account for 99.9% of observed INL wind fields. The number of clusters that was kept in the final solution was determined by requiring that the results be unchanged regardless of which seed points were used to initiate the analysis. The eight wind patterns that are presented in the following discussions are based on five-minute averaged data from the 32 NOAA INL

Mesonet stations, 13 of which are within the INL boundaries. At all but three locations, wind sensor height is 15 m.

Wind Pattern 1

Wind pattern 1, Drainage Flow, typically involves northeasterly winds at less than 10 mph throughout the ESRP. On an annual basis, it is the most common wind pattern, occurring 26.3% of all annual hours. It is most common during summer mornings (Jul-Sep 0300 - 0900 MST [45-62%]) when regional pressure gradients are small. It is least common during summer afternoons and evenings (Mar-Oct 1100 – 2100 MST [2-12%]) when strong solar radiation creates up-valley flow, and when surface winds are linked to upper level gradient winds. Pattern 1 wind vectors at the NOAA INL Mesonet stations are shown in Fig. 15.

Arrows shown on the figure are one-hour average speed-direction vectors, with the length scaled to the mean wind speed in mph. Tower locations without vectors had biased or incomplete data in the assessment period, and were not included in the example pattern.

The percentages for which wind pattern 1 occurs by month and hour of day is presented by Fig. 16. For example, during the first hour (between midnight and 0100 MST) for days in January, wind pattern 1 occurs 33% of the time. Percentages are contoured by color-coding. The legend at the lower right of the diagram shows the function of hour of the day and month of the year. Numbers shown in the squares are percentages of the total (10-

year, April 1993 through March 2006) hours for that month percentage ranges covered by each color, with the numbers shown being the highest and lowest percentages included in that color. The most frequent occurrences are shown in magenta (June to September, 0300 – 1000 MST). The least frequent occurrences are shown in red (April to September, 1300 – 1800 MST).

Figure 17 depicts the likelihood of wind pattern 1 persisting on an hour-by-hour basis once it becomes established, and the relative likelihoods of its evolution into another wind pattern type with the passage of time. The *boxed bar* is the percent of the time that the winds have persisted in the original wind pattern for the duration of hours shown. The *unboxed bar* of the same color is the percent of the time that the winds at the duration shown are again in the original wind pattern, after having evolved to some separate wind pattern in the interim. For example, in Fig. 16, the wind field starts in wind pattern 1, represented by red, and is unaltered in type during the first hour. After 24 hours, the boxed red bar is about 5% long, meaning that 5% of the time, wind pattern 1 persisted for 24 hours. After 24 hours, the unboxed portion of the red bar is about 35% long, meaning that 35% of the time, wind pattern 1 transitioned to at least one other pattern before returning to wind pattern 1 within the 24 hour elapsed time. In this example, 40% of the time, wind pattern 1 was observable 24 hours after wind pattern 1 was identified. The legend at the lower right of the diagram shows the color-coding for each wind pattern type.

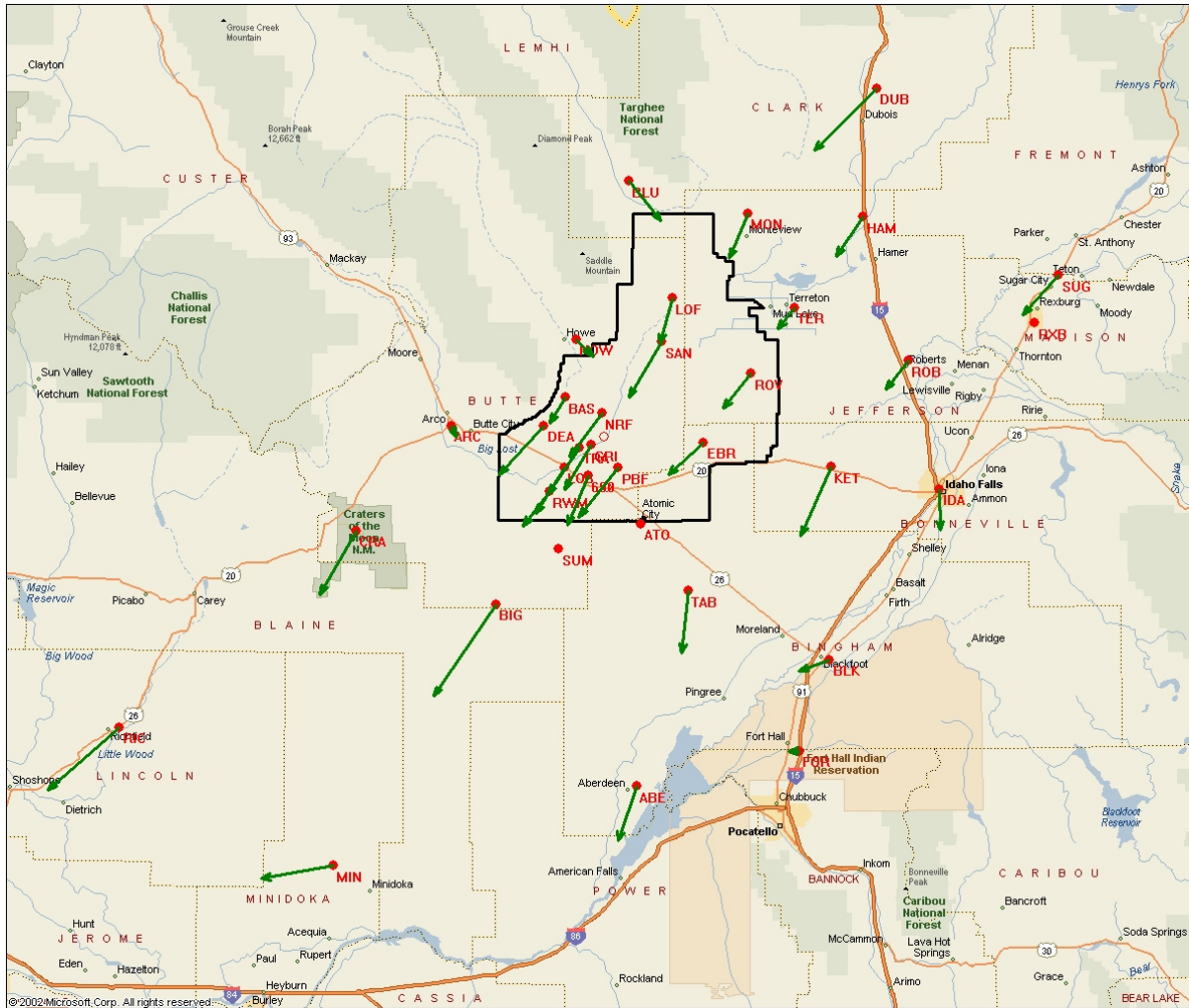


Figure 15. Wind pattern 1 wind vectors – low wind speed drainage flow from the northeast.

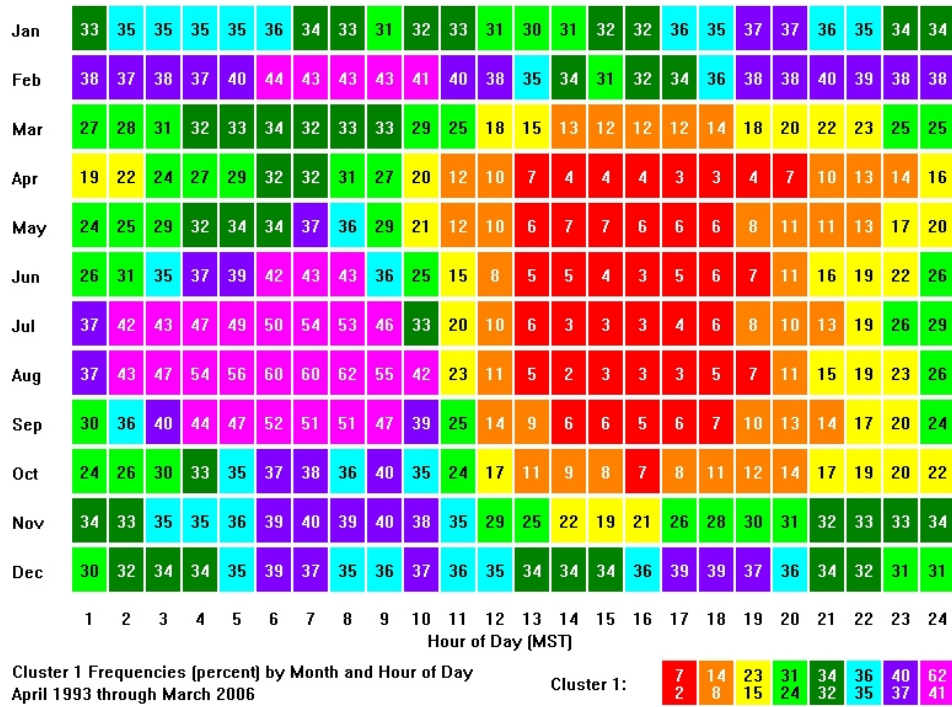


Figure 16. Temporal occurrence of wind pattern 1 - low wind speed drainage flow from the northeast.

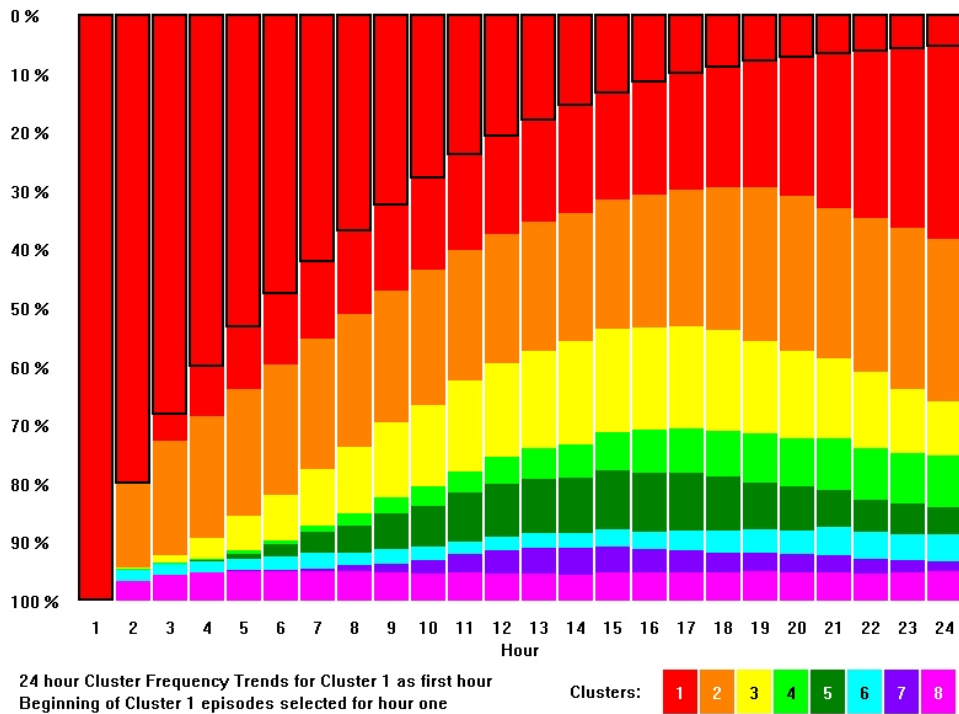


Figure 17. Persistence of wind pattern 1 - low wind speed drainage flow from the northeast.

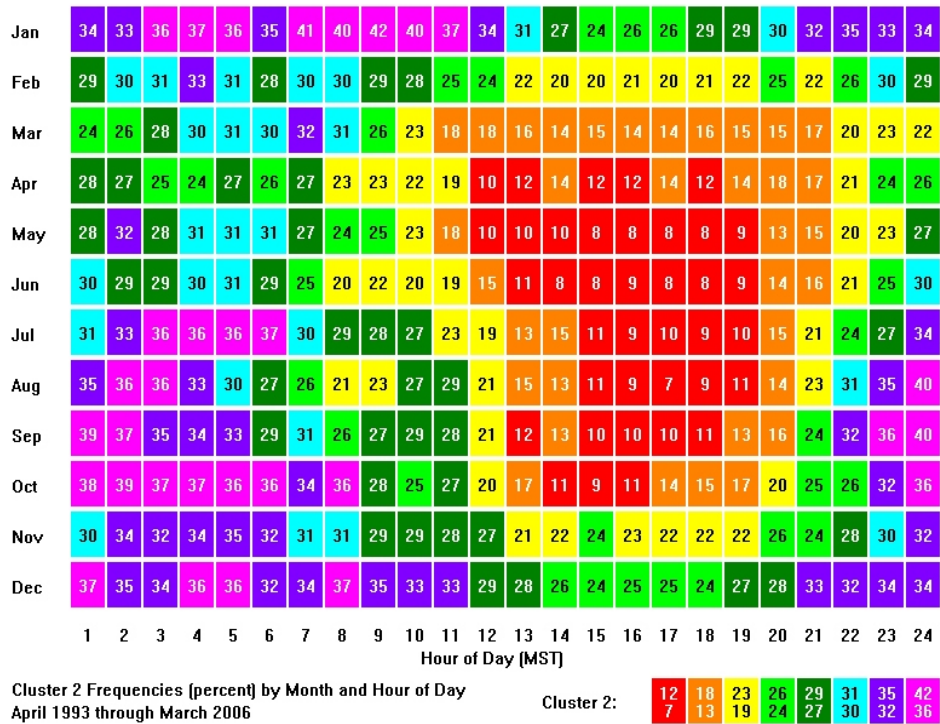


Figure 19. Temporal occurrence of wind pattern 2 – light winds and variable direction.

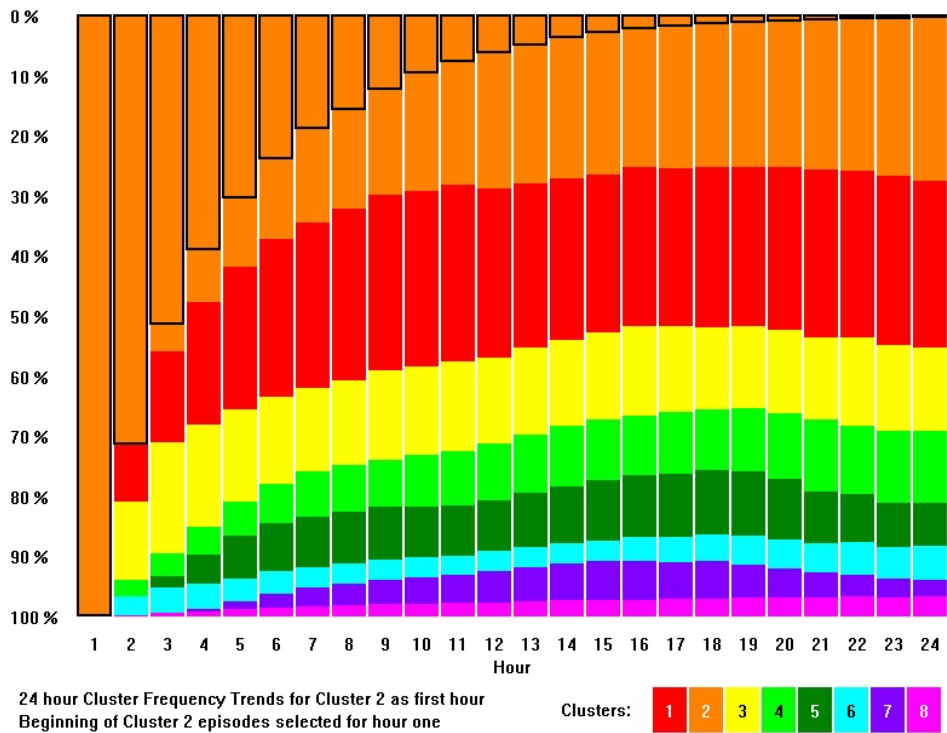


Figure 20. Persistence of wind pattern 2 – light winds and variable direction.

Wind Pattern 3

Wind pattern 3, Moderate Upslope Flow, typically consists of south-southwest winds at 7-11 mph throughout the ESRP. On an annual basis, it is the third most common wind pattern, occurring 12.6% of all annual hours (less than half as frequently as types 1 or 2). It is most common (26-38%) during summer afternoons (Jul-Sep 1100-2100 MST) when a strong solar forcing function is present. It is least common (2-12%) during night-time conditions (0100-0800 MST) at any time of year since, at that time, no solar radiation is available to create an up-valley

flow. Pattern 3 wind vectors at the NOAA INL mesonet stations are shown in Fig. 21. Figure 22 quantifies the seasonal occurrence of this wind pattern. Although pattern 3 is well defined on a seasonal and daily basis, Fig. 23 shows that the likelihood of it persisting once it becomes established is much less than for patterns 1 or 2, because the pattern is more easily overcome by other diurnal influences as the day progresses. Within an hour or two, pattern 3 can transition into patterns 2, 4, or 5. If pattern 3 persists for 4-5 hours it can transition into pattern 1, which would likely occur near sunset.

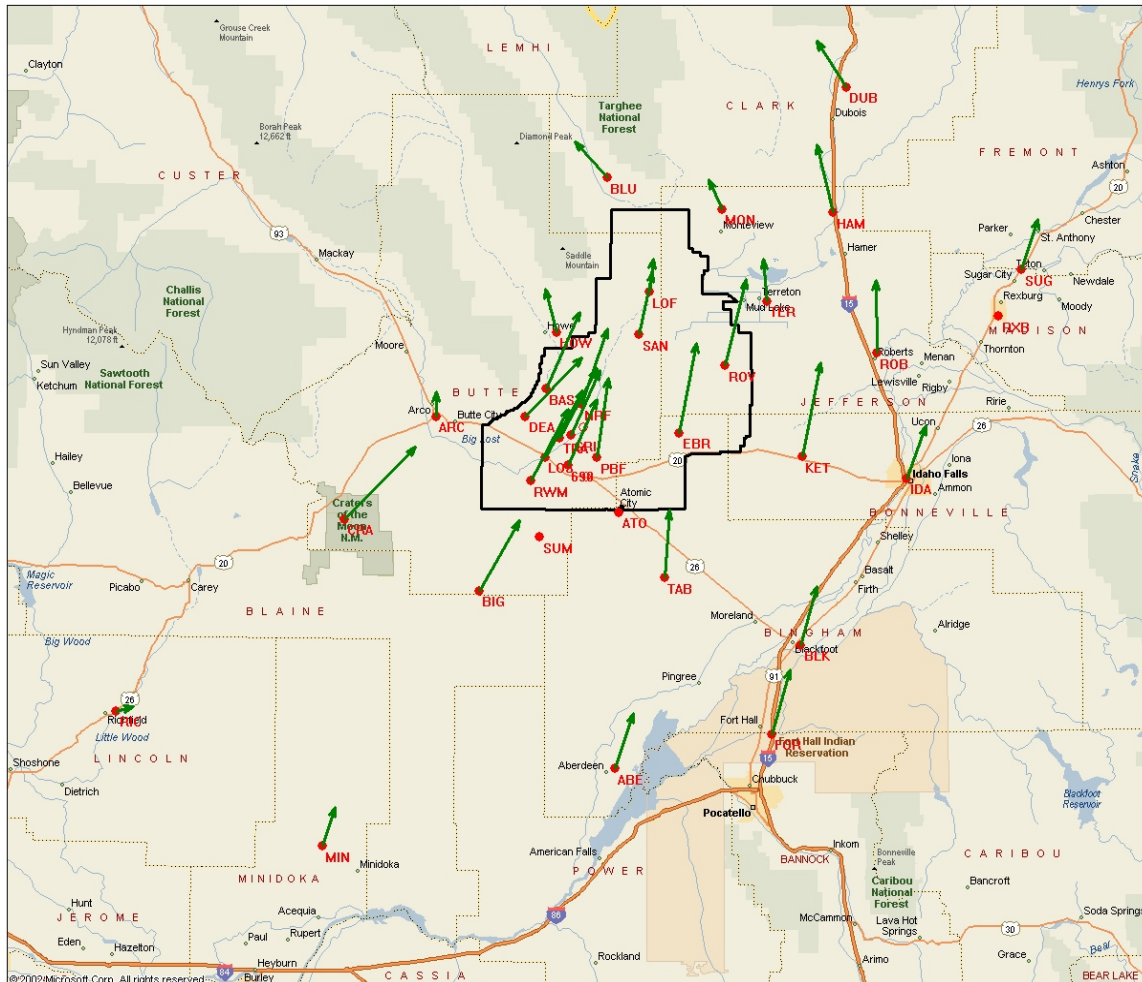


Figure 21. Wind vectors for wind pattern 3 – moderate upslope flow.

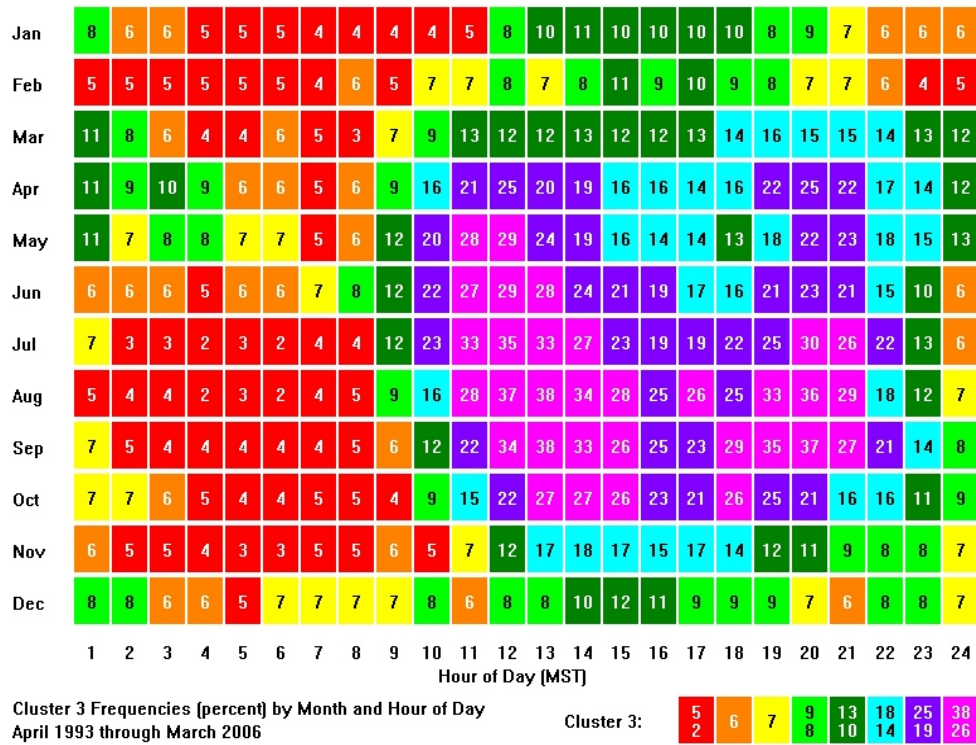


Figure 22. Temporal occurrence of wind pattern 3 – moderate upslope flow.

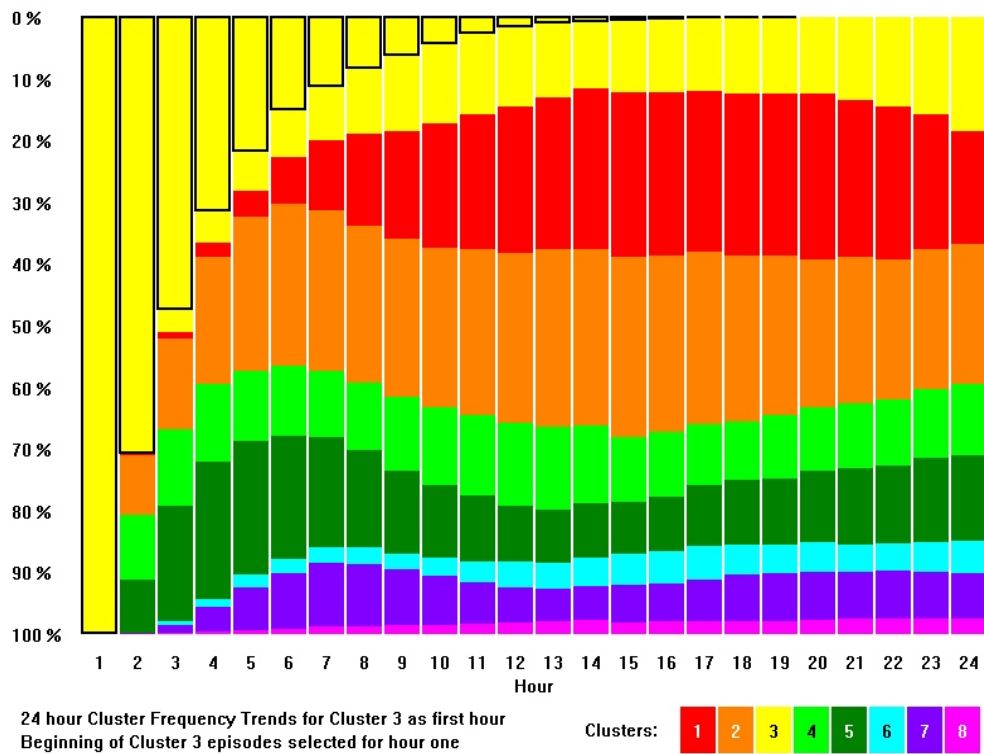


Figure 23. Persistence of wind pattern 3 – moderate upslope flow.

Wind Pattern 4

Wind pattern 4 occurs during conditions when synoptic weather patterns exert only a moderate influence and when upslope flows are decreasing after sunset. Near the north end of the ESRP, winds are variable in direction at 6-11 mph, and elsewhere throughout the INL winds are southwesterly at 12-16 mph. On an annual basis, it is the fourth most common wind pattern, occurring 11.5% of all annual hours. It is most common (15-23%) during mid-winter afternoons and early evenings (Jan-Mar 1300-1800 MST) and in spring evenings (Mar-Sep 2000-2300 MST). It is least

common during summer mornings (Jul-Sep 0100-1400 MST, 2-9%). Pattern 4 wind vectors at the NOAA INL Mesonet stations are shown in Fig. 24. Figure 25 quantifies the seasonal occurrence of this wind pattern. The most frequent occurrences are shown in magenta (March to July, 1900 – 2200 MST). The least frequent occurrences are shown in red (July to September, 0300 – 1200 MST). Figure 26 depicts the likelihood of wind pattern 4 persisting on an hour-by-hour basis once it becomes established, and the relative likelihoods of its evolution into another wind pattern type with the passage of time. Evolution from pattern 4 to pattern 2 is the most likely transition.

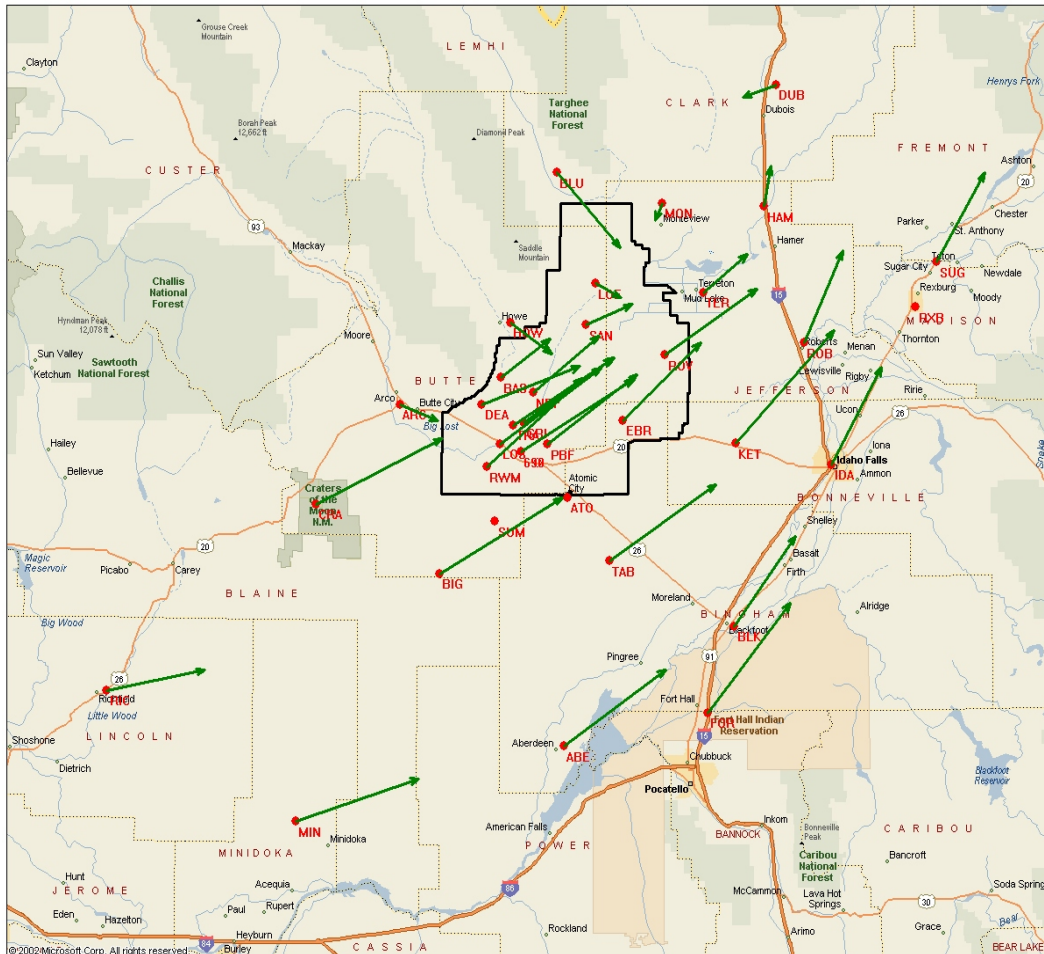


Figure 24. Wind vectors for wind pattern 4 – moderate synoptic effects and decreasing upslope flow after sunset.

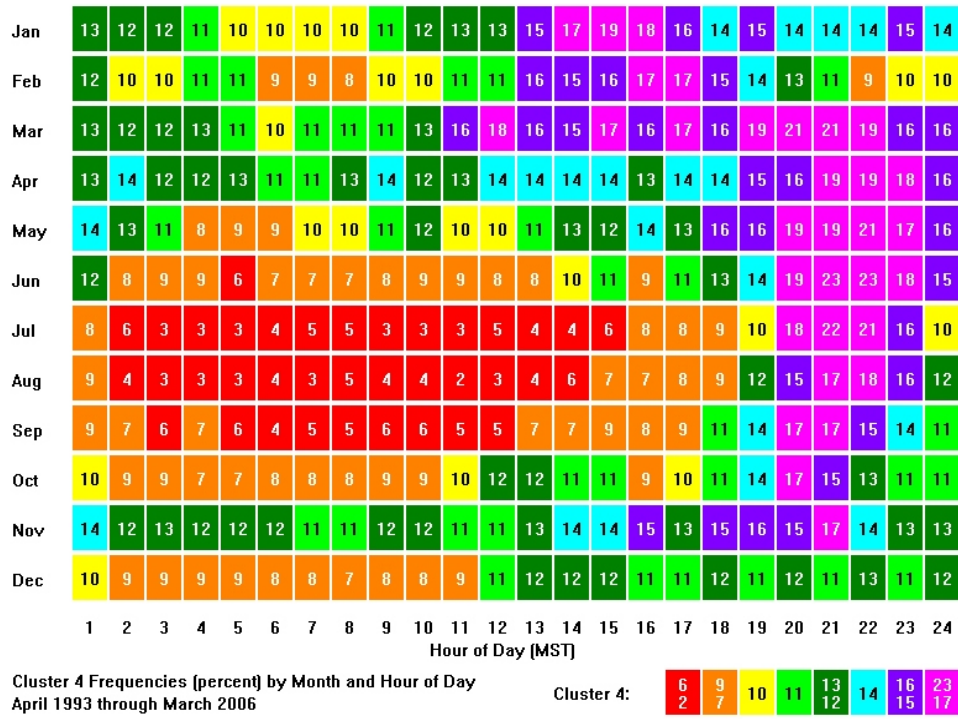


Figure 25. Temporal occurrence of wind pattern 4 – moderate synoptic effects and decreasing upslope flow after sunset.

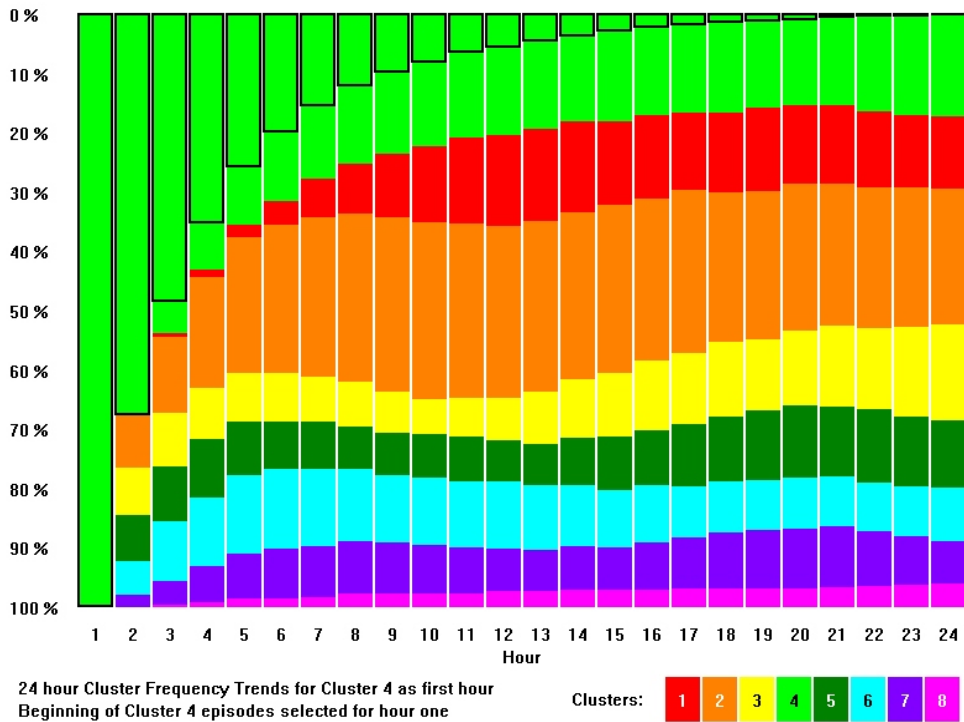


Figure 26. Persistence of wind pattern 4 – moderate synoptic effects and decreasing upslope flow after sunset.

Wind Pattern 5

Wind pattern 5, well-developed upslope flow, typically involves south southwest winds at 11-18 mph throughout the ESRP. On an annual basis, it is the 5th most common wind pattern, occurring 8.7% of all annual hours. It is most common (21-32%) during summer afternoons (May-Sep 1300-1800 MST) when solar heating is strong. It is least common (<1-5%) during the night and morning period (2300-0800 MST) at all times of year since solar radiation to create an up-valley flow is absent at those times. Pattern 5

wind vectors at the NOAA INL Mesonet stations are shown in Fig. 27. Figure 28 quantifies the seasonal occurrence of this wind pattern and shows the strong linkage to summer afternoon conditions. Figure 29 depicts the likelihood of wind pattern 5 persisting on an hour-by-hour basis once it becomes established, and the relative likelihoods of its evolution into another wind pattern type with the passage of time. After one to two hours of persistence, this pattern transitions into patterns 3, 4, and 7. If this pattern persists for four to eight hours, it can also transition into patterns 1 and 2.

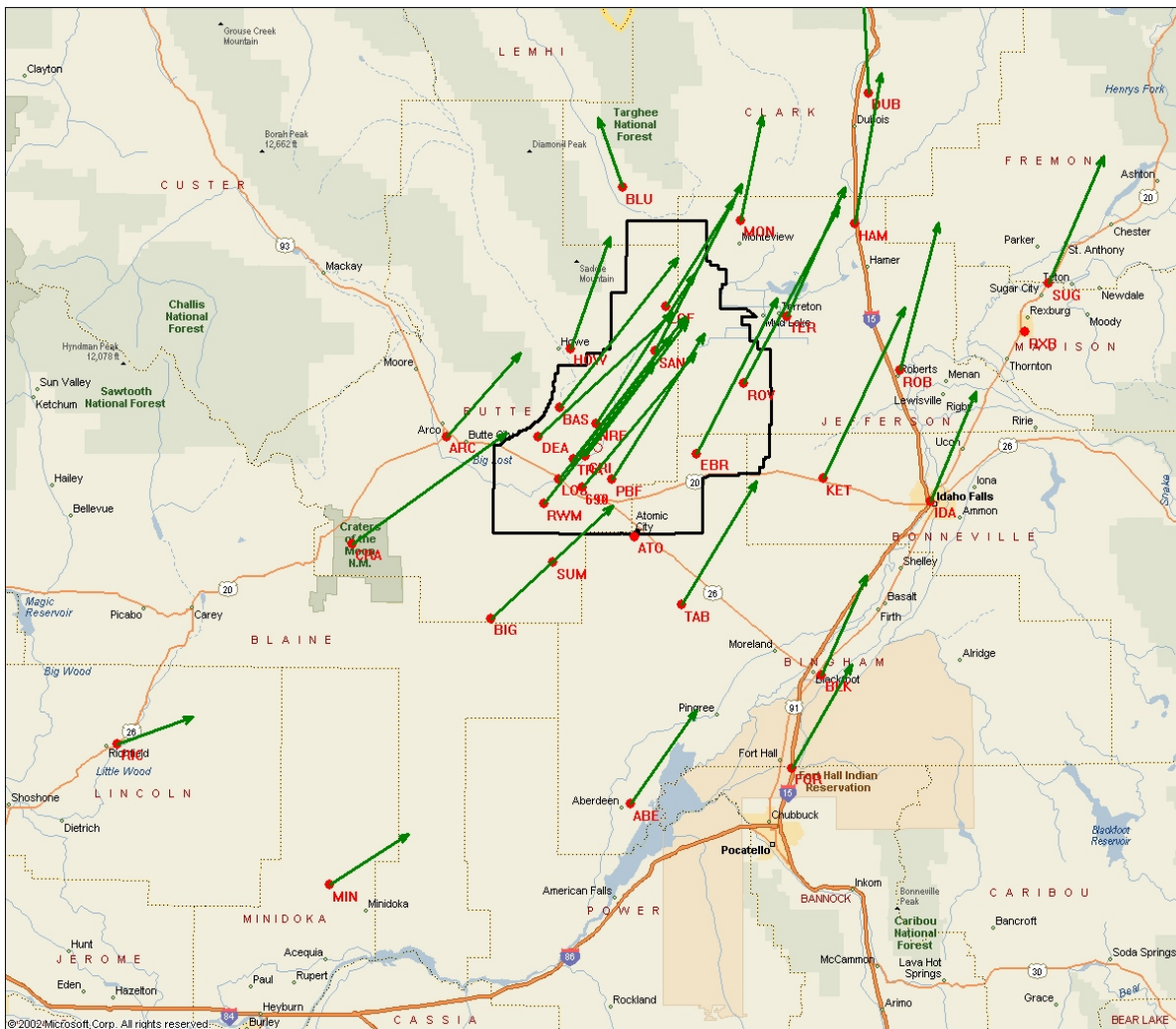


Figure 27. Wind vectors for wind pattern 5 – well developed upslope flow.

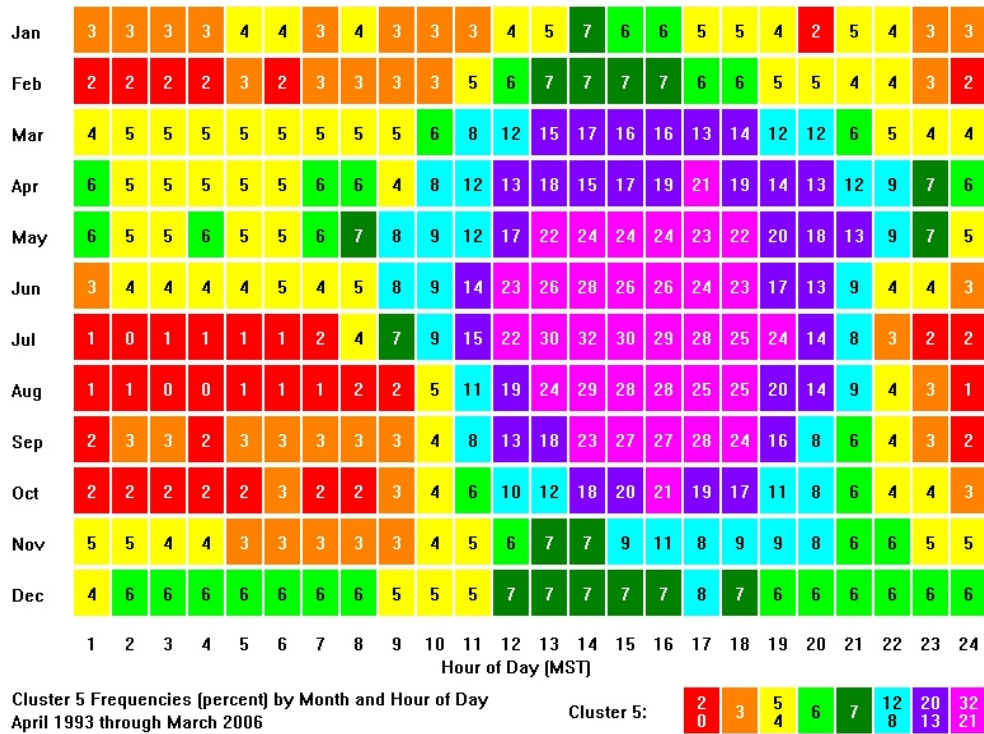


Figure 28. Temporal occurrence of wind pattern 5 – well developed upslope flow.

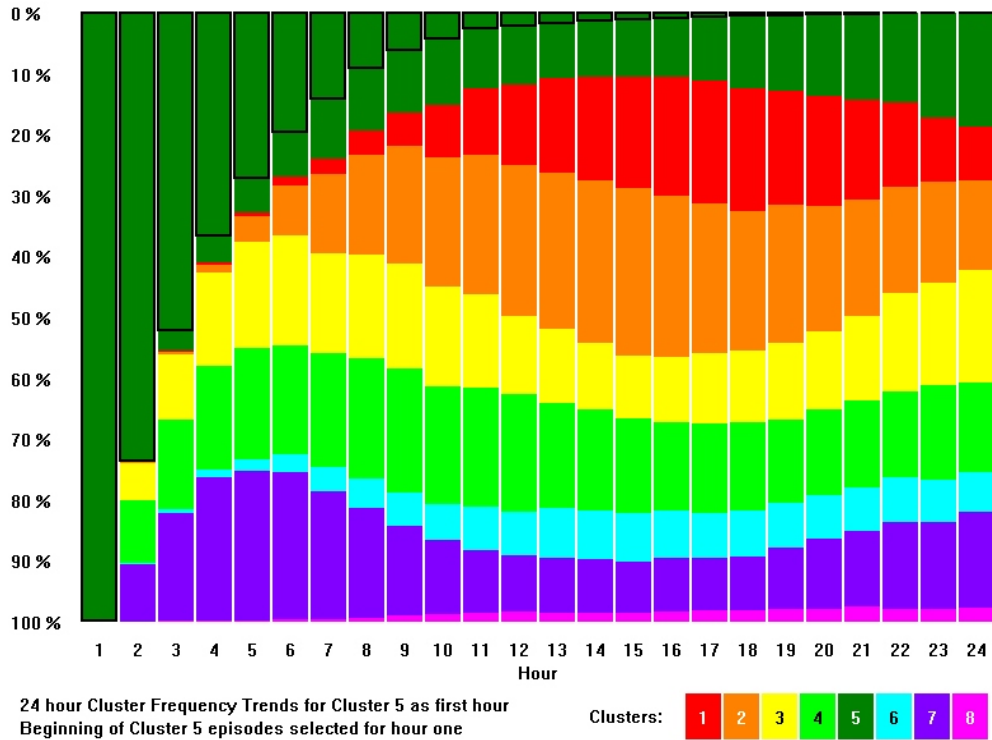


Figure 29. Persistence of wind pattern 5 – well developed upslope flow.

Wind Pattern 6

Wind pattern 6, drainage flow through northwest-southeast canyons aided by synoptic features, typically involves north to northwest winds at 10-20 mph (locally higher) at the north end of the INL, west to northwest winds at 5-15 mph through much of the remainder of the ESRP except for southwest winds on the far east side of the ESRP. On an annual basis, it is the sixth most common wind pattern, occurring 6.4% of all annual hours. It is most common (13-15%) during April nights (1700-0400 MST) and during the spring and summer season evenings (Mar-Jul 2300-0300 MST) during those times when surface winds are well-coupled to

northwesterly winds aloft by strong thermal mixing. It is least common (< 1-4%) during summer mornings (May-June 0900-1500 and July-Sep 0600-1500 MST), when regional pressure gradients are typically light. Pattern 6 wind vectors at the NOAA INL Mesonet stations are shown in Fig. 30. Figure 31 quantifies the seasonal occurrence of this wind pattern. Figure 32 depicts the likelihood of wind pattern 6 persisting on an hour-by-hour basis once it becomes established, and the relative likelihoods of its evolution into another wind pattern type with the passage of time. Wind pattern 6 is most likely to evolve into wind patterns 1, 2, or 4; all of which are transition regimes in which light winds prevail.

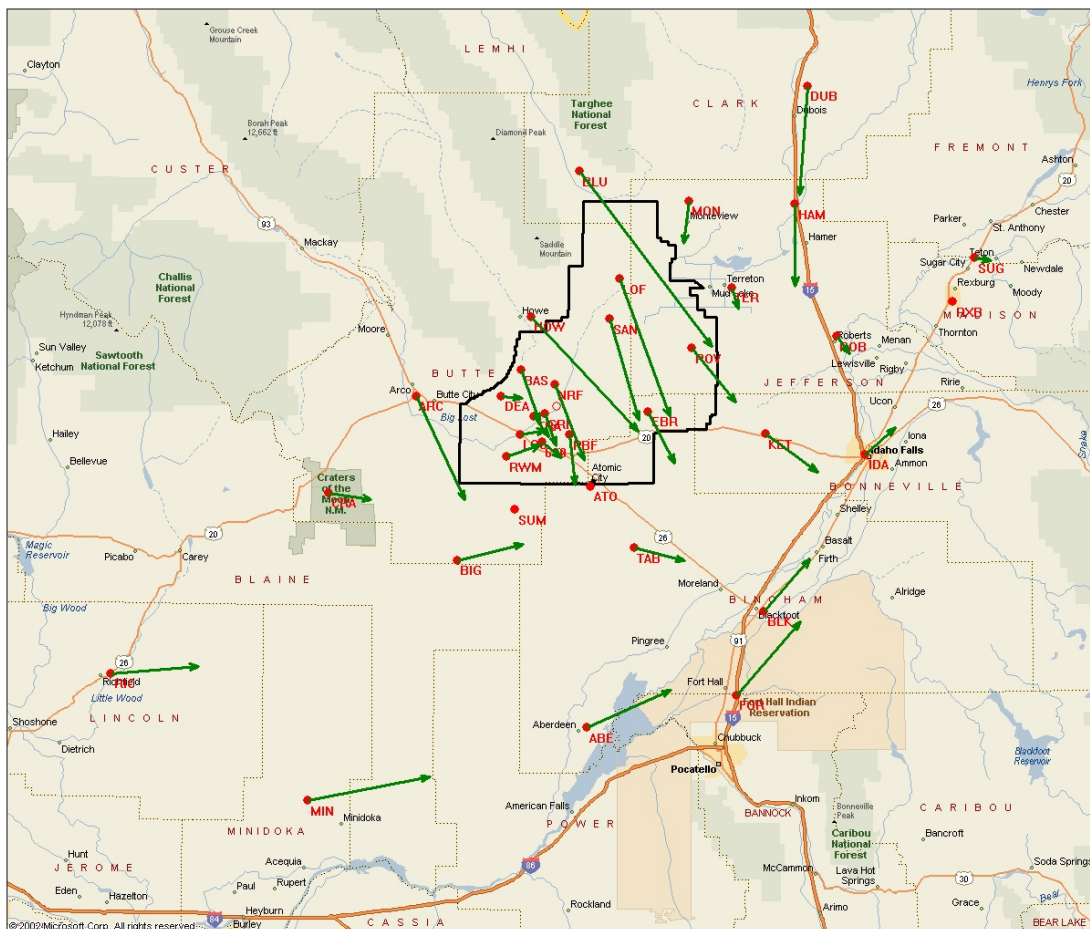


Figure 30. Wind vectors for wind pattern 6 – down-canyon drainage flow aided by synoptic features.

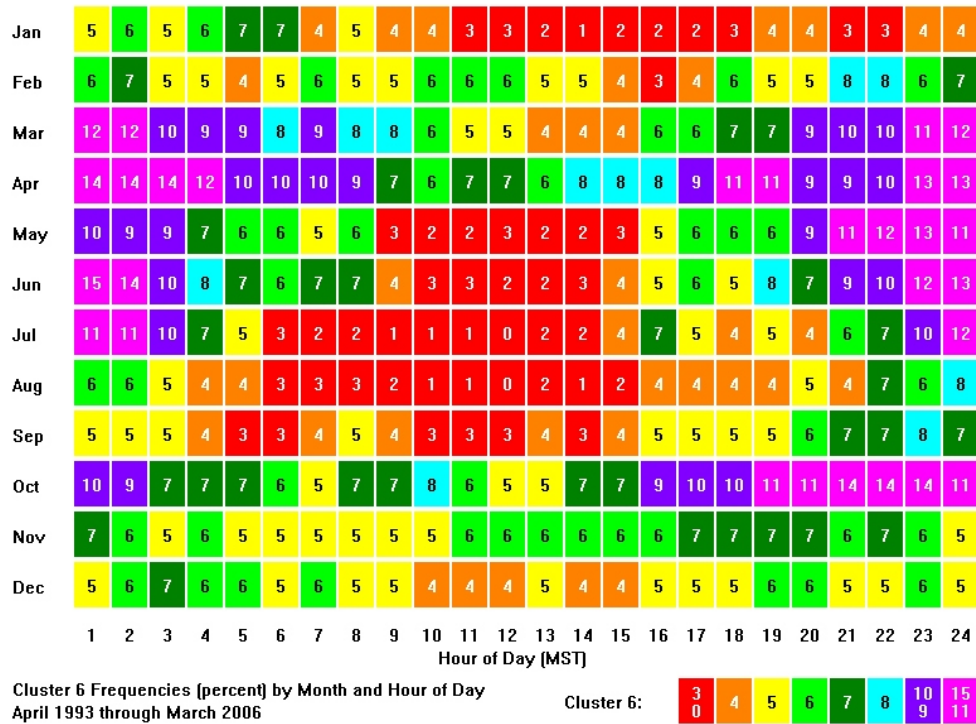


Figure 31. Temporal occurrence of wind pattern 6 – down-canyon drainage flow aided by synoptic features.

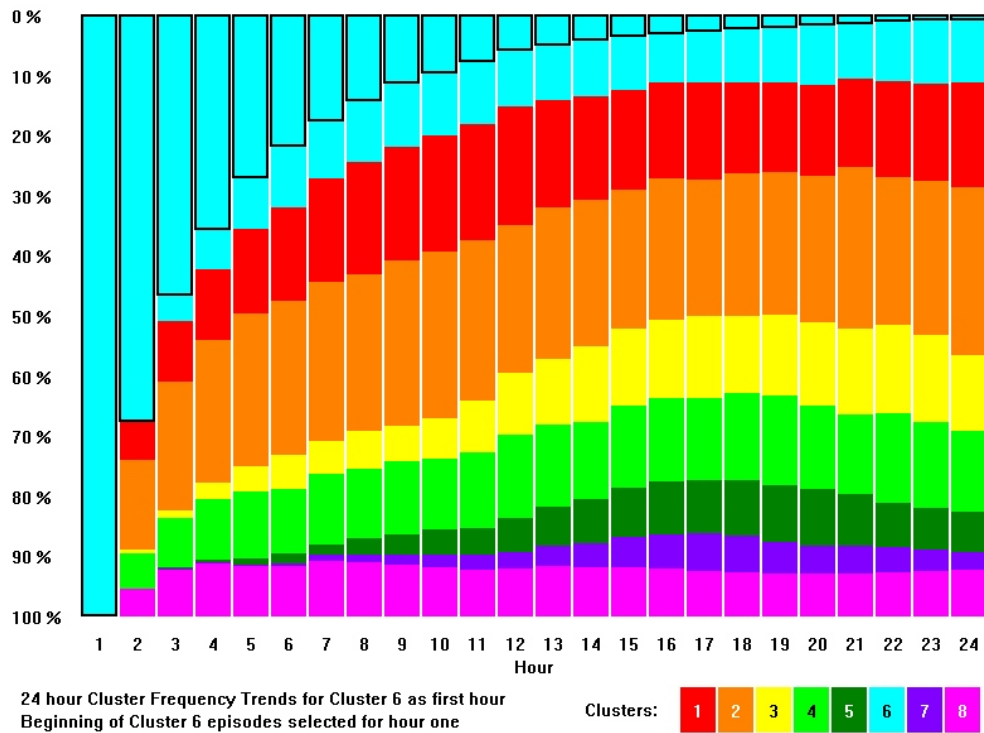


Figure 32. Persistence of wind pattern 6 – down-canyon drainage flow aided by synoptic features.

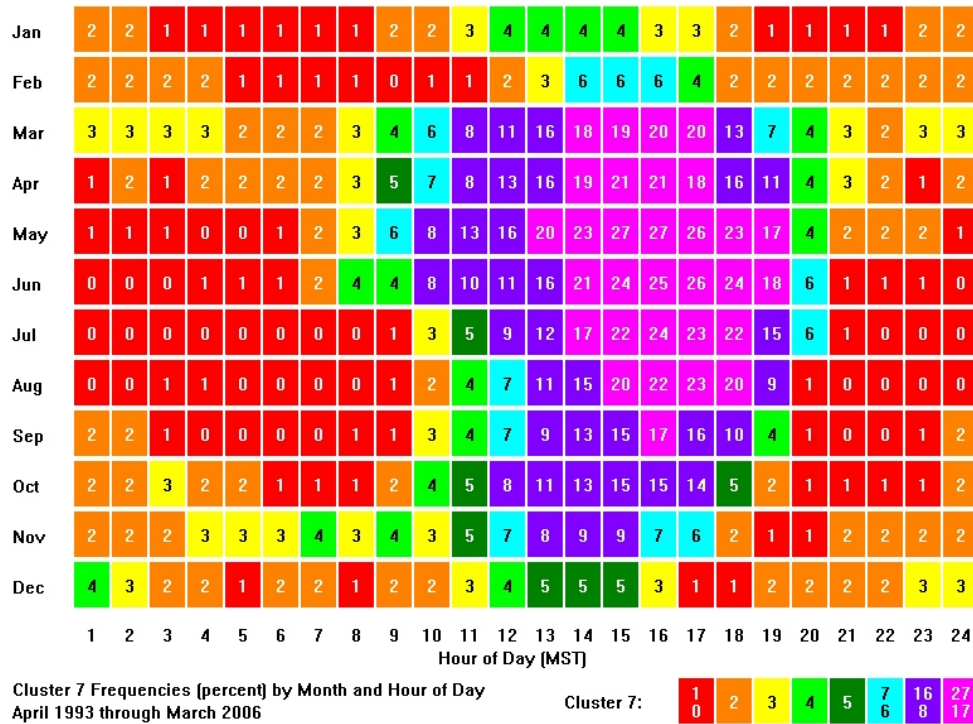


Figure 34. Temporal occurrence of wind pattern 7 – strong synoptic effects yield SW winds.

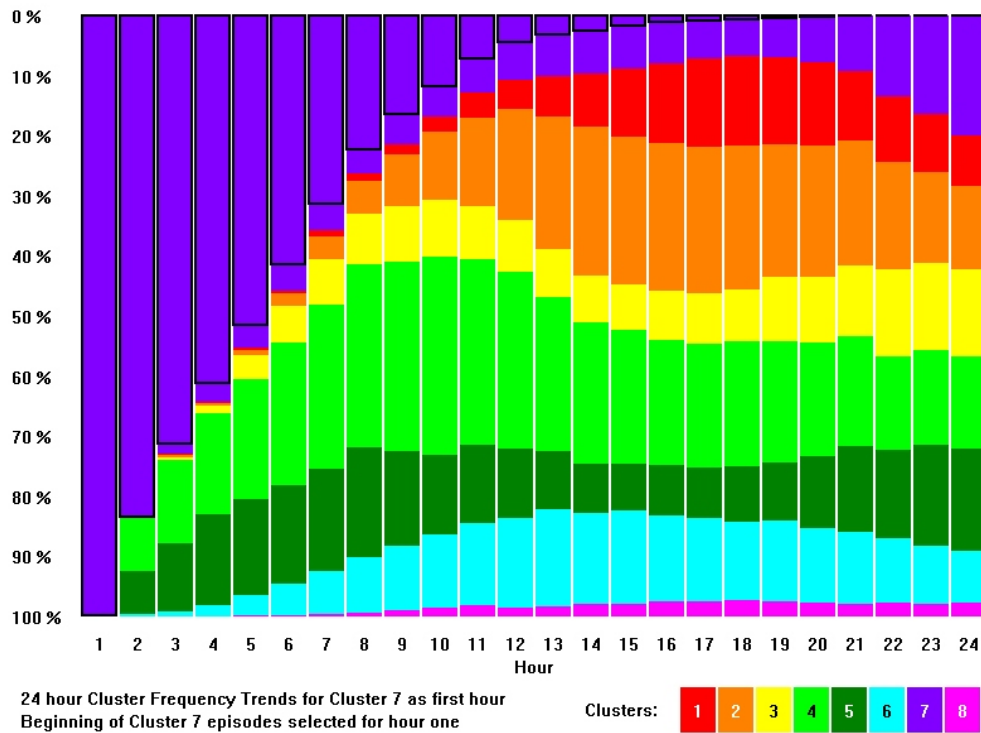


Figure 35. Persistence of wind pattern 7 – strong synoptic effects yield SW winds.

Wind Pattern 8

Wind pattern 8, Strong synoptic effects driving northerly winds, typically involves north to northeasterly winds at 10-20 mph throughout the ESRP. On an annual basis, it is the eighth most common wind pattern, occurring 4.1% of all annual hours. It is most common (8-10%) during spring nights (Apr 1800-1000 MST and May 0200-0500 MST). It is least common (<1-3%) during summer (0500-1600 MST) when strong solar radiation links surface winds with mostly southerly and westerly upper level gradient winds. It is also uncommon all hours of the

winter months (Nov-Jan). Pattern 8 wind vectors at the NOAA INL Mesonet stations are shown in Fig. 36. Figure 37 quantifies the seasonal occurrence of this wind pattern. Figure 38 depicts the likelihood of wind pattern 8 persisting on an hour-by-hour basis once it becomes established, and the relative likelihoods of its evolution into another wind pattern type with the passage of time. Pattern 8 is most likely to evolve into pattern 1 (downslope winds) or pattern 2 (light and variable) winds as the influence of synoptic storm energy diminishes. Wind patterns can be greatly modified by unusual synoptic conditions and local storms.

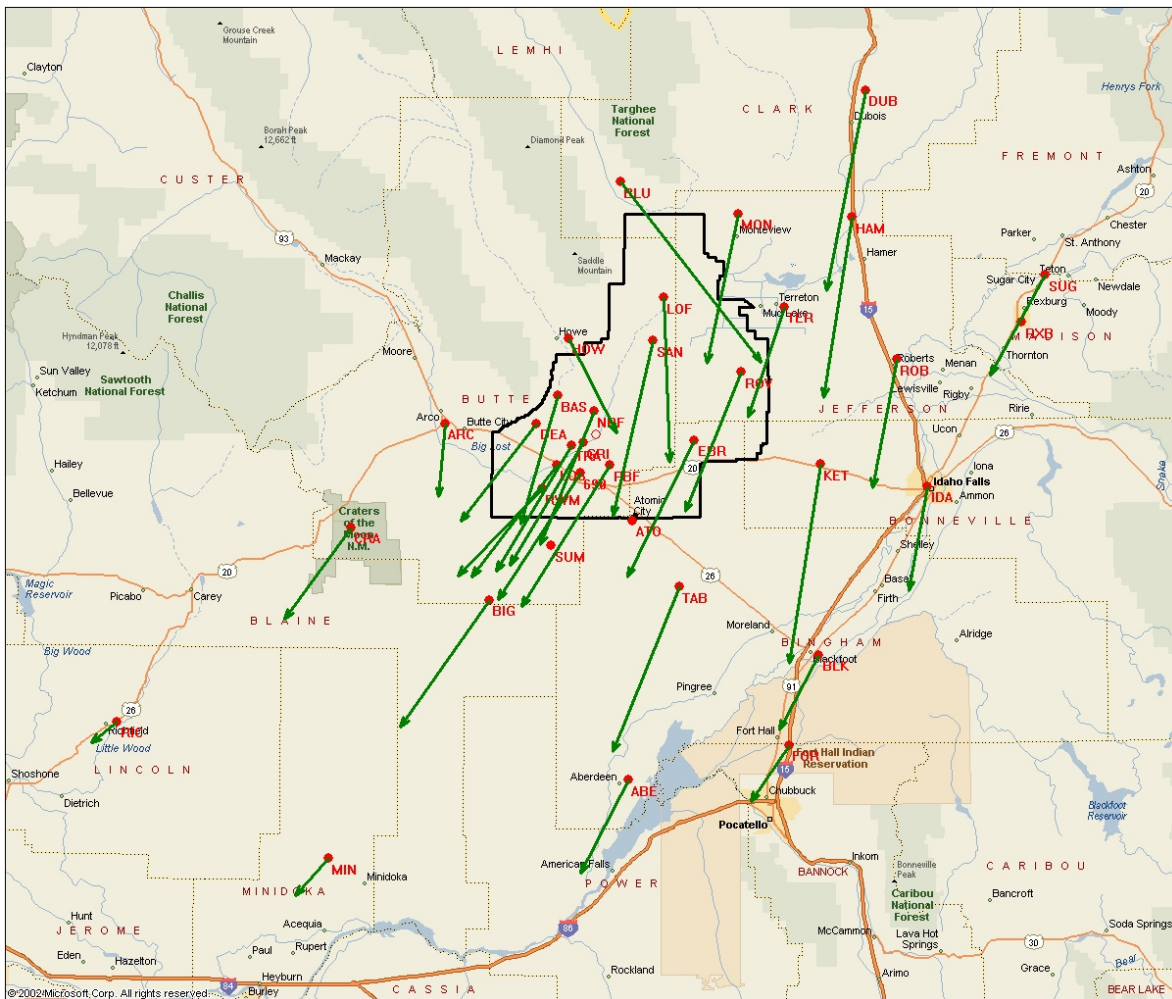


Figure 36. Wind vectors for wind pattern 8 – strong synoptic effects yield NNE winds.

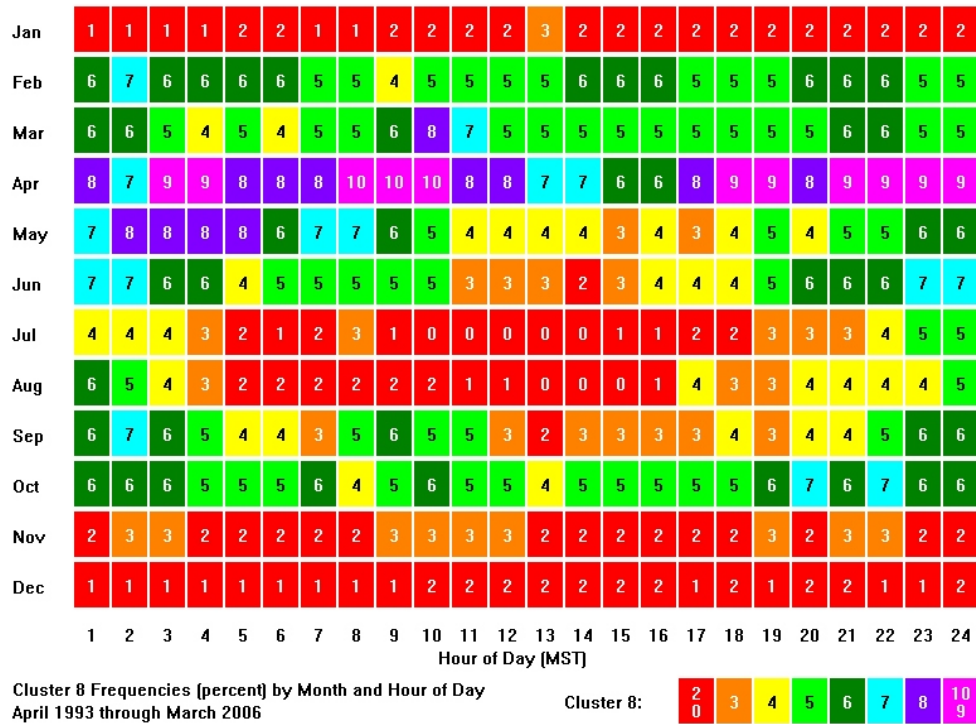


Figure 37. Temporal occurrence of wind pattern 8 – strong synoptic effects yield NNE winds.

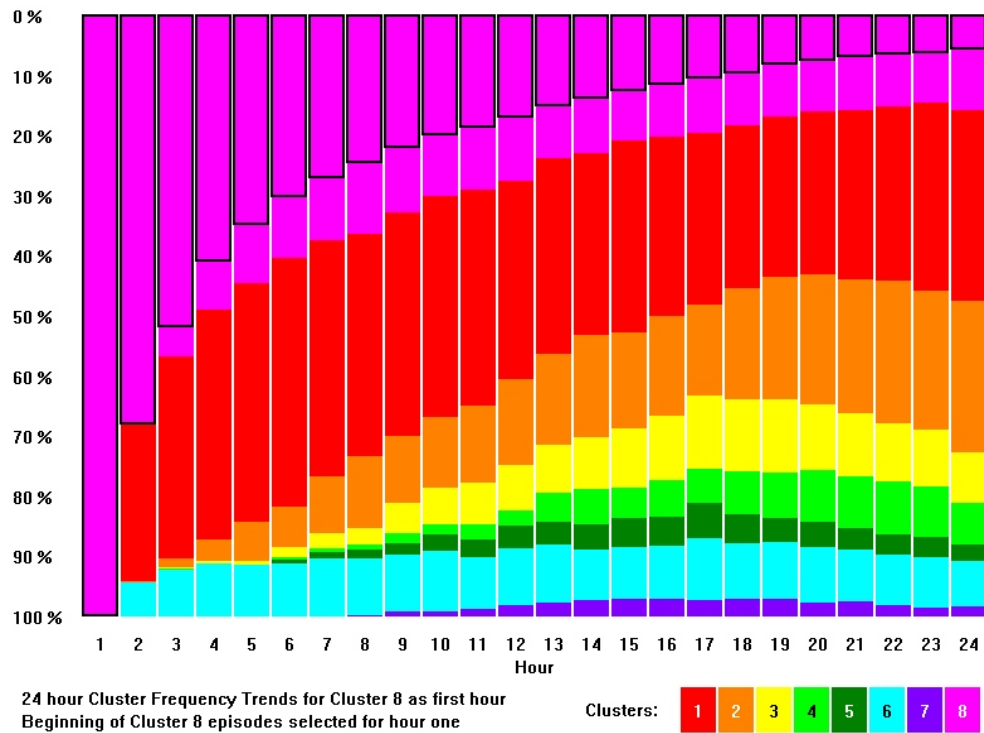


Figure 38. Persistence of wind pattern 8 – strong synoptic effects yield NNE winds.

Occurrence of Wind Patterns by Season

Figures 39 through 50 present information on the relative frequencies of INL wind pattern types by month as the seasons

change. In January and February, pattern types 1 (drainage flow), 2 (light and variable), and 4 (decreasing upslope winds) dominate, with little occurrence of other flow pattern types.

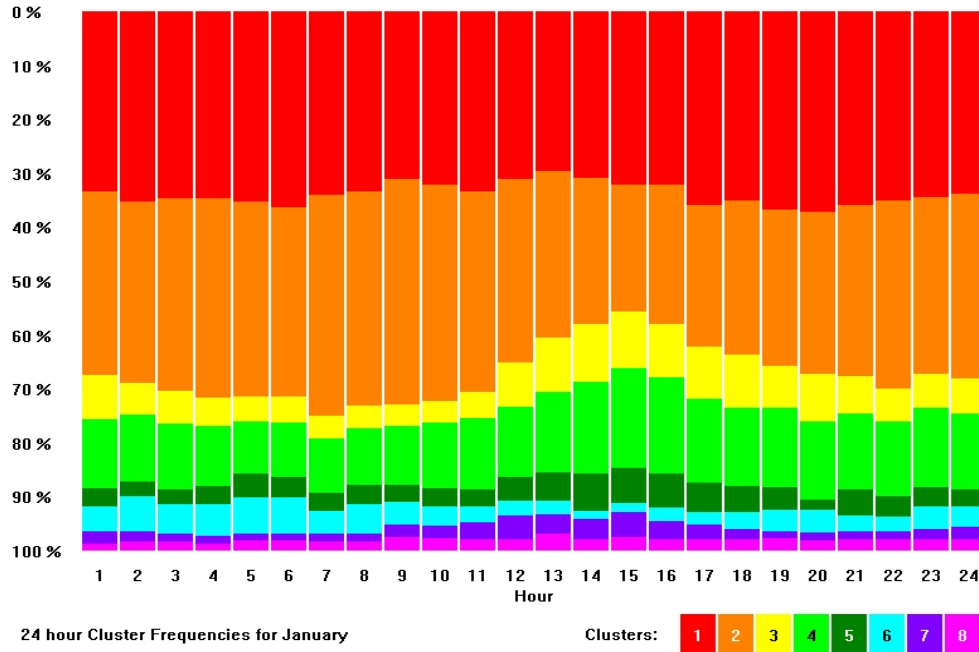


Figure 39. Typical wind pattern occurrence during January.

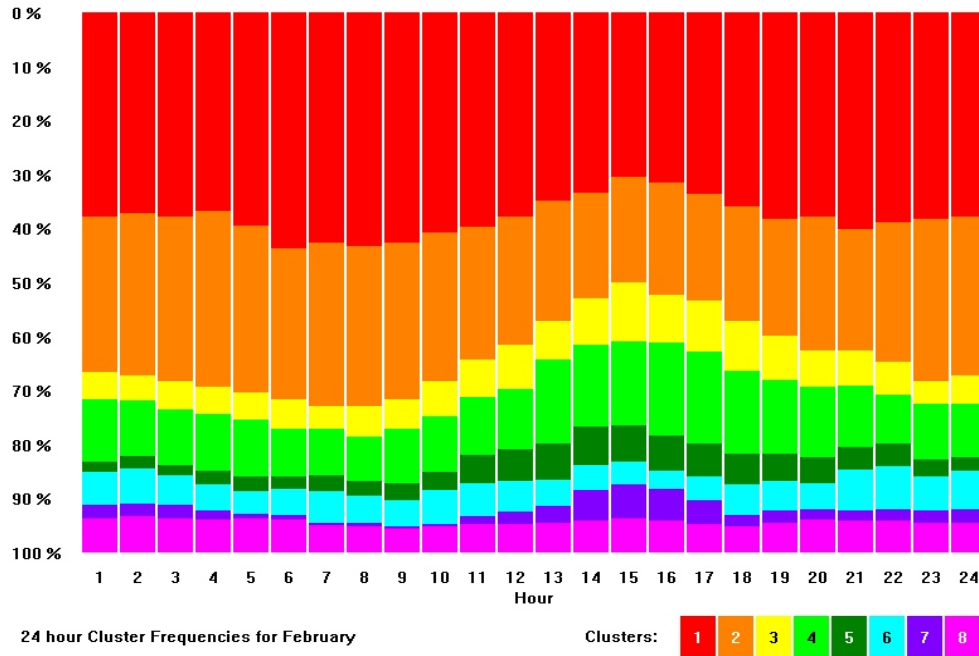


Figure 40. Typical wind pattern occurrence during February.

During March and April, all eight wind pattern types occur, with conspicuous increases in Wind Pattern 7 in which strong

synoptic effects drive southwesterly winds during the afternoon.

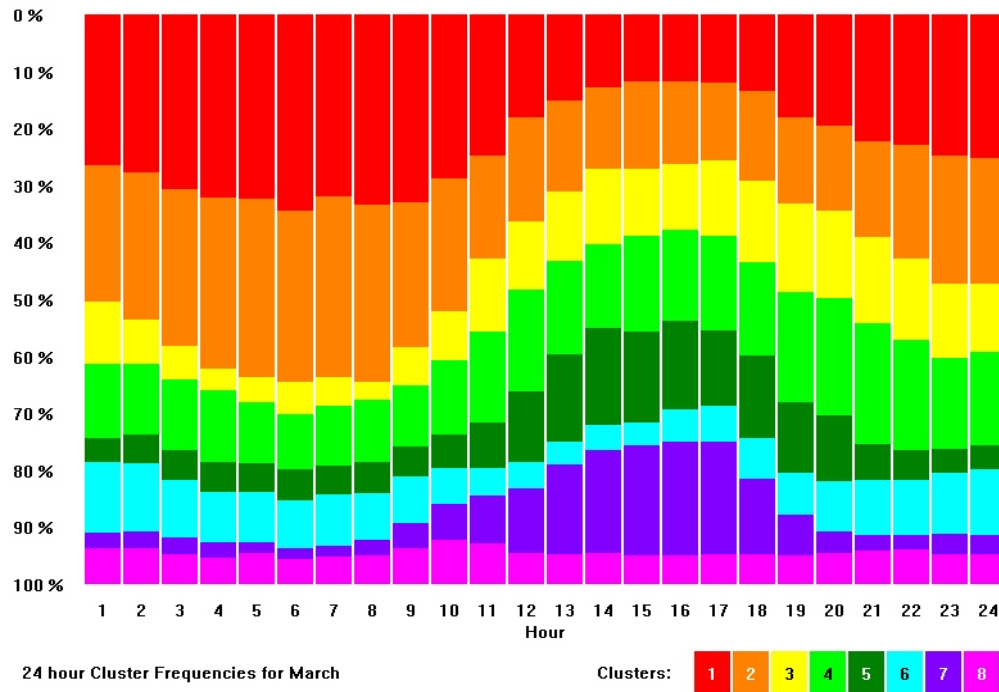


Figure 41. Typical wind pattern occurrence during March.

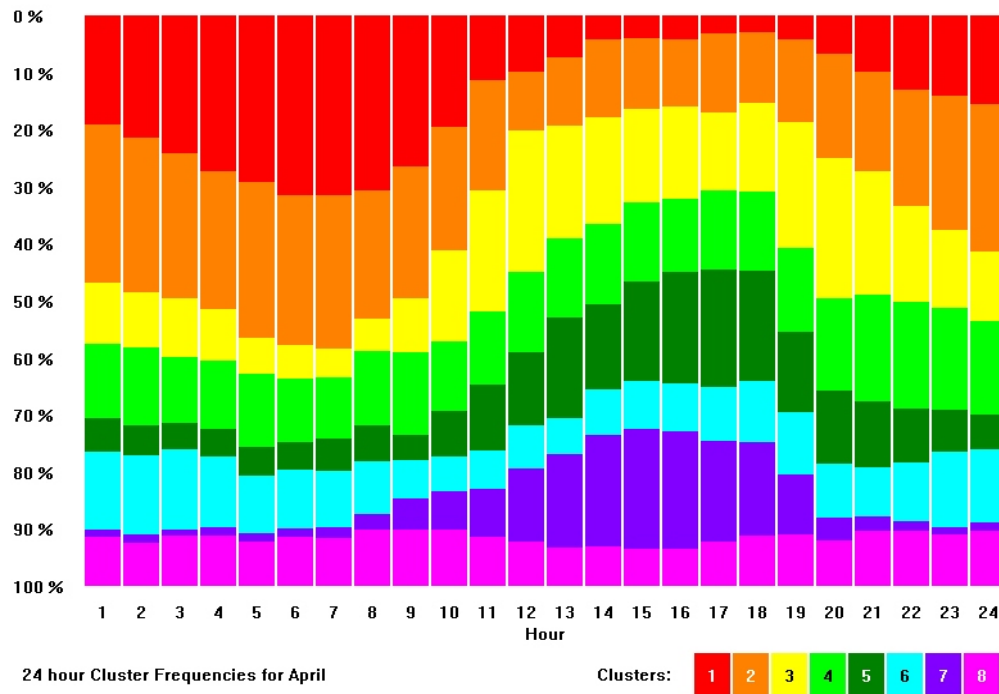


Figure 42. Typical wind pattern occurrence during April.

During May and June, all eight wind pattern types occur, with continuing strong occurrence of wind pattern 7 (strong synoptic effects drive southwesterly winds) occurring

earlier in the day, and wind pattern 5 (well-developed upslope flow) markedly increasing as solar heating reaches its maximum and upper air temperatures remain relatively cool.

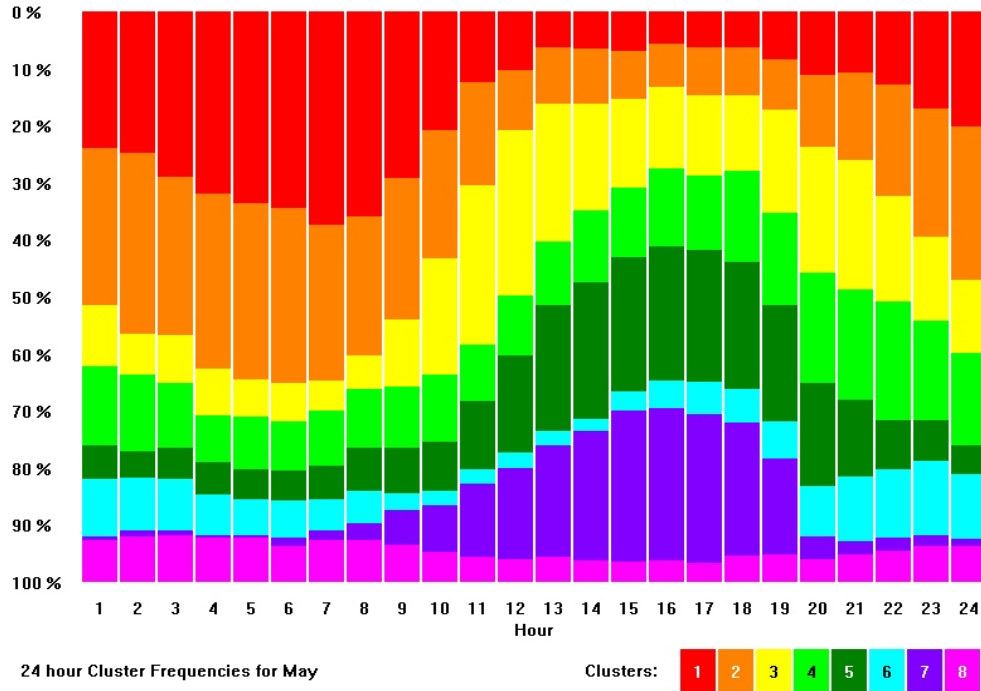


Figure 43. Typical wind pattern occurrence during May.

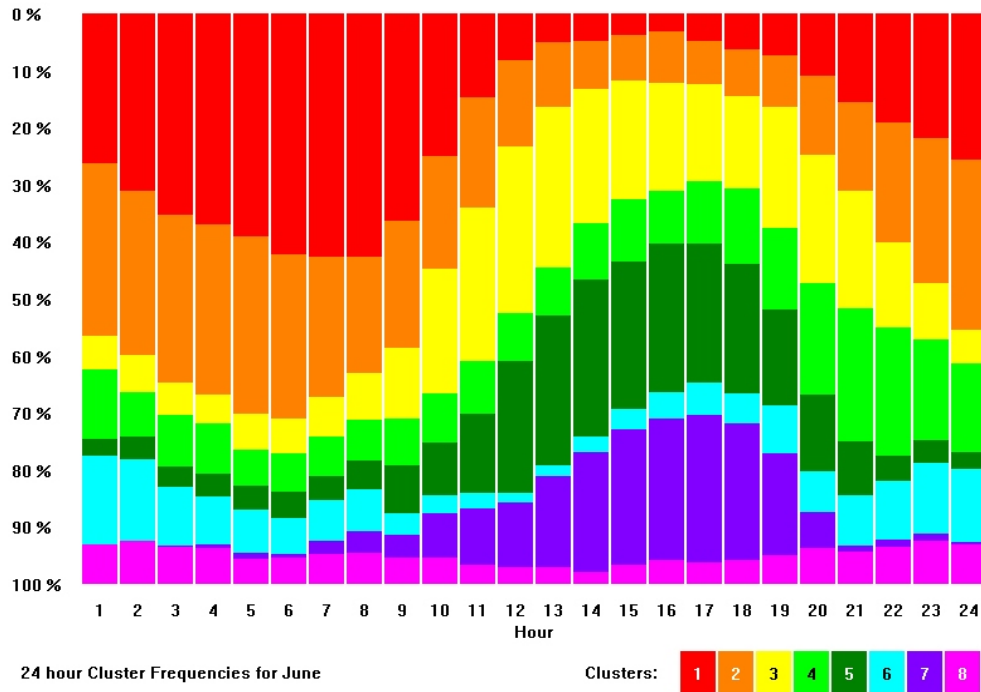


Figure 44. Typical wind pattern occurrence during June.

During July and August occurrences of wind patterns 4, 6, and 8 (decreasing upslope flow after sunset, down-canyon drainage flow aided by synoptic features, and strong synoptic effects yielding NNE winds)

are rarities. Patterns 5 (well-developed upslope flow) and 7 (strong synoptic effects driving southwesterly winds) are prominent afternoon and evening features. Patterns 1 and 2 are very common at night.

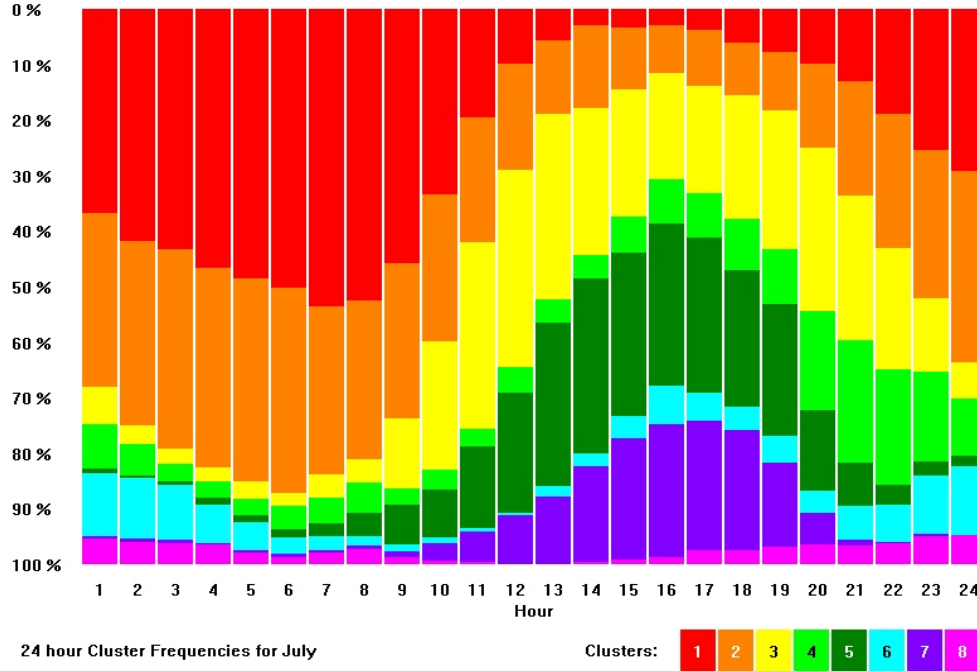


Figure 45. Typical wind pattern occurrence during July.

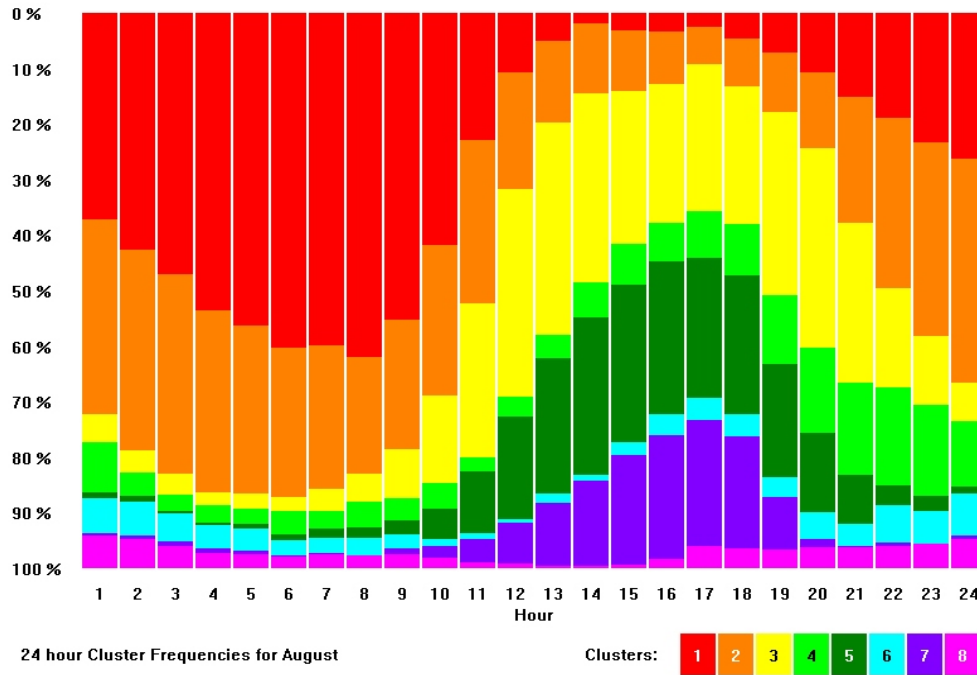


Figure 46. Typical wind pattern occurrence during August.

During September and October, occurrences of wind patterns 5 (well-developed upslope flow) and 7 (strong synoptic effects driving southwesterly winds) become less prominent in the afternoon, and

reveal a step-wise discontinuity at sunset times during the fair “Indian-summer” fall evenings. Patterns 1 and 2 are again prevalent at night.

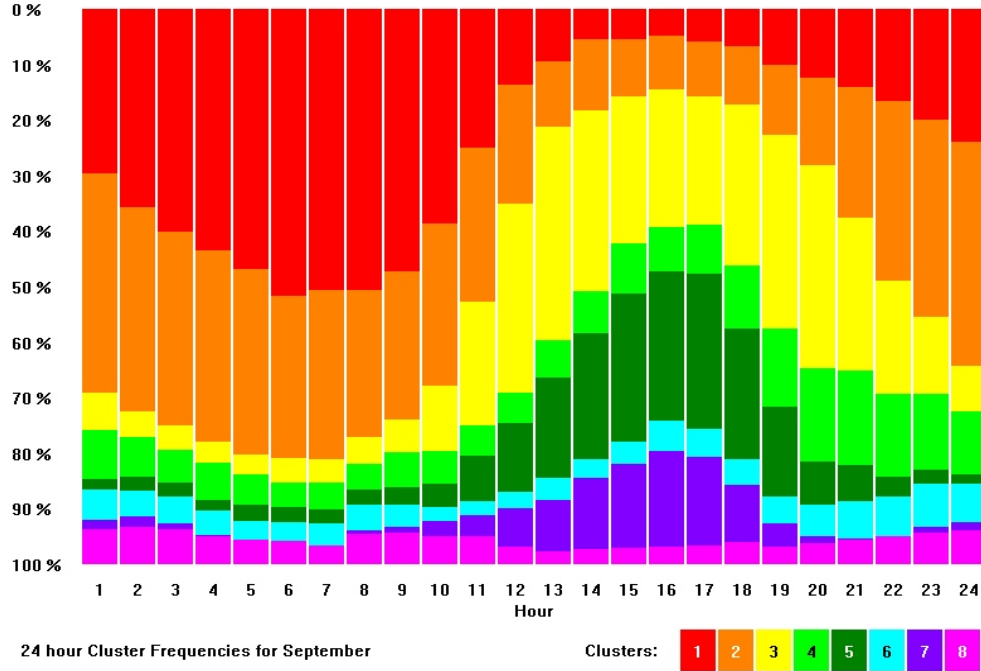


Figure 47. Typical wind pattern occurrence during September.

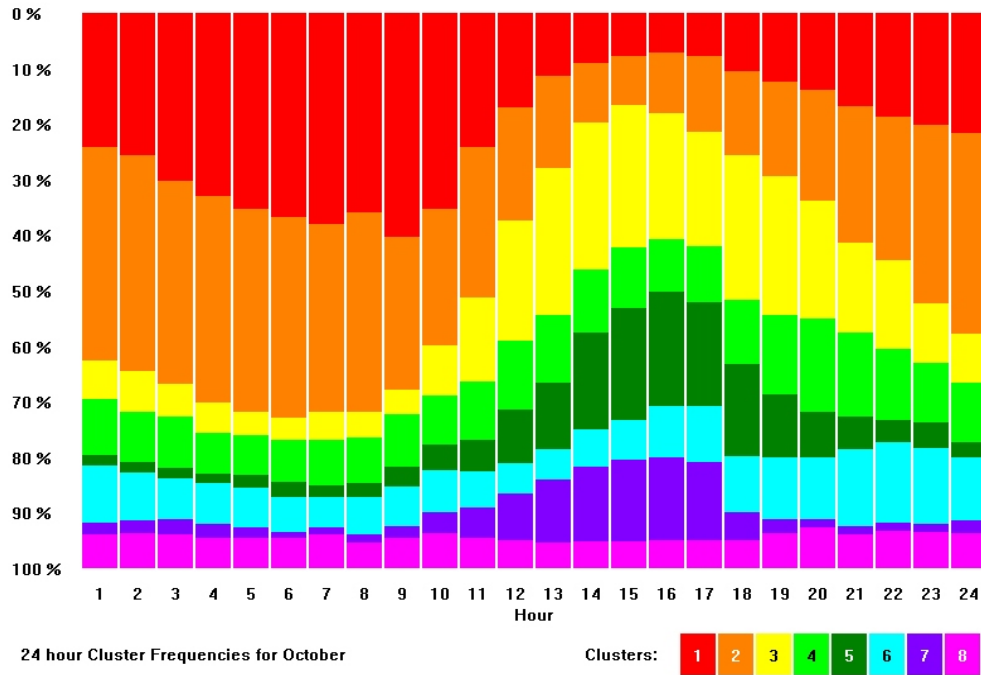


Figure 48. Typical wind pattern occurrence during October.

During November and December, pattern types 1 (drainage flow), 2 (light and variable) and 4 (decreasing upslope winds)

dominate as the winter weather regime is again reestablished.

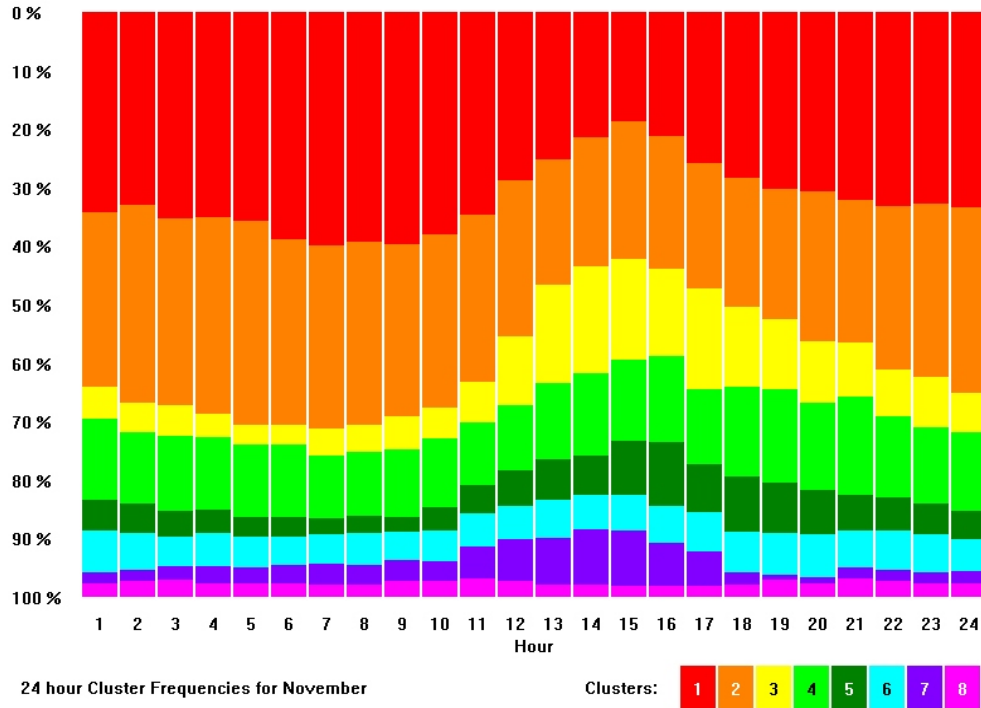


Figure 49. Typical wind pattern occurrence during November.

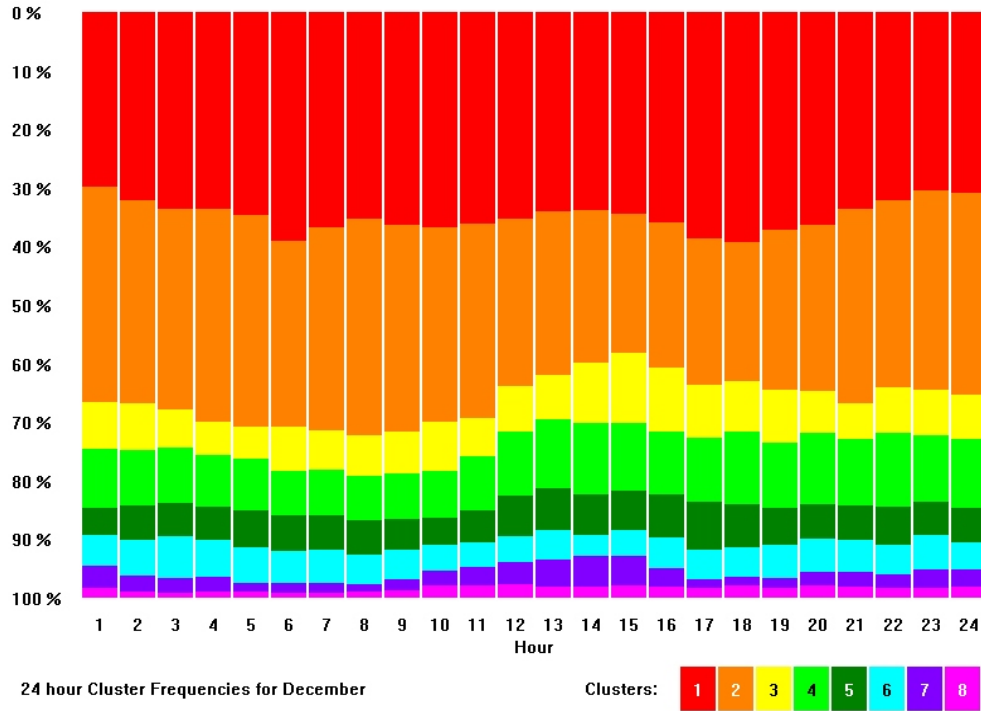


Figure 50. Typical wind pattern occurrence during December.

Winds Aloft

An extensive record of upper air observations was assembled from routine daily PIBAL observations from 1950 to 1965, and was published in the 2nd Edition Climatology (Clawson et al., 1989). Since 1994, 30-minute averages of upper air data have been acquired by a radar wind profiler (for winds aloft) and a RASS (for temperature profiles) at the INL. The system is located in the Grid 3 atmospheric research area north of INTEC. The radar wind profiler and RASS have the advantage of providing continuous wind and temperature data, as opposed to one pibal sounding per day providing winds only. Pibals were tracked up to heights of 14,000 ft msl. RASS sounding depths are made to a height of 17,000 ft msl.

Radar Profiler

To date, 30-minute averaged wind profile data have been acquired using the radar wind profiler's "low-resolution / high-range" sampling mode, which utilizes 48 range gates from 152 to 4,920 m above the ground, with a resolution of about 96 m. Data availability in this sampling mode is not as sensitive to diurnal changes of the atmosphere as is a higher resolution, shorter range option. At least 50% or better data capture is found up to approximately 2,000 m elevation (Fig. 51).

Questionable data acquired by the radar have been identified and removed using automatic algorithms developed by Weber and Wuertz (1991) and Weber et al. (1993).

A contour plot of the mean scalar wind speeds over an 12-year period of record is provided in Fig. 52. In general, the wind speed increases with height from 4 m s^{-1} at the lowest reported range gates (ca. 100 to 500 m) up to 15 m s^{-1} above 4,500 m. Above 1,200 m, the winds tend to be the same magnitude over the course over the entire day. However, the radar data suggest that the wind speeds decrease in magnitude below 1,200 m between 0400 MST and 1000 MST.

The radar profiler time / height vector plot is presented in Fig. 53. Average winds are light ($< 2 \text{ m s}^{-1}$) and variable throughout the morning from the surface up to 1,000 m. Above 1,200 m, the winds increase sharply to 6 m s^{-1} by 1,800 m and then gradually to 11 m s^{-1} by 5,000 m.

RASS

Temperatures aloft have been measured continuously since 1994 using a RASS that is co-located with the radar wind profiler at Grid 3 (Fig. 8). Unambiguous signal inversion of the RASS reaches through approximately one-half the depth of the profiler, with at least 50% or better data capture up to 900 m elevation (Fig. 54).

A contour plot of the mean virtual temperature derived from the RASS over an 12-year period of record is provided in Fig. 55. Mixing due to solar heating is evident in the average vertical temperature profile during the period of 1400 to 1900 MST, with only small changes in the height range 600 – 1,000 m along the mean top of the surface temperature inversion.

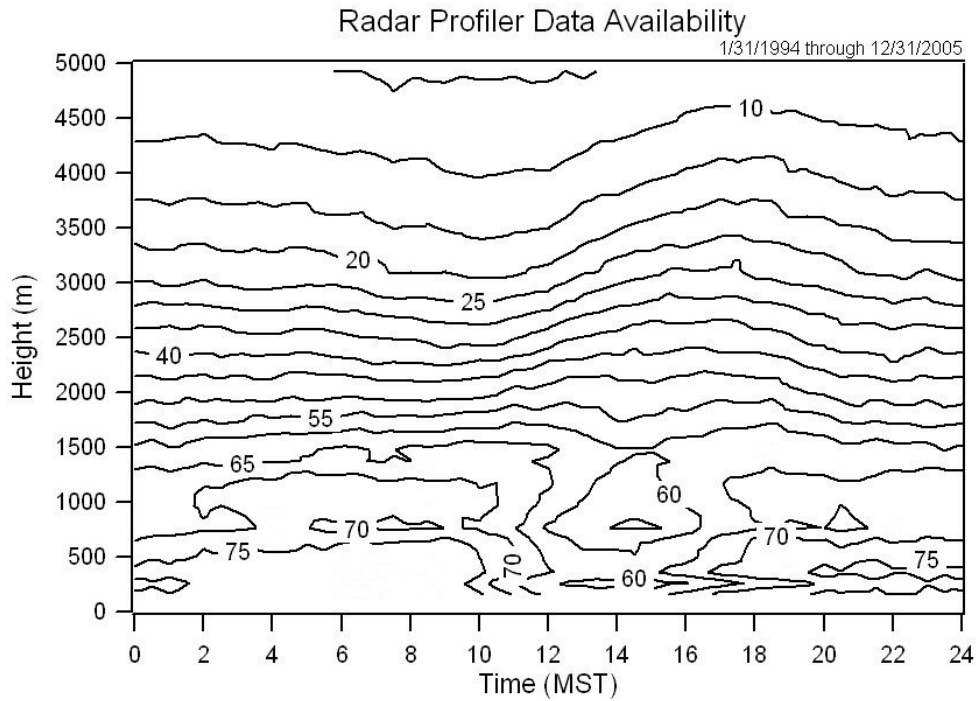


Figure 51. Radar (Mode 2) data availability (%) as a function of time and height.

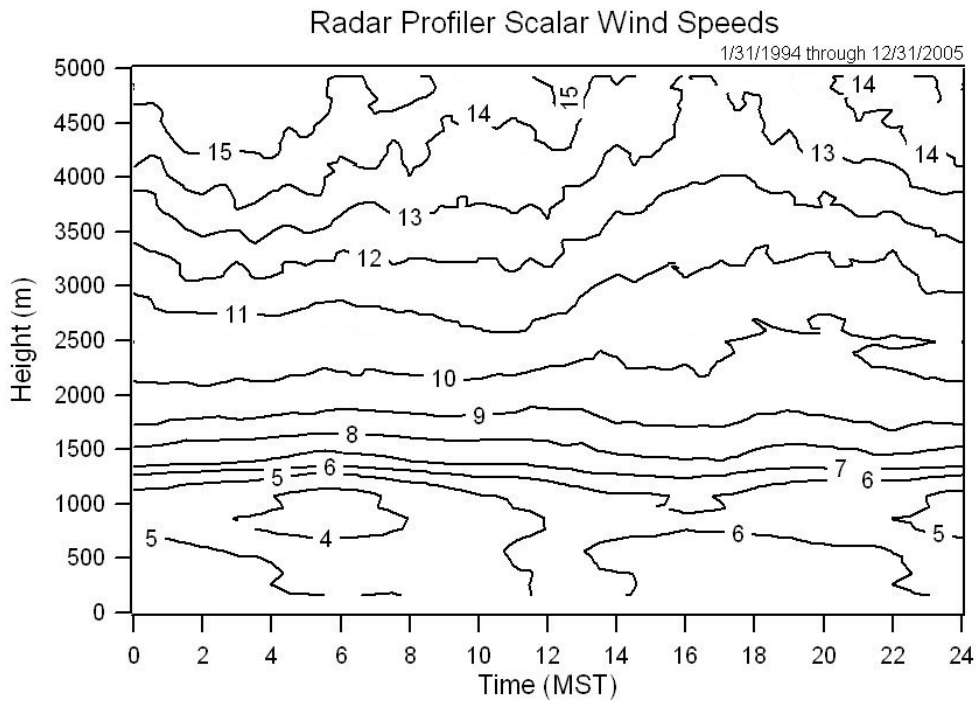


Figure 52. Radar (Mode 2) scalar wind speed (m s^{-1}) as a function of time and height.

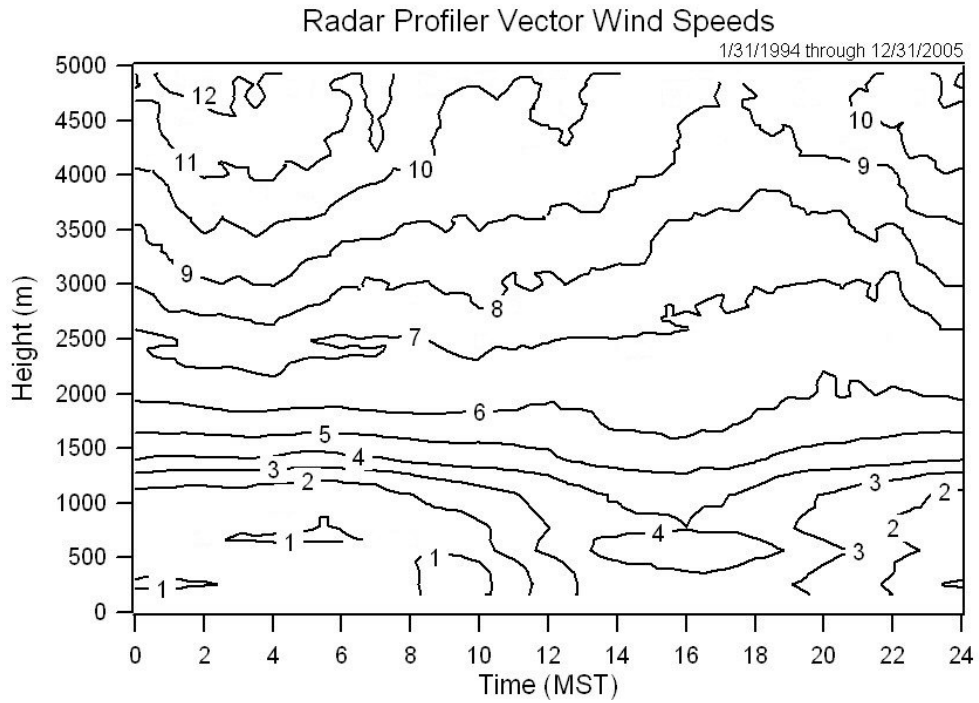


Figure 53. Radar (Mode 2) vector wind speed (m s^{-1}) as a function of time and height.

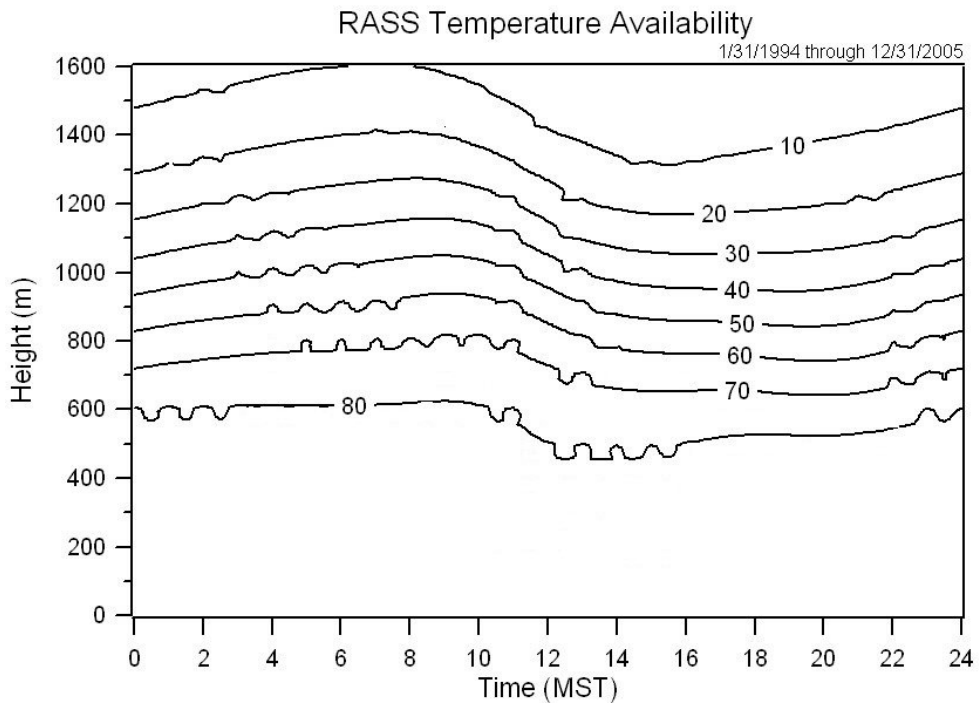


Figure 54. RASS data availability (%) as a function of time and height.

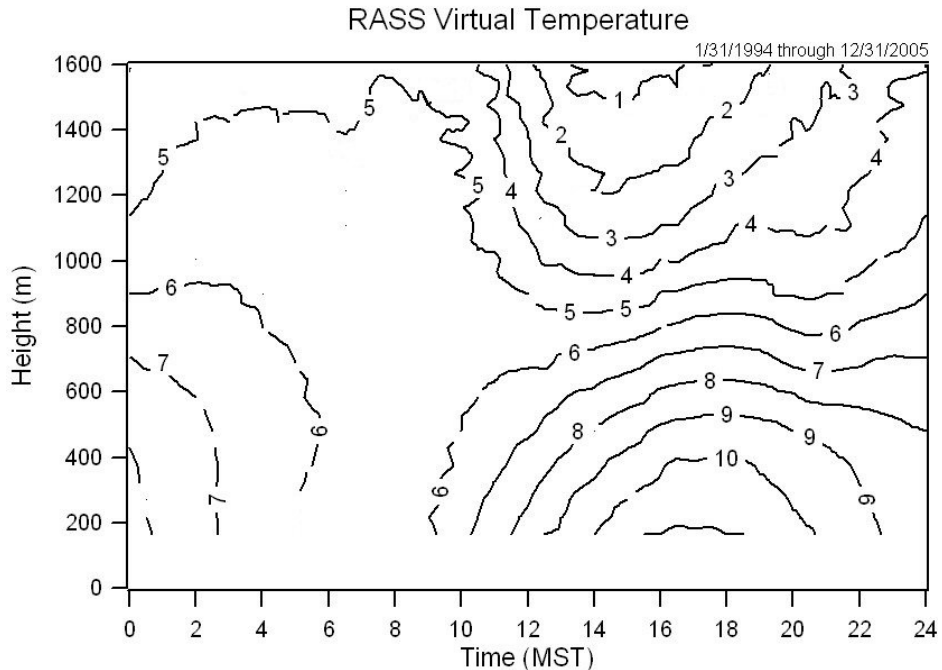


Figure 55. RASS virtual temperature (C) as a function of time and height.

Mean Winds and Persistence

Figure 56 is a contour plot of the persistence of the wind in the lower troposphere where the radar profiler is most effective. Persistence is the ratio of the vector wind speed to the scalar wind speed. A value near 100% would represent a "persistent" wind that varies little over an averaging period, while a low value represents a random wind flow. The most persistent winds aloft are the westerly winds observed above 1,000 m. Near the surface, the northeasterly winds seen between midnight and 0400 MST, and the southwesterly winds in the period noon to 2000 MST can be identified in the first several hundred meters of the atmosphere. In general, these flows are repeated almost daily during the late summer.

Surface Wind Channeling Mechanisms in the Snake River Plain

It is clear from the previous wind roses that the winds within the Snake River Plain are generally channeled along the southwest-northeast axis of the topography. Channeling of this type is common in valleys, but the detailed physical mechanisms that cause it are not currently well understood. Since the last edition of this climatology, however, significant progress has been made in understanding several different mechanisms that can cause such channeling. Much of this progress has been related to a more widespread use of mesoscale numerical models (Pielke, 2002), which has allowed researchers to simulate the three-dimensional structure of the winds within valleys.

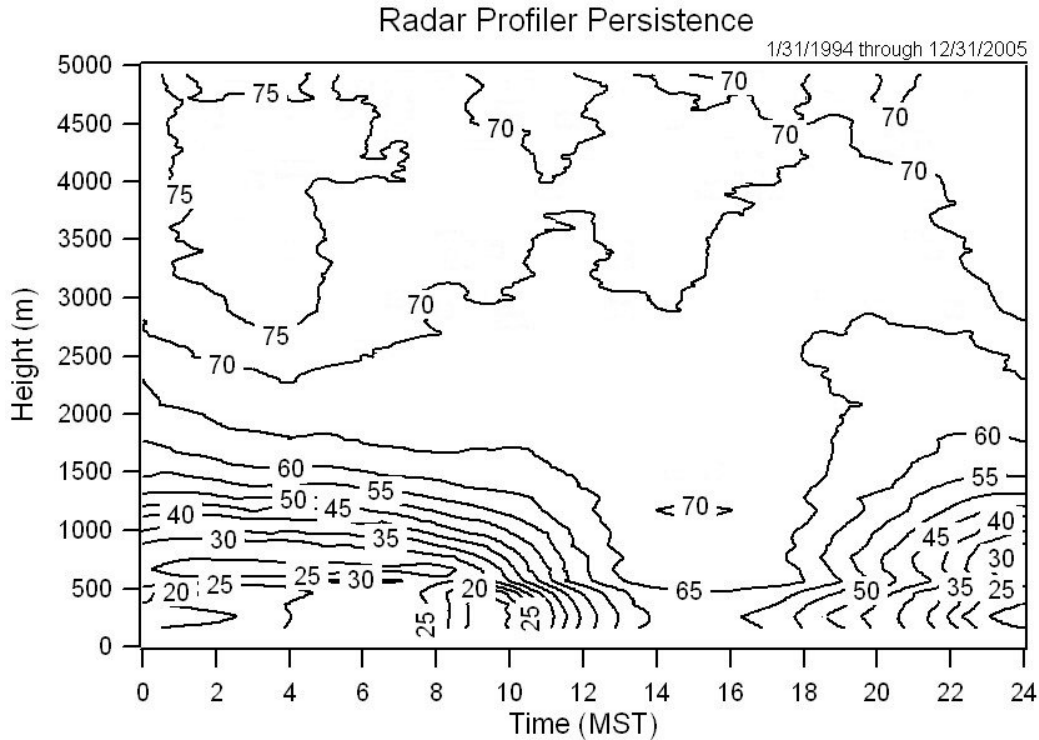


Figure 56. Radar (Mode 2) persistence (%) as a function of time and height.

The type of channeling that has been studied the longest is thermally driven winds (Egger, 1990; Whiteman, 1990). These are winds caused by differential heating and cooling within a valley, resulting in up-valley winds during the day and down-valley winds at night. Thermally forced wind systems are most likely to be observed when synoptic-scale winds are light. Due to the general orientation, thermally driven winds in the Snake River Plain are expected to produce southwest winds during the day and northeast winds at night.

Channeling in valleys can also be produced by interactions of synoptic-scale flows with the topography. Whiteman and Doran (1993) identified two potential mechanisms by which synoptic-scale winds can be channeled along a valley axis. One mechanism, called forced channeling,

assumes that the valley sidewalls simply act as obstacles that tend to block the cross-valley component of the synoptic-scale wind while providing little hindrance to the along-valley component. The wind within the valley is channeled in the direction that matches the along-valley component of the synoptic-scale wind.

The second mechanism by which synoptic-scale winds can be channeled is called pressure-driven channeling. It was first suggested to explain the observed winds within the shallow Upper Rhine Valley in Germany (Wippermann, 1984; Gross and Wippermann, 1987). The channeling arises from imbalances in the forces acting on the air within the valley. In flat terrain outside the valley, the wind direction is determined by a balance among the synoptic-scale pressure-gradient force, the Coriolis force, and surface

drag. The winds are roughly parallel to the isobars, with some turning towards low pressure due to the surface drag. Within a valley, however, blockage by the sidewalls tends to hinder the accelerations associated with the Coriolis force, resulting in a more dominant pressure-gradient force. As a result, the wind accelerates along the valley axis from high to low pressure.

Pressure-driven channeling is an important mechanism in broad, shallow valleys such as the Upper Rhine Valley and the Tennessee River Valley in eastern Tennessee (Whiteman and Doran, 1993; Eckman, 1998). Forced channeling appears to be more important in small valleys and canyons, such as the smaller corrugations that run along the floor of the Tennessee River Valley (Eckman, 1998). Both of these mechanisms are expected to be more important in stable conditions when the valley sidewalls are a more effective barrier to cross-valley winds. In daytime convective conditions the valley sidewalls may become less of a barrier to the wind. Additionally, deep, turbulent mixing that can develop on sunny days tends to couple the winds at the surface to the winds aloft. Under such conditions, neither forced nor pressure-driven channeling may be effective, and the valley

winds may be closely aligned with the winds aloft. Whiteman and Doran (1993) call this scenario downward momentum transport, because vertical mixing by turbulence is a major factor in masking the channeling effects. Eckman (1998) simply calls this “un-channeled flow”, as it represents a situation in which the topography has little effect on the near-surface winds.

In considering the importance of these various channeling mechanisms for the Snake River Plain, the question arises as to how they can be distinguished. One method is to compare the wind direction within the valley with the wind direction aloft just above the valley. Each mechanism produces a distinct relationship between these winds. For the ESRP, the mechanisms are expected to produce the relationships shown in Fig. 57. Thermally driven winds are decoupled from the winds aloft, therefore the valley wind can be either up-valley or down-valley for any direction of wind aloft. Both forced channeling and pressure-driven channeling produce abrupt shifts in the valley wind direction at certain directions of winds aloft, but the shift points for the two mechanisms differ by 90°. With un-channeled flow, the wind direction aloft and wind direction in the valley are the same.

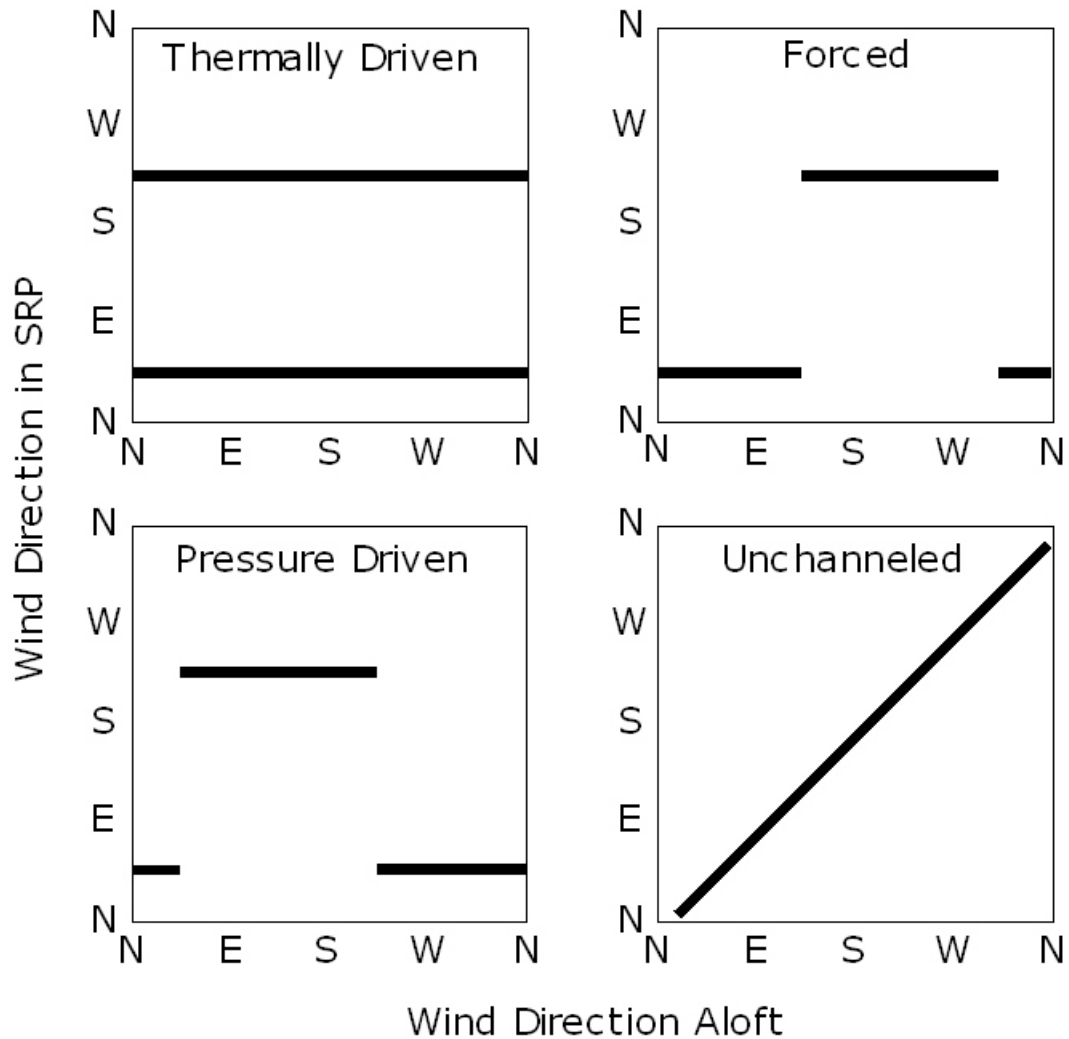


Figure 57. Expected relationship of surface winds within the Snake River Plain to winds aloft for different channeling mechanisms.

Both the wind data presented earlier in this climatology and the data used by Stewart et al. (2002) suggest that thermally driven flows can be important in the Snake River Plain when the synoptic winds are light. However, they are by no means the dominant feature. Figure 58, for example, shows wind roses for the GRI 10 m level representing both nighttime (0000-0600 MST) and daytime

(1200-1800 MST) conditions. If thermally driven flows were dominant, one would expect daytime southwesterly winds and nighttime northeasterly winds. While the figure does show an increased frequency of lighter northeasterly winds at night, southwesterly winds are common during both time periods.

Figure 59 shows day and night wind roses for the BLU tower located within the Birch Creek tributary valley. This location shows a much more distinct diurnal wind reversal from northwesterly (down-valley) winds at night to southeasterly (up-valley) winds during the day. Hence, thermally

driven flows appear to be more of a factor in the tributary valleys to the west of INL than in the Snake River Plain itself. However, northwesterly daytime winds at BLU are not uncommon, suggesting that other channeling mechanisms are still at work in Birch Creek.

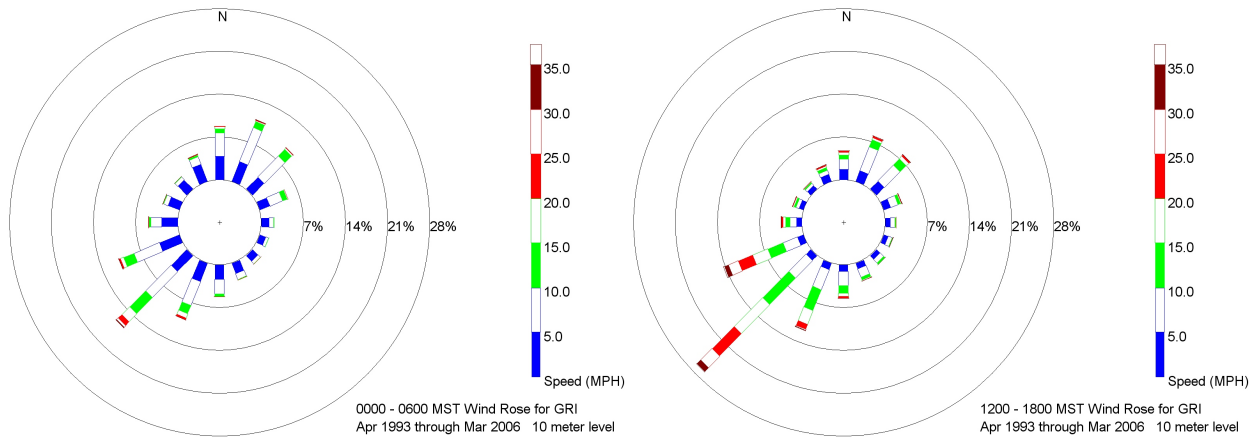


Figure 58. Wind roses at the GRI tower 10 m level for night and daytime periods.

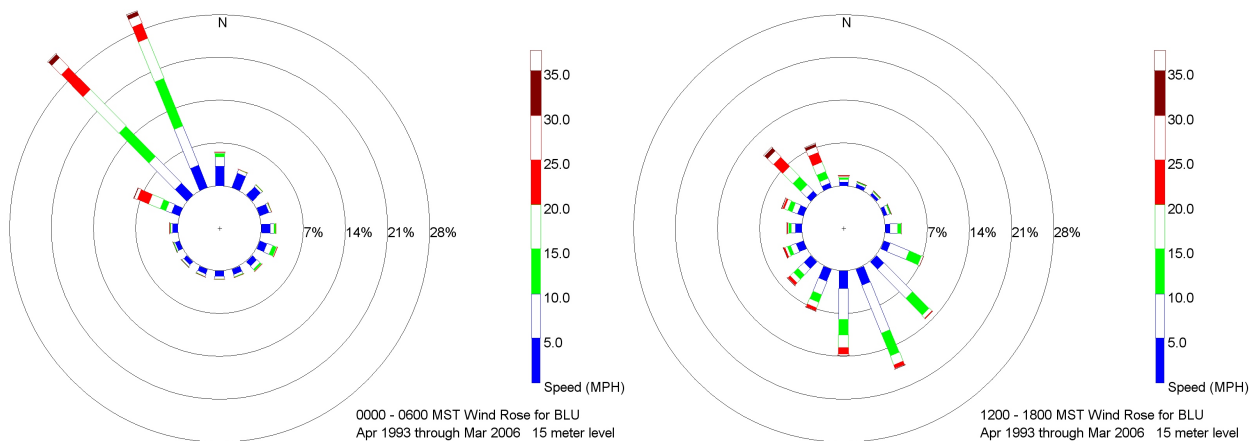


Figure 59. Wind roses at the BLU tower for night and daytime periods.

Kossmann et al. (2002) reported some preliminary work in the Snake River Plain regarding the relative importance of forced and pressure-driven channeling, and concluded that pressure driven channeling appears to be more dominant. However, they used winds at the 700 hPa level from the Boise, Idaho rawinsonde as a surrogate for the winds aloft in all of the Snake River Plain. Given that Boise is over 250 km from the eastern part of the plain, this could result in considerable error. Unfortunately, a more detailed analysis of these channeling mechanisms in the Snake River Plain has not been performed.

The wind profiler that is in operation at INL has the potential to provide a better data set for investigating the channeling. Figure 60, for example, shows the wind direction from the 10 m level on the GRI tower plotted against the profiler wind direction at 1,577 m AGL. This latter height was chosen because it is near the 700 hPa pressure level. Periods of light synoptic forcing when the 1,577 m wind speed was less than 5 m s^{-1} were excluded from the analysis. The sizes of the rectangles in the plot are scaled according to their relative frequency within 5° bins along the x axis.

Shift points in the GRI direction are observed when the upper-level wind is between about 170° and 340° . In comparison with Fig. 57, these data appear to be in better agreement with forced channeling than pressure-driven channeling, which contradicts the Kossmann et al. (2002) results and is somewhat surprising given the results obtained in other wide valleys. However, a closer inspection of the Kossmann et al.

(2002) study reveals that the data for the eastern part of the Snake River Plain may in fact be more consistent with forced channeling than pressure-driven channeling.

One caveat with Fig. 60 is that the analysis and plotting procedures may be masking the importance of other mechanisms to some degree. It has previously been noted that periods with light upper-level winds ($< 5 \text{ m s}^{-1}$) were excluded. This eliminates many of the periods with thermally-driven winds at the surface. Additionally, the normalization method for the rectangles obscures the fact that westerly winds aloft are far more frequent than easterly winds. Many of the rectangles on the left side of the plot are based on relatively few cases. Un-channeled flow (downward momentum transport) may be more important than indicated in the plot. Many of the high-wind events at the INL are associated with approaching storm systems, when the upper-level winds are out of the southwest. Downward mixing is clearly a major contributor to these events. However, both forced channeling and unchanneled flow lead to the same result when the wind aloft is out of the southwest (Fig. 57). The unchanneled flow may therefore be masked because it occurs preferentially for southwesterly winds aloft.

Clearly, there is still considerable work to be done in understanding the channeling within the eastern Snake River Plain. The data from the INL profiler is expected to be useful in this effort, as shown by the preliminary data given in Fig. 60, and may be summarized in future additions of this climatology.

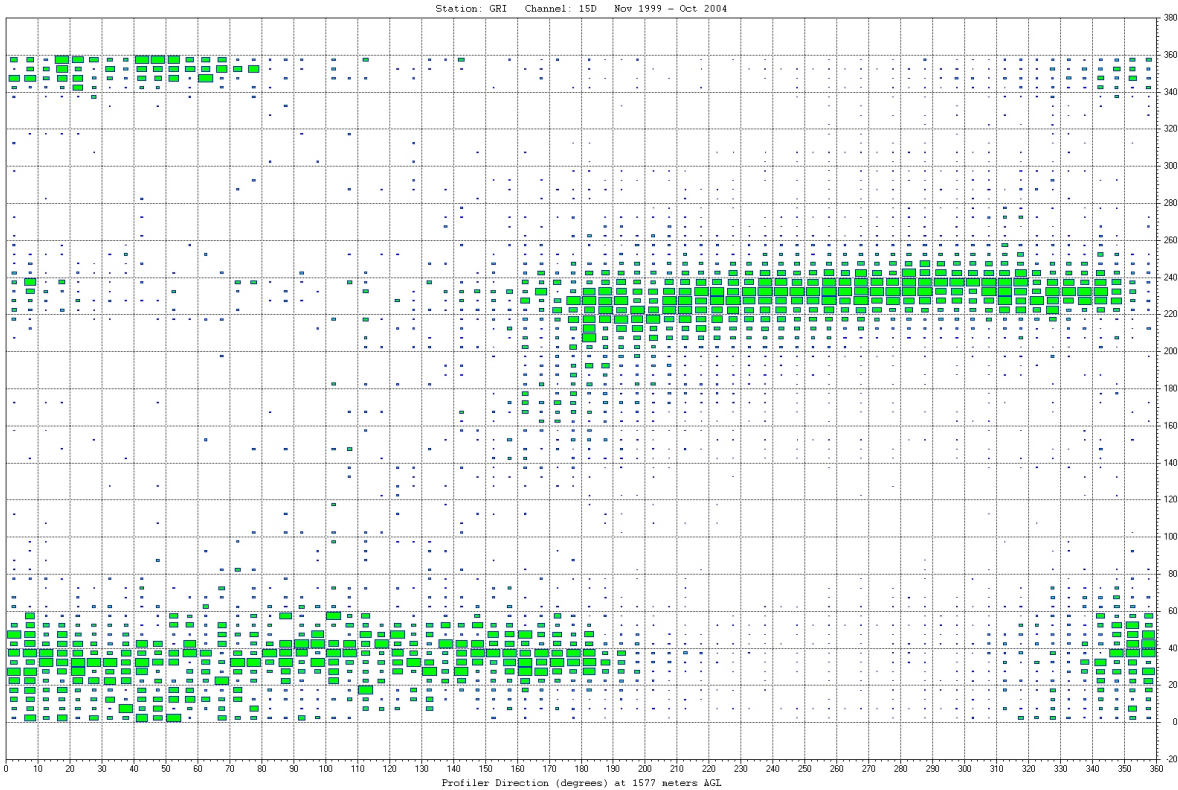


Figure 60. Frequency Diagram: GRI Tower 10 m Wind Direction vs Radar Profiler 1,577 m Wind Direction. (Rectangle sizes are scaled according to relative frequency of the GRI winds within 5° bins along the x axis).

AIR TEMPERATURE

Knowledge of air temperatures is necessary for appropriate facility design. Furthermore, knowledge of the atmospheric thermal characteristics is an important contributor to forecasting and to airborne effluent dispersion calculations.

Surface air temperatures at the INL are best characterized by two stations: CFA and TAN. Although somewhat similar to conditions at CFA, a third regime is known to exist around the MFC area. This edition of the INL climatology emphasizes CFA temperature parameters that are based on an extensive (over 50-year) quality-controlled period of record. The 2nd Edition

climatology (Clawson et al., 1989) included a 15-year period of record for TAN that had been normalized to a conventional 30-year period using the records from surrounding stations with full 30-year records, based on standard NCDC procedures. The reader is referred to the 2nd edition climatology for TAN data. The MFC air temperature database is not extensive enough to fully define its characteristics at this time.

Daily Surface Air Temperature Ranges

Monthly and annual averages of diurnal air temperature ranges for CFA are presented in Table 8. The data indicate that the average daily air temperature range for the 56-year period of record at CFA ranges from

Table 8. Average and maximum daily air temperature ranges summarized by month for CFA.

	Mean (deg F)	Maximum (deg F)
January	23	52
February	24	50
March	24	53
April	28	57
May	30	55
June	33	55
July	38	57
August	38	59
September	37	59
October	34	59
November	25	52
December	23	54
ANNUAL	30	59

Note: Data period of record spans January 1950 through December 2006.

a low of 23° F in December and January, to a high of 38° F during July and August. Larger means during the period May to October reflect the relative absence of clouds during these months that moderate radiational cooling of the ground surface at night. Maximum diurnal temperature ranges at CFA exceed 50° F during all months, a reflection of the INL’s altitude and typically low humidity. Maximum diurnal temperature events occur almost exclusively during clear-sky conditions, with largest ranges occurring in the fall, before the ground loses its accumulated summer heat.

Surface Air Temperature Means and Extremes

The means and extremes of daily temperatures at CFA from 1950 through 2006 are summarized in Table 9. The maximum air temperature recorded at CFA was 105° F, while the minimum was -47° F. In comparison, the maximum and minimum air

temperatures recorded for TAN are 103° F and -49° F, respectively.

Temporal and Spatial Variability of Surface Air Temperature Means and Extremes

Monthly and annual average air temperatures for CFA are given in Table 10. This table also includes the historical highest and lowest of those monthly and annual averages, together with averages of daily extremes during those time periods. The large year-to-year variability of average monthly temperatures – especially in the winter season – can be readily seen in this table. For example, the highest monthly average air temperature at CFA has been 34.1° F in February, while the lowest monthly average air temperature in that same month has been 7.1° F. The difference in this case, 27° F, indicates a rather large deviation in monthly air temperatures from year to year. Only one-third as much year-to-year variability occurs in late summer.

Table 9. Daily air temperature extremes summarized by month for CFA.

	Highest Daily Maximum (deg F)	Lowest Daily Minimum (deg F)	Highest Daily Average (deg F)	Lowest Daily Average (deg F)
January	55	-40	44	-20
February	60	-36	45	-23
March	73	-28	54	-6
April	86	6	63	22
May	96	13	76	30
June	100	23	83	39
July	105	28	83	49
August	102	24	83	46
September	96	12	74	30
October	87	-6	64	10
November	67	-24	57	-9
December	57	-47	47	-28
ANNUAL	105	-47	83	-28

Note: Data period of record spans January 1950 through December 2006.

Table 10. Monthly and annual air temperature averages and extreme averages for CFA.

	Average			Maximum			Minimum		
	Average (deg F)	High (deg F)	Low (deg F)	Average (deg F)	High (deg F)	Low (deg F)	Average (deg F)	High (deg F)	Low (deg F)
January	16.6	30.0	7.0	28.0	37.9	19.5	5.2	22.4	-8.8
February	21.6	34.1	7.1	33.7	46.0	21.2	9.6	22.3	-7.1
March	31.6	41.5	18.4	43.9	56.8	31.4	19.4	26.6	4.5
April	42.2	49.3	35.4	56.4	68.6	46.1	27.9	33.1	22.5
May	51.6	58.5	45.3	66.7	77.7	59.9	36.5	40.8	30.2
June	60.0	67.5	54.9	76.5	86.4	69.1	43.6	49.7	39.5
July	68.4	73.5	59.1	87.3	94.8	76.1	49.4	53.6	42.0
August	66.3	70.9	60.3	85.3	90.2	75.4	47.3	53.4	43.0
September	56.0	62.3	48.6	74.2	82.3	64.1	37.7	45.2	31.9
October	43.9	51.0	38.2	60.8	71.7	53.7	27.1	32.8	20.8
November	29.6	36.3	20.3	42.1	51.5	30.8	17.1	24.3	6.4
December	18.5	26.9	7.0	30.0	37.0	20.8	7.0	17.6	-7.3
ANNUAL	42.3	45.5	37.7	57.2	61.3	52.4	27.4	30.1	22.9

Note: Data period of record spans January 1950 through December 2006.

The largest within-month differences are observed for the minimum air temperatures in the winter; particularly in January, where the difference is 31.2° F. The smallest within-month differences are observed for the minimum temperatures during the spring, summer, and fall months. The variability of the annual air temperature extremes listed in Table 10 is much smaller than the variability of the within-month extremes.

The average annual temperature progression at CFA increases from the first week in January until the third week in July (Fig. 61). However, a winter thaw has been observed on a number of occasions in mid January, followed by more cold weather in February. After the summer maximum in late

July, the temperatures decline through the end of December. The decline in air temperature during this time is much shorter than the spring and summer rise. The time span from the winter minimum to the summer maximum is approximately seven months. Conversely, the time span from the summer maximum to the winter minimum is approximately five months.

INL air temperatures may be highly variable from place to place for short periods of time. Simultaneous observations at CFA and TAN have occasionally shown temperature differences in excess of 25° F during the winter (Clawson et al., 1989). However, the spatial variation in the summer is not typically as large. Air temperatures from several locations on and surrounding the

CFA 30-Year Average Daily Maximum and Minimum Air Temperature

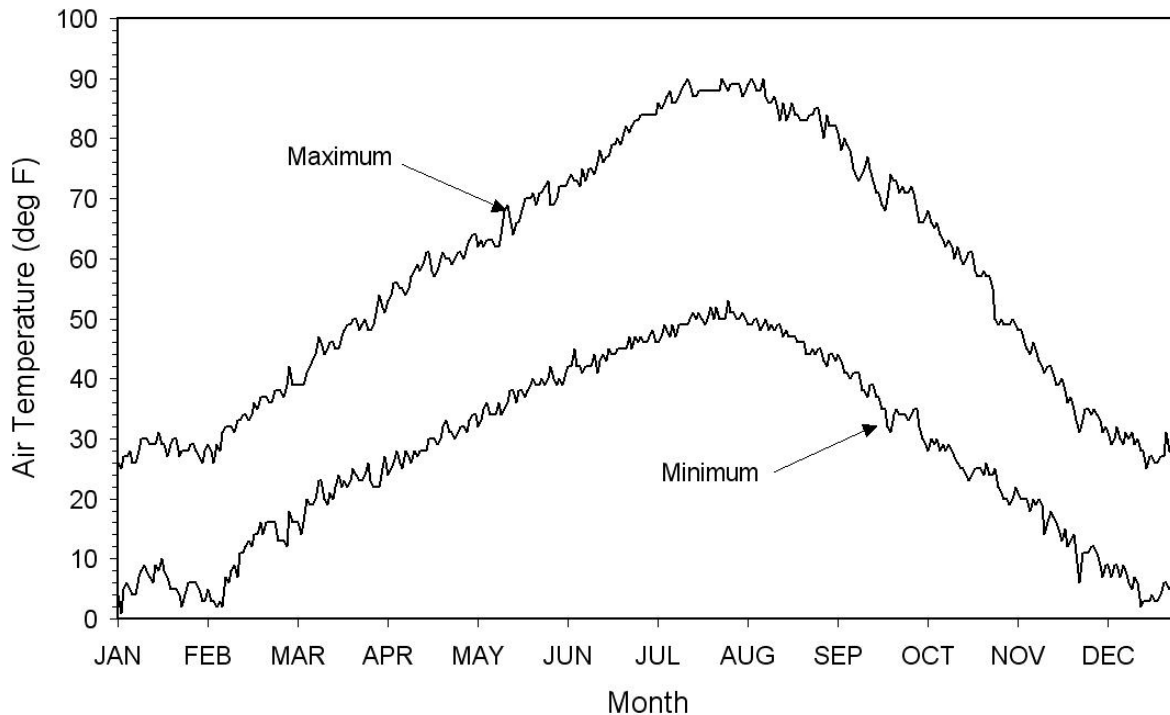


Figure 61. CFA 30-year average daily maximum and minimum air temperature from 1976 to 2005.

INL were compared on days when the extreme highest maximum and extreme lowest minimum air temperatures were observed. On the day the highest maximum air temperature was recorded at CFA (July 13, 2002), the temperatures varied from 96° F at Rexburg to 106° F at the Sand Dunes. On the day the lowest minimum air temperature was recorded (December 23, 1983), the temperatures ranged from -23° F at Blackfoot to -49° F at TAN. In general, these data show that the area near TAN experiences the lowest minimum and the highest maximum air temperatures.

Specific Surface Air Temperatures

The occurrences of specific temperatures are frequently of interest in the analysis of climate. The average, highest, and lowest number of days per month or per year (expressed as a percentage) when the maximum air temperature is less than or equal to 32° F, or greater than or equal to 90° F, are

presented in Table 11 for CFA. These data show that the air temperature on approximately 2/3 of the days in January usually remains below freezing at CFA. There has also been at least one February during the period of record when the air temperature rose above 32° F everyday. However, the air temperature has remained below freezing during the entire month of February during at least one year. Conversely, the air temperature usually rises above 90° F 43% of the time during July at CFA. The frequency of occurrence of this phenomenon at CFA has ranged from as large as 84%, to as small as 3%. Table 12 is similar to Table 11 in that it highlights the average, highest, and lowest number of days per month or per year (expressed as a percentage) when the minimum air temperature was less than or equal to 32° F or less than or equal to 0° F. These data indicate that the air temperature has dropped to freezing or below at least one time during every month of the year,

Table 11. Monthly and annual average number of days (%) when the maximum daily air temperature was at or below 32° F and at or above 90° F at CFA.

	Number of Days with Maximum ≤ 32° F			Number of Days with Maximum ≥ 90° F		
	Average (%)	Highest (%)	Lowest (%)	Average (%)	Highest (%)	Lowest (%)
January	66	97	19	0	0	0
February	42	100	0	0	0	0
March	12	61	0	0	0	0
April	0	0	0	0	0	0
May	0	0	0	0	10	0
June	0	0	0	9	43	0
July	0	0	0	43	84	3
August	0	0	0	34	68	3
September	0	0	0	5	23	0
October	1	10	0	0	0	0
November	18	73	0	0	0	0
December	57	94	19	0	0	0
ANNUAL	16	35	8	8	16	1

Note: Data period of record spans January 1950 through December 2006.

Table 12. Monthly and annual average number of days (%) when the minimum daily air temperature was at or below 32° F at CFA.

	Number of Days with Minimum ≤ 32° F			Number of Days with Minimum ≤ 0° F		
	Average (%)	Highest (%)	Lowest (%)	Average (%)	Highest (%)	Lowest (%)
January	99	100	94	38	77	0
February	99	100	89	26	86	0
March	95	100	81	6	42	0
April	72	97	37	0	0	0
May	30	65	3	0	0	0
June	5	17	0	0	0	0
July	0	6	0	0	0	0
August	2	16	0	0	0	0
September	26	57	0	0	0	0
October	74	97	39	0	3	0
November	94	100	73	7	23	0
December	98	100	84	31	68	0
ANNUAL	58	64	51	9	24	3

Note: Data period of record spans January 1950 through December 2006.

including the summer months, at CFA. The minimum air temperature at CFA is also, on the average, at or below freezing over 90% of the days during November, December, January, February, and March. The highest minimum air temperature during February has been at or below 0° F up to 86% of the time at CFA.

Heat Index

A unit of measure that takes into account the apparent air temperature during the summer is called the heat index. The heat index is a measure of the how the temperature really feels when relative humidity is combined with the air temperature. The heat index is calculated when the relative humidity and air temperature rises above 40% and 80° F, respectively. Due to the relatively dry climate across the ESRP on average there is less than 2 heat days a year in which the relative humidity and air temperature is

above 40% and 80° F, respectively (Table 12).

The heat index is still calculated when the air temperature is above 80° F and the relative humidity is lower than 40%, however, the heat index calculates to near or slightly below the actual air temperature. Nonetheless, caution (heat index between 80-89° F) is advised to INL outdoor workers on average of 74-84 days a year at the INL because fatigue is possible with prolonged exposure and/or physical activity. Extreme caution (heat index between 90-104° F) is urged for those workers on an average of 20-30 days a year because one may experience sunstroke, heat cramps, and heat exhaustion with prolonged exposure and/or physical activity. Since 1950 there have been no observations that indicate that the heat index reached the danger (105-124° F) or extreme danger (>125° F) heat index categories at the INL (Table 13).

Table 13. Average number of days per year in each heat index category and average number of days of heat days a year.

Station	Mean Annual # of Days in Caution Category (80 - 89° F)	Mean Annual # of Days in Extreme Caution Category (90 - 104° F)	Mean Annual # of Days in Danger Category (105 - 124° F)	Mean Annual # of Days in Extreme Danger Category (> 125° F)	Mean Annual # of Heat Days Per Year (>40% RH & >80° F)
690	79.9	26.2	0	0	1.8
MFC	74.7	20.9	0	0	0.3
GRI	83.6	29.6	0	0	1.4
SMC	80.8	24.3	0	0	1.0
RWM	79.9	24.6	0	0	1.0

Note: Data period of record spans January 1994 through December 2006.

Wind Chill

A unit of measure that takes into account the apparent air temperature during the winter is called wind chill. The wind chill is a measure of the how the temperature really feels when the wind is combined with the air temperature on exposed skin. The wind chill is calculated when the temperature is at or drops below 50° F and the wind speeds are greater than 3 mph. The higher the wind speeds the lower the wind chill temperature and thus the faster that one could get frostbite. Frostbite occurs in just 30 minutes when wind chill temperatures dip to -20° F. There are an average of 13 days per year at GRID 3 in which the wind chill temperatures drop below -20° F. Wind chill temperatures are

usually the lowest during December, January, and February. The lowest recorded wind chill temperature at GRID 3 was -50° F and occurred on February 2, 1996.

Warm Season Duration

The dates at which the last recorded minimum air temperatures of 32°, 28°, and 24° F are observed in the spring and the first occurrence of these temperatures in the fall are often required for agriculture, construction work and biological studies. Table 14 presents these data for CFA. The number of days between the various dates are also listed. The average frost-free period at CFA is 88 days. The shortest frost-free period at CFA has been 40 days during 1993.

Table 14. Dates of the last minimum air temperature of 24°, 28°, and 32° F in the spring, the first fall occurrence of these temperatures, and number of days between those dates for CFA.

Year	Last Spring Occurrence			First Fall Occurrence			Number of Days		
	Min of 24° F or below	Min of 28° F or below	Min of 32° F or below	Min of 32° F or below	Min of 28° F or below	Min of 24° F or below	Between Last Spring First Fall Occurrence		
							24° F	28° F	32° F
1950	20-May	3-Jun	4-Jun	12-Sep	27-Sep	28-Sep	131	116	100
1951	14-May	8-Jun	10-Jun	12-Sep	12-Sep	27-Sep	136	96	94
1952	22-Apr	30-Apr	16-Jun	13-Sep	14-Sep	15-Sep	146	137	89
1953	22-May	23-May	25-Jun	5-Sep	25-Sep	3-Oct	134	125	72
1954	2-May	2-Jun	19-Jun	27-Aug	27-Aug	19-Sep	140	86	69
1955	28-May	28-May	30-Jun	22-Sep	22-Sep	22-Sep	117	117	84
1956	1-May	15-May	22-Jun	31-Aug	6-Sep	22-Sep	144	114	70
1957	27-Apr	28-Apr	1-May	11-Sep	14-Sep	22-Sep	148	139	133
1958	30-Apr	3-May	10-Jun	16-Sep	25-Sep	17-Oct	170	145	98
1959	7-May	21-May	31-May	22-Sep	22-Sep	29-Sep	145	124	114
1960	19-May	19-May	24-May	25-Aug	3-Oct	14-Oct	148	137	93
1961	3-May	8-May	13-May	3-Sep	24-Sep	2-Oct	152	139	113
1962	30-Apr	7-Jun	7-Jun	31-Aug	9-Sep	9-Sep	132	94	85
1963	24-Apr	25-Apr	30-Jun	10-Oct	15-Oct	24-Oct	183	173	102
1964	7-May	9-May	20-Jun	29-Aug	3-Sep	19-Sep	135	117	70
1965	18-May	27-May	27-May	30-Aug	4-Sep	17-Sep	122	100	95
1966	25-Jun	25-Jun	26-Jun	27-Sep	1-Oct	10-Oct	107	98	93
1967	13-May	26-May	31-May	12-Sep	13-Sep	4-Oct	144	110	104
1968	9-May	23-May	30-Jun	4-Sep	23-Sep	8-Oct	152	123	66
1969	30-Apr	30-Apr	29-Jun	31-Aug	4-Sep	3-Oct	156	127	63
1970	14-May	31-May	31-May	9-Sep	10-Sep	10-Sep	119	102	101
1971	18-May	19-May	29-Jun	15-Sep	15-Sep	18-Sep	123	119	78
1972	12-May	13-May	21-May	7-Sep	13-Sep	24-Sep	135	123	109
1973	27-May	18-Jun	2-Jul	15-Sep	17-Sep	3-Oct	129	91	75
1974	16-May	31-May	8-Jun	2-Sep	14-Sep	14-Sep	121	106	86
1975	26-May	26-May	29-May	29-Aug	29-Aug	21-Sep	118	95	92
1976	30-Apr	27-Jun	27-Jun	9-Sep	9-Sep	5-Oct	158	74	74
1977	28-May	30-May	30-May	31-Aug	9-Sep	2-Oct	127	102	93
1978	31-May	20-Jun	26-Jun	15-Aug	18-Aug	19-Sep	111	59	50
1979	8-Jun	9-Jun	15-Jun	11-Sep	12-Sep	4-Oct	118	95	88
1980	17-Apr	19-Apr	7-Jun	1-Sep	4-Sep	17-Oct	183	138	86
1981	17-Apr	14-Jun	8-Jul	3-Sep	20-Sep	26-Sep	162	98	57
1982	5-May	20-May	9-Jun	29-Sep	6-Oct	6-Oct	154	139	112
1983	14-May	16-May	22-May	6-Sep	10-Sep	20-Sep	129	117	107
1984	17-May	2-Jun	12-Jun	7-Sep	22-Sep	24-Sep	130	112	87
1985	13-May	14-May	14-May	20-Sep	20-Sep	23-Sep	133	129	129

Table 14 (Continued).

Year	Last Spring Occurrence			First Fall Occurrence			Number of Days		
	Min of 24° F or	Min of 28° F or	Min of 32° F or	Min of 32° F or	Min of 28° F or	Min of 24° F or	Between Last Spring First Fall Occurrence		
	below	below	below	below	below	below	24° F	28° F	32° F
1986	23-May	6-Jul	6-Jul	19-Sep	21-Sep	21-Sep	121	77	75
1987	20-Apr	2-Jun	2-Jun	17-Aug	17-Sep	18-Sep	151	107	76
1988	3-May	20-May	8-Jun	15-Sep	18-Sep	18-Sep	138	121	99
1989	26-May	21-Jun	21-Jun	10-Sep	13-Sep	16-Oct	143	84	81
1990	1-May	10-May	13-Jun	3-Oct	8-Oct	8-Oct	160	151	112
1991	5-May	28-May	15-Jun	15-Sep	4-Oct	4-Oct	152	129	92
1992	12-May	12-May	12-May	24-Aug	25-Aug	26-Aug	106	105	104
1993	28-Apr	9-May	18-Jul	27-Aug	31-Aug	21-Sep	146	114	40
1994	30-Apr	17-Jun	17-Jun	5-Sep	22-Sep	19-Oct	172	97	80
1995	24-Apr	24-Apr	7-Jun	19-Aug	21-Sep	21-Sep	150	150	73
1996	28-Apr	31-May	19-Jun	6-Sep	6-Sep	6-Sep	131	98	79
1997	9-May	19-May	3-Jul	17-Sep	28-Sep	11-Oct	155	132	76
1998	27-Apr	5-Jun	27-Jun	23-Sep	3-Oct	5-Oct	161	120	88
1999	9-Jun	9-Jun	26-Jun	1-Sep	8-Sep	26-Sep	109	91	67
2000	1-May	12-May	17-Jun	7-Sep	7-Sep	23-Sep	145	118	82
2001	21-May	5-Jun	14-Jun	7-Sep	10-Sep	5-Oct	137	97	85
2002	12-May	17-May	11-Jun	9-Sep	22-Sep	22-Sep	133	128	90
2003	20-May	20-May	20-May	13-Sep	13-Sep	14-Sep	117	116	116
2004	30-Apr	30-Apr	25-May	4-Sep	11-Oct	25-Oct	178	164	102
2005	16-Apr	9-Jun	19-Jun	1-Sep	14-Sep	19-Sep	156	97	74
2006	10-May	13-May	13-May	31-Aug	31-Aug	18-Sept	131	110	110
Average	10-May	25-May	12-Jun	8-Sep	16-Sep	27-Sep	140	114	88
Longest	24-Apr	25-Apr	1-May	11-Sep	15-Oct	24-Oct	183	173	133
Shortest	12-May	20-Jun	18-Jul	27-Aug	18-Aug	26-Aug	106	59	40

Near-Surface Freeze/Thaw Cycles

A measure of the amount of weathering various materials may be exposed to is the frequency at which daily freeze/thaw cycles occur. A freeze/thaw cycle in this instance is defined as a day in which the maximum air temperature exceeds 32° F and the minimum air temperature falls to or below 32° F. The temperatures used for this purpose are measured at a height of 5 ft. AGL. As such, the air temperature at 5 ft. may be cooler during the day and warmer at night than at ground level. Therefore, the actual number of

daily freeze / thaw cycles closer to the ground surface may potentially be greater than what is determined using this calculation procedure.

The summary of freeze/thaw cycles for CFA is contained in Table 15. The greatest number of cycles occurs, as expected, in the spring and fall seasons. Freeze/thaw cycles occurred every day during February and March. Conversely, the air temperature has remained below freezing for the entire month of February at CFA, resulting in no freeze/thaw cycles. On the average, however,

Table 15. Monthly and annual summary of daily freeze/thaw cycles for CFA^a.

	Average Number of Cycles (%)	Maximum Number of Cycles (%)	Minimum Number of Cycles (%)
January	33	81	3
February	57	100	0 ^b
March	83	100	39
April	72	97	37
May	30	65	3
June	5	17	0
July	0	6	0
August	2	16	0
September	26	57	0
October	74	97	39
November	77	97	27
December	42	81	6
ANNUAL	42	54	23

a. Data period of record spans January 1950 through December 2006.

b. Air temperatures remained below freezing the entire month.

42% of the days in a year contain a freeze/thaw cycle. July usually is the only month that, on average, does not have a freeze/thaw cycle. However, July has also had as much as 6% of the days that exhibited freeze/thaw cycles.

Degree Days Based on Surface Air Temperatures

Another unit of measure based on a specific air temperature is the degree-day. The degree-day concept can be applied to heating or cooling and is used as a basis for establishing heating and cooling energy requirements and building design considerations. A single heating degree-day is accumulated for each degree the average air

temperature is less than 65° F in one day. Conversely, a single cooling degree-day is accumulated for each degree the average daily air temperature is greater than 65° F.

The monthly and annual heating degree-day summary for CFA is presented in Table 16. January has the highest average degree-day total of almost 1,500 and July has the lowest average total of 28. Monthly heating degree-day totals as large as 1,799 have been recorded at CFA. The table shows that the highest single heating degree-day at CFA has been 93. On the average, the locations inside the INL can expect to record approximately 8,600 heating degree-days annually.

Table 16. Monthly and annual average and extreme heating degree days (HDD) for CFA.

	Average (HDD)	Highest (HDD)	Lowest (HDD)	Daily Extremes	
				Highest (HDD)	Lowest (HDD)
January	1,501	1,799	1,086	85	22
February	1,226	1,623	865	88	21
March	1,034	1,446	728	71	11
April	684	889	471	44	2
May	417	610	206	35	0
June	180	305	44	26	0
July	28	192	0	16	0
August	51	192	2	20	0
September	279	493	100	36	0
October	653	832	433	55	2
November	1,062	1,342	860	74	8
December	1,442	1,799	1,181	93	18
ANNUAL	8,557	10,268	7,604	93	0

Note: Data period of record spans January 1950 through December 2006.

A monthly and annual summary of the cooling degree-days at CFA is presented in Table 17. Cooling is usually not required except during the months of June, July, and August. However, a significant accumulation of cooling degree-days has been observed in both May and September. Conversely, there has been at least one incident in which the accumulation of cooling degree-days in May and September has been zero. On the average, an annual total of 262 cooling degree-days accumulates at CFA.

The daily extremes of cooling degree-days given in Table 17 yield further information on the cooling equipment design capacity requirements. The largest single cooling degree-day observed has been 18. This has been recorded in the months of June, July, and August. There have also been days during all of the summer months in which no cooling degree-days were accumulated.

Table 17. Monthly and annual average and extreme cooling degree days (CDD) for CFA^a.

	Average (CDD)	Highest (CDD)	Lowest (CDD)	Daily Highest (CDD)	Extremes Lowest (CDD)
January	0	0	0	0	0
February	0	0	0	0	0
March	0	0	0	0	0
April	0	0	0	0	0
May	2	26	0	11	0
June	31	137	3	18	0
July	132	265	8	18	0
August	91	194	23	18	0
September	8	41	0	9	0
October	0	0	0	0	0
November	0	0	0	0	0
December	0	0	0	0	0
ANNUAL	264	538	35	18	0

a. Data period of record spans January 1950 through December 2006.

Upper Air Temperatures

The vertical variation of temperature above the ground surface is extremely important for evaluating atmospheric dispersion characteristics. These data are needed to properly evaluate reactor sites, as well as for determining the location, height, and design of chimneys and monitoring stations.

A discussion of the vertical temperature variation and its relationship to dispersal of effluents will not be undertaken here, but is deferred to Chapter 6. However, a brief discussion of stability categories follows.

The data trends indicate that inversion conditions are more prevalent at SMC (54%) than at GRI (46%). The reverse is true for lapse conditions at GRI. Weak lapse conditions occurred with nearly identical frequency (11%) at both sites. This was also the case for weak inversion conditions (25%).

Strong inversions were observed more frequently at SMC, while strong lapse conditions were observed more frequently at GRI. These differences are due primarily to the lower elevation of SMC, the close proximity of SMC to the mountains, and the more frequent occurrence of afternoon clouds at SMC in the summer as compared to the GRI location.

A summary of the diurnal shift from a daytime air temperature lapse to a nighttime air temperature inversion was derived from eight years of record at CFA (Johnson and Dickson, 1962). The data were compiled as the air temperature difference between 5 and 250 ft. AGL. An attempt was made to eliminate from the data set the cases in which the formation or dissipation of the inversion was obviously controlled by factors other than incoming solar or outgoing terrestrial radiation. These data are presented in Table 18 and illustrated graphically in Fig. 62.

Table 18. Average onset and dissipation times of inversion and lapse air temperature profiles together with intensity values for CFA^a

	Inversion Formation		Inversion Dissipation		Inversion	
	Average Time of Onset (MST)	Average Deviation Before Sunset (Minutes)	Average Time of Dissipation (MST)	Average Deviation After Sunrise (Minutes)	Average Number of Hours Per Day	Maximum Number of Hours Recorded Per Day
January	1657	23	0959	116	17.0	24
February	1740	22	0919	108	15.7	23
March	1836	02	0805	80	13.5	18
April	1919	-04	0704	74	11.8	14
May	1941	09	0626	78	10.8	15
June	2000	15	0614	84	10.2	13
July	1950	21	0630	85	10.7	15
August	1919	17	0700	83	11.7	14
September	1839	04	0729	78	12.8	15
October	1746	03	0805	79	14.3	17
November	1706	02	0851	85	15.1	21
December	1646	10	0933	96	16.8	24

	Inversions			Lapse	
	Maximum Intensity (°F)	Longest Period of Duration (Hours)	Average Number of Days Without Inversion	Maximum Intensity ^b (°F)	Longest Period of Duration (Hours)
January	33.8	46	1	7.0	84
February	33.7	24	1	9.4	81
March	24.9	20	2	7.7	94
April	24.5	14	2	9.6	77
May	24.4	13	1	12.4	67
June	22.5	15	1	8.7	61
July	23.2	15	1	9.8	37
August	23.6	14	1	9.9	42
September	28.5	18	1	9.8	58
October	27.1	17	1	7.4	67
November	24.3	21	1	8.1	105
December	33.4	66	1	6.9	62

a. Data period of record spans January 1953 through December 1960.

b. Air temperature difference between 5 and 250 ft. AGL.

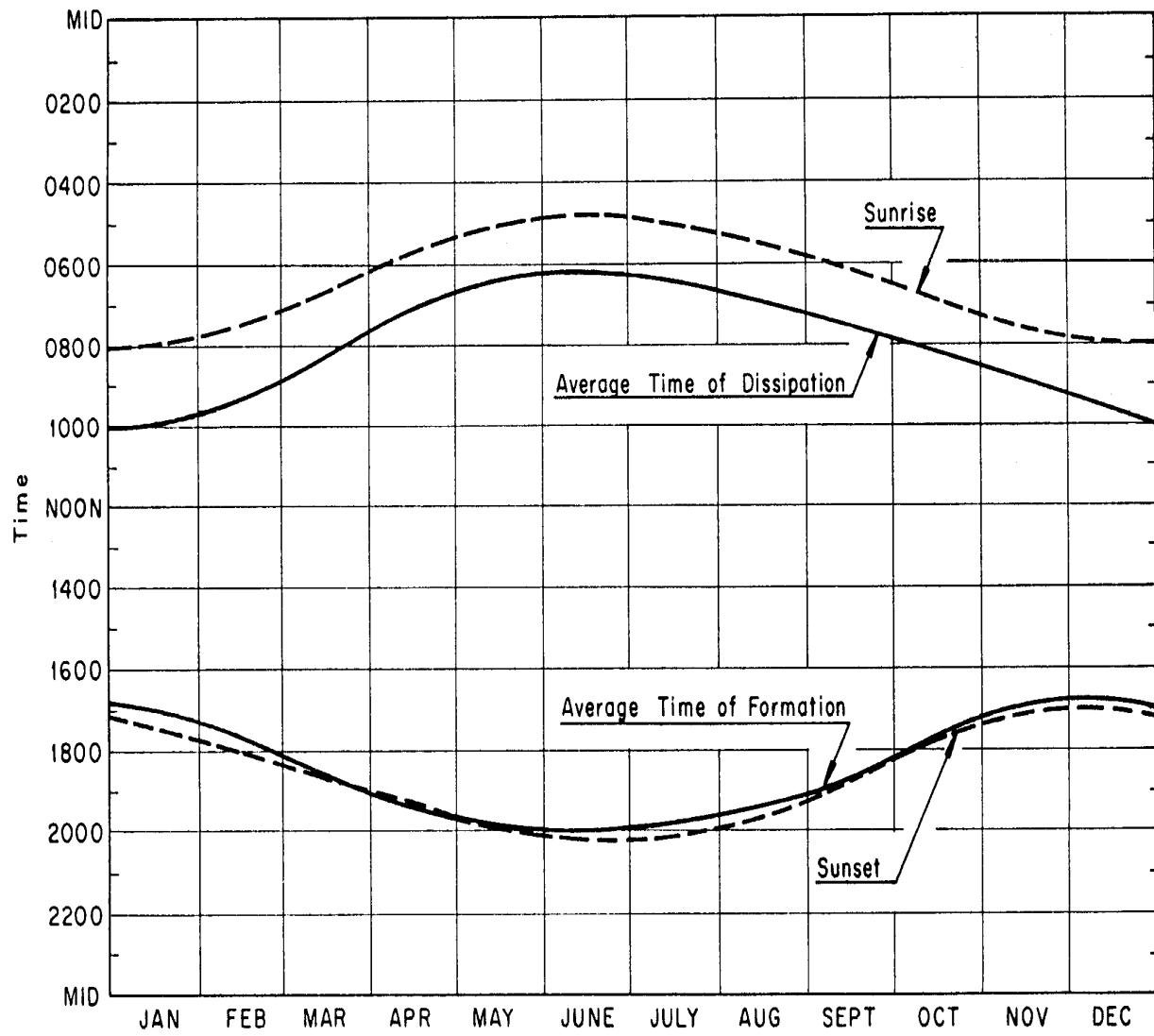


Figure 62. Average time of onset and dissipation of the nocturnal inversion as a function of time of year.

The dependence of the nocturnal inversion formation and dissipation on the time of sunset and sunrise is readily apparent in the data. The nocturnal inversion does not dissipate for more than 1 to 2 hours after sunrise and reforms usually around sunset. The more intense inversions also occur during the winter months. However, a nocturnal inversion can be expected to form on almost every day of the year (96.2% of the time). Similar conditions are expected to exist at all other locations at the INL.

Profile Characteristics Above 250 ft. AGL

Temperature profile characteristics reflect the thermal stability of the atmosphere, and are widely used as indicators of turbulence levels and the dispersive capability of the lower atmosphere. Both historical studies that used balloons and more recent continuous monitoring that uses the RASS have provided valuable diffusion climatology data.

Two studies were made of the air temperature profiles above 250 ft. at CFA and were reported in the 2nd Edition Climatography (Clawson et al., 1989). The first study made use of tethered blimps (tethersondes) with accompanying thermistor elements to obtain air temperature soundings to a height of approximately 1,000 ft. AGL. Profile measurements were obtained every 2-3 hours throughout the day during the four seasons. The second study measured temperature profiles with T-sondes that contained a small radio transmitter combined with a thermistor, which transmitted a temperature modulated signal to a ground receiving station. The T-sondes were attached to free-lift balloons and were tracked by double theodolites.

Since 1994, the RASS system has provided continuing upper air sounding data at

INL that has validated the work of the earlier field studies.

The data readily show the formation and dissipation of the nocturnal inversion caused by surface heating and cooling, although the effects of wind slightly modified some of the profiles. The winter nocturnal inversions tended to be rather shallow, while the spring and summer inversions tended to be rather deep. The air temperature difference from the bottom to the top of the inversion was as large as 18° F. The T-Sonde profiles showed that the nocturnal inversion during the winter dissipated near the surface during the day due to surface heating, but persisted at the higher levels throughout the day. The profile taken at sunrise in the winter also shows a distinct "kink" at about 1,800 ft. AGL below which the profile appeared to become lapse, and above which the profile continued to indicate an inversion for approximately another 3,000 ft. This kind of trace was not indicated in the tethersonde upper air profiles because of the limited maximum altitude of the profiles. The T-Sonde data showed that, in the summer, the inversion formed by radiative cooling only extended to about 1,300 ft.

A few other generalizations may be made from the data. Considerable day-to-day fluctuations in the maximum height of the inversion were observed. The height of the inversion top varied from a few hundred feet to over 5,000 ft. AGL.

The entire inversion usually dissipated during the daytime hours in the summer. In the winter, the inversion often did not dissipate at all or dissipated only in the lower few hundred feet of the atmosphere and the inversion frequently persisted at the higher levels for several days.

The temperature difference between the surface and the top of the inversion was as extreme as 40° F.

The development of well-mixed profiles from the surface upward at midday during the summer was accompanied with upper level wind flows of light-to-moderate speeds.

Soil Temperatures

Soil temperatures were measured at INL during three programs in the periods 1951-1955, 1955-61, and 1956-1963. Soil temperatures above and below asphalt surfaces and undisturbed soils were recorded in conjunction with air temperatures at the 5-foot level. Major findings included:

- Surface temperatures as high as 160° F over asphalt and as high as 138° F over undisturbed soils were recorded.
- Under asphalt surfaces, soil temperatures averaged approximately 10° F higher in the summer near the surface compared to measurements in native soils. In the winter, colder temperatures were observed over a longer period and to a greater depth.

- The maximum average depth of freezing temperatures in the soil below a bare soil surface was approximately 3.3 ft. while that depth was approximately 3.8 ft. below the asphalt surface.
- Average soil surface temperatures were as much as 35-45° F warmer than air temperature during the summer, depending on surface soil color. Little difference in the average daily lows of soils with differing colors was observed, however.
- The onset of the prolonged freeze usually occurred in late November and lasted three months or more before ending in late February or early March. The maximum deviations between air and soil temperatures occurred in the winter and the summer seasons. Conversely, the smallest deviations were observed in the spring and the fall seasons.

The interested reader is referred to the 2nd Edition *Climatology* (Clawson et al., 1989) for additional details on these studies. Soil temperatures are also being measured at GRI as part of the surface energy flux measurements. A brief summary of these measurements are located later in this chapter.

PRECIPITATION

General Characteristics

Daily precipitation values have been measured at CFA since March 1950. Stations at other locations inside and outside the INL have been measuring five - minute precipitation totals as part of the NOAA INL Mesonet since April 1993. Therefore, most of the daily precipitation statistics described in this section utilizes data from CFA, which has a period of record of over 50 years.

Monthly and annual precipitation is presented in Table 19. A pronounced precipitation peak occurs in May and June. The average for these two months is approximately 1.2 in. at CFA. The average annual precipitation at CFA is 8.51 in. The greatest monthly precipitation total measured at CFA was 4.64 in. during June 1995. There have been instances of no measurable precipitation recorded at CFA (traces excluded) for every month of the year except May.

The greatest daily totals (midnight to midnight) of precipitation for CFA is given in Table 20. The greatest daily precipitation value during the period of record is 1.64 in.. On the average, daily precipitation totals of 1 inch or greater have occurred less than once every five years. Snowfall is discussed later in this document.

Table 21 lists the monthly and annual average number of days (from midnight to

midnight) as a percentage of occurrences during which specified amounts of precipitation fell at CFA. The data indicate that the frequency of days with a trace of precipitation was higher during the winter, spring, and early summer months. During the late summer and autumn months the frequency of occurrence in the heavier categories was extremely low. For precipitation amounts of 0.10 in. or greater, the frequency of occurrence was less than 15% for all months and as low as 4%.

Table 21 also shows that less than a tenth of an inch of precipitation was recorded on most days when precipitation fell. During the months of July through October, precipitation exceeding one hundredth of an inch was measured on approximately 12% of the days. That amount was exceeded on approximately 20% or more of the days during the rest of the year. It can also be seen that days on which more than 1 inch of precipitation was recorded were rare. Storms of that intensity are usually of the thunderstorm variety and occurred in April, mid-Summer and again in September.

Long periods without precipitation are not uncommon at the INL. Table 22 presents a list of the longest periods without measurable precipitation at CFA. Since 1950, there have been 20 periods with at least 40 days of no measurable precipitation. The longest dry period was 73 days from October 12, 1959 through December 23, 1959. More than 80% of the periods occurred in the summer and autumn seasons.

Table 19. Average total monthly and annual precipitation (water equivalent) for CFA^a

	Average (in.)	Highest (in.)	Lowest (in.)
January	0.68	2.56	0.00 ^b
February	0.61	2.40	0.00
March	0.62	2.03	0.00
April	0.77	2.50	0.00
May	1.22	4.42	0.02
June	1.18	4.64	0.00
July	0.48	2.29	0.00
August	0.50	3.27	0.00
September	0.64	3.52	0.00
October	0.51	1.67	0.00
November	0.61	1.74	0.00
December	0.71	3.43	0.00
ANNUAL	8.51	14.40	4.45

a. Data period of record spans March 1950 through December 2006.

b. Trace amounts are not considered as precipitation.

Table 20. Ten greatest daily precipitation totals from CFA.

Greatest CFA Daily Precipitation	
(in.)	Date
1.64	Jun 10, 1969
1.55	Sep 18, 1961
1.55	Jun 5, 1995
1.51	Apr 20, 1981
1.36	Jun 10, 1954
1.25	Jul 23, 1979
1.14	Jun 10, 1963
1.10	Sep 30, 1994
1.09	Sep 9, 1961
1.07	Dec 22, 1964

Note: Data period of record spans March 1950 through December 2006.

Table 21. Monthly and annual average number of days (%) on which precipitation was recorded at CFA.

	Trace or More ^a (%)	0.01 in. or More ^b (%)	0.10 in. or More ^b (%)	0.50 in. or More ^b (%)	1.0 in. or More ^b (%)
January	40	23	7	0.6	0.0
February	35	19	7	0.6	0.0
March	32	19	7	0.3	0.0
April	31	21	8	0.8	0.1
May	35	25	13	1.4	0.0
June	34	22	11	1.9	0.2
July	17	12	4	0.7	0.1
August	21	12	5	0.8	0.0
September	19	13	6	0.8	0.2
October	20	13	6	0.5	0.0
November	27	18	7	0.4	0.0
December	35	22	8	0.5	0.1
ANNUAL	28	18	7	0.8	0.0

a. Data period of record spans March 1950 through September 1983.

b. Data period of record spans March 1950 through December 2006.

Table 22. Longest periods at CFA without measurable (0.01 in. or greater) daily precipitation.

Beginning of Period	Ending of Period	Length of Period (days)
12 Oct 1959	23 Dec 1959	73
3 Oct 1976	4 Dec 1976	63
12 Sep 1952	11 Nov 1952	61
26 Aug 1987	23 Oct 1987	59
25 Jun 2003	20 Aug 2003	57
4 Sep 1999	27 Oct 1999	54
1 Jun 1994	22 Jul 1994	52
1 Oct 1977	21 Nov 1977	52
13 Jun 1953	1 Aug 1953	50
18 Jan 1988	5 Mar 1988	48
13 Jan 1991	28 Feb 1991	47
14 Aug 1967	29 Sep 1967	47
24 Sep 1958	8 Nov 1958	46
24 Aug 1975	6 Oct 1975	44
12 May 2003	23 Jun 2003	43
19 Mar 1977	30 Apr 1977	43
29 Jul 1969	8 Sep 1969	42
18 Sep 2002	29 Oct 2002	42
10 Aug 1962	19 Sep 1962	41
8 Jun 1974	17 Jul 1974	40

Note: Data period of record spans March 1950 through December 2006.

Design Storm and Return Periods

To designate the precipitation intensities for which structures must be designed, or for assessing flood potential, the idea of a "design basis storm" has arisen. Structures are designed to withstand storm intensity, as defined by the design basis storm that will be expected to occur only during some specified number of years.

(Hershfield, 1961) developed isopluvial maps from which estimates of the return years of storms could be made. Over forty years of additional data has been added to the database since the publication of that document. Sagendorf (1996) used this larger database to analytically specify INL design basis storms.

Figure 63 contains precipitation amount versus return years computed from the complete duration precipitation data from 43 years of daily data from CFA. The solid red line represents data from the entire year while the dotted blue line represents only data measured between November 15 and March 15.

Understanding winter time precipitation, when large storm systems typically bring precipitation to a considerable portion of the ESRP, is important because of its linkage to flooding episodes associated with winter time thaws, where rain was combined with melting snow on a frozen surface. Equation (1) describes the winter season design storm return period derived (Sagendorf, 1996) from the winter time

precipitation at CFA, and is applicable to other INL locations. Using equation (1) the winter season precipitation amounts may be calculated as a function of return years.

$$\text{Precip} = 0.478 + 0.394 \times \log(\text{Return Years}) \quad (1)$$

During the summer season, storms are typically convective in nature and affect a relatively small area, so that storm return statistics that apply to one station may not be applicable at other ESRP locations. Throughout the ESRP, the wettest months are April, May, and June, with May usually contributing the most precipitation, and June contributing the second highest amounts.

The summer season design storm return period is shown in equation (2).

$$\text{Precip} = 0.700 + 0.737 \times \log(\text{Return Years}) \quad (2)$$

Engineers and hydrologists are sometimes required to estimate the potential precipitation that may occur in intervals shorter than one day. Hourly precipitation data permits calculation of precipitation return periods for storms less than 24 hours in duration.

Equation (3) is a 4th order polynomial fitting (Sagendorf, 1996) of period-of-record data from all ESRP precipitation stations. F is the multiplication factor to apply to INL 24-hour storm results for a desired storm duration D, in hours.

$$F = 0.358 + 0.149D - 0.014D^2 + 0.0006857D^3 - 0.00001309D^4 \quad (3)$$

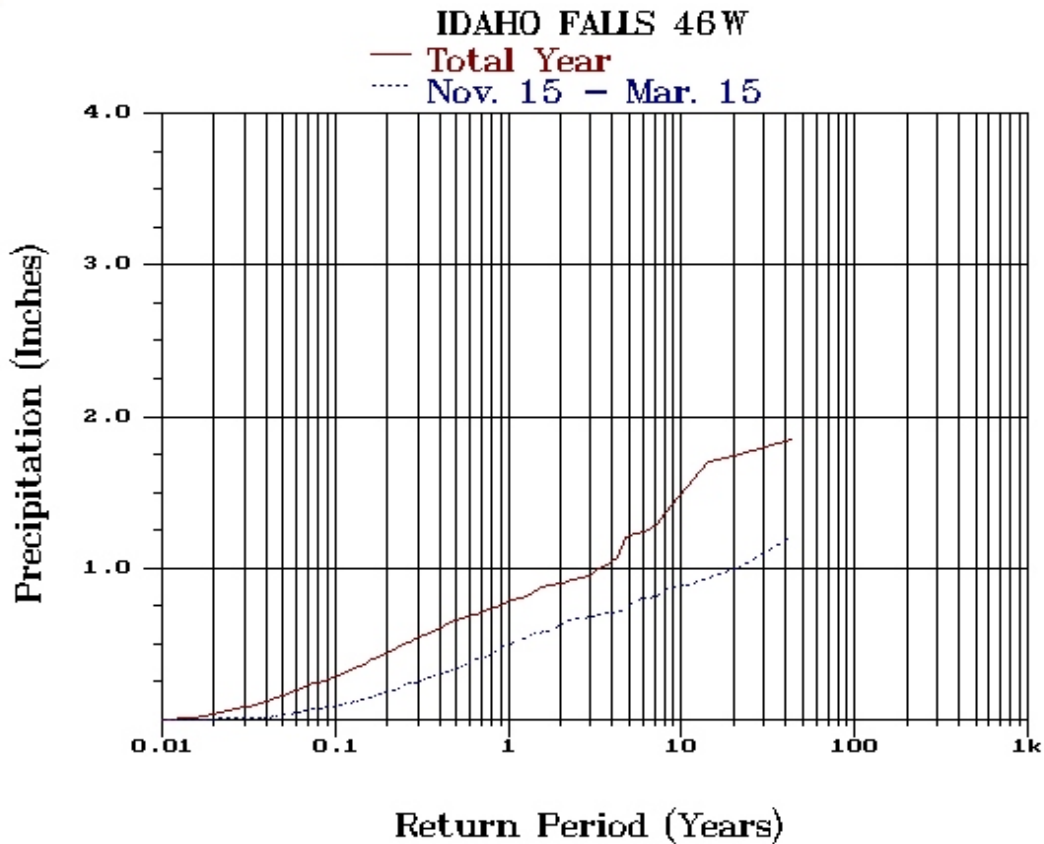


Figure 63. Idaho Falls 46W (CFA) precipitation amount versus return years.

Precipitation Characteristics Based on Mesonet Five-Minute Data

There are currently five NOAA INL Mesonet stations located near INL facilities that employ tipping bucket rain gages to measure five-minute rain totals. This section describes precipitation characteristics based on those data.

For this section, precipitation events have been defined as periods with one or more five-minute intervals for which precipitation was detected without a dry period of six hours or greater between these intervals. The event begins at the end of a dry period of six or more hours and ends at the beginning of the next dry period of six or more hours.

Grid 3 (GRI), located about one mile north of the INTEC facility inside the INL is used as the representative station for these data. Summaries of the precipitation events during the 13 year period of January 1994 through December 2006 appear in Tables 23, 24, and 25.

The greatest precipitation event during the period of record was 1.51 in. The longest event duration was over 61 hours. Only 8 events have lasted more than 24 hours. The greatest precipitation amounts recorded at GRI are shown in Table 24 for each month and annually. The greatest amount recorded during a five minute period was 0.38 in., for a one hour period 0.58 in., and for a 24 hour period 1.51 in. There were an average of 70 events

per year with 0.01 in. (the least amount measurable) or greater. The months with the greatest occurrences were April and May. There were only 2.0 events per year with 0.50

in. or greater precipitation, and 0.2 events per year with one inch or greater precipitation (Table 25).

Table 23. Greatest precipitation events^a with longest duration from station GRI^b.

Event Length (hours)	Beginning of Event	Ending of Event	Event Total (in.)
61.6	1225 MST 04 May 1995	0200 MST 07 May 1995	1.24
36.0	0045 MST 03 Dec 1994	1245 MST 04 Dec 1994	0.22
35.5	0405 MST 01 Jan 1997	1535 MST 02 Jan 1997	0.84
34.8	2245 MST 09 May 2005	0935 MST 11 May 2005	0.94
30.9	1835 MST 29 Oct 2000	0130 MST 31 Oct 2000	0.44
28.1	0835 MST 22 Mar 2005	1240 MST 23 Mar 2005	0.59
25.3	0045 MST 05 Apr 2006	0205 MST 06 Apr 2006	0.52
24.9	0120 MST 02 Jan 2006	0215 MST 03 Jan 2006	0.95
24.5	2305 MST 29 Sep 1994	2335 MST 30 Sep 1994	1.27
22.8	2050 MST 15 Sep 1996	1935 MST 16 Sep 1996	0.42
22.1	0415 MST 01 Dec 2005	0220 MST 02 Dec 2005	0.49
22.0	2150 MST 26 Dec 2002	1950 MST 27 Dec 2002	0.10
21.6	1415 MST 10 Mar 1995	1150 MST 11 Mar 1995	0.61
21.2	1625 MST 06 Feb 1999	1335 MST 07 Feb 1999	0.35
20.2	1120 MST 16 May 1994	0730 MST 17 May 1994	0.40
19.9	1315 MST 05 Jun 1995	0910 MST 06 Jun 1995	1.51
19.0	0700 MST 23 Apr 1997	0200 MST 24 Apr 1997	0.59
18.8	0900 MST 16 May 2005	0350 MST 17 May 2005	0.61
18.7	2010 MST 30 Apr 1999	1450 MST 01 May 1999	0.46
18.7	0050 MST 21 May 2002	1930 MST 21 May 2002	0.33

a. Events are separated by six or more continuous hours without precipitation.

b. Data period of record spans from January 1994 through December 2006.

Table 24. Greatest precipitation amounts (inches) during selected periods at GRI.

Period	5 min	10 min	15 min	20 min	30 min	1 hr	2 hr
January	0.04	0.07	0.09	0.12	0.14	0.17	0.22
February	0.02	0.03	0.05	0.06	0.07	0.14	0.22
March	0.04	0.05	0.06	0.07	0.09	0.14	0.19
April	0.06	0.10	0.13	0.15	0.19	0.25	0.31
May	0.10	0.14	0.16	0.18	0.20	0.25	0.30
June	0.18	0.24	0.30	0.32	0.41	0.52	0.61
July	0.38	0.46	0.51	0.51	0.52	0.55	0.56
August	0.10	0.15	0.18	0.18	0.18	0.22	0.32
September	0.18	0.31	0.37	0.46	0.55	0.58	0.62
October	0.23	0.43	0.46	0.47	0.48	0.49	0.49
November	0.05	0.07	0.08	0.08	0.08	0.11	0.16
December	0.03	0.04	0.06	0.08	0.09	0.13	0.25
ANNUAL	0.38	0.46	0.51	0.51	0.55	0.58	0.62
Period	3 hr	4 hr	6 hr	8 hr	12 hr	24 hr	
January	0.30	0.38	0.49	0.57	0.70	0.93	
February	0.32	0.41	0.44	0.44	0.44	0.45	
March	0.30	0.35	0.42	0.42	0.46	0.61	
April	0.43	0.53	0.64	0.78	0.78	0.78	
May	0.37	0.42	0.47	0.47	0.66	0.74	
June	0.63	0.82	1.06	1.14	1.17	1.51	
July	0.56	0.56	0.56	0.61	0.69	0.69	
August	0.35	0.35	0.35	0.35	0.35	0.35	
September	0.63	0.65	0.83	0.96	1.11	1.26	
October	0.49	0.54	0.74	0.91	1.10	1.25	
November	0.20	0.22	0.28	0.28	0.29	0.32	
December	0.33	0.38	0.48	0.48	0.53	0.71	
ANNUAL	0.63	0.82	1.06	1.14	1.17	1.51	

Note: Data period of record spans January 1994 through December 2006.

Table 25. Average number of monthly precipitation events^a at GRI.

	0.01 in. or More	0.10 in. or More	0.50 in. or More	1.00 in. or More
January	6.6	2.0	0.2	0.0
February	5.1	1.5	0.0	0.0
March	4.3	1.8	0.2	0.0
April	9.0	2.6	0.3	0.0
May	8.6	3.3	0.4	0.1
June	6.6	2.8	0.5	0.1
July	3.9	1.2	0.1	0.0
August	3.9	1.1	0.0	0.0
September	4.2	1.4	0.2	0.0
October	4.9	1.5	0.2	0.1
November	4.4	1.3	0.0	0.0
December	6.7	2.1	0.2	0.0
ANNUAL	68.5	22.7	2.0	0.2

a. Events are separated by six or more continuous hours without precipitation.

b. Data period of record spans from January 1994 through December 2006.

Snow

CFA is the location of snowfall and snow depth data since it is the only INL location where these measurements have consistently been made. Snowfall is the amount of snow that falls within a given period, regardless of the amount that accumulates on the ground. Since snow may melt as it falls, the snowfall amount must occasionally be estimated from the water equivalent of snow.

Average monthly and annual snowfall amounts are listed in Table 26. Also listed are the highest daily snowfalls for a given month. The days with the greatest snowfalls for the entire period of record were listed in Table 27.

The highest monthly average snowfall occurs in January with a total of 6.2 in. December also receives an amount comparable to January (6.1 in.). Snowfall as late as May and as early as September has been observed at the

INL. Considerable snowfall variation was also noted within months, particularly December, which exhibited a snowfall range of 22.3 in. Every month has recorded no snowfall at least once during the period of record. The maximum snowfall amounts in any 24-hour period were 9.0 and 8.6 in., recorded during January and March, respectively.

The average percentage of days (from midnight to midnight) in a given month on which a specified amount of snowfall was recorded is listed in Table 28. Maximums and minimums are also noted. January (19%) and December (18%) have the largest number of days with snowfall. Snowfall has been observed on as many as 55% of the days in January and 45% of the days in December.

The monthly averages and extremes of snow depths are listed in Table 29. The highest average monthly snow depth ever recorded was 25.1 in., occurring during February 1993. The greatest daily snow depth

was 30 in., occurring during several days in 1993.

Table 30 shows the longest periods at CFA with continuous snow cover of 1 inch or greater during the period of record. The longest period was 131 days, with five other

periods of 120 days or more. Table 30 also shows the greatest snow depths during these periods. The 30 in. measured on February 23, 1993 (among other days) is the highest snow depth during the period of record.

Table 26. Monthly and annual snowfall totals and monthly and daily extreme totals for CFA.

	Average (in.)	Maximum (in.)	Minimum (in.)	Largest Daily Maximum (in.)
January	6.2	18.1	0.0	9.0
February	4.7	16.1	0.0	7.5
March	3.0	10.2	0.0	8.6
April	1.9	16.5	0.0	6.7
May	0.5	8.3	0.0	4.4
June	0.0	0.0	0.0	0.0
July	0.0	0.0	0.0	0.0
August	0.0	0.0	0.0	0.0
September	0.0	1.0	0.0	1.0
October	0.5	7.2	0.0	4.5
November	3.1	12.3	0.0	6.5
December	6.1	22.3	0.0	8.0
ANNUAL	25.9	59.7	6.8	9.0

Note: Data period of record spans March 1950 through December 2006.

Table 27. Greatest daily snowfall totals at CFA.

Greatest CFA Daily Snowfall	
(in.)	Date
9.0	Jan 2, 2006
8.6	Mar 22, 1973
8.5	Jan 20, 1957
8.0	Dec 29, 1992
7.5	Feb 8, 1960
7.2	Feb 19, 1971
7.0	Dec 4, 1983
6.7	Apr 28, 1970
6.5	Nov 24, 1981
6.5	Dec 1, 1982
6.5	Apr 19, 1970

Note: Data period of record spans March 1950 through December 2006.

Table 28. Monthly and annual average number of days (%) and extreme number of days with snowfall amounts, of equal to or greater than 0.1, 1.0, and 3.0 in. for CFA.

	>=0.1 in.			>=1.0 in.			>=3.0 in.		
	Ave (%)	Max (%)	Min (%)	Ave (%)	Max (%)	Min (%)	Ave (%)	Max (%)	Min (%)
January	19	55	0	8	19	0	1	6	0
February	14	39	0	6	25	0	2	7	0
March	10	29	0	4	13	0	1	6	0
April	5	33	0	2	13	0	1	7	0
May	1	10	0	1	10	0	0	6	0
June	0	0	0	0	0	0	0	0	0
July	0	0	0	0	0	0	0	0	0
August	0	0	0	0	0	0	0	0	0
September	0	3	0	0	3	0	0	0	0
October	2	13	0	1	6	0	0	3	0
November	9	23	0	4	17	0	1	10	0
December	18	45	0	8	26	0	2	6	0
ANNUAL	7	13	2	3	5	1	1	2	0

Note: Data period of record spans March 1950 through December 2006.

Table 29. Monthly and annual average snow depths on the ground and extreme snow depths for CFA.

	Average (in.)	Maximum (in.)	Minimum (in.)
January	4.7	20.4	0.0
February	4.8	25.1	0.0
March	2.2	20.0	0.0
April	0.1	0.9	0.0
May	0.0	0.2	0.0
June	0.0	0.0	0.0
July	0.0	0.0	0.0
August	0.0	0.0	0.0
September	0.0	0.0	0.0
October	0.0	0.3	0.0
November	0.4	3.6	0.0
December	2.6	12.0	0.0
ANNUAL	1.2	5.6	0.1

Note: Data period of record spans March 1950 through December 2006.

Table 30. Longest periods at CFA with continuous snow cover of 1.0 inch or greater.

Beginning of Period	Ending of Period	Period Length (days)	Greatest Snow Depth (in.)	Depth during Period Date
25 Nov 1984	4 Apr 1985	131	25	6 Mar 1985
24 Nov 1963	1 Apr 1964	130	12	2 Mar 1964
20 Nov 1983	27 Mar 1984	129	17	16 Feb 1984
22 Nov 1992	26 Mar 1993	125	30	23 Feb 1993
13 Nov 1988	15 Mar 1989	123	16	19 Feb 1989
24 Nov 2001	23 Mar 2002	120	13	3 Jan 2002
23 Dec 1951	5 Apr 1952	105	23	11 Mar 1952
11 Nov 1985	22 Feb 1986	104	14	5 Jan 1986
1 Dec 1970	12 Mar 1971	102	11	15 Jan 1971
22 Nov 1993	27 Feb 1994	98	6	21 Feb 1994
29 Nov 1982	4 Mar 1983	96	13	23 Dec 1982
18 Dec 1977	17 Mar 1978	90	16	12 Feb 1978
14 Dec 2000	12 Mar 2001	89	11	23 Feb 2001
29 Nov 1967	20 Feb 1968	88	10	19 Dec 1967
25 Dec 1959	20 Mar 1960	87	13	8 Feb 1960
27 Nov 1971	21 Feb 1972	87	12	27 Dec 1971
13 Dec 1974	8 Mar 1975	86	13	9 Feb 1975
29 Dec 1972	19 Mar 1973	81	12	14 Feb 1973
24 Dec 2003	8 Mar 2004	76	10	16 Feb 2004
1 Jan 1979	15 Mar 1979	74	10	2 Feb 1979

Note: Data period of record spans March 1950 through December 2006.

ATMOSPHERIC MOISTURE

Atmospheric moisture is a meteorological parameter that is important in facility design and operation. Atmospheric moisture has been continuously monitored at the INL since 1950. The primary observation location has been CFA. Originally, atmospheric moisture was recorded as hourly wet bulb temperatures. After discontinuing the hourly observations, atmospheric moisture was recorded as relative humidity using a hydro-thermograph. Atmospheric humidity has more recently been recorded as dew point temperature with a chilled mirror. Wet bulb temperature, relative humidity, and dew point

temperature are related variables, i.e., each variable can be converted into the other using an appropriate formula along with other joint variables such as pressure, temperature, etc. Each atmospheric moisture variable has a particular application in building and equipment design and engineering. The discussions pertain to the atmospheric moisture content observed at CFA. However, average atmospheric moisture varies only slightly over the local scale distances within the INL boundaries. Hence, the moisture discussions derived from data collected at CFA are generally applicable to the entire INL 1950 through December 2006.

Wet Bulb Temperature

Wet bulb temperature is defined as the lowest temperature to which air can be cooled by evaporating water. For this reason, wet bulb temperatures are frequently used as design criteria for evaporative cooling systems.

Monthly and annual averages of five-minute wet bulb temperature observations are given in Table 31 for the time period of January 1994 through December 2006. The average monthly wet bulb temperatures range from a low of 16.3° F in January to a high of 52.9° F in July. The lowest single monthly average was recorded in February at 7.0° F. The highest single monthly average was recorded in July at 55.7° F. Table 31 also contains absolute maximum and minimum five-minute wet bulb temperatures stratified

by month. The lowest five-minute wet bulb temperature recorded was in February at -31.3° F. The highest five-minute wet bulb temperature recorded was in July at 67.1° F. Although this wet bulb temperature is high, the greatest cooling efficiency is during the summer months. During this time period the potential for cooling, i.e., the dry bulb/wet bulb temperature gradient is the greatest.

Table 32 contains the monthly and annual averages of the daily maximum and minimum wet bulb temperatures. It also contains the monthly and annual extreme averages of the daily maximum and minimum wet bulb temperatures. The largest monthly average daily range was observed in October with a value of 20.6° F. The smallest monthly average daily range was observed in June with a value of 15.4° F.

Table 31. Monthly and annual averages and extremes of hourly wet bulb temperatures for station CFA.

	Monthly Values			Five-Minute Extreme Values	
	Average (deg F)	Highest Average (deg F)	Lowest Average (deg F)	Maximum (deg F)	Minimum (deg F)
January	16.3	22.7	9.9	47.9	-28.9
February	18.0	27.7	7.0	48.2	-31.3
March	29.3	31.8	22.6	49.9	-17.7
April	36.2	38.2	33.0	56.0	4.8
May	43.0	46.4	41.1	66.0	12.7
June	48.4	50.8	46.7	63.3	22.0
July	52.9	55.7	49.8	67.1	24.2
August	50.6	52.9	48.0	65.6	21.3
September	44.0	50.9	40.3	65.6	11.3
October	35.2	38.8	30.8	57.2	-6.9
November	26.1	31.1	19.5	52.1	-10.1
December	17.5	23.1	8.9	46.8	-30.6
ANNUAL	35.5	38.1	32.8	67.1	-31.3

Note: Data period of record spans January 1994 through December 2006.

Table 32. Monthly and annual averages of daily maximum and minimum wet bulb temperatures for station CFA.

	Average		Highest Average		Lowest Average	
	Maximum (deg F)	Minimum (deg F)	Maximum (deg F)	Minimum (deg F)	Maximum (deg F)	Minimum (deg F)
January	25.4	5.4	32.1	13.5	19.9	-3.2
February	27.3	6.8	36.2	19.1	19.2	-5.7
March	37.0	19.3	39.7	23.7	30.9	11.2
April	43.1	26.6	45.1	30.2	40.3	22.7
May	49.4	33.6	53.1	36.9	47.4	30.9
June	54.4	39.0	56.8	41.9	53.0	35.5
July	59.0	43.0	61.3	46.5	56.5	38.0
August	57.4	40.1	59.3	44.1	54.8	36.7
September	51.9	32.8	57.3	41.3	49.0	27.6
October	44.2	23.6	46.0	30.3	40.8	17.4
November	35.3	15.2	40.4	20.4	28.5	7.6
December	26.3	6.7	30.9	13.5	17.9	-2.7
ANNUAL	43.2	25.1	45.1	28.3	40.8	22.1

Note: Data period of record spans January 1994 through December 2006.

Relative Humidity

Another measure of atmospheric moisture is relative humidity. This is defined as the ratio of the amount of water vapor contained in a given volume of air to the amount required for saturation at the same temperature and pressure. Relative humidity varies with changes in temperatures and pressure. Pressure changes are small in comparison to temperature changes. Therefore, relative humidity is almost entirely a function of air temperature.

Monthly and annual relative humidity averages, mean maximums, and mean minimums are listed in Table 33. The average maximums and minimums were computed from five-minute rather than daily values. Therefore, the indicated values will be a few percent higher for the maximums and a few percent lower for the minimums than would be the case if average maximums and

minimums were computed from daily values. Absolute maximums and minimums are also listed in Table 33. Absolute maximum relative humidity values of 100% were observed in every month of the year during the 13-year time frame from January 1994 through December 2006. The lowest relative humidity observed was 4% in July. This is indicative of the very dry summers experienced at the INL in particular, and across the entire ESRP in general. Within each of these months, general diurnal features persist over the entire year. The highest diurnal values usually occur near sunrise, while the lowest values occur during mid-afternoon. The peaks and valleys usually occur simultaneously with the minimum and maximum air temperatures. The highest relative humidity is observed in January, when the average mid-day relative humidity is about 74%. The lowest relative humidity is observed in July and August when the average mid-day relative humidity is about 14%.

Table 33. Monthly and annual relative humidity averages and extremes for CFA.

	Average			Absolute	
	Average (%)	Maximum (%)	Minimum (%)	Maximum (%)	Minimum (%)
January	89	97	74	100	25
February	83	95	64	100	18
March	70	93	43	100	9
April	59	89	31	100	10
May	54	84	28	100	7
June	46	78	22	100	5
July	35	66	14	100	4
August	34	64	14	100	5
September	44	73	20	100	5
October	55	82	29	100	8
November	76	94	51	100	10
December	86	96	69	100	14
ANNUAL	61	84	38	100	4

Note: Data period of record spans January 1994 through December 2006.

This seasonal dependence is due to lower temperature and linked temperature range observed in the winter compared to the summer.

Dew Point Temperature

Dew point temperature is defined as the temperature to which air must be cooled at constant pressure for saturation to occur. Monthly and annual average dew point temperatures are given in Table 34. These temperatures were computed from the corresponding monthly and annual average air and wet bulb temperatures for the time period January 1994 through December 2006. The lowest monthly averaged dew point temperature was 14.0° F in January. The corresponding highest monthly averaged dew point temperature is 37.3° F in July. These dew point temperatures correspond with the lowest and highest monthly average air

temperatures of 17.3° and 71.4° F respectively.

Mixing Ratio

Mixing Ratio is a conservative moisture parameter, not variable with changes in temperature or pressure. It is the mass of water per unit mass of dry air, normally expressed in units of grams of water per kilogram of dry air. Calculated values of the mixing ratio covering the same time period as that for dew point temperature are given in Table 35. Mixing ratios in this table include the calculated monthly and annual averages for the 10-year period and the single monthly extremes. The lowest average mixing ratio occurred in December and January (2.6 g/kg) when average temperatures are low, and the highest average occurred in July (6.2 g/kg), when average temperatures are high.

Table 34. Monthly and annual averages of dew point temperatures and corresponding air (dry bulb) and wet bulb temperatures for CFA.

	Average Dew Point Temperature (deg F)	Average Dry Bulb Temperature (deg F)	Average Wet Bulb Temperature (deg F)
January	14.0	17.3	16.3
February	14.3	19.7	18.0
March	22.7	33.6	29.3
April	26.8	43.6	36.2
May	32.3	53.1	43.0
June	36.3	61.6	48.4
July	37.3	71.4	52.9
August	34.1	68.6	50.6
September	29.7	57.3	44.0
October	24.0	43.5	35.2
November	20.8	29.3	26.1
December	14.6	18.7	17.5
ANNUAL	26.0	44.1	35.5

Note: Data period of record spans January 1994 through December 2006.

Table 35. Monthly and annual mixing ratio averages and extremes for station CFA.

	Average (g/kg)	Highest (g/kg)	Lowest (g/kg)
January	2.6	7.7	0.2
February	2.7	6.9	0.1
March	3.4	9.1	0.4
April	4.0	9.0	0.8
May	5.0	14.6	0.9
June	5.8	13.8	1.2
July	6.2	16.5	1.2
August	5.5	15.8	1.2
September	4.8	15.1	0.9
October	3.7	11.6	0.6
November	3.2	8.8	0.5
December	2.6	7.4	0.2
ANNUAL	4.1	16.5	0.1

Note: Data period of record spans January 1994 through December 2006.

ATMOSPHERIC PRESSURE

Station Pressure

Atmospheric pressure is an important consideration in many phases of design and operations at the INL. Pressure has been recorded nearly continuously at CFA since February, 1950 (Clawson et al., 1989), and is currently measured at 17 NOAA INL Mesonet locations. The CFA record from January 1994 through December 2006 is summarized in Table 38. Atmospheric pressure values given in Table 36 are the actual measured values at CFA (“station pressure”) and are not adjusted to equivalent sea level values. The “standard atmosphere” correction for station pressure recorded at CFA’s elevation is +5.03 inches to yield equivalent sea level pressure.

The 13-year data between January 1994 and December 2006 indicate that the average station pressure is 25.05 inches of mercury (in. Hg). The monthly average atmospheric pressure ranges from 24.97 in. of mercury in April to 25.10 in. of mercury in August and December. The extreme lowest and highest atmospheric pressures ever recorded were 24.33 and 25.68 in. of mercury, respectively. This range indicates that the extreme limits of station pressure would probably be bounded by 24.00 and 26.00 in.

An examination of the average daily maximums and minimums indicates the development of more intense pressure systems in the winter compared to the weaker systems prevalent in the summer months. The annual mean daily pressure range was 0.16 in, varying from near 0.12 inches in the summer to 0.19 inches in the winter.

An evaluation of the synoptic and climatological records of the surrounding area indicates that the maximum expected atmospheric pressure change would be approximately 0.1 in. of mercury per hour. A similar evaluation of the records for the maximum change in a 24-hour time period yields a value of 1.0 in. of mercury per day. This is supported by the largest measured change of 0.680 in. of mercury per day.

Air Density

The average density of air at the INL is a value of some interest and is related to atmospheric pressure and temperature. It can be computed from the equation of state using average values of air temperature, atmospheric pressure, and atmospheric moisture. Using an average air temperature and atmospheric pressure of 42.0° F and 25.06 in. of mercury for CFA, respectively, the equation of state yields an average air density value of 1.06 kg/m³.

Table 36. Monthly and annual atmospheric station pressure^a averages and daily pressure extremes for CFA^b.

	Monthly Average (in. Hg)	Average Daily Maximum (in. Hg)	Average Daily Minimum (in. Hg)	Extreme Daily Maximum (in. Hg)	Extreme Daily Minimum (in. Hg)
January	25.07	25.16	24.98	25.63	24.33
February	25.04	25.13	24.95	25.68	24.40
March	25.00	25.08	24.91	25.59	24.46
April	24.97	25.06	24.89	25.46	24.50
May	24.99	25.06	24.92	25.44	24.46
June	25.02	25.08	24.95	25.41	24.60
July	25.09	25.15	25.03	25.38	24.66
August	25.10	25.16	25.03	25.40	24.73
September	25.08	25.15	25.01	25.51	24.66
October	25.07	25.15	24.99	25.54	24.46
November	25.08	25.17	24.99	25.58	24.50
December	25.10	25.19	25.00	25.65	24.47
ANNUAL	25.05	25.13	24.97	25.68	24.33

a. Pressures are not adjusted to sea level.

b. Note: Data period of record spans January 1994 through December 2006.

SOLAR AND TERRESTRIAL RADIATION

Solar radiation is the source of the energy for all movement of the atmosphere. It can be measured in terms of global, direct, diffuse, and net radiation. It can also be parameterized in terms of percent possible sunshine, percent sky cover, and day length, among others. Some of these measurements have been quantified at the INL and are described below. The net radiation is described in the next section on flux measurements.

Sunrise and Sunset Times

Day length is a parameter of interest in determining the time available for reception of

solar radiation. Longer days in the summer provide opportunity for more solar heating, while shorter days bring a cooling of the earth's surface. Sunrise and sunset times for CFA are listed in Table 37. All times listed are Mountain Standard Time (MST). The data indicate that the sun rises as early as 4:50 and sets as late as 20:17 hours MST. It also rises as late as 8:05 and sets as early as 16:55 hours MST. The longest day of the year is 15 hours, 26 minutes. The shortest day of the year is 8 hours, 57 minutes. Sunrise and sunset times on February 29 are considered to be equal to those on February 28. The resulting uncertainty is approximately one minute. Local topographic effects and resultant shadows have a much larger influence on sunrise and sunset times than does leap year.

Solar Radiation

Total daily solar radiation has been measured at 20 NOAA INL Mesonet locations for over 10 years and more than five years at all stations. These data are summarized in Table 38. Monthly and annual average of daily totals, and daily maximums of total solar radiation are presented in the SI units of megajoules per square meter. The solar radiation values are expressed in total, (or global) solar radiation. Global radiation on a

horizontal surface is the sum of the direct solar beam and diffuse sky radiation (skylight). The data indicates that the average daily total global radiation in July at CFA is expected to be 27.4 MJ per square meter. That value drops to 5.7 MJ per square meter per day in December. The average total daily global radiation value for the entire year is 16.6 MJ per square meter. Diffuse radiation is assumed to contribute about 30% of this value.

Table 37. Sunrise and sunset times for station CFA.

Day	January		February		March		April		May		June	
	Rise h m	Set h m										
1	0805	1706	0749	1743	0707	1821	0613	1859	0524	1935	0453	2006
2	0805	1707	0748	1744	0706	1823	0611	1900	0522	1936	0453	2007
3	0805	1707	0746	1745	0704	1824	0609	1901	0521	1937	0452	2008
4	0805	1708	0745	1747	0702	1825	0607	1903	0520	1938	0452	2009
5	0805	1709	0744	1748	0701	1826	0606	1904	0518	1939	0452	2009
6	0805	1710	0743	1749	0659	1828	0604	1905	0517	1940	0451	2010
7	0805	1711	0742	1751	0657	1829	0602	1906	0516	1942	0451	2011
8	0805	1712	0740	1752	0655	1830	0600	1907	0515	1943	0451	2011
9	0804	1714	0739	1754	0654	1831	0559	1909	0513	1944	0451	2012
10	0804	1715	0738	1755	0652	1833	0557	1910	0512	1945	0450	2012
11	0804	1716	0736	1756	0650	1834	0555	1911	0511	1946	0450	2013
12	0803	1717	0735	1758	0648	1835	0553	1912	0510	1947	0450	2014
13	0803	1718	0734	1759	0647	1836	0552	1913	0509	1948	0450	2014
14	0803	1719	0732	1800	0645	1838	0550	1914	0508	1949	0450	2014
15	0802	1720	0731	1802	0643	1839	0548	1916	0507	1950	0450	2015
16	0802	1722	0729	1803	0641	1840	0547	1917	0506	1951	0450	2015
17	0801	1723	0728	1804	0640	1841	0545	1918	0505	1953	0450	2016
18	0800	1724	0726	1806	0638	1842	0544	1919	0504	1954	0450	2016
19	0800	1725	0725	1807	0636	1844	0542	1920	0503	1955	0450	2016
20	0759	1727	0723	1808	0634	1845	0540	1922	0502	1956	0451	2016
21	0759	1728	0722	1810	0632	1846	0539	1923	0501	1957	0451	2017
22	0758	1729	0720	1811	0631	1847	0537	1924	0500	1958	0451	2017
23	0757	1731	0719	1812	0629	1848	0536	1925	0459	1959	0451	2017
24	0756	1732	0717	1814	0627	1850	0534	1926	0458	2000	0452	2017
25	0755	1733	0716	1815	0625	1851	0533	1928	0458	2000	0452	2017
26	0755	1735	0714	1816	0623	1852	0531	1929	0457	2001	0452	2017
27	0754	1736	0712	1817	0622	1853	0530	1930	0456	2002	0453	2017
28	0753	1737	0711	1819	0620	1854	0528	1931	0456	2003	0453	2017
29	0752	1739	0709	1820	0618	1856	0527	1932	0455	2004	0454	2017
30	0751	1740			0616	1857	0525	1933	0454	2005	0454	2017
31	0750	1741			0614	1858			0454	2006		

Table 37 (Continued).

Day	July		August		September		October		November		December	
	Rise h m	Set h m										
1	0455	2016	0522	1954	0556	1906	0630	1812	0708	1722	0746	1656
2	0455	2016	0523	1952	0557	1904	0631	1810	0709	1721	0747	1656
3	0456	2016	0524	1951	0558	1903	0632	1808	0711	1720	0748	1656
4	0457	2016	0525	1950	0559	1901	0633	1807	0712	1718	0749	1656
5	0457	2015	0526	1949	0601	1859	0635	1805	0713	1717	0750	1655
6	0458	2015	0527	1947	0602	1857	0636	1803	0715	1716	0751	1655
7	0459	2015	0528	1946	0603	1856	0637	1801	0716	1715	0752	1655
8	0459	2014	0529	1945	0604	1854	0638	1800	0717	1714	0753	1655
9	0500	2014	0530	1943	0605	1852	0639	1758	0718	1712	0754	1655
10	0501	2013	0532	1942	0606	1850	0640	1756	0720	1711	0754	1655
11	0502	2013	0533	1940	0607	1848	0642	1754	0721	1710	0755	1655
12	0502	2012	0534	1939	0608	1847	0643	1753	0722	1709	0756	1656
13	0503	2012	0535	1937	0609	1845	0644	1751	0724	1708	0757	1656
14	0504	2011	0536	1936	0611	1843	0645	1749	0725	1707	0758	1656
15	0505	2010	0537	1934	0612	1841	0647	1748	0726	1706	0758	1656
16	0506	2009	0538	1933	0613	1839	0648	1746	0728	1705	0759	1656
17	0507	2009	0539	1931	0614	1837	0649	1744	0729	1705	0800	1657
18	0508	2008	0541	1930	0615	1836	0650	1743	0730	1704	0800	1657
19	0509	2007	0542	1928	0616	1834	0651	1741	0731	1703	0801	1658
20	0510	2006	0543	1926	0617	1832	0653	1740	0733	1702	0801	1658
21	0510	2005	0544	1925	0618	1830	0654	1738	0734	1701	0802	1659
22	0511	2004	0545	1923	0620	1828	0655	1737	0735	1701	0802	1659
23	0512	2004	0546	1922	0621	1826	0657	1735	0736	1700	0803	1700
24	0513	2003	0547	1920	0622	1825	0658	1734	0738	1700	0803	1700
25	0514	2002	0548	1918	0623	1823	0659	1732	0739	1659	0804	1701
26	0515	2001	0549	1917	0624	1821	0700	1731	0740	1658	0804	1702
27	0516	1959	0551	1915	0625	1819	0702	1729	0741	1658	0804	1702
28	0518	1958	0552	1913	0626	1817	0703	1728	0742	1658	0804	1703
29	0519	1957	0553	1911	0628	1815	0704	1726	0743	1657	0805	1704
30	0520	1956	0554	1910	0629	1814	0705	1725	0744	1657	0805	1705
31	0521	1955	0555	1908			0707	1724			0805	1705

Table 38. Monthly and annual averages and maximums of total daily solar radiation (in megajoules/square meter) for the Mesonet stations.

	CFA ^a		GRI ^a		IDA ^b		SMC ^a	
	Avg	Max	Avg	Max	Avg	Max	Avg	Max
January	6.8	11.8	6.7	11.7	5.2	10.2	6.6	12.8
February	11.1	17.6	10.9	17.5	9.2	16.3	10.6	17.7
March	16.2	23.5	16.3	24.0	14.1	23.3	15.4	23.6
April	19.0	29.1	19.3	29.0	18.3	28.8	18.8	30.3
May	23.6	34.0	23.7	32.3	23.0	32.2	22.8	31.8
June	26.3	35.2	26.3	33.5	26.2	33.4	25.4	32.6
July	27.4	35.0	27.2	32.7	27.0	32.7	26.3	32.6
August	24.0	32.6	23.5	29.7	23.3	29.6	22.8	29.0
September	18.6	28.1	18.2	25.0	17.5	25.0	17.8	25.1
October	12.9	20.0	12.6	19.0	11.5	17.9	12.3	18.4
November	7.9	13.3	7.7	12.9	6.6	12.6	7.7	13.3
December	5.7	10.1	5.5	8.9	4.6	8.8	5.4	9.4
Annual	16.6	35.2	16.5	33.5	15.6	33.4	16.0	32.6

a. Data period of record spans January 1996 through December 2006.

b. Data period of record spans April 1997 through December 2006.

SURFACE ENERGY FLUX

The global energy cycle is the balance of energy between incoming solar radiation into the atmosphere and the energy lost. About 51% of all solar radiation is absorbed by the surface of the earth. The surface energy balance is then the balance of the 51% solar energy absorbed and later lost through the surface of the earth. Since 2001, surface energy flux measurements have been recorded in 30-minute averages at Grid 3 using the surface flux towers to gain a better understanding of how the INL climate interacts with the surface energy balance. Several components of the surface energy balance including soil temperatures, net radiation, and soil heat flux are described in this section. A more complete understanding of the INL climate on the surface energy

balance may be included in a future climatology report.

Soil Temperatures

The soil temperatures fluctuate yearly and daily depending on the air temperature and solar radiation. Table 39 lists the monthly mean soil temperatures. Similarly to the air temperatures, the soil temperatures have a natural seasonal dependency where the highest soil temperatures are found in the summer and coldest in the winter. The monthly average maximum soil temperature is in July at 80.9° F. Conversely, the coldest monthly average soil temperatures are recorded in December and January at 27.4 and 27.5° F, respectively. The average soil temperature usually drops below freezing in late November and increases above freezing in late February to early March.

Table 39. Monthly mean soil temperature values from the Grid 3 surface flux station.

Mean Soil Temperature	
Month	(deg. F)
January	27.5
February	28.9
March	37.4
April	49.7
May	61.6
June	70.4
July	80.9
August	76.3
September	63.5
October	47.7
November	32.5
December	27.4

Net Radiation

Net radiation is a meteorological parameter used in the determination of the amount of solar energy available to evaporate water (latent heat flux) or to warm the air (sensible heat flux). Net radiation is defined as the balance between incoming and reflected solar and incoming and emitted terrestrial radiation.

The sign of the flux of net radiation is positive when directed toward the earth's surface (incoming) and negative when directed outward from the earth's surface to the atmosphere (outgoing).

Net radiation was measured for a period of six years with a net radiometer from 2001 through 2007. The monthly data so obtained are summarized in Figure 64. The top two curves of the figure trace the net radiation during daylight hours only. The top curve represents the monthly maximum total net radiation observed on any given day during the six - year measurement period. The lower

of the top two curves represents the monthly average total daily net radiation. The bottom curve of the figure traces the monthly average total daily net radiation during nocturnal hours. The last remaining curve is a combination of the monthly average daytime daylight and monthly average nocturnal curves. It is the total amount of net radiation (incoming minus outgoing) measured during 24 hours.

The monthly maximum total daytime net radiation recorded for a particular day (top curve of Fig. 64) is the maximum amount that would be expected on a day with completely clear skies and with a minimum amount of atmospheric turbidity. During a clear day in the summer, the INL can be expected to average about 20 MJ net incoming irradiation per square meter per day during the daylight hours. The total nocturnal net radiation (bottom curve) usually averages about -1.5 and seldom exceeds -2.0 MJ per square meter per day. When these two values are compared, the maximum total 24-hour net radiation expected on a clear day is about 12.4 MJ per square meter per day.

The curves in Fig. 64 illustrate a natural seasonal dependency. In January, the daylight net radiation decreases to about 1.0 MJ per square meter per day. The nocturnal and daylight net radiation values are nearly equal but opposite in sign during the height of the winter season. The low angle of the sun combined with high reflection from clouds and snow produces the near-zero values of total daily net radiation observed in the winter. Lower net radiation values during the winter effect diminished convective activity compared to the summer months. This decrease results in a deep vertical stable layering of the atmosphere. Thus, a reduced

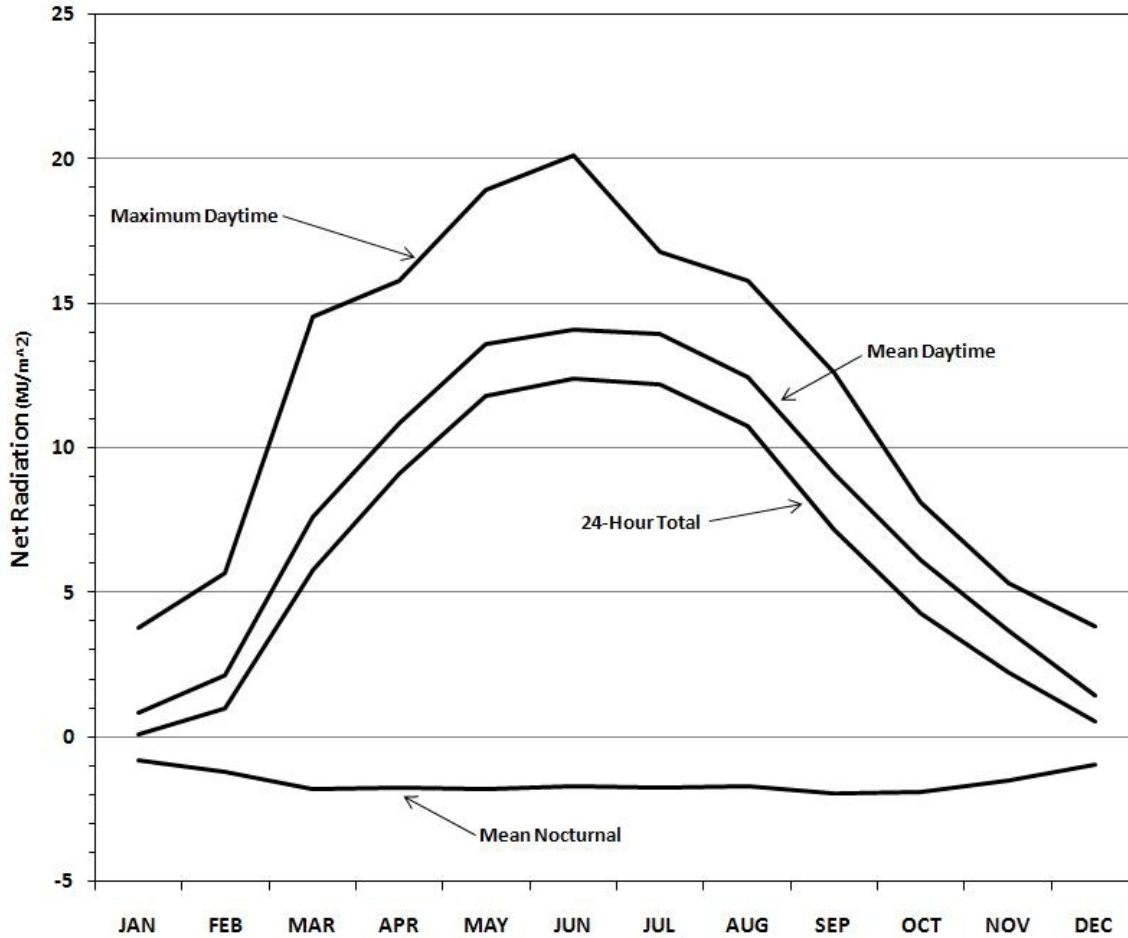


Figure 64. Monthly traces of maximum daytime, average daytime, 24-hour, and nocturnal total daily net radiation.

intensity and depth of vertical dispersion of effluents is to be expected during the winter.

Surface Soil Heat Flux

Surface soil heat flux is defined as the amount of heat that flows into or out of the soil. Soil heat flux is important in regards to the overall energy balance. Even though the magnitude of the values are small and the annual seasonal values are almost zero, the soil heat flux consumes up to 15% of the net radiation.

The soil heat flux is measured by heat flux plates, buried 8 cm beneath surface that measure the thermal energy at that depth. The surface soil heat flux is then the measurement of the flux by the heat plates and the heat stored in the soil above the plates. The information needed for calculating the heat stored above the plates includes, soil bulk density, soil water fraction, and change in soil temperatures and air temperatures.

The sign convention used is the same as for net radiation, i.e., it is positive if the flux

is to the surface and negative if it is away from the surface. Heat applied to the soil surface in the daytime by the sun causes energy to flow into the soil (negative flux). At night, the soil is warmer than the air, so heat flows from the soil to the surface (positive flux).

Table 40 displays the monthly average surface soil heat flux at the Grid 3 surface flux station from 2001 through 2007. The highest monthly soil heat flux to the surface is found during November at $6.80 \text{ W m}^{-2}\text{day}^{-1}$. Net radiation is near its minimum with soil temperatures still above freezing allowing for the soil heat flux to the surface. The highest monthly heat flux into the soil is found in the middle of the summer when soil temperatures are at the highest and there is maximum net radiation.

Table 40. Final monthly soil heat flux means from the Grid 3 surface flux station.

Month	Final Soil Heat Flux Means (W/m^2)
January	3.55
February	2.95
March	-1.64
April	-4.36
May	-6.80
June	-6.33
July	-7.32
August	-4.06
September	0.96
October	5.61
November	6.71
December	4.85

SPECIAL PHENOMENA

Several other types of meteorological phenomena occur at the INL that have not been addressed in the preceding sections. Among these are thunderstorms, blowing snow, and tornadoes. Each of these subjects is discussed below in the order of its frequency of occurrence.

Dew

Dew forms on the surfaces of objects, e.g., vegetation or vehicles, whenever the temperature of the object reaches the dew point. Dew has been observed to form on nearly any clear or mostly clear summer night. It may form as early as sunset and may not dissipate until as late as three to four hours after sunrise. Its formation and dissipation can usually be expected to approximately coincide with the formation and dissipation of the nocturnal temperature inversion.

Thunderstorms

A thunderstorm-day is defined by the NWS as a day on which thunder is heard at a given observing station. According to the definition, lightning does not have to be seen, and rain fall and/or hail is not required. Following this strict definition, the INL may experience an average of two or three thunderstorm days during each of the summer months from June through August, with considerable year-to-year variation. Several individual thunderstorms may occur during

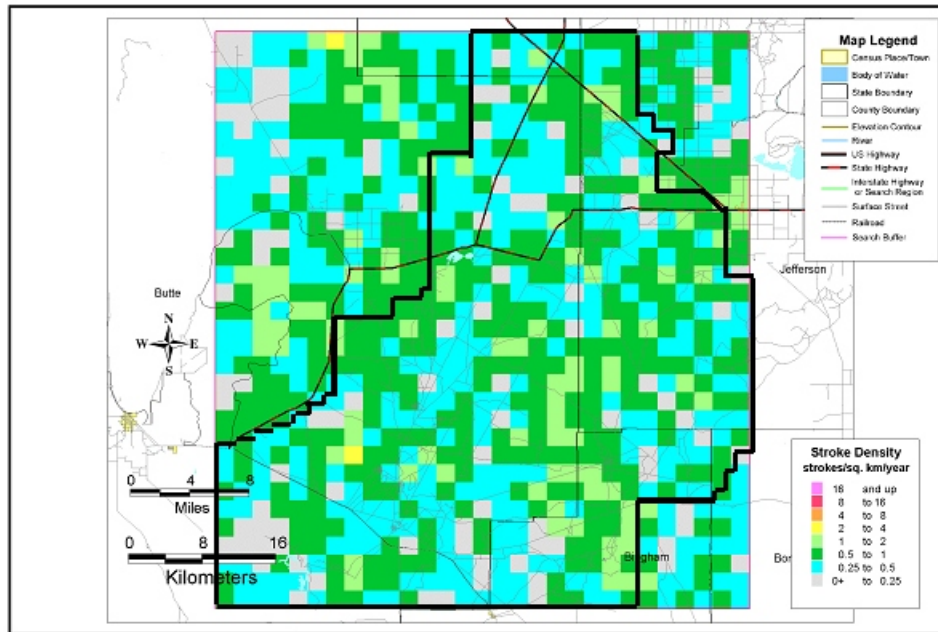
each of those thunderstorm days. At the INL, thunderstorms have been observed during every month of the year. They are, however, seldom observed during the months of November through February.

Thunderstorms over the INL are usually much less severe than what is normally experienced in the mountains surrounding the ESRP, or east of the Rocky Mountains. This is due, in part, to high cloud-base altitudes. Hence, the precipitation from many thunderstorms evaporates before reaching the ground (*virga*). The frequent result is little or no measurable precipitation. Occasionally, however, rain amounts exceeding the long-term average may result from a single thunderstorm.

Thunderstorms at the INL may be accompanied by micro bursts, i.e., strong, localized, gusty winds. These micro bursts can produce dust storms and occasional wind damage. The dust storms are sometimes visible in the NWS WSR88-D radar that is used to remotely observe precipitation and tornados. Thunderstorms may also be accompanied by cloud-to-ground as well as cloud-to-cloud lightning.

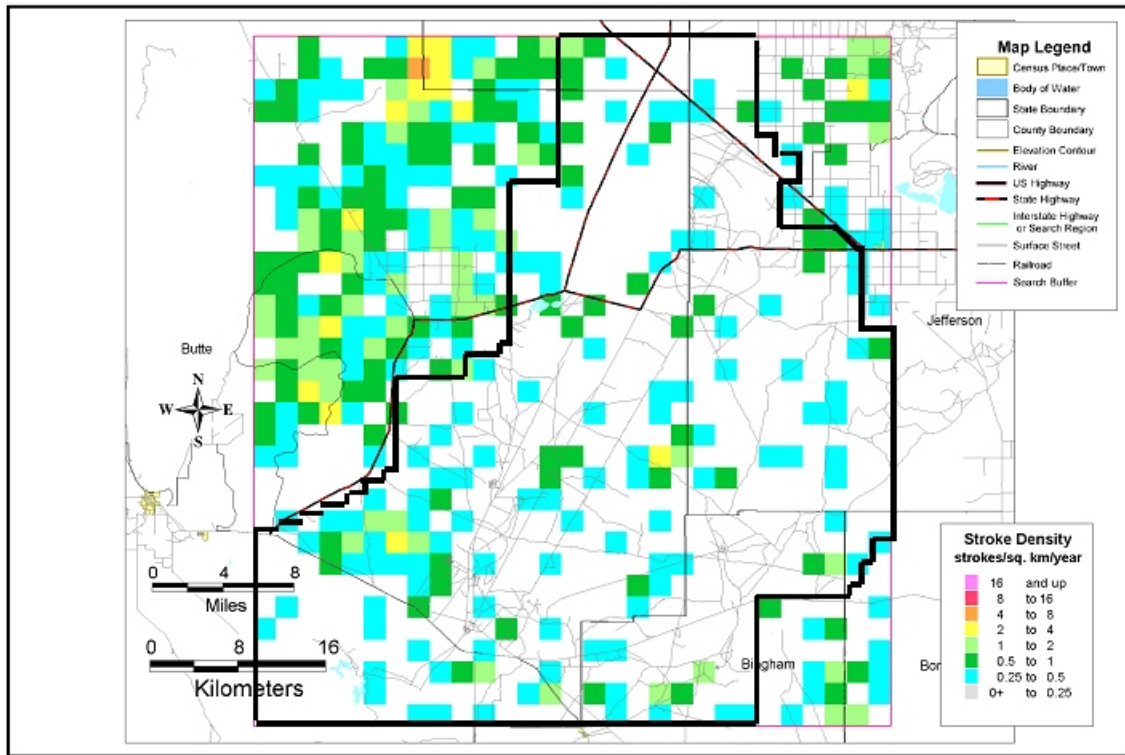
Lightning

The INL is currently monitored by the U.S. Bureau of Land Management Interagency Fire Center lightning detection system. This system detects the location and number of lightning strikes in real time for wild fire control. Figure 65 presents the geographical distribution of lightning strike density in the INL vicinity for the 5-year period January 2000 through December 2004. The distribution is somewhat uniform, with little dominance of mountainous terrain over the flat plains indicated in the data. Considerable year-to-year variability is evident, however. Figure 66 presents the geographical distribution of lightning strike density for calendar year 2001, a low lightning activity year. Figure 67 presents similar data for calendar year 2004, a high lightning activity year. The year-to-year, and typical month-to-month variability in lightning activity at INL is shown in Table 39. The lack of natural targets and the poor conductivity of the dry desert soil and underlying lava rock cause man-made structures at the INL to be susceptible to lightning strikes.



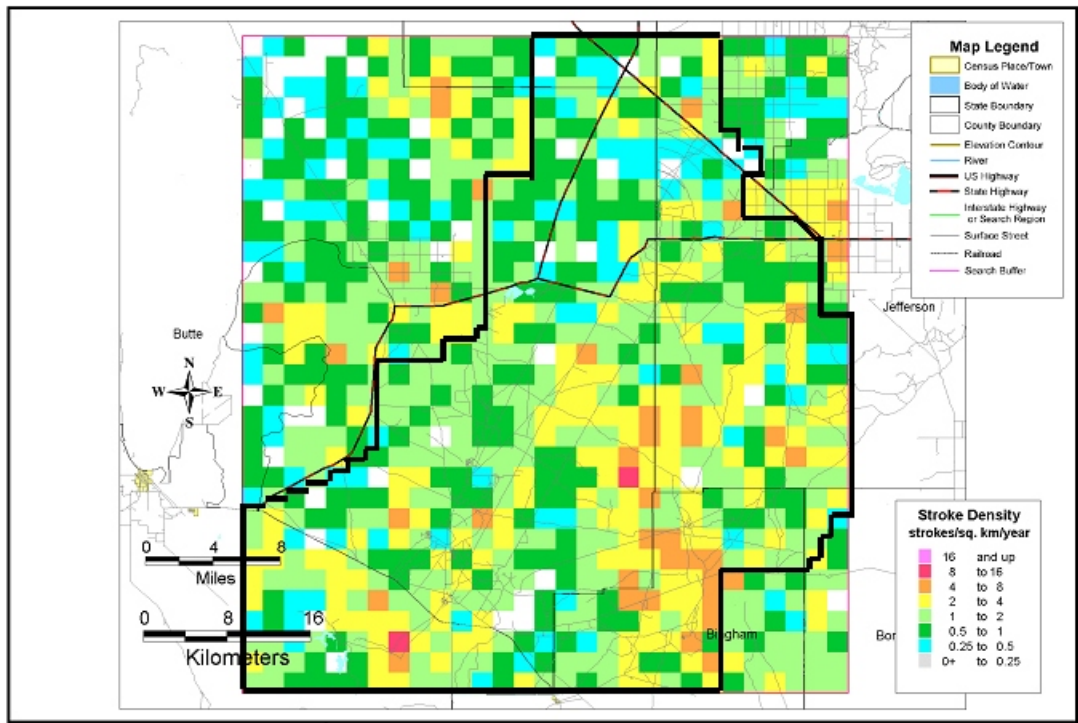
Lightning Strike 5-year Average Density
Jan 1, 2000 to Dec 31, 2004

Figure 65. Lightning strike 5-year average density for period January 2000 through December 2004.



2001 Lightning Strike Average Density
Jan 1, 2001 to Dec 31, 2001

Figure 66. Lightning strike density across the INL during 2001.



2004 Lightning Strike Average Density
Jan 1, 2004 to Dec 31, 2004

Figure 67. Lightning strike density across the INL during 2004.

Table 41. Lightning strike variability for the INL from 2000 through 2004^a.

	Year				
	2000	2001	2002	2003	2004
January	0	0	0	0	0
February	4	0	0	0	0
March	0	0	0	1	0
April	5	28	32	41	42
May	49	48	2	95	63
June	33	5	137	552	916
July	279	514	403	11	2,162
August	377	147	230	275	1,326
September	1,004	100	109	573	515
October	10	1	1	226	0
November	0	1	7	0	0
December	0	0	0	0	0
ANNUAL	1,761	844	921	1,774	5,024

a. Source: BLM Interagency Fire Center lightning detection statistics (VIASALA, 2005).

Hail

Small hail has been observed to occasionally occur in conjunction with thunderstorms. Hail size is usually smaller than 1/4 in. in diameter. Diameter may range up to 3/4 in., however, on very rare occasions. No hail damage has ever been reported at the INL. Crop damage from hail is not unusual, however, on neighboring farms across the ESRP. Property damage in the city of Idaho Falls has been reported as well as in other local cities. Damage from hail still remains a possibility at the INL.

Airborne Dust and Sand

A study of airborne dust at the INL was made in 1952 and 1953 (Humphrey et al., 1953) in disturbed areas and areas of natural vegetation. Dust concentrations ranged from a low of 14.1 $\mu\text{g}/\text{m}^3$ over a total snow cover to a high of 772 $\mu\text{g}/\text{m}^3$ during the summer. In an undisturbed area, even with dust devils present, a concentration of only 151 $\mu\text{g}/\text{m}^3$ was recorded. The annual average of 24-hour particulate samples was approximately 30 $\mu\text{g}/\text{m}^3$. Median sizes of dust particles in undisturbed areas ranged from 0.330 to 0.425 μm . Less than 1 % of the particles were larger than 10 μm but these ranged in size up to several hundred μm . Petrographic examination of the dust resulted in a moderately abrasive classification of the particles.

During the daylight hours under conditions of strong winds, the concentration of dust sharply decreases with height up to approximately 70 ft. AGL. Vehicular traffic and construction equipment contribute more to high dust concentrations than do strong winds over undisturbed areas, however. It is

therefore recommended that building fresh air inlets and motor vehicle air intakes should be located as high above the ground surface as possible.

Blowing dust and drifting sand can be a nuisance when the winds are strong in certain areas of the INL. These conditions may particularly affect the activities of construction personnel during the spring months after the winter thaw, when strong frontal systems pass through the ESRP, and during the summer months when thunderstorms are near.

Dust Devils

Dust devils are small atmospheric vortices that are generated over hot land surfaces. Dust devils are common in the summer at the INL when intense solar heating of the ground makes dust devil formation possible. They usually occur on calm, sunny days. Dust devils pick up dust and pebbles, and can overturn, blow down, or carry off unsecured objects. The dust cloud may be several hundred yards in diameter and extend several thousand feet into the air.

Blowing Snow

Blowing and/or drifting snow sometimes becomes a hazard as well as a nuisance during the winter months at the INL. Blowing snow greatly reduces visibility and slows down transportation. On rare occasions, the visibility has been reduced to zero in extreme blizzard conditions. Blowing snow usually accumulates in drifts on the leeward side of buildings, vehicles, fence posts, vegetation, etc. Drifts may occasionally render parking lots and highways

on the INL and access highways to the INL impassable and cause traffic to be rerouted.

Icing

Rime ice occurs when fog droplets impinge upon objects at temperatures below freezing. The meteorological conditions for the formation of rime ice may persist for several days when the ground is covered with snow and an accompanying persistent high pressure system is present. This makes the formation of supercooled fog or low stratus clouds and subsequent rime ice formation a distinct possibility. The accumulation of rime ice on power lines and air intakes has not been a constraint to operations at the INL.

Severe glaze icing, which accompanies freezing rain, rarely occurs at the INL. The meteorological condition which most frequently permits the formation of glaze ice is the transition period from rain to snow. Glaze ice results in slippery sidewalks and roads, and slows transportation. Glaze ice accumulation has been insufficient to damage power lines or communication cables at the INL.

Tornadoes

A tornado is defined as a violent local vortex in the atmosphere. When the vortex reaches the ground, it is classified as a tornado. If the vortex does not reach the ground, it is classified as a funnel cloud. The vortex is usually accompanied by a funnel shaped cloud with spiraling winds of very high velocity that may be greater than 300 mph. Tornadoes and funnel clouds always occur in association with thunderstorms, especially those which produce hail.

Most of the tornado activity in the U.S. occurs east of the Rocky Mountains. The total number of tornadoes in Idaho reported to the Storm Prediction Center (SPC) for the years 1950 through 2006 was 181. They occur most frequently during the month of June (25% of occurrences), but are also common in April, May, July and August (14, 18, 14, and 13% of occurrences, respectively). Tornadoes occurred most frequently (66%) between the hours of 1200 to 1700 MST.

Idaho tornado statistics must be interpreted with some caution. For example only 5 tornados were reported to the Idaho State Weather Service Office during the period of 1916 through 1950 (Bob Glodo, personal communication). Since then 181 tornados have been reported across the state. The rise in tornado sightings is due to an increase in population density and better communications rather than an increase in frequency. In the past, a lack of trained weather spotters and a poor local weather radar led to misidentification of tornadoes. In fact, some observers reported thunderstorm downpours as funnel clouds and tornadoes. Today, the NWS uses Doppler Radar which can help identify storms capable of producing tornadoes but still relies on trained weather spotters and the general public for tornado sightings. Tornados are only confirmed once the NWS investigates and assesses the damage from the storm.

Each tornado is classified using the Fujita Scale (F-scale) system that rates the degree of damage to the strength of the winds. The F-scale ranges from F0 (little damage) to F5 (most intense damage). Sixty-one percent of all Idaho tornadoes reported during this period were F0 (“Gale Tornado”, 40-72 mph,

some damage to chimneys; breaks branches off trees; pushes over shallow-rooted trees; damages sign boards), 33% were F1 (“Moderate Tornado”, 73-112 mph, peels surface off roofs; mobile homes pushed off foundations or overturned; moving autos pushed off the roads; attached garages may be destroyed), and 6% were F2 (“Significant Tornado”, 113- 157 mph, considerable damage. Roofs torn off frame houses; mobile homes demolished; boxcars pushed over; large trees snapped or uprooted; light object missiles generated). To date, Idaho has not experienced a “Severe Tornado” or tornado exceeding F2 in classification. This potentiality is low, given Idaho’s mountain setting and characteristically dry (when compared to US Midwest) air masses.

Locations of tornadoes which have been sighted in the ESRP and reported to the SPC through 2006 are illustrated in Fig. 68. Still today most tornado sightings have been located near higher populated areas. The large area where only a few tornadoes have

been reported are less populated areas and should not be taken that there is any less chance of a tornado occurring in those areas than populated areas. Nonetheless, six tornadoes have been reported across the INL. A supplemental record of funnel clouds and tornado sightings has been maintained by NOAA personal for the INL. Table 40 combines both the supplemental record and the SPC reports of the funnel clouds and tornado activity that have been observed on the INL since 1950.

The calculated return period for a tornado at the INL with wind speeds exceeding 120 mph, according to Coats and Murray (1985), is 1×10^6 years. This value is based on national tornado statistics, maximum atmospheric moisture content, surrounding geography, and other variables. Additional tornado characteristics such as typical and design basis tornadoes for the INL can be found in Coates and Murray (1985) and in various local U. S. DOE publications.

Table 42. Funnel cloud and tornado sightings observed on the INL^a.

Date	Time (MST)	Location	Type of Activity
28 April 1954	1220	6 mi. northeast of Atomic City	F0 Tornado ^d
9 June 1954	1210	5.5 mi. northeast of Atomic City	F0 Tornado ^d
6 June 1967	1200	1 mi. southeast of MFC	F0 Tornado ^d
27 July 1972	1330	3 mi. north northeast of MFC	F1 Tornado ^d
20 July 1974	1253	Within a triangle formed by Howe, TRA, and NRF	2 Funnel Clouds ^c
8 May 1975	M ^b	Near Middle Butte	2 Funnel Clouds ^c
23 July 1984	1225	10 mi. west south-west of TRA	1 Funnel Cloud ^c
16 June 1998	0915	3 mi. east of DEA	F0 Tornado ^d
1 September 2000	1600	10 mi. east of Arco	1 Funnel Cloud ^d
4 April 2006	1905	5 mi. south west of Montevue	F0 Tornado ^d

a. Data period of record spans from January 1950 through December 2006.

b. Data is missing.

c. Data recorded by ARLFRD.

d. Data recorded by the National Data Climatic Center.

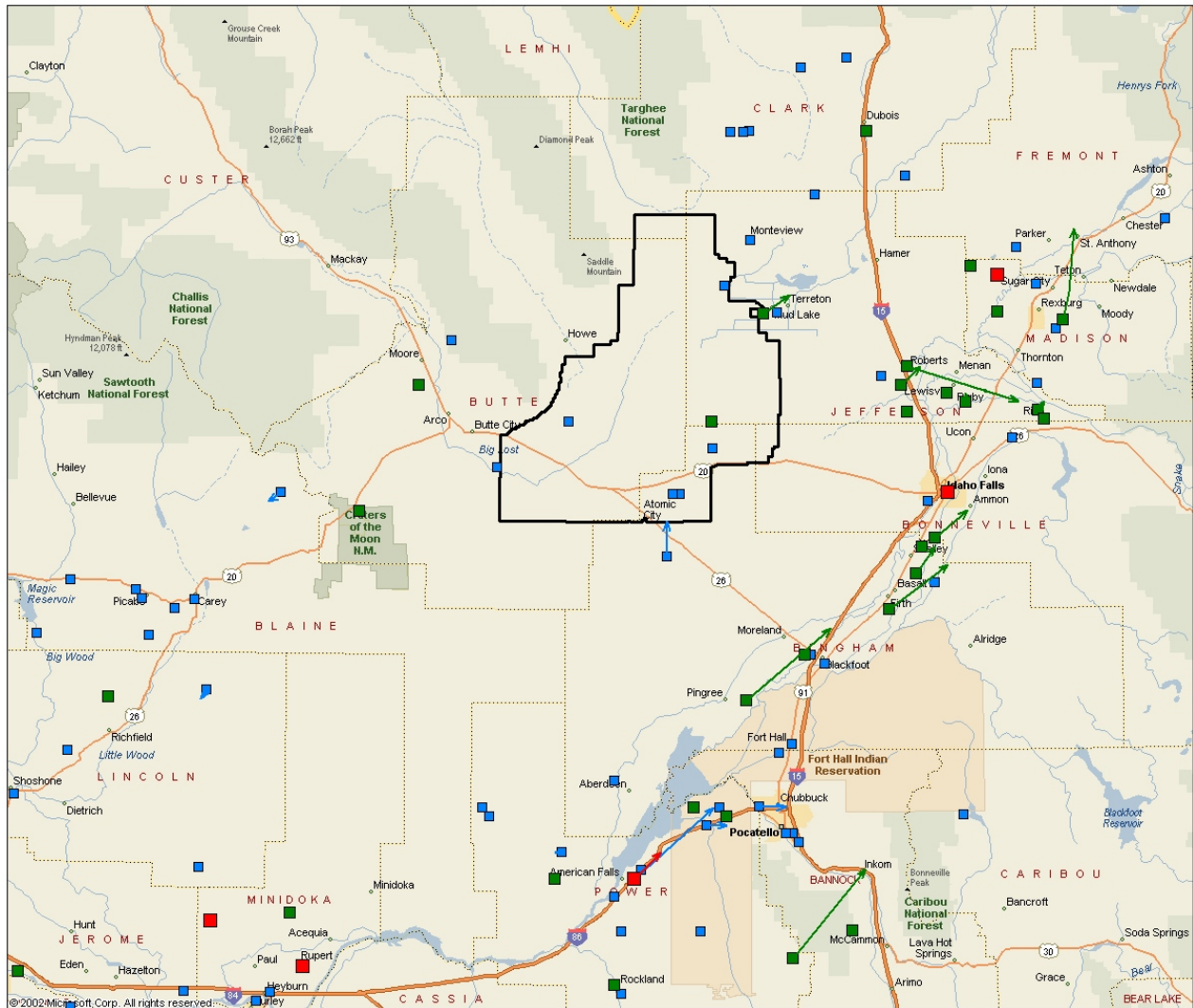


Figure 68. Tornado sightings in the ESRP according to National Climatic Data Center from 1950 through 2006. Each sighting is indicated by the strength (F0-blue dot, F1-green dot, and F2-red dot) and direction (arrow).

RANGE FIRES

From 1994 to 2006 over 200,000 acres of the INL and several hundred thousand acres of Bureau of Land Management managed public lands burned on the Snake River Plain of southeast Idaho. Range fires have threatened INL facilities and have exposed soils to wind erosion, resulting in severe dust storms that have impacted operations and created traffic hazards that persisted for weeks.

Figure 69 depicts the burned areas for fires that occurred in the period 1994 through 2003. No major fires have occurred on the INL since 2003.

Major fires (more than 15,000 acres in size) occurred on the INL in 1994, 1996, 1999, and 2000. Some of these fires burned through areas in which NOAA INL Mesonet stations were installed. In particular, the 1994 fire burned around the DEA and BAS stations and

the 2000 fire burned around the RTC station. A graph of the five-minute average air temperature spike from the range fire on July 1, 1994 at BEA and BAS is shown in Fig. 70. The maximum air spike temperature during the time the fire burned through each station was 169° and 154° F for BAS and DEA, respectively. Although range fires have burned around a couple of NOAA INL Mesonet stations, the fires progressed so rapidly that no equipment was harmed.

Statewide, approximately 65% of Idaho range fires are lightning-caused (DOE, 2003). At INL, range fires typically occur in the late summer and fall, when annual grasses are dry, lightning activity is high, and dry atmospheric conditions evaporate much of the storm's rain (virga) before it reaches the ground. Lightning-caused fires spread rapidly when fanned by high winds that frequently accompany thunderstorms. The wind vector persistence of thunderstorm winds is limited, however.

Human-caused wildfires have been most damaging when started during conditions of persistent strong southwesterly winds that are a common occurrence at the INL, when strong solar heating links the surface winds with strong southwesterly synoptic winds aloft.

Winds affect not only the spread of wildfires, but also the natural propagation of seeds of grasses and forbs, including sagebrush. Restoration of sagebrush is highly desirable in order to maintain a balance of desirable natural plant and animal species (DOE, 2003). Deposition of wind-blown materials shifts and impacts the balance of moisture-retaining soils at the INL, and thereby influences areas where natural fuels may preferentially grow and accumulate in the future. The southwest-to-northeast striations in vegetated areas that are visible in Fig. 70 southwest of Mud Lake show the effect of horizontal vortices in the strong southwesterly winds in producing these micro-climates.

1994 - 2007 INL Fire Map

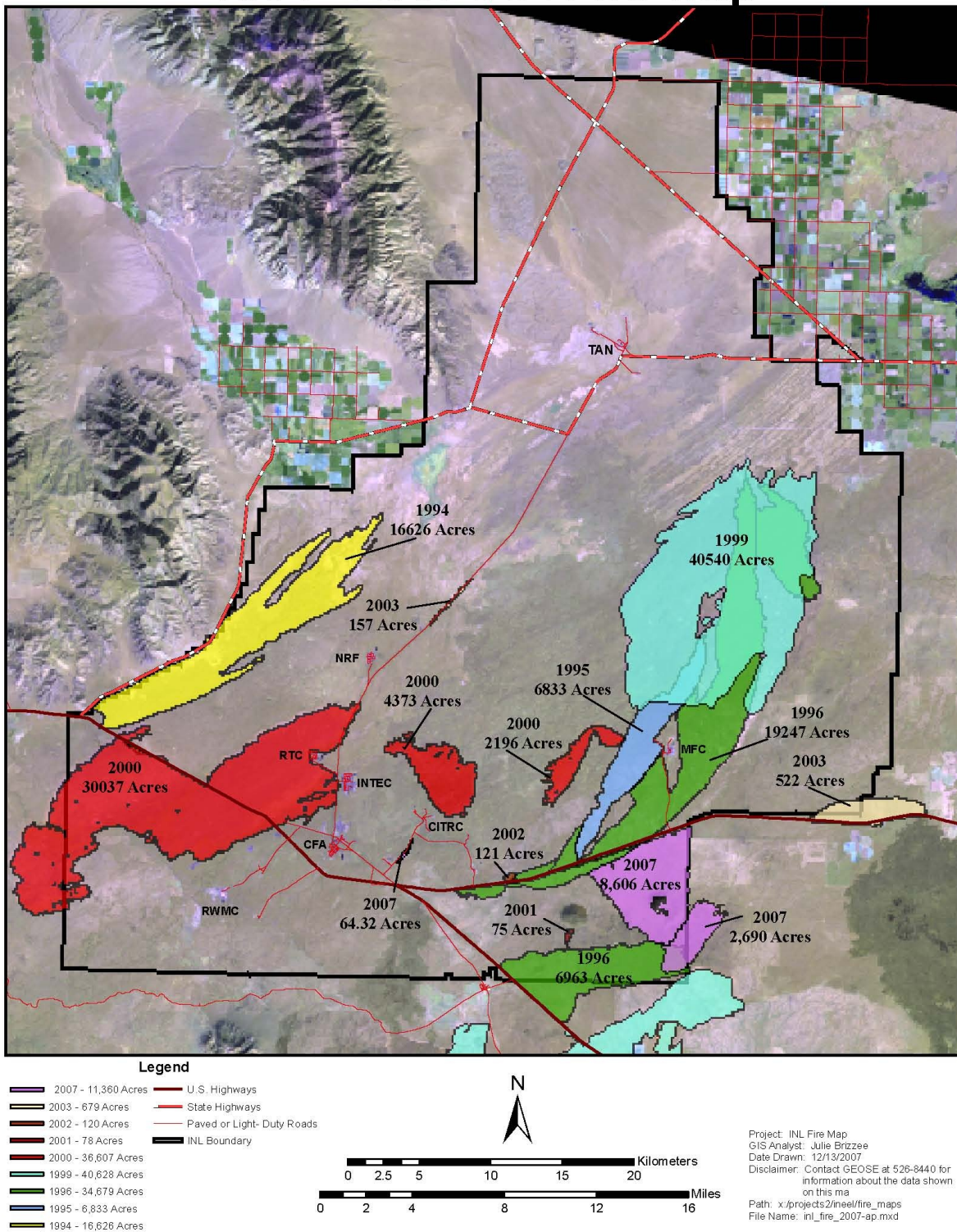


Figure 69. Wildland fire areas at INL from 1994 through 2007.

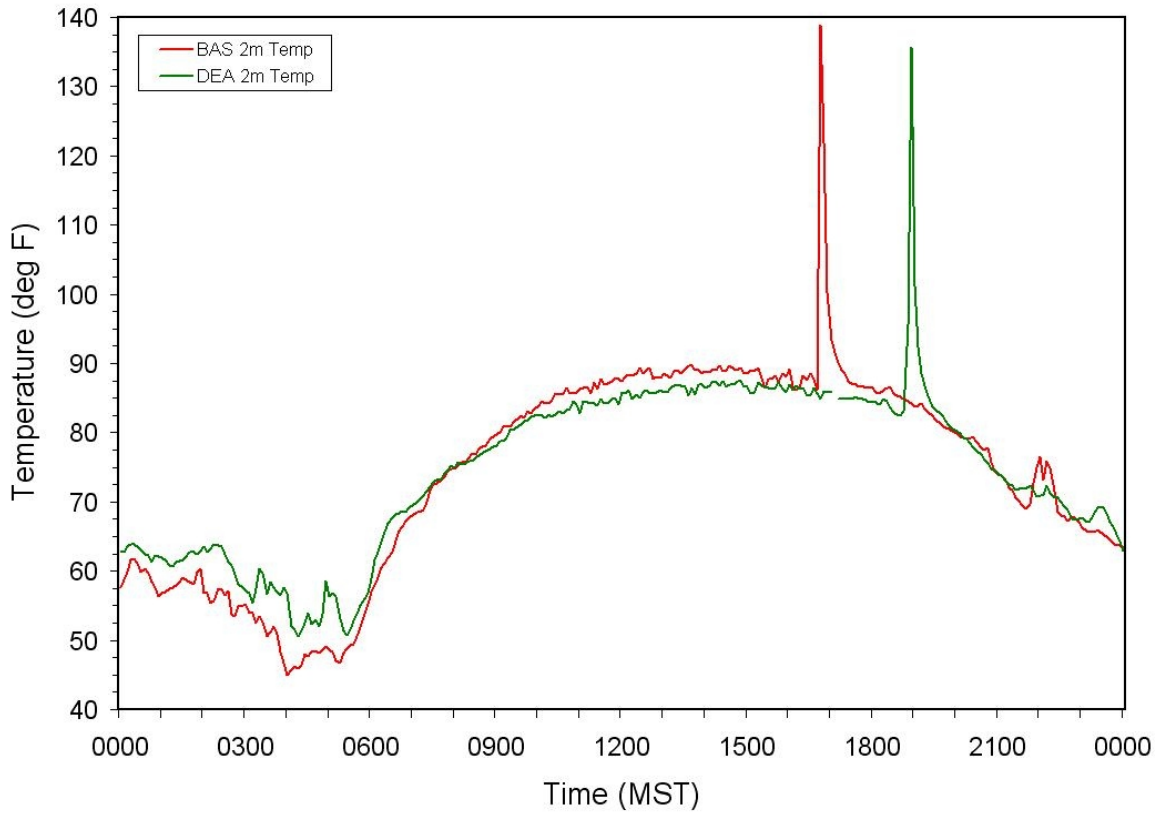


Figure 70. Five-minute air temperature spike from July 1, 1994 range fire at DEA and BAS.

ATMOSPHERIC TRANSPORT AND DIFFUSION

Operations at the INL frequently require a means of estimating the potential impacts of routine or accidental effluent releases into the atmosphere. The atmosphere has two primary effects on an effluent: transport and diffusion. Transport is the bulk motion of the effluent cloud caused by the wind. It is associated with atmospheric circulations having length scales significantly larger than the size of the cloud. Winds in the atmosphere are actually a composite of atmospheric circulations spanning a wide range of scales, from the 1000 km scale of synoptic weather systems down to local turbulent eddies having scales as small as 1 mm. Only those circulations significantly larger than the size of an effluent cloud are effective in bulk transport. Smaller circulations tend to shred the effluent cloud apart and mix it with the surrounding clear air. This turbulent mixing process is called diffusion. The combination of transport and diffusion is often called atmospheric dispersion.

Any computer model that estimates the impact of an effluent release must deal with both the transport and diffusion of the cloud. To be successful, such models must contain a realistic description of atmospheric structure. Most dispersion models focus on effluent releases near the surface where people live, so they must accurately describe the structure of the lowest part of the atmosphere, known as the atmospheric boundary layer (ABL).

The Atmospheric Boundary Layer

The ABL is the part of the atmosphere that responds directly to the presence of the earth's surface. Everyone is aware of the

normal diurnal air-temperature cycle with warming during the day and cooling at night. This cycle is caused by daytime solar heating at the surface and radiative cooling at night. The air just above the surface responds quickly to these changes in surface heating and cooling, but the atmosphere far above the surface shows no such response. Typically, only the atmosphere within the first few kilometers above the surface exhibits a direct response to diurnal changes at the earth's surface, and this lowest layer is the ABL. The atmosphere above the ABL is usually called the free atmosphere or free troposphere. The ABL responds to more than just surface heating and cooling. Aerodynamic drag at the surface also tends to reduce wind speeds. Winds within the ABL are directly affected by this surface drag and are therefore typically have lower speeds than in the free atmosphere above.

Vertical mixing by turbulence is the primary mechanism that allows the ABL to respond to changes in surface conditions. Anything released near the surface, whether it is energy from the sun or an effluent, is mixed upward by turbulence through the ABL. Turbulence is generated in two primary ways (Garratt, 1992). Mechanical production of turbulence occurs when velocity shears develop within a mean wind flow. The drag exerted by the earth's surface is one common source of velocity shear, so mechanical turbulence is ubiquitous near the surface. Since mechanical turbulence derives its energy from an existing mean flow, larger atmospheric circulations such as synoptic weather systems must be present to sustain the mean flow. Energy is continually extracted from the larger circulations to maintain the

mechanical turbulence. Generally, rough surfaces generate more mechanical turbulence than smooth surfaces, so the turbulence level over a forest is usually higher than over a smoother surface such as short grass.

The second primary turbulence generation mechanism is buoyant production. If the earth's surface is warmer than the overlying air, as is normally the case over land on sunny days, buoyant parcels of air will form and rise upward as convective thermals. These thermals are an additional source of turbulence within the ABL and can coexist with mechanical turbulence. Since buoyancy-generated turbulence derives its energy from temperature differences, it can exist even when no mean airflow is present.

ABL structure during fair weather over land. The depth and structure of the ABL varies widely from day to night. Shortly after sunrise the heating at the earth's surface causes a rapid increase in the buoyant production of turbulence. The convective thermals tend to penetrate higher and higher as the morning wears on, so there is a rapid growth of the boundary layer until it reaches a quasi-steady depth of typically 1-3 km during the afternoon. Because the daytime boundary layer is dominated by convection, it is often called the convective boundary layer (CBL). The CBL is frequently capped by a temperature inversion which tends to block the continued upward motion of the thermals. However, some mixing of CBL and free-atmosphere air takes place at this level, so the capping layer is sometimes called the entrainment layer.

Figure 71 is an idealized diagram of

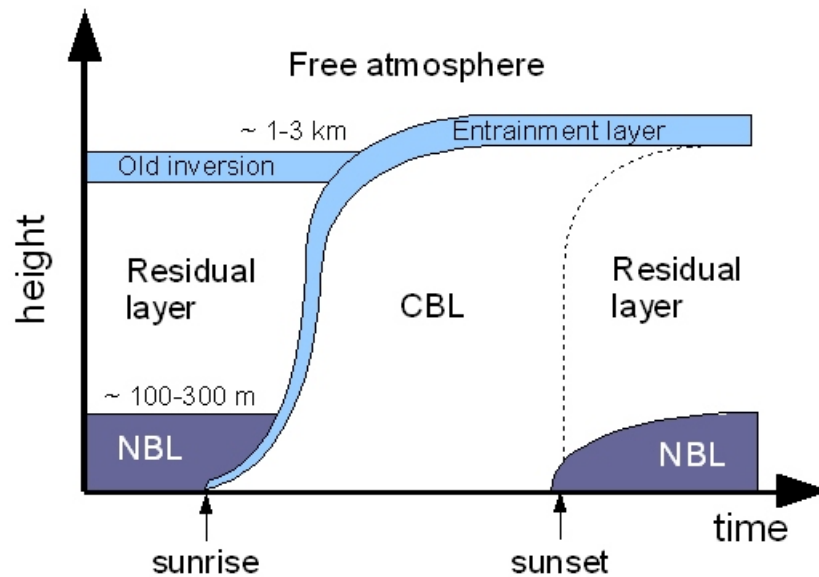


Figure 71. Schematic diagram of ABL structure in fair weather.

Near sunset the solar heating at the surface ceases, so there is a rapid decrease in buoyant turbulence production. This results in a collapse of the ABL depth as the convective thermals dissipate and only mechanical turbulence remains. After sunset, radiative cooling at the surface causes a surface-based inversion to develop and grow. The temperature profile within the inversion tends to suppress the production of mechanical turbulence, so the depth of the nocturnal boundary layer (NBL) is usually far less than that of the CBL.

Above the NBL is the residual layer (RL), which is basically the remnants of the previous day's CBL. The temperature profile within the RL remains similar to what it was during the day, but there is no longer any steady turbulence production within this layer. Since the RL is cut off from the surface, it is not really part of the ABL. However, intermittent bursts of turbulence are possible within the RL due to a variety of mechanisms, including shears related to low-level jets and gravity waves.

Defining the depth of the NBL is not straightforward, because there is no capping inversion that clearly separates the NBL from the RL above. A variety of definitions have been proposed (Stull, 1988), including the total depth of the surface-based inversion and the height of the lowest-level wind jet. For dispersion applications, however, the depth that matters is the depth of the surface turbulence layer. Generally, the NBL turbulence layer is shallower than the inversion depth (Garratt, 1992) and is typically on the order of 100 m when moderate winds are present but can be less than 50 m in light winds.

ATMOSPHERIC STABILITY

Transport and diffusion models usually require some kind of input related to atmospheric stability. The well-known Pasquill stability classes (Pasquill 1961), with class A representing very unstable conditions and class F representing moderately stable conditions, are one type of stability input that has found common use in dispersion modeling. One can ask how this notion of stability is related to the ABL structure briefly described above. The problem here is that atmospheric stability has been defined in more than one way within the meteorology literature, and this often leads to confusion when applying this concept to dispersion.

Many meteorology textbooks discuss the idea of static stability (e.g., Wallace and Hobbs, 1977), which is associated with the behavior of an air parcel when it is vertically displaced. An atmospheric layer is said to be statically stable when an air parcel that is vertically displaced experiences a buoyancy force that causes it to settle back to its original level. Statically unstable conditions exist when a vertically displaced air parcel experiences a buoyancy force that causes it to continue moving away from its original level. Neutral stability exists when the displaced air parcel experiences no buoyancy force and therefore remains at its new level. Static stability is determined by the temperature profile within the atmospheric layer. Neutral conditions exist when the atmospheric temperature decreases at the dry adiabatic lapse rate of $9.8^{\circ}\text{C km}^{-1}$. Any layers that have a lapse rate less than this are statically stable, whereas layers with larger lapse rates are unstable. The presence of water in the atmosphere adds additional complications to

this simple concept of stability, but this is not discussed here.

Static stability is clearly a spatially local definition that can vary from point to point. The concept of stability that is more relevant for dispersion modeling is a bulk definition that applies to the whole ABL. From Fig. 70 it is clear that the daytime CBL corresponds overall to an “unstable” boundary layer, whereas the NBL fits the role of a “stable” boundary layer. The primary difference between the CBL and NBL is the direction of heat flow at the surface. This is quantified as the sensible heat flux H at the surface, which is the thermal energy passing through a unit area of the earth's surface per unit time (e.g., units of W m^{-2}). Positive values of H denote an upward heat flux from the surface to the atmosphere; negative values represent a downward flux that transfers energy from the atmosphere to the surface. From this, it is clear that the ABL is generally unstable when H is large and positive, and generally stable when H is negative.

Although the bulk ABL stability is related to the concept of static stability discussed above, they do not entirely overlap. Large portions of the CBL actually have a nearly neutral static stability. Buoyant thermals are generated near the surface in the CBL, and then rise up through the statically neutral middle portions. The turbulence observed in the middle CBL is therefore largely caused by nonlocal buoyant production originating at the earth's surface. Static stability is only useful as an indicator of local turbulence production within the layer where it is measured, so it has limited utility in situations, such as the CBL, where most of the turbulence is generated nonlocally.

From Fig. 70 it is not clear how one defines an ABL with neutral bulk stability.

Neutral conditions should prevail when the surface heat flux H is close to zero, with neither buoyant production nor suppression of the turbulence. Under such conditions the ABL structure is determined mainly by mechanical turbulence acting in a layer with a nearly neutral static stability. In the fair weather depicted in Fig. 70, a neutral ABL is expected to exist only during short transitory periods near sunrise and sunset. One would expect a near-neutral ABL to be present for more extended periods in cloudy conditions when H is small or in windy conditions with only weak solar heating (e.g., in winter).

TRANSPORT AND DIFFUSION MODELING

Various approaches have been used to model the transport and diffusion of effluents. Over time, a better understanding of ABL structure and continually increasing computer speeds have allowed ever more complex dispersion models to be developed. However, the most complex models are not always the best models for a particular application. Complex models usually contain a large number of input variables that are not always easy to obtain from field measurements. If a lack of field measurements forces the user to guess at some important model inputs, a complex model may actually end up performing worse than a simpler model with fewer inputs. As a general rule, the most suitable model complexity will depend both on the specific model application and on what kind of field measurements are available.

Broadly, all dispersion models can be classified as using either an Eulerian or Lagrangian framework. In an Eulerian model, the properties of the effluent are tracked at a series of fixed points in space. Normally, this involves solving a conservation-of-mass

equation for the effluent on a fixed grid of points. Eulerian models are most commonly used to estimate regional air pollution, because they are well suited to area emissions of pollutants and can include algorithms for chemical transformations. Such models are not well suited for individual plume or puff releases, because they would require an extremely dense grid of points to properly resolve the plume or puff.

Lagrangian models are commonly used to model effluent releases from a single source or from a small number of individual sources. These models track the motion of the air parcels containing the effluent as these parcels are dispersed by the atmosphere. Various simplifying assumptions are used to reduce the number of model parameters that are required to keep track of the effluent cloud. Depending on the level of simplification, the number of parameters required to track a single effluent cloud can be quite small, which is why Lagrangian models are highly favored for single plume or puff releases. Although Lagrangian models do not use fixed grids of points for computing the dispersion, they often include algorithms for interpolating the model outputs (e.g., concentrations) to a fixed grid. This is done for the convenience of the model end users, who usually want to know how the effluent cloud is expected to affect specific locations.

At INL, almost all of the effluents of concern come from a relatively small number of point sources. Hence, all the dispersion modeling at INL has so far been performed with Lagrangian models. The following subsections describe in more detail some of the general categories of Lagrangian models in common use. No further discussion is devoted to Eulerian models, since they are currently not in use at INL.

Gaussian Plume Model

The Gaussian plume model is one of the simplest models for continuous emissions from a point source. It assumes that the concentration in both the horizontal and vertical directions follows a Gaussian (normal) distribution about the plume centerline. Moreover, the wind speed U , wind direction, and the turbulence levels are assumed to be constant in both space and time. For a point source with constant effluent release rate q , the ground-level concentration $\chi(x, y, 0)$ according to this model is

$$\chi(x, y, 0) = \frac{q}{\pi \sigma_y \sigma_z U} \exp \left[-\frac{y^2}{2\sigma_y^2} - \frac{h^2}{2\sigma_z^2} \right] \quad (1)$$

where x is downwind distance from the source, y is crosswind distance from the plume centerline, h is the height of the plume centerline, and σ_y and σ_z are respectively the horizontal and vertical standard deviations for the plume. This particular form of the model assumes that any portion of the plume extending underground is “reflected” at the surface.

The standard deviations σ_y and σ_z vary with downwind distance x and are interpreted as a measure of the horizontal and vertical sizes of the plume. Much of the effort associated with any Gaussian model is related to determining the rate of growth of these standard deviations. This is where the ABL structure described earlier comes into play. The growth rate of these parameters is directly linked to the level of turbulence present in the ABL.

While mathematically simple, the Gaussian plume model has significant limitations. It assumes the wind remains constant in speed and direction as the effluent is transported from the source to the receptor location at (x, y) . Likewise, both the release rate q and the turbulence responsible for the growth of σ_y and σ_z are also assumed to remain constant. In practice, these assumptions are usually valid for only relatively short distances from the source. At INL, for example, it is usually reasonable to assume a constant transport wind out to distances on the order of a kilometer or so, but at longer ranges the wind often changes due to the influence of the topography or other factors. Even in flat terrain, the temporal changes in ABL structure shown in Fig. 70 can invalidate the underlying assumptions of the plume model for effluent travel times beyond an hour or so.

Gaussian Puff Model

Some of the limitations of a straight-line plume model are avoided by treating the effluent cloud as a series of instantaneous puffs. Each puff is assumed to have a Gaussian distribution in all three directions. For a puff containing a mass Q of effluent, the concentration at a location (x_c, y_c, z_c) relative to the puff's center is

$$\chi(x_c, y_c, z_c) = \frac{Q}{(2\pi)^{3/2} \sigma_x \sigma_y \sigma_z} \cdot \exp\left[-\frac{x_c^2}{2\sigma_x^2} - \frac{y_c^2}{2\sigma_y^2} - \frac{z_c^2}{2\sigma_z^2}\right] \quad (2)$$

where the standard deviations σ_x , σ_y , and σ_z respectively apply to the alongwind, crosswind, and vertical directions. The wind

speed U does not appear in this equation, because the coordinates (x_c, y_c, z_c) are defined relative to an origin at the puff's center. A separate computation is therefore required to estimate the transport of the puff's center by the wind. For simplicity, surface reflection of the puff is ignored in Eq. (2), although it can be added as in Eq. (1).

To model a continuous source, puff models simply release a sequence of puffs at fixed intervals. If the time interval is too long, the model plume will have unrealistic gaps between the individual puffs. If the interval is too short, the model becomes bogged down tracking a large number of puffs. Most models therefore seek an intermediate puff-release interval that provides a realistic representation of the plume but is still computationally efficient. The total plume concentration at a fixed receptor is obtained by adding the contributions from all the nearby puffs.

A primary advantage of puff models is that they can deal with both temporal and spatial changes in the meteorological conditions. After a puff is released, its transport is broken down into a sequence of time steps δt . Both the wind speed and direction at the puff's center can vary from one time step to another. This may be due either to temporal changes in the wind or to the puff moving into a region with different winds. A puff model can therefore deal with complex wind fields where a plume's centerline will no longer be straight. These models can even simulate recirculations, where a reversal in wind direction causes some of the puffs to move back over the original release location at a later time. The growth of the puff standard deviations is likewise computed in time steps, which allows changes in ABL turbulence to be factored into the model.

Puff models tend to be more realistic than straight-line models in complex flows, but this comes at a price. First, the user must have either measurements or forecast-model output that describes the complex, time-varying wind field. If such information is not available, a puff model may not perform any better than a simpler plume model. Second, puff models are computationally more expensive than plume models. This is less of an issue now than in the past, but some effort must still be made to keep the number of puffs being tracked to a reasonable level. An incorrectly configured puff model can still bog down to the point where the output is not available in a timely manner.

Currently, the MDIFF puff model (Sagendorf et al. 2001) is the primary dispersion model in use at INL for emergency management. The puff transport is determined by the wind observations from the NOAA INL Mesonet. This mesonet can detect both spatial and temporal changes in the wind field near INL, and therefore provides the level of detail necessary for a puff model.

Puff models are a significant step up in realism from straight-line plume models, but they still have limitations. Many of these limitations are related to the steep gradients of meteorological variables that often exist in the vertical. Because of surface drag, vertical wind shear is almost always present in parts of the ABL. Generally, the vertical changes of winds and turbulence within the ABL are much larger than the horizontal changes. This can cause problems in Gaussian formulations such as Eq. (2), because there is an implicit assumption that the atmosphere is relatively uniform inside the volume occupied by the puff. This assumption can be quickly invalidated in the vertical even for values of σ_z as small as 10 m.

Several alterations have been proposed to account for the large vertical shears in the ABL. One of the most common is to simply break a puff vertically into smaller puffs when σ_z becomes too large. Another is to increase the growth of σ_x and σ_y in response to the presence of vertical wind shear. A less common approach is to skew the vertical axis of each puff as a function of the observed wind shear.

All the Gaussian models also come under some criticism for not taking into account the known structure of buoyancy-generated turbulence in the daytime CBL. As discussed earlier, much of the turbulence within the CBL is caused by thermals that are created near the surface and then rise up through the CBL. On average, these thermals occupy less than 50% of a given horizontal area; the remainder of the area contains a mean subsidence that offsets the mass transported upward by the thermals. The end result is that the vertical turbulence within the CBL has a skewed distribution, with larger but less frequent upward motions balanced by smaller but more frequent downward motions. This skewness directly affects the expected vertical distribution of an effluent cloud, so that the simple Gaussian distribution may not accurately reflect the true distribution in a CBL.

Lagrangian Particle Models

The increasing capabilities of computers have allowed an alternate type of dispersion model called a Lagrangian particle model to be employed (Luhar and Britter, 1989; Wilson and Sawford, 1996). These models use a large cloud of particles to represent the effluent. Unlike a puff, each particle is assumed to be small enough (e.g.,

an air parcel) that its internal growth can be ignored. Hence, the particles are treated as points that move with the wind but have no internal structure. To represent an instantaneous release, a particle model must simultaneously release a large number of particles within a limited volume near the source. A continuous release is obtained by repeatedly releasing particles at some fixed interval.

Since the particles do not grow in size, both the transport and diffusion of the effluent must be accounted for in the particle motion. Each particle is assumed to have a mean velocity vector \mathbf{U} that can vary with position and time. This mean velocity accounts for the bulk transport of the effluent, and performs a similar role to the mean motion of the puff centers in a puff model. To account for diffusion, an additional turbulent velocity increment is added to each particle's velocity components. This is done using a Markov equation for the velocity increment over a time interval from t to $t + \delta t$. Taking the particle velocity v along the y axis as an example, the Markov equation is

$$v(t + \delta t) = R(\delta t)v(t) + \sqrt{1 - R(\delta t)^2} \sigma_v \zeta \quad (3)$$

Here, $R(\delta t)$ is the velocity auto correlation for time lag δt , σ_v the standard deviation of the v velocity component, and ζ is a computer-generated random number from a unit normal distribution. The first term on the right side accounts for the observation that atmospheric turbulence has memory, whereas the second term is a random forcing that maintains the energy of the turbulence.

Equation (3) is applied independently to each particle, so over time the particles tend to spread apart at a rate proportional to the

velocity standard deviation σ_v . In real particle models, this simple Markov equation is normally only used for the horizontal diffusion. The equation for the vertical diffusion is usually more complex to account for the rapid variation with height of the turbulence (e.g., Wilson et al., 1983). However, Eq. (3) still provides the gist of how Lagrangian particle models work. To obtain the concentration distribution from these models, the region of interest is divided into a series of rectangular volumes $\delta V = \delta x \delta y \delta z$, and the number of particles within each volume is counted.

The big advantage of particle models is that they can realistically simulate dispersion in the presence of complex velocity shears. As already noted, vertical wind shear is nearly always present near the earth's surface. Since each particle is driven by the wind and turbulence at its own location, particle models can directly simulate the stretching of an effluent cloud related to shear. These models are also capable of handling cases where plumes are split apart by topography. At INL, for example, an effluent cloud can under the right conditions be split apart so that a portion of the cloud is drawn up one of the nearby tributary valleys (i.e., the Lost River or Birch Creek Valleys), whereas the remainder stays within the Snake River Plain. This type of plume splitting is much easier to simulate with a particle model than with the simpler Gaussian models.

The primary drawback of Lagrangian particle models is that a large number of particles must be released to produce a reasonably continuous concentration distribution. If too few particles are released, the resulting concentration distribution will be highly irregular because most of the grid volumes δV will contain only a small number

of particles. The NOAA HYSPLIT model (Draxler and Hess, 1997) reduces the number of required particles by including a hybrid configuration that combines the puff and particle approaches. As noted earlier, vertical wind gradients are usually much larger than horizontal gradients. Hence, the particle approach provides the most benefit for vertical diffusion. HYSPLIT includes an option that uses the puff approach to model horizontal diffusion and the particle approach to model vertical diffusion. The resulting particles/puffs resemble flat disks that grow horizontally but move randomly in the vertical based on a particle-type equation. This provides most of the benefits of the particle approach but requires far fewer particles/puffs than would be required in a full 3D particle simulation.

Turbulence Estimation

With all the Lagrangian models, it is necessary to estimate the strength of the turbulence that is diffusing the effluent cloud. In the Gaussian models the turbulence levels directly affect the growth of the plume standard deviations such as σ_y and σ_z . In particle models the turbulence shows up directly through the velocity standard deviations such as σ_v in Eq. (5). At short ranges from the source, there is actually a simple relation between the plume growth and the corresponding velocity standard deviation (Taylor 1921). Taking the horizontal standard deviation σ_y as an example, the short-range Taylor formula is

$$\sigma_y^2 = \sigma_o^2 + \sigma_v^2 T^2 \quad (4)$$

where σ_o is the initial cloud standard deviation, and T is the travel time since

release. When σ_o is negligible, this equation reduces to the even simpler form $\sigma_y = \sigma_v T$.

At longer ranges, Eq. (4) overestimates the cloud diffusion, but there is still a direct proportionality between cloud size (e.g., σ_y) and the velocity standard deviation (σ_v) when the turbulence is relatively constant. A generalized Taylor formula for σ_y at these longer ranges, ignoring σ_o , is (Arya, 1999)

$$\sigma_y = \sigma_v T f(T) \quad (5)$$

with $f(T)$ being some function that approaches unity at short ranges and varies with $T^{-1/2}$ at long ranges (to match the far-field limit of the Taylor theory). A similar formula can be used to relate σ_z to the standard deviation σ_w of the vertical velocity. Equations of this form are commonly used in Gaussian dispersion models to compute σ_y and σ_z from the turbulence parameters σ_v and σ_w .

Clearly, the ABL structure and its bulk stability directly affects the turbulence levels present at any given time. There are three general approaches that are used to relate bulk ABL stability to the dispersion parameters:

1. Empirical diffusion curves based on field data.
2. Formulas based on the theory of ABL structure.
3. Direct turbulence measurements.

The first approach was the earliest, partly because in pre-computer days it allowed dispersion estimates to be quickly derived from sets of graphs. Some of the best known examples of this approach are the Pasquill-Gifford curves (Gifford, 1961; Slade,

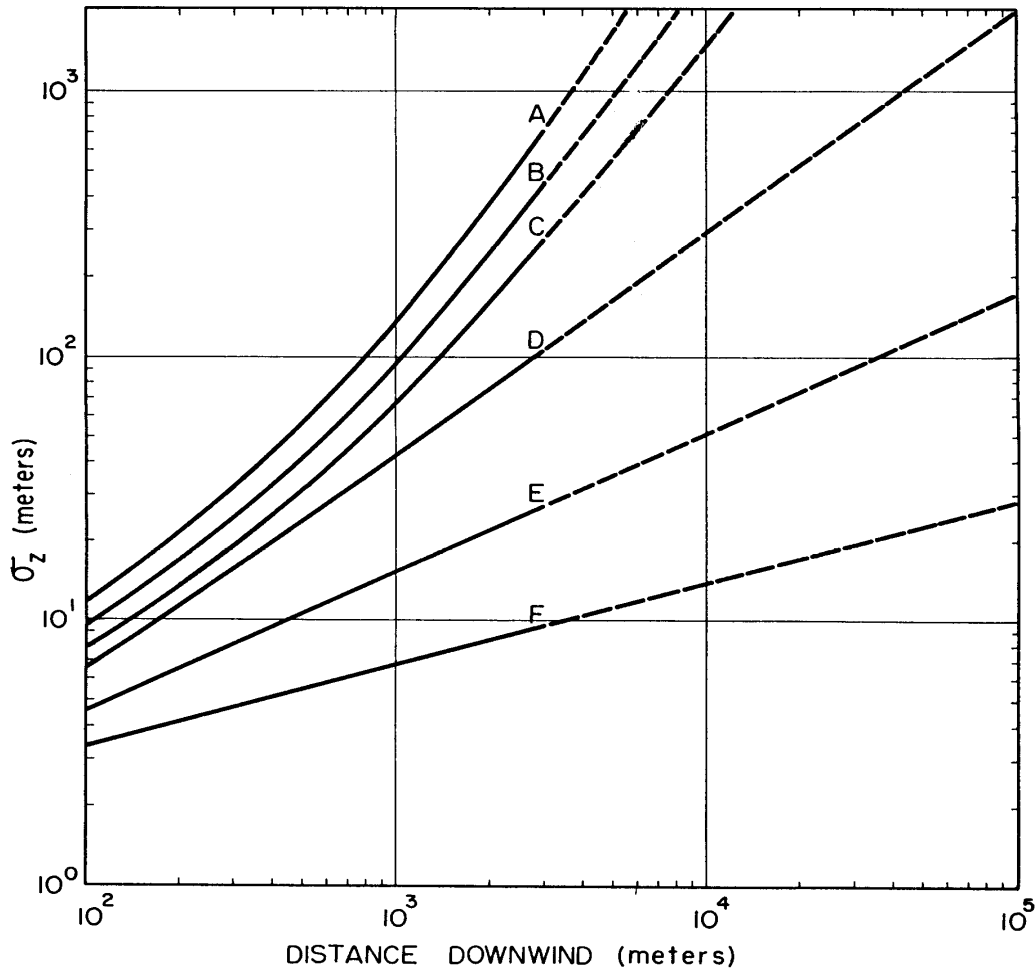


Figure 72. Plots of σ_z versus downwind distance as obtained by Markee (1963) for the five Pasquill stability classes.

1968), which are based on the A through F Pasquill stability categories mentioned previously. These curves were obtained by fitting smoothed lines to sets of data collected in tracer field studies. Markee (1963) developed a modified set of curves based partly on data collected at INL. Figure 72 shows one example of the Markee curves for the vertical-dispersion parameter σ_z . A modified version of the Markee curves is used in the MDIFF puff model (Sagendorf et al., 2001), which has been one of the primary dispersion models used at INL.

A primary advantage of the empirical diffusion curves is that they do not require specialized turbulence measurements, such as an instrument that can directly measure σ_v and σ_w . In the original description of the stability categories (Pasquill 1961), the category could be determined from routine measurements of time-of-day, wind speed, cloud cover, and a qualitative estimate of daytime solar insolation (i.e., strong, moderate, or slight). A primary disadvantage of the approach is that the curves are really only valid for the specific conditions under

which the underlying tracer data were taken. The Pasquill-Gifford curves, for example, were derived from a mix of data taken over flat and moderately rough terrain, and the data correspond to averaging times of 3-10 minutes. Differing topography, vegetation, and averaging times generally require a different set of empirically derived curves, although to some extent these variations can be accounted for by adjusting a base set of curves (Gifford, 1976).

A second way to estimate turbulence levels for dispersion applications is to make use of the models that have been developed to describe ABL structure. As noted in the section on atmospheric stability, the sensible heat flux H at the earth's surface is a primary parameter describing ABL structure. Another major parameter is the momentum flux at the earth's surface, since it represents the drag exerted by the surface and is therefore directly related to mechanical turbulence production. The momentum flux is normally represented by a variable called the friction velocity u_* , which is positive and increases as the momentum flux increases. A third parameter needed to describe the ABL is its depth h .

Based on a combination of field data and theory, researchers have developed expressions that relate turbulence levels in the ABL to H , u_* , and h . Many different formulas have been proposed (Stull, 1988) for convective, neutral, and stable boundary layers, and the details are beyond the scope of this report. As a simple example, both σ_v and σ_w are directly proportional to u_* near the surface in neutral conditions. In stable conditions, Nieuwstadt (1984) suggested the formula

$$\sigma_w = 1.4 u_* \left(1 - \frac{z}{h} \right)^{3/4} \quad (6)$$

to describe the variation of σ_w throughout the depth of the ABL. This equation produces a maximum value of σ_w at the surface, with a less-than-linear decline to zero at the top of the ABL.

These ABL models have the advantage that they are not as location-specific as the empirical diffusion curves. Differences in surface characteristics such as roughness will directly affect H , u_* , and h , so relations such as Eq. (6) are expected to be valid over a range of surface types. As one example, the semi-arid conditions at INL during the summer will normally lead to significantly larger daytime values of H compared to locations in wetter environments such as the Eastern U.S. Larger heat fluxes also tend to increase the ABL depth h , which is why the average summertime ABL depths are larger over the Western U.S. than in the eastern part of the country (Holzworth 1964). ABL models of turbulence are also useful in that numerical weather prediction models (Pielke, 2002), such as those used by the NWS for general weather forecasting, often include ABL variables such as H , u_* , and h in their standard output. This allows dispersion forecasts to be made based on the output of the weather prediction models.

A third general approach for estimating turbulence is to obtain direct turbulence measurements using specialized instruments. Until relatively recently, such instruments tended to be research-grade designs that were expensive and not well suited for extended deployments. This was particularly true of instruments capable of measuring the vertical turbulence fluctuations σ_w . More recently, three-axis sonic anemometers have fallen in price and become robust enough to be a viable option in many dispersion applications. These

instruments can directly measure the velocity standard deviations in all three directions, so that the diffusion can be directly computed either from formulas like Eq. (5) in the case of Gaussian models or like Eq. (3) in the case of Lagrangian particle models.

Although the cost of turbulence instrumentation has dropped significantly, it still has not replaced more conventional tower instruments such as cup anemometers and vanes. At INL, NOAA operates over 30 conventional towers with cups and vanes, but currently only has a single 3D sonic anemometer near the center of the site. Lack of spatial coverage is the most serious problem with using a direct-measurement approach, particularly in complex terrain. If only a single turbulence measurement site is available, there is no easy method to extrapolate these observations to other locations in complex terrain. One way to mitigate this problem is by blending the direct-measurement and ABL-modeling approaches in a way that provides a reasonable estimate of the spatial variability of the turbulence.

Processes Affecting Transport and Diffusion

The Gaussian and Lagrangian-particle models represent general approaches for describing the dispersion of effluents. Depending on the situation, a variety of specific processes can have significant effects on the dispersion. Failure to account for these processes may compromise the overall skill of a model. The most important processes are briefly described here.

Effects of Source Configuration

Various aspects of the effluent source can have major effects on the resulting concentration distribution. Often the effluent has a significant vertical exit velocity at the source, and its initial temperature may be significantly higher than the ambient temperature. Either of these events can cause the plume to rise well above its initial release location before it stabilizes. Many different formulas of different complexity have been derived to estimate plume rise (Briggs, 1984; Weil, 1988; Arya, 1999). As discussed by Arya (1999), the main variables related to plume rise are:

1. Initial vertical momentum of the effluent
2. Initial buoyancy of the effluent cloud
3. Ambient wind speed
4. Time of travel when considering transitional effects
5. Level of atmospheric turbulence

Most of the plume-rise formulas are intended for routine stack emissions, but accidental releases can also involve considerable plume rise if an explosion or fire is involved.

Another potential source effect is building wakes. An isolated building can produce complex distortions of the oncoming flow, including a horseshoe vortex extending around the building and a wake cavity on the leeward side (Hosker, 1984). Overall, the wake tends to enhance the level of mechanical turbulence for some distance downwind of the building. In many Gaussian dispersion

models, the dispersion coefficients σ_y and σ_z are enhanced at short ranges when the release is from a large building (Huber and Snyder, 1976; Scire and Schulman, 1980). The Schulman-Scire procedure also accounts for the observation that the enhanced mechanical turbulence from the building tends to reduce the total plume rise. Even when the effluent is released from a tall stack, the wake of the stack can draw the effluent down and reduce the effective release height (Briggs, 1984).

Removal Processes

An effluent can be removed from the atmosphere by several processes. One of these is the deposition of the material on the earth's surface. Material can be deposited by gravitational settling when it consists of particles that are heavy enough to have a terminal fall velocity. Smaller particles and gases can still be deposited through the interaction of the surface and the turbulent air just above it. Dry deposition is the general term used for this transfer of material. The mechanism of dry deposition is highly complex (Sehmel, 1980; Arya, 1999), involving many properties of the atmosphere, surface, and the effluent. Atmospheric turbulence has a strong influence on dry deposition, because it determines the rate at which the effluent is mixed downward to the vicinity of the surface. The friction velocity u_* therefore is one of the main atmospheric parameters that appears in deposition models.

Dry deposition is often parameterized by a deposition velocity v_d , which is related to the surface flux F (upward positive) and near-surface concentration χ of an effluent by

$$v_d = \frac{F}{\chi} \quad (7)$$

If χ has units of, say, g m^{-3} , then F has units of $\text{g m}^{-2} \text{s}^{-1}$ and thus represents a mass per unit area per unit time. Although some aspects of v_d can be modeled through ABL theory, there is still much empiricism related to its estimation. For example, some gases are taken up by the stomata of plant leaves, so v_d is dependent on plant physiology in these cases.

Dispersion models can treat deposition in a couple of different ways (Arya, 1999). Source-depletion models account for deposition by reducing the effective amount of material released at the source. In the Gaussian plume of Eq. (1), this means reducing q to account for the material lost to deposition. This is clearly somewhat unrealistic, since it assumes that material is lost equally throughout the depth of the effluent cloud. Surface-depletion models are more realistic in that the deposited material is assumed to come largely from the lower part of the cloud near the surface. Lagrangian particle models can account for deposition either by reducing the mass of individual particles when they get near the surface or by assigning a probability that particles near the surface will be totally removed from the atmosphere.

Precipitation scavenging is another process that can remove effluent from the atmosphere (Slade, 1968; Chate et al., 2003). Usually, a distinction is made between in-cloud scavenging, called rainout, and below-cloud scavenging, called washout. In either case, the common approach to account for

scavenging in dispersion models is to assume an exponential decay of the concentration χ over a time step δt :

$$\chi(t + \delta t) = \chi(t) \exp(-\Lambda \delta t) \quad (8)$$

Λ is a scavenging coefficient that depends on precipitation rate and type and on the chemical composition of the effluent. Unlike dry deposition, it is realistic to remove material throughout the depth of the effluent cloud when considering precipitation scavenging.

Both dry deposition and precipitation scavenging remove material from the atmosphere, but this does not eliminate the deposited material from consideration. For toxic chemicals, the deposited material can contaminate water supplies or get into the food chain. Radionuclides will continue to emit radiation after being deposited, and this groundshine can be a significant component of the total dose to exposed individuals. In windy conditions, deposited material can be resuspended, which creates a potential area source of effluent that must be considered in modeling the atmospheric dispersion.

The total atmospheric mass of an effluent can also be changed by transformations. Chemical reactions can either increase or decrease the concentration of a particular species. Such reactions are important for many of the pollutants found in urban areas, including ozone, sulfur dioxide, and nitrogen oxides. Dispersion models that are designed for air quality applications must account for these reactions. With radionuclides, transformation by radioactive decay is an important issue. The radioactive decay removes some of the initial effluent, but it creates daughter products that may have to be

tracked. It is treated in dispersion models using an exponential decay similar to Eq. (8), with the coefficient in this case being directly proportional to the half-life of the radionuclide.

Climatological Dispersion Patterns

Eckman (2003) conducted a study of dispersion climatology at INL using nine years of data from the NOAA INL Mesonet. The study was based on the MDIFF puff model (Sagendorf et al., 2001), which at the time was ARLFRD's main model for supporting INL operations. Some of the results from that study are reproduced here, because they are instructive in understanding the general characteristics of dispersion at INL. Because much of the focus at INL is on accidental releases of radioactive materials, the study focused on the total integrated concentration (TIC), which is the time integral of the concentration χ at a fixed location:

$$\text{TIC} = \int \chi dt \quad (9)$$

The integral extends over the duration of the model run. For radionuclides, the TIC is more useful than χ because it is more directly related to the radiological dose.

Figure 73 shows contours of TIC for surface releases at four of the INL facilities: INTEC, RWMC, SMC, and RTC. These plots were obtained by starting a new MDIFF run every hour during the period from April 1993 to December 2001, with a release duration of 2.5 hours for RTC and 1 hour for the other facilities. Over 76,000 individual MDIFF runs were therefore performed for each facility. The contours in Fig. 73 represent the 95th percentile values obtained from these sets of runs, which Eckman (2003) took as representative of worst-case dispersion

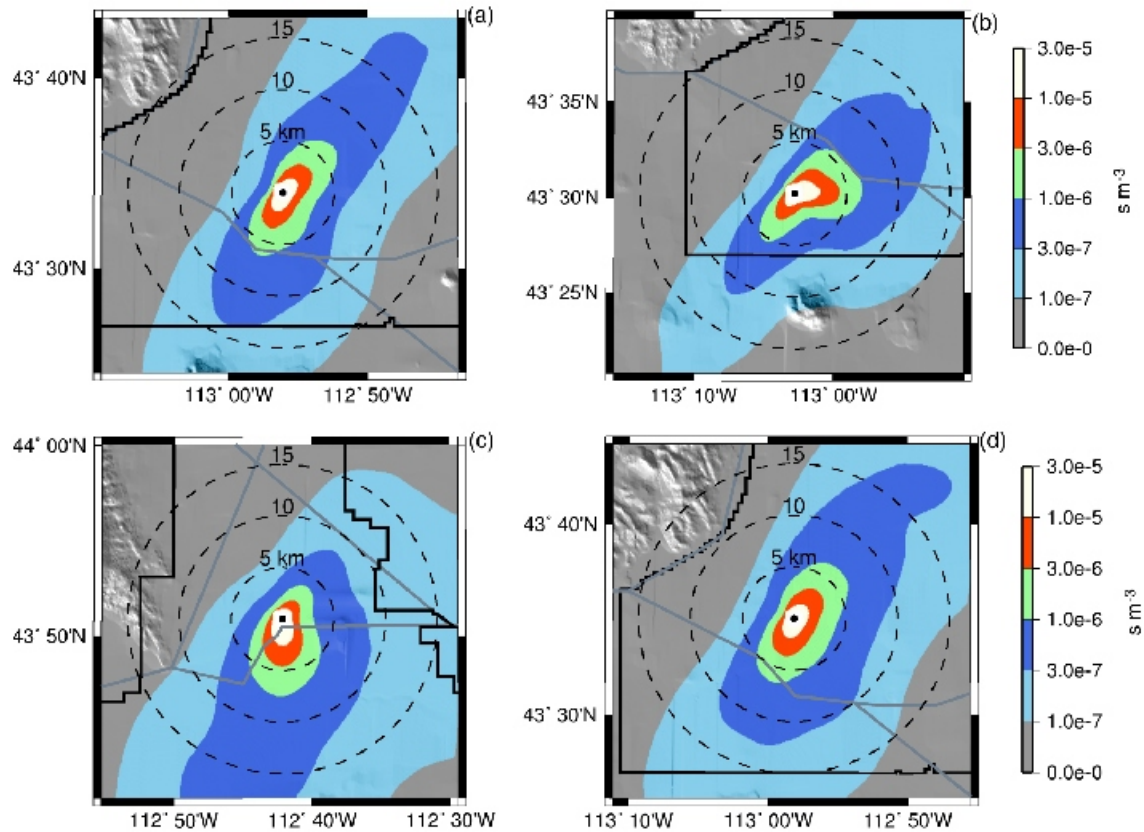


Figure 73. Contours of the 95th percentile TIC derived from hourly MDIFF model runs spanning the period from April 1993 to December 2001. The TIC values are normalized by the total mass Q of material released. The release points are (a) INTEC, (b) RWMC, (c) SMC, and (d) RTC.

conditions. Each TIC value was normalized by the total quantity Q of material released, so the contours have normalized units of $s\ m^{-3}$.

For both INTEC and RTC, the contours are generally elongated along a southwest to northeast axis, reflecting the channeling of the wind by the orientation of the Snake River Plain. The inner contours are to an approximation symmetric about the INTEC and RTC release points, indicating that the peak TIC values observed for up-valley (southwest) and down-valley (northeast) winds are similar in magnitude. Given the overall shape of the contours, it

appears that straight-line pollutant transport may be a reasonable assumption out to 5-10 km from these two sources. A simple Gaussian plume model may therefore be appropriate out to such distances, at least when considering average dispersion over long time periods. Of course, the contours in the figure are based on statistics from a large number of runs. Additional complications arise when attempting to model a specific event (e.g., a real accident), such as wind reversals and recirculations. Such effects cannot be represented in a straight-line plume model.

RWMC is further south and west compared to the other facilities, and this has a significant effect on the 95th percentile TIC contours in Fig. 73. The contours to the south of the facility are similar in shape to those at INTEC and RTC, indicating that there is often a regional northeasterly wind that affects all three facilities in similar ways. However, RWMC also shows high TIC values extending to the east of the release point. The most likely explanation for this is associated with RWMC lying closer to the Big Lost River Valley that exits into the Snake River Plain at Arco. In fact, the bed of the Big Lost River passes near RWMC. It is reasonable to conclude that RWMC sometimes sees westerly drainage winds exiting out of the Big Lost River Valley.

SMC also has an unusual pattern in Fig. 73, with most of the high TIC values extending to the south of the facility. This site is affected both by regional downvalley winds within the Snake River Plain and more local drainage winds coming out of the Birch Creek Valley just to the northwest of SMC. These

northerly flows appear to dominate the 95th percentile TIC values for SMC.

Figure 73 was based on higher resolution concentration grids that extended out to only 15-20 km from the release points. Eckman (2003) also performed MDIFF runs using a larger grid extending about 60 km from the release point. Figure 74 shows the 95th percentile TIC values for INTEC and RTC using this larger grid. The general southwest-to-northeast channeling of the dispersion is still evident at the larger scales. However, the contours have various bends in them that indicate the effects of the nearby topography on changing the direction of pollutant transport. Using a straight-line plume model based on a wind rose at the release point clearly can lead to transport errors at these larger scales. One caution with this figure is that the outermost contours may be affected by model algorithms. The version of MDIFF used for the study dropped puffs that were more than 20 km from any mesonet tower, so areas with poor tower coverage are artificially forced to have low TIC values.

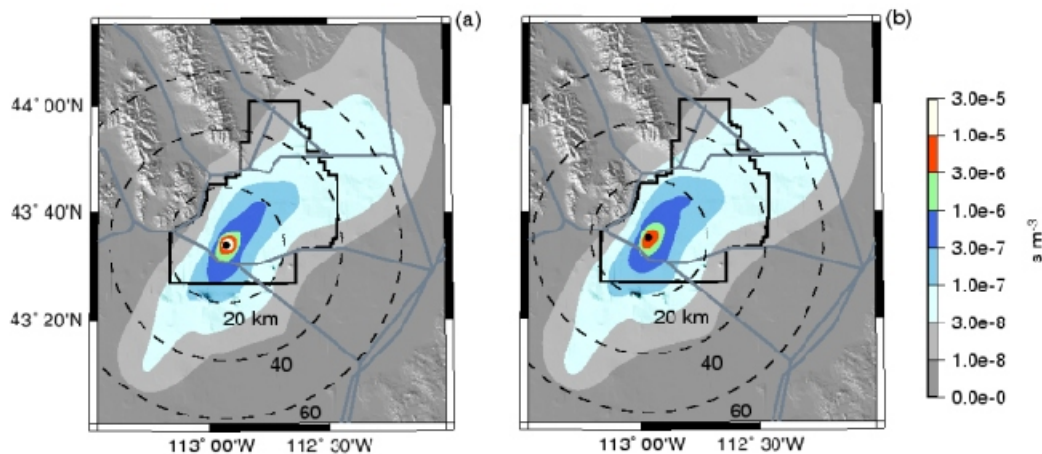


Figure 74. Contours of the 95th percentile TIC for (a) INTEC and (b) RTC using a larger model domain extending to about 60 km from the release points. As in Fig. 73, the TIC values are normalized by the total mass Q of material released.

ACKNOWLEDGMENTS

Funding for this project was provided by the U. S. Department of Energy, Idaho Operations Office.

In presenting this latest INL climatography, the current editors pay tribute to the talent and efforts of the authors and data analysts who developed the initial climatologies for INL, including G. A. DeMarrais, G. R. Yanskey, E. H. Markee, Jr., and A P. Richter. The legacy work of these individuals continues to be seen in many of the data summary tables and in the "Markee" atmospheric dispersion curves, based on INL field experiments, that continue to be utilized.

The current editors also acknowledge the historical leadership of C. R. Dickson, G. E. Start, and F.E. White, who oversaw implementation of the telemetered "mesonet" of meteorological towers, installation of the RASS, and development of the 2nd Edition

INL Climatography (Clawson et al., 1989). J. F. Sagendorf and G. R. Ackermann played key roles in data analyses and acquisition programming, respectively.

This latest edition of the "Climatography of the Idaho National Laboratory" is the culmination of the efforts of various personnel, both past and present, employed by the Field Research Division of the Air Resources Laboratory (ARLFRD), and the efforts of others funded by special supporting contracts. Most currently, the contributions of the present staff of the ARLFRD are gratefully acknowledged. N. F. Hukari, provided the data acquisition, statistical programming systems, and data processing for the statistical data found in the tables. R.M. Eckman summarized the "state-of-the-science" of atmospheric transport and dispersion at INL contained in this volume.

This page intentionally left blank.

REFERENCES

- Arya, S. P., 1999: *Air Pollution Meteorology and Dispersion*. Oxford University Press, 310 pp.
- Briggs, G. A., 1984: Plume rise and buoyancy effects. In *Atmospheric Science and Power Production*, D. Randerson, ed., U. S. Dept. of Energy, Oak Ridge, TN, 327-366.
- Carter, R. G., N. Hukari, and J.D. Rich, 2008: Identifying Natural Clusters in Eastern Idaho Wind Fields. *unpublished manuscript.*, NOAA Air Resources Laboratory Field Research Division, Idaho Falls, ID March 28, 2000.
- Chate, D. M., P. S. P. Rao, M. S. Naik, G. A. Momin, P. D. Safai, and K. Ali, 2003: Scavenging of aerosols and their chemical species by rain. *Atmos. Environ.*, **37**, 2477-2484.
- Clawson, K. L., G. E. Start, and N. R. Ricks, 1989: Climatography of the Idaho National Engineering Laboratory, 2nd Edition, Report DOE/ID-12118, U. S. Department of Energy, Idaho Operations Office, Idaho Falls, ID, 155pp.
- Coats, D. W. and R. C. Murray, 1985: Natural Phenomena Hazards Modeling Project: Extreme wind / tornado models for Department of Energy Sites., UCRL-53526, Rev 1, Lawrence Livermore National Laboratory, Livermore, CA.
- DeMarrais, G. A. 1958a: The climatography of the National Reactor Testing Station. U.S. AEC Rep. IDO-12003. U.S. Dept. of Comm., U.S. Weath. Bur., Idaho Falls, ID.
- DeMarrais, G. A. 1958b: The engineering climatography of the National Reactor Testing Station. U.S. AEC Rep. IDO-12004. U.S. Dept. of Comm., U.S. Weath. Bur., Idaho Falls, ID.
- DeMarrais, G. A., and N. F. Islitzer 1960. Diffusion climatography of the National Reactor Testing Station. U.S. AEC Rep. IDO-12015. U.S. Dept. of Comm., U.S. Weath. Bur., Idaho Falls, ID.
- Draxler, R. R. and G. D. Hess, 1997: Description of the HYSPLIT_4 modeling system. NOAA Technical Memorandum ERL ARL-224, NOAA Air Resources Laboratory, Silver Spring, Maryland, 25 pp.
- Eckman, R. M., 1998: Observations and numerical simulations of winds within a broad forested valley. *J. Appl. Meteor.*, **37**, 206-219.

- Eckman, R. M., 2003: A statistical investigation of atmospheric dispersion at the Idaho National Engineering and Environmental Laboratory (INEEL). NOAA Technical Memorandum OAR ARL-246, NOAA Air Resources Laboratory, Silver Spring, Maryland, 37 pp.
- Egger, J., 1990: Thermally forced flows: Theory. In *Atmospheric Processes over Complex Terrain*, W. Blumen, ed., American Meteorological Society, Boston, MA, 43-58.
- Garratt, J. R., 1992: *The Atmospheric Boundary Layer*. Cambridge University Press, 316 pp.
- Gifford, F. A., 1961: Use of routine meteorological observations for estimating atmospheric dispersion. *Nucl. Saf.*, **2**, 47-51.
- Gifford, F. A., 1976: Turbulent diffusion typing schemes: A review. *Nucl. Saf.*, **17**, 68-85.
- Gross, G. and F. Wippermann, 1987: Channeling and countercurrents in the Upper Rhine Valley: Numerical simulations. *J. Climate Appl. Meteor.*, **26**, 1293-1304.
- Hershfield, D. M., 1961: *Rainfall Frequency Atlas of the United States*. U.S. Weather Bureau Technical Paper 40, U.S. Department of Commerce, Washington, D. C.
- Holzworth, G. C., 1964: Estimates of mean maximum mixing depths in the Contiguous United States. *Mon. Wea. Rev.*, **92**, 235-242.
- Hosker, R. P., 1984: Flow and diffusion near obstacles. In *Atmospheric Science and Power Production*, D. Randerson, ed., U. S. Dept. of Energy, Oak Ridge, TN, 241-287.
- Huber, A. H. and W. H. Snyder, 1976: Building wake effects on short stack effluent. Preprints, *Third Symposium on Atmospheric Diffusion and Air Quality*, Raleigh, NC, Amer. Meteor. Soc., 235-242.
- Humphrey, P. A., E. M. Wilkins, and D. M. Morgan, 1953: *Atmospheric Dust at the National Reactor Testing Station, Final Report*, U. S. Department of Commerce Weather Bureau Office, Idaho Falls, ID.
- Johnson, O. J., and C. R. Dickson, 1962. An eight year summary of the temperature gradient below 250-feet at the National Reactor Testing Station. U. S. AEC Rep. IDO-12025. U. S. Dept. of Comm., U. S. Weath. Bur., Idaho Falls, ID.
- Kossmann, M., C. D. Whiteman, and X. Bian, 2002: Dynamic airflow channeling over the Snake River Plain, Idaho. In Preprints, 10th Conference on Mountain Meteorology , American Meteorological Society, 17-21 June 2002, Park City, Utah, Paper P3.14.

- Luhar, A. K. and R. E. Britter, 1989: A random-walk model for dispersion in inhomogeneous turbulence in a convective boundary layer. *Atmos. Environ.*, **23**, 1911-1924.
- Markee, E. H. Jr., 1963: Methods of estimating air pollutant dispersion over relatively smooth terrain from routine meteorological observations, Tech rep presentation, 219th Nat. Mtg. Of the American Meteorological Society, 20 Jun 1963, Palo Alto, CA.
- Nace, R. L., P. T. Voegeli, J. R. Jones, and M. Deutsch, 1975. Generalized geologic framework of the National Reactor Testing Station, Idaho. USGS Prof. Paper 725-B. U.S. Gov. Print. Off., Washington, DC.
- Nieuwstadt, F. T. M., 1984: The turbulent structure of the stable, nocturnal boundary layer. *J. Atmos. Sci.*, **41**, 2202-2216.
- Pasquill, F., 1961: The estimation of the dispersion of windborne material. *Meteor. Mag.*, **90**, 33-49.
- Pielke, R. A., Sr., 2002: *Mesoscale Meteorological Modeling*. Academic Press, San Diego, CA, second edition.
- Sagendorf, J. F., 1996: *Precipitation Frequency and Intensity at the Idaho National Engineering Laboratory*, NOAA Technical Memorandum ERL ARL-238, Silver Spring, MD, 23 pp.
- Sagendorf, J. F., R. G. Carter, and K. L. Clawson, 2001. *MDIFF Transport and Diffusion Models*, NOAA Technical Memorandum ERL ARL-215, Silver Spring, MD, 26 pp.
- Scire, J. S. and L. L. Schulman, 1980: Modeling plume rise from low-level buoyant line and point sources. Proceedings, *Second Point Conference on Applications of Air Pollution Meteorology*, New Orleans, LA, Amer. Meteor. Soc., 133-139.
- Sehmel, G. A., 1980: Particle and gas dry deposition: A review. *Atmos. Environ.*, **14**, 983-1011.
- Slade, D. H., (Ed.) , 1968: *Meteorology and Atomic Energy*. U. S. Atomic Energy Commission, Office of Information Services, available as TID-24190 from National Technical Information Service, 445 pp.
- Stewart, J. Q., C. D. Whiteman, W. J. Steenburgh, and X. Bian, 2002: A climatological study of thermally driven wind systems of the U. S. Intermountain West. *Bull. Amer. Meteor. Soc.*, **83**, 699-708.
- Stull, R. B., 1988: *An Introduction to Boundary Layer Meteorology*. Kluwer Academic Publishers, 666 pp.

- Taylor, G. I., 1921: Diffusion by continuous movements. *Proc. London Math. Soc. (2)*, **20**, 196-212.
- U. S. Department of Energy (DOE), 2003: Idaho National Engineering and Environmental Laboratory Final Wildland Fire Management, Environmental Assessment, DOE/EA-1372, April, 2003. U.S. Department of Energy, Idaho Falls, ID.
- VAISALA, 2005. Project 202324 Lightning Stroke FSA Report, © 2005 VAISALA, Inc., Tucson, AZ, 7 April, 2005.
- Wallace, J. M. and P. V. Hobbs, 1977: *Atmospheric Science, An Introductory Survey*. Academic Press, 467 pp.
- Weber, B. L., and D. B. Wuertz, 1991: Quality control algorithm for profiler measurements of winds and temperatures. NOAA Technical Memorandum ERL WPL-212, Boulder, CO, 32 pp.
- Weber, B. L., D. B. Wuertz, D. C. Welsh, and R. McPeck, 1993: Quality controls for profiler measurements of winds and RASS temperatures. *J. Atmos. Oceanic Technol.*, **10**, 452-464.
- Weil, J. C., 1988: Plume rise. In *Lectures on Air Pollution Modeling*, A. Venkatram and J. C. Wyngaard, eds., American Meteorological Society, Boston, MA, 119-166.
- Whiteman, C. D., 1990: Observations of thermally developed wind systems in mountainous terrain. In *Atmospheric Processes over Complex Terrain*, W. Blumen, ed., American Meteorological Society, Boston, MA, 5-42.
- Whiteman, C. D. and J. C. Doran, 1993: The relationship between overlying synoptic-scale flows and winds within a valley. *J. Appl. Meteor.*, **32**, 1669-1682.
- Wilson, J. D. and B. L. Sawford, 1996: A review of Lagrangian stochastic models for trajectories in the turbulent atmosphere. *Bound.-Layer Meteor.*, **78**, 191-210.
- Wilson, J. D., B. J. Legg, and D. J. Thompson, 1983: Calculation of particle trajectories in the presence of a gradient in turbulent velocity variance. *Bound.-Layer Meteor.*, **27**, 163-169.
- Wippermann, F., 1984: Air flow over and in broad valleys: Channeling and countercurrent. *Beitr. Phys. Atmos.*, **57**, 92-105.
- Yanskey, G. R., E. H. Markee, Jr., and L.P. Richter, 1966: Climatography of the National Reactor Testing Station. USAEC Rep. IDO-12048. U.S. Dept. Of Comm., Environ. Sci. Serv. Admin., Inst. for Atmos. Sci., Air Resour. Field Res. Off., Idaho Falls, ID.

APPENDIX A

SURFACE AIR TEMPERATURE EXTREMES

The following are the daily extreme surface air temperature records and corresponding year(s) observed at CFA from January 1950 through December 2005. The data include the highest and lowest maximum and the highest and lowest minimum air temperatures.

Table A-1. CFA daily surface air temperature extremes for January.

January								
Day	Highest Maximum (° F)	Year of Highest Maximum	Lowest Maximum (° F)	Year of Lowest Maximum	Lowest Minimum (° F)	Year of Lowest Minimum	Highest Minimum (° F)	Year of Highest Minimum
1	50	1981	0	1979	-28	1979	38	1997
2	48	1997	6	1979	-29	1974 1978	36	1997
3	42	1998	6	1993	-23	1952	28	1998
4	46	1963	0	1972	-32	1973	28	1994
5	43	1954 1965	0	1971	-28	1971	32	1956
6	44	1966	3	1971	-30	1979	33	1983
7	46	1956	5	1982	-33	1979	34	1983
8	46	1961	3	1989	-26	1979	32	1990
9	50	1990	6	1977	-28	1974	32	1953
10	50	1990	11	1962	-22	1977	35	1990
11	44	1981	-3	1963	-30	1977	30	1995 2000
12	47	1953	-2	1963	-35	1963	32	1953
13	48	1981	1	1963	-22	1963	34	1969 1980
14	42	1995	6	1972	-19	1972	33	1980
15	44	2000	9	1984	-23	1964	35	1974
16	51	1974	10	1960	-22	1957	36	1974
17	42	1961 1974 1981 1998	3	1984	-27	1960	35	1971
18	47	1981	-6	1984	-34	1984	33	1953
19	44	1997	2	1984	-32	1960	31	1953 1972
20	48	1981	0	1984	-31	1984	34	1969
21	42	1953 1981	6	1962	-40	1962	32	1969
22	49	1981	7	1962	-38	1962	31	1950 1970
23	45	1970	2	1962	-37	1962	32	1970
24	48	1992	13	1957 1962	-22	1964	31	1959
25	49	1953	9	1989	-20	1989	28	1953 2000
26	46	1987	10	1980	-28	1957	31	1995
27	45	2003	12	1979	-28	1957	31	2003
28	44	1988	2	1951	-29	1957	30	1954
29	45	1953	5	2002	-26	1951 1979	34	1954
30	50	2003	3	1979	-28	1957	32	2003
31	55	2003	-1	1985	-35	1985	31	1986 2003

Table A-2. CFA daily surface air temperature extremes for February.

FEBRUARY								
Day	Highest Maximum (° F)	Year of Highest Maximum	Lowest Maximum (° F)	Year of Lowest Maximum	Lowest Minimum (° F)	Year of Lowest Minimum	Highest Minimum (° F)	Year of Highest Minimum
1	53	2003	-9	1985	-36	1985	33	2003
2	44	1987 1995	3	1989	-29	1956	31	1987
3	53	1953	2	1989	-31	1996	37	1963
4	45	1954	3	1985	-34	1985	31	1963
5	57	1963	1	1982	-32	1982	30	1963
6	57	1963	5	1982	-29	1982	31	1978
7	54	1963	8	1989	-27	1989	34	1996
8	53	1963	11	1989	-24	1989	28	1953 1961 1995
9	50	1970	12	1982	-21	1989	35	1976
10	48	1970 1987	8	1982	-25	1981	34	1961
11	53	1961	14	1984	-24	1982	32	1962
12	52	1987	12	2004	-17	2004	33	1954
13	48	1967 1991 1996	15	2004	-16	2004	34	1979
14	47	1987	13	1952	-16	1964	33	1979
15	49	1961	14	2002	-16	1989	33	1982
16	50	1970	4	1956	-24	1993	34	1991
17	48	1977	10	1993	-27	1993	33	1986
18	47	1977 1996	15	1952	-22	1990	35	1980
19	56	1981	20	1978	-17	1955 1990	34	1980
20	56	1991	11	1984	-21	1975	38	1992
21	53	1982	18	1952	-15	1952 1971 1973	32	1992
22	58	1991	11	1952	-17	1952 1975	30	1982 1986 1992 2000
23	49	1954 1958 1991	18	1984	-13	1955 1960	34	1986
24	57	1995	12	1960	-15	1952	32	1957 1958
25	55	1995	13	1952	-20	1952	30	1957
26	56	1992	9	2002	-21	2002	33	1983
27	59	1992	11	1960 1962 1993	-25	1960	35	1976
28	60	1992	20	1960	-22	1993	35	1972
29	57	1988	9	1960	-31	1960	27	1976 1980

Table A-3. CFA daily surface air temperature extremes for March.

MARCH								
Day	Highest Maximum (° F)	Year of Highest Maximum	Lowest Maximum (° F)	Year of Lowest Maximum	Lowest Minimum (° F)	Year of Lowest Minimum	Highest Minimum (° F)	Year of Highest Minimum
1	59	1986 1992	14	1993	-28	1960	35	1974
2	61	1986	19	1993	-14	1960	37	1983
3	63	1986	11	2002	-18	2002	38	1992
4	58	1968	15	1985	-14	1985	35	1991
5	59	1986	16	1955	-15	1955	32	1990
6	58	1986	22	1952 1955	-10	1955	39	1987
7	55	1954 1970	21	1985	-6	1955	36	1987
8	56	1957	25	2002	-11	1964	34	1986 1987
9	65	1972	22	1969 2002	-13	1969	36	1954
10	62	1972	23	1969	-7	1969	41	1995
11	62	1992	24	1950	-14	1969	36	1982 1995
12	65	1992	20	1993	-9	1962 1969	34	2003
13	70	2003	25	1952	-10	1969	35	1983
14	68	1994	19	1952	-12	1952	34	1984
15	72	1994	26	2002	-5	1952 1962 1985	32	1982
16	63	1994	29	2002	-3	1962	31	1981 1993
17	66	1972	22	1965	-1	1971	33	1974 1992
18	63	2004	21	1965	-7	1971	33	1990 2003
19	67	1997	25	1952	-1	1971	36	2004
20	64	1997 2004	24	1955	-13	1955	36	2001
21	67	2004	29	1985	2	1952 1955	36	1997
22	69	1972	26	1952	-8	1952	35	1998
23	70	2004	29	1964	3	1964	38	1998
24	66	2004	23	1965	2	1964	38	1998
25	63	1966 1999	29	1955	3	1965	38	1998
26	66	1966	28	1975	4	1955	34	1971 1974 1989 1998
27	69	1986	21	1975	8	1955	38	1990
28	73	1986	24	1975	2	1985	37	1968
29	70	1978 1986	31	1977	-3	1985	38	1986
30	71	2004	32	1980	6	1985	34	1978 1983
31	70	1966	31	1975	6	1954	38	1966 1978

Table A-4. CFA daily surface air temperature extremes for April.

APRIL

Day	Highest Maximum (° F)	Year of Highest Maximum	Lowest Maximum (° F)	Year of Lowest Maximum	Lowest Minimum (° F)	Year of Lowest Minimum	Highest Minimum (° F)	Year of Highest Minimum
1	72	1966	34	1975	7	1952 1997	38	1978 2003
2	75	1990	36	1982	6	1953	41	2004
3	75	1992	33	1955	9	1953	37	1988 1994
4	72	1960 1987 1990 2000	35	1958	13	1966	37	1992
5	75	1960	34	1997	9	1961	45	1991
6	73	1960	38	1957	9	1983	41	1995
7	75	1989	36	1953	9	1992	43	2004
8	78	1977	35	1975	7	1982	42	2004
9	79	1996	36	1999	8	1959	41	1992
10	73	2003	38	1999	9	1988	41	1992
11	72	1988	37	1970	10	1953	43	1978
12	77	1988	39	1974	6	1997	39	2000
13	74	1951 1988	40	1970	13	1997	43	1954
14	78	1990	41	1970	14	1981 1983	44	2002
15	79	1990	34	1967	15	1953 1977 2005	45	1989
16	76	1987 1994	41	1978	11	1982 1995	45	1987
17	81	1994	43	1968	12	1963	44	1988
18	79	1994	38	1966	12	1968	43	1985
19	82	1962	35	1970	15	1982	46	1981
20	81	1994	35	1970	11	1982	44	1965
21	79	1994	34	1963	9	1982	44	1965 1989
22	79	1969	39	1958	16	1968	48	1980
23	78	1977	37	1964	12	1972	44	1969 1980
24	81	1977	39	1964	13	1992 2002	45	1980
25	82	1977	35	1984	14	1950	49	1959
26	82	1987 1992	34	1976	17	1972 1988	45	1952
27	82	1987	41	1963	19	1966	44	1954
28	79	1987 1992	39	1970	15	1966 1984	44	2000
29	86	1992	36	1967	18	1994	46	1987
30	78	1977	33	1967	16	1950	49	1992

Table A-5. CFA daily surface air temperature extremes for May.

MAY								
Day	Highest Maximum (° F)	Year of Highest Maximum	Lowest Maximum (° F)	Year of Lowest Maximum	Lowest Minimum (° F)	Year of Lowest Minimum	Highest Minimum (° F)	Year of Highest Minimum
1	82	1985	43	1995	13	1972	45	1980
2	83	1985	42	1964	16	1973	45	1982
3	84	1966	42	1964	19	1965	48	1971
4	84	1966	36	1975	17	2001	48	1962
5	85	1992	45	1975	14	1982	49	1979
6	89	1992	35	1965	18	1968	48	2004
7	87	1992	45	1979 2000	19	1984	52	1989
8	85	1987	42	1979	16	2002	47	1989
9	84	1954	42	1983	14	2002	49	1962
10	84	1960	45	1970 1991	19	1953	49	1954
11	87	1960	42	1983	18	1999	49	1994
12	87	2001	45	1989	22	1992	51	1996
13	82	1959 1996	47	1995	17	1985	54	1987
14	85	1987	48	1955	21	1970	52	1984
15	86	1987	39	1955	22	1986	49	2001
16	87	1988	43	1955	16	1974	51	1987
17	85	1992	49	1977	24	1984	49	1972
18	86	1954	48	1978	23	1971	50	2001
19	91	1954	47	1959	24	1950 1960	52	1956
20	89	1958	46	1974	18	2003	57	1954
21	86	1958	43	1972	20	2001	54	1958
22	87	1967	50	1986	22	1953	51	2000
23	87	1988	49	1980	17	1966	50	1990
24	88	1992 2001 2003	48	1980	25	1989	53	1979
25	89	2001	42	1980	23	1975	54	1958
26	88	1958	54	1980	20	1978	52	1992
27	88	1958	53	1959	21	1973	53	1974
28	95	2003	48	1982	23	1955 1977	52	1990
29	96	2003	50	1953	28	1977	52	1961 1983 2005
30	92	2003	44	1988	25	1974 1977	59	2003
31	90	1986	52	1955 1990	23	1978	52	2003

Table A-6. CFA daily surface air temperature extremes for June.

JUNE								
Day	Highest Maximum (° F)	Year of Highest Maximum	Lowest Maximum (° F)	Year of Lowest Maximum	Lowest Minimum (° F)	Year of Lowest Minimum	Highest Minimum (° F)	Year of Highest Minimum
1	89	1977 1986 2001	53	1971	27	1984	53	2002
2	89	1986	50	1950 1953	26	1954	51	1960 2001
3	89	1988	50	1989	27	1950	58	1986
4	92	1988	50	1980	30	1955	53	1997
5	93	1977	51	1954 1991	26	1998	56	1957 1985
6	93	1977	45	1995	28	1962	57	1977
7	92	1985	44	1950	27	1951 1962	59	1977
8	92	1996	51	1995	23	1979	59	1996
9	91	1952	54	2002	24	1999	56	1977
10	91	1956	47	1984	30	1999 2002 2005	55	1990
11	89	1979	56	1976	29	2002	54	1961 1962 1992
12	94	1959	51	1970	30	1984	54	1955 1961
13	93	1974	50	1976	29	1966 1993	60	1959
14	96	1974	56	1973	25	1976	58	1959
15	97	1974	56	1957	29	1981	59	1987
16	95	1974	55	1998	32	1952	58	1951 1974
17	95	1974	53	1964 1973	27	1994	56	2002
18	96	1974	51	1975	27	1973	53	1997 2003
19	97	1988	58	1964	29	1954 1973	60	1991
20	95	1961 1994	62	1989	28	1978	66	1988
21	98	1988	54	1964	26	1989	62	1994
22	97	1961 2001	62	1963 1989	30	1956	62	1971
23	97	1988 1992	61	1993	33	1951 1996	69	1988
24	100	1988	51	1952	29	1997	65	2001
25	100	1988	55	1969	24	1966	63	1988
26	97	1990 2002	59	1965	30	1999	60	1988
27	96	2002	58	1969	28	1976	63	1961
28	94	1966 1979	62	1969	35	1975 1976 1998	60	1988
29	98	1990	54	1959	32	1969 1971	59	2002
30	97	1990	65	1970	29	1955	56	1976 1980

Table A-7. CFA daily surface air temperature extremes for July.

JULY

Day	Highest Maximum (° F)	Year of Highest Maximum	Lowest Maximum (° F)	Year of Lowest Maximum	Lowest Minimum (° F)	Year of Lowest Minimum	Highest Minimum (° F)	Year of Highest Minimum
1	97	1990 2001	63	1955	33	1984	60	1981
2	98	2001	69	1983	32	1973	59	1977
3	100	2001	67	1993	31	1997	62	2002
4	99	1985	57	1982	33	1994	59	2001
5	98	1985	65	1982	33	1999	61	1954 2001
6	98	1976 1985	68	1994	28	1986	66	1981
7	99	1989	68	1981	33	1988	71	1985
8	96	1975 2005	74	1959 1993	29	1981	60	1975 1976 1985
9	99	1985	78	1982	33	1993	60	1960 1989 1996
10	100	2002	61	1951	37	1999	61	1956
11	102	2002	64	1983	37	1983	65	1985
12	103	2002	60	1997	36	1951	61	1962 1988
13	105	2002	63	1962	32	1993	63	1964
14	102	2002	73	1962	35	1993	62	1991
15	100	2005	74	1993	40	1970 1981 1984	66	1953
16	99	1998 2003	65	1983	34	1983	65	1987
17	101	1998	66	1987	36	1993	71	1976
18	100	1998 2003	63	1987	29	1993	62	1977
19	100	1960	73	1987	35	1987	66	1951
20	102	2003	57	1972	36	1952 1996	60	2004
21	102	2003	64	1987	34	1983	63	1956 1966
22	102	2003	64	1973 1993	39	1952	70	2005
23	102	2003	56	1993	33	1954	66	1982
24	99	1978 1988	67	1977	35	1970	64	1959
25	99	1978 1988	73	1965	41	1995	66	2003
26	96	1959 1960 1989 1994	71	1993	40	1953 1997 1999	61	1954
27	98	1975	77	1962	38	1993	65	1998
28	98	2000	75	1978	39	1963 1967	67	1960
29	99	2000	71	1950	37	1959	65	1975
30	100	2000	61	1975	35	1950	65	1960
31	102	2000	71	1975	35	1995	61	1959 1966 2002

Table A-8. CFA daily surface air temperature extremes for August.

AUGUST									
Day	Highest Maximum (° F)	Year of Highest Maximum	Lowest Maximum (° F)	Year of Lowest Maximum	Lowest Minimum (° F)	Year of Lowest Minimum	Highest Minimum (° F)	Year of Highest Minimum	
1	102	2000	74	1975	36	1995 2001	62	1951	
2	101	1992	67	1953	36	1963	65	1974	
3	97	1961	66	1976	40	1970 1981	62	1980	
4	98	1961 1979 1994	73	1951 1996	36	1996	60	1951	
5	97	1994	66	1950	35	1980	63	1964	
6	99	2001	72	1950	38	1950 1962	64	1961 1971	
7	100	1990	73	1979	35	1996	62	1979	
8	101	1990	70	1995	39	1956 1967	67	1983	
9	98	1972	73	1968 1974	35	1970 1985 2002	60	1963 1983 2000 2001	
10	99	1969	74	1997	38	2002	64	1954	
11	99	1996	64	1985	38	1970 1980	65	1969	
12	99	1992	69	1988	38	1985	60	1963	
13	99	1992	70	1978	39	1957 1969 1982 2000	63	2001	
14	101	2003	62	1968	38	1959 1978 1993	64	1991	
15	98	2003	62	1968	32	1978	67	2003	
16	96	1958	55	1978	36	1968 1987	62	2004	
17	95	1981 1982	55	1968	32	1987	67	1958	
18	98	1986	54	1968	28	1978	61	1977	
19	96	1961 1992	53	1968	31	1995	64	1999	
20	95	1982 2003	54	1968	33	1964	62	1961	
21	95	1976 1982 1991	58	1968	33	1974	64	1951	
22	96	1969	60	1968	33	1954 1988 1996	58	2003	
23	96	1991	59	1960	30	1978	64	1995	
24	98	1988	58	1989	31	1992	59	1961	
25	99	1988	65	1977	26	1992	61	1969	
26	95	2001	64	2004	24	1992	59	1970	
27	94	1981 1986 2001	61	1956	28	1954	59	1991	
28	94	1986	61	1964	31	1960	59	1958	
29	95	1990	61	1964	28	1975	57	1958 1981	
30	96	1954	68	1951 1965	30	1964 1975	56	2000	
31	95	1955	64	1999	26	1993	57	1954	

Table A-9. CFA daily surface air temperature extremes for September.

SEPTEMBER

Day	Highest Maximum (° F)	Year of Highest Maximum	Lowest Maximum (° F)	Year of Lowest Maximum	Lowest Minimum (° F)	Year of Lowest Minimum	Highest Minimum (° F)	Year of Highest Minimum
1	96	1950	50	1973	29	1965	54	1991
2	95	1950	60	2000	29	1975	56	1954
3	96	1950	52	1971	27	1964 1975	58	1978
4	96	1950	67	1971	27	1964	58	1982 1990
5	94	1976	48	1970	30	1964	58	1978
6	96	1955	59	2001	24	1996	63	1976
7	93	1955 1977 1979	62	2002	26	1996 2000	60	1963
8	90	1979 1990 1994 2005	59	1962	27	1999	58	1950
9	90	1988 1990	59	1961	22	1962	56	1998
10	90	1959	52	1972 1978	24	1970	59	1950
11	94	1990	52	1978	29	1957 1964	57	1976
12	92	1953	52	1978	27	1951 1979	55	1998
13	90	1953	54	1970	25	1989	55	1953 1959
14	93	1990	50	1982	21	1970	54	1973
15	93	2000	52	1982	21	1970	49	1984
16	89	1995 2000	38	1965	20	1970	57	1953
17	90	1981	41	1965	24	1965	58	2000
18	89	1956 1981	43	1978	14	1965	49	1963
19	89	1956	48	1986	16	1965	54	1973
20	84	1966 1991	46	1983	14	1983	50	1963
21	87	1987	44	1968	16	1983	50	1952
22	90	1987	47	2000	17	1993 1995	50	1976
23	92	1987	49	1961	21	1996	47	1966
24	91	1987	48	1984	15	2000	50	1999
25	88	2001	48	1955	12	1970	47	1951
26	85	1991 1994	51	1986 1999	18	1970	56	1997
27	86	1963 1991 2001	47	1959	19	1964	52	1983
28	88	1994	48	1965 1985	18	1999	54	1991
29	86	1992	43	1971	15	1999	54	1994
30	88	1992	38	1971	15	1985	51	1994

Table A-10. CFA daily surface air temperature extremes for October.

OCTOBER								
Day	Highest Maximum (° F)	Year of Highest Maximum	Lowest Maximum (° F)	Year of Lowest Maximum	Lowest Minimum (° F)	Year of Lowest Minimum	Highest Minimum (° F)	Year of Highest Minimum
1	87	1992	38	1971	15	1950	45	1953 1957
2	84	1987 1992	47	1989	19	1950	55	1976
3	84	1987	42	1994	16	1973	55	1974
4	82	1980 1988 1993	46	1957	16	1973	46	1975
5	82	1988	51	1955 1962 1982	16	1981	47	1963
6	81	1979	49	1990	11	1955	50	1993
7	80	1979 1980 1987	41	1961	15	1955	47	1960
8	81	1979 1988	31	1985	17	1974 1977	45	1956
9	81	1996	44	1985	12	1968	49	1983
10	84	1991	50	1960 1977 1985	13	2001	45	1962
11	83	1991	42	1960	12	1977	47	1989
12	81	1991	36	1969	11	2002	51	1962
13	79	1958	35	1969	10	2002	53	1962
14	81	1958	44	1981 1983	7	1969	44	1957
15	79	1958 1991	43	1994	7	1970	46	1979
16	77	1973	36	1969	9	1970 1984	49	1988
17	77	1973	34	1984	4	1996	40	1950 1988
18	78	2003	39	1984	12	1964	40	1986
19	75	1974 2003	40	1984	8	1982	48	1955
20	79	2003	40	1984 1996	7	1982	43	1986
21	78	2003	42	1951 1953	6	1996	46	1975
22	80	2003	34	1975	9	1958	43	1991
23	72	1952 1965	36	1975	9	1980 1995	44	1983
24	75	1992	32	1975	8	1980	42	1989
25	73	1990 1992	35	1975	10	1997 2002 2003	41	1963
26	70	1999	38	1970	10	2002	41	1995
27	71	1990	38	1970	9	1954	47	1994
28	70	1952 1987 1990	28	1971	5	1991	46	2001
29	70	1968	30	1991	8	1971	43	1950
30	71	1962	26	2002	1	1991	42	1950
31	68	1988	26	2002	-6	2002	41	1987

Table A-11. CFA daily surface air temperature extremes for November.

NOVEMBER

Day	Highest Maximum (° F)	Year of Highest Maximum	Lowest Maximum (° F)	Year of Lowest Maximum	Lowest Minimum (° F)	Year of Lowest Minimum	Highest Minimum (° F)	Year of Highest Minimum
1	67	1965	27	1991	-5	2002	44	1987
2	66	1978	23	2002	-3	1955	45	1987
3	65	1962 1965 1976 1981	23	1991	-4	1973 2002	41	1987
4	62	1965 1983 1999 2001	28	1991	1	2002	41	1999
5	67	1980	33	2003	-10	2003	44	1983
6	66	1999	35	1971 1992	-5	2003	38	1966
7	64	1980	31	1990	-6	2003	39	1980
8	65	1976	29	2000	6	1955 1977 1993	36	1973
9	65	1958 1973	25	1950	0	1977	36	1970 1982 1991
10	63	1954	20	1950	-6	1950	32	1973 1980
11	63	1953 1999	26	1978	-3	2000	38	1983
12	66	1999	23	1955	1	1975	39	1954
13	63	1999	25	1978 2000	-6	1955	38	1981
14	62	1963 1999	24	1978	-2	1959	37	1981
15	60	1999	9	1955	-19	1955	39	1953
16	60	1953	7	1955	-24	1955	35	1975
17	57	1976	20	1958	-2	1958 1978	38	1983
18	60	1995	19	2000	-2	1951 1977	36	1965
19	55	2003	18	1985	-5	1953 1977	42	1996
20	59	1966	18	1977	-6	2000	39	1955
21	58	1954	16	1985	-12	1977	33	1962 2001
22	54	1976 1995	17	1985	-20	1985	33	1974
23	60	1959	4	1985	-21	1985	35	1961
24	58	1995	16	1993	-19	1993	34	1960
25	56	1990	8	1993	-24	1993	41	1995
26	55	1998	14	1993	-23	1993	37	1999
27	55	1950	20	1952	-21	1993	31	1951
28	49	1953	15	1952	-13	1952	35	1998
29	51	1995	16	1975	-19	1979	37	1995

Table A-12. CFA daily surface air temperature extremes for December.

DECEMBER

Day	Highest Maximum (° F)	Year of Highest Maximum	Lowest Maximum (° F)	Year of Lowest Maximum	Lowest Minimum (° F)	Year of Lowest Minimum	Highest Minimum (° F)	Year of Highest Minimum
1	57	1995	15	1985	-13	1967	37	1995
2	47	1972 1975	19	1984	-11	1984	35	1987
3	55	1958	18	1984	-16	1984 1992	35	1980
4	49	1975	6	1992	-28	1992	33	1980
5	51	1987	0	1972	-37	1972	30	1974
6	52	1987	10	1972	-21	2005	32	1975
7	47	1965 1991	6	2005	-30	2005	35	1975
8	44	1968 1976	1	1972	-29	2005	30	1975
9	46	1990	0	1972	-35	1972	30	1975
10	52	1990	-6	1972	-40	1972	33	1996
11	43	1995	3	1972	-34	1972	34	1995
12	46	1995	5	1972	-19	1963 1985	35	1995
13	45	1956	6	1972	-26	1972	31	1995
14	47	2002	9	1984	-21	1972	36	1977
15	45	1977	9	1972	-29	1972	38	1977
16	48	1962	12	1967 1992	-20	1964	32	1957
17	47	1962	0	1964	-33	1964	32	1957
18	43	1962 1979	12	1964 1983 1992	-26	1964	29	1950
19	43	1979	6	1998	-21	1984	30	1952
20	44	1958	-2	1990	-27	1998	30	1952 1957 1964 1969
21	45	1974	-4	1990	-38	1983	33	1955 1964
22	51	1964	-9	1990	-38	1990	37	1964
23	50	1955	-8	1983	-47	1983	34	1964
24	45	1964	-1	1990	-38	1983	33	1964
25	43	1980	1	1990	-24	1990	30	1980
26	49	1976	8	1988	-20	2001	31	1980
27	53	1980	3	1988	-28	1988	32	1996
28	42	2004	7	1983	-20	1983	33	2005
29	42	1965	5	1988 1990	-27	1990	33	1996
30	43	1996	-4	1990	-29	1978	31	1996
31	47	1980	3	1978	-37	1978	35	1996

This page intentionally left blank.

APPENDIX B

PRECIPITATION EXTREMES

The following are the daily precipitation extreme records and corresponding year(s) observed at CFA from January 1950 through December 2005. The data include the greatest daily accumulation of precipitation, greatest daily snowfall, and greatest daily snow depth.

Table B-1. CFA daily precipitation extremes for January.

JANUARY						
Day	Greatest Daily Precipitation (.in)	Year of Greatest Daily Precipitation	Greatest Daily Snowfall (.in)	Year of Greatest Daily Snowfall	Greatest Daily Snow Depth (.in)	Year of Greatest Daily Snow Depth
1	0.43	1997	3.5	1955	18	1993
2	0.31	1997	2.8	1951	18	1993
3	0.23	2002	3.0	2002	18	1993
4	0.27	1977	5.0	1977	18	1993
5	0.25	1976	3.0	1976	17	1993
6	0.44	1965	1.5	1959	17	1993
7	0.47	1965	5.0	2005	17	1993
8	0.52	1975	3.0	1975	18	1993
9	0.12	1970 1985	1.4	1970	18	1993
10	0.18	1978	5.0	1978	18	1993
11	0.25	1979	4.0	1971	20	1993
12	0.22	1960	3.3	1960	20	1993
13	0.45	1980	3.1	1957	20	1993
14	0.58	1990	4.0	1990	21	1993
15	0.35	1990	2.0	1952 1988 1990	20	1993
16	0.51	1978	5.0	1978	20	1993
17	0.24	1998	4.0	1998	20	1993
18	0.37	1974	3.0	2000	20	1993
19	0.79	1969	4.4	1969	20	1993
20	0.61	1957	8.5	1957	22	1993
21	0.65	1985	5.0	1985	23	1993
22	0.31	1993	4.0	1982	25	1993
23	0.40	1954	5.0	1972	24	1993
24	0.25	1965	2.6	1967	24	1993
25	0.12	1997	3.4	1956	23	1993
26	0.32	1969	3.5	1956	23	1993
27	0.44	1996	4.0	1996	23	1993
28	0.52	1987	2.0	1981	22	1993
29	0.21	1981	2.5	1981	22	1993
30	0.25	1981	3.0	1981	22	1993
31	0.72	1963	2.6	1967	22	1993

Table B-2. CFA daily precipitation extremes for February.

FEBRUARY						
Day	Greatest Daily Precipitation (.in)	Year of Greatest Daily Precipitation	Greatest Daily Snowfall (.in)	Year of Greatest Daily Snowfall	Greatest Daily Snow Depth (.in)	Year of Greatest Daily Snow Depth
1	0.43	1963	2.5	1952	21	1993
2	0.44	1961	5.0	1961	20	1993
3	0.16	1963	0.5	1975	20	1993
4	0.17	1974	1.0	1976	19	1993
5	0.13	1978	3.5	1975	19	1993
6	0.28	1998	3.0	1966 1998	19	1993
7	0.29	1999	2.0	2004	18	1993
8	0.77	1960	7.5	1960	19	1993
9	0.58	1962	4.0	1978 1993	23	1993
10	0.58	1962	5.0	1984	25	1993
11	0.54	1962	5.6	1973	25	1993
12	0.20	1978	2.1	1969	25	1993
13	0.54	1954	6.4	1973	25	1993
14	0.46	1998	5.0	1998	25	1993
15	0.61	1986	3.2	1962	27	1993
16	0.39	1986	4.0	1952	27	1993
17	0.25	1994	2.1	1955	27	1993
18	0.79	1986	2.0	1961 1989 1999	27	1993
19	0.64	1993	7.2	1971	28	1993
20	0.36	1981	3.2	1956	28	1993
21	0.30	1999	4.0	1999	28	1993
22	0.16	1977	1.0	1974 1977 1980 1984	28	1993
23	0.55	2001	5.0	2001	30	1993
24	0.47	1969	5.1	1969	30	1993
25	0.30	1958	2.4	1966	30	1993
26	0.21	1957	0.7	1964	30	1993
27	0.15	1965	2.0	1979	30	1993
28	0.10	1976 1983	2.5	1983	30	1993
29	0.40	1976	2.0	1976	19	1952

Table B-3. CFA daily precipitation extremes for March.

MARCH						
Day	Greatest Daily Precipitation (.in)	Year of Greatest Daily Precipitation	Greatest Daily Snowfall (.in)	Year of Greatest Daily Snowfall	Greatest Daily Snow Depth (.in)	Year of Greatest Daily Snow Depth
1	0.42	1964	4.9	1964	30	1993
2	0.27	1974	3.0	1979	30	1993
3	0.26	1985	3.0	1985	30	1993
4	0.89	1991	2.0	1956	30	1993
5	0.29	1996	2.3	1960	30	1993
6	0.59	2002	3.0	2002	29	1993
7	0.25	1960	1.8	1960	29	1993
8	0.17	1989	0.5	1951	28	1993
9	0.35	1986	2.0	2000	27	1993
10	0.19	1995	2.0	1952	26	1993
11	0.55	1995	2.7	1954	26	1993
12	0.33	1967	3.3	1967	26	1993
13	0.39	2002	4.0	2002	25	1993
14	0.43	1983	0.3	1988	25	1993
15	0.18	1958	3.6	1958	23	1993
16	0.21	1970	1.9	1971	22	1952 1985 1993
17	0.25	1950	3.0	1982	21	1952 1985
18	0.16	1995	1.0	1977 1982	21	1952
19	0.19	2000	1.5	1989	21	1952
20	0.26	1995	0.9	1964	21	1952
21	0.39	1958	1.0	1980 1981	20	1952
22	0.61	1973	8.6	1973	20	1952
23	0.44	2005	3.0	2005	19	1952
24	0.16	1995	0.7	1954	18	1952
25	0.30	1993	3.0	1975	16	1952
26	0.45	1975	0.6	1958	14	1952
27	0.35	1981 1985	5.0	1985	17	1985
28	0.47	1996	2.0	1996	17	1985
29	0.45	1982	2.0	1970	16	1985
30	0.20	1951	1.2	1959	15	1985
31	0.34	1997	2.0	1997	14	1985

Table B-4. CFA daily precipitation extremes for April.

APRIL						
Day	Greatest Daily Precipitation (.in)	Year of Greatest Daily Precipitation	Greatest Daily Snowfall (.in)	Year of Greatest Daily Snowfall	Greatest Daily Snow Depth (.in)	Year of Greatest Daily Snow Depth
1	0.18	1978	0.7	1967	12	1985
2	0.75	1996	3.0	1955	8	1985
3	0.43	1958	0.9	1958	5	1985
4	0.23	1993	1.0	1980	3	1952
5	0.34	1953	0.9	1964	1	1952 1958
6	0.48	1957	3.4	1957	2	1957
7	0.39	1965	2.4	1965	1	1957 1965
8	0.54	1990	2.0	1999	1	1999
9	0.31	1984	1.0	1984	1	1984
10	0.24	1966	0.4	1955	0	ALL
11	0.17	2001	1.0	1975	1	1975
12	0.20	1993	2.0	1993	2	1975
13	0.24	1973	0.5	1975	2	1975
14	0.14	2003	0.2	1955 1970 1973 1995	0	ALL
15	0.36	2002	2.0	2002	1	2002
16	0.19	1978	0.3	1959 1975	1	1970 1971
17	0.11	2004	0.4	1968	0	ALL
18	0.48	2000	1.0	1996	0	ALL
19	0.54	1970	6.5	1970	1	1957 1963
20	1.51	1981	1.0	1963	6	1970 1971
21	0.37	1958	3.0	1958	3	1970 1971
22	0.42	1958	3.4	1958	1	1958
23	0.54	1997	3.9	1964	5	1964
24	0.52	1994	2.2	1961	2	1960 1961
25	0.67	1975	3.0	1984	3	1984
26	0.57	1963	1.5	1976	2	1976
27	0.88	1963	4.7	1963	6	1976
28	0.49	1999	6.7	1970	6	1970 1971
29	0.24	1983	2.0	1967	2	1970 1971
30	0.21	1999	0.0	ALL	1	1967

Table B-5. CFA daily precipitation extremes for May.

MAY						
Day	Greatest Daily Precipitation (.in)	Year of Greatest Daily Precipitation	Greatest Daily Snowfall (.in)	Year of Greatest Daily Snowfall	Greatest Daily Snow Depth (.in)	Year of Greatest Daily Snow Depth
1	0.82	1959	0.0	ALL	0	ALL
2	0.30	1960	0.0	ALL	0	ALL
3	0.49	1993	0.0	ALL	0	ALL
4	0.37	1993	0.0	ALL	0	ALL
5	0.57	1995	2.0	1978	2	1978
6	0.40	1965 1995	3.9	1965	0	ALL
7	0.68	2000	4.4	1965	5	1965
8	0.47	1991	1.0	1979	0	ALL
9	0.61	1979	2.0	1979	2	1979
10	0.70	1998	0.0	ALL	0	ALL
11	0.60	1966	1.7	1966	0	ALL
12	0.76	1957	0.7	1970	0	ALL
13	0.70	1957	0.2	1951 1970	0	ALL
14	0.40	1962	0.2	1955	0	ALL
15	0.58	1961	1.8	1955	1	1955
16	0.95	1987	2.7	1955	0	ALL
17	0.46	1987	0.0	ALL	0	ALL
18	0.59	1957	1.1	1960	0	ALL
19	0.33	1957	1.2	1959	0	ALL
20	0.30	1970	0.0	ALL	0	ALL
21	0.48	1972	0.0	ALL	0	ALL
22	0.21	1991	0.0	ALL	0	ALL
23	0.56	1959	0.0	ALL	0	ALL
24	0.70	1953	0.0	ALL	0	ALL
25	0.30	1956	0.0	ALL	0	ALL
26	0.32	1964	0.0	ALL	0	ALL
27	0.28	1960	0.0	ALL	0	ALL
28	0.65	1964	0.0	ALL	0	ALL
29	0.85	1971	4.0	1979	4	1979
30	0.47	1999	0.0	ALL	0	ALL
31	0.21	1990	0.0	ALL	0	ALL

Table B-6. CFA daily precipitation extremes for June.

JUNE						
Day	Greatest Daily Precipitation (.in)	Year of Greatest Daily Precipitation	Greatest Daily Snowfall (.in)	Year of Greatest Daily Snowfall	Greatest Daily Snow Depth (.in)	Year of Greatest Daily Snow Depth
1	0.51	2005	0	ALL	0	ALL
2	0.56	1964	0	ALL	0	ALL
3	0.33	1993	0	ALL	0	ALL
4	0.61	1991	0	ALL	0	ALL
5	1.55	1995	0	ALL	0	ALL
6	0.78	1993	0	ALL	0	ALL
7	0.66	1968	0	ALL	0	ALL
8	0.55	1984	0	ALL	0	ALL
9	0.81	1984	0	ALL	0	ALL
10	1.64	1969	0	ALL	0	ALL
11	0.16	1968	0	ALL	0	ALL
12	0.21	1955	0	ALL	0	ALL
13	0.84	1967	0	ALL	0	ALL
14	0.43	1992	0	ALL	0	ALL
15	0.50	1962	0	ALL	0	ALL
16	0.39	1976	0	ALL	0	ALL
17	0.49	1997	0	ALL	0	ALL
18	0.56	1995	0	ALL	0	ALL
19	0.34	1995	0	ALL	0	ALL
20	0.31	1977	0	ALL	0	ALL
21	0.28	1995	0	ALL	0	ALL
22	0.38	2002	0	ALL	0	ALL
23	0.47	1972	0	ALL	0	ALL
24	0.49	1989	0	ALL	0	ALL
25	0.79	1965	0	ALL	0	ALL
26	0.65	1965	0	ALL	0	ALL
27	0.55	1959	0	ALL	0	ALL
28	0.32	2004	0	ALL	0	ALL
29	0.47	1962	0	ALL	0	ALL
30	0.08	1957 1992	0	ALL	0	ALL

Table B-7. CFA daily precipitation extremes for July.

JULY						
Day	Greatest Daily Precipitation (.in)	Year of Greatest Daily Precipitation	Greatest Daily Snowfall (.in)	Year of Greatest Daily Snowfall	Greatest Daily Snow Depth (.in)	Year of Greatest Daily Snow Depth
1	0.79	1987	0	ALL	0	ALL
2	0.10	2004	0	ALL	0	ALL
3	0.46	1980	0	ALL	0	ALL
4	0.12	1961	0	ALL	0	ALL
5	0.10	1950 2001	0	ALL	0	ALL
6	0.13	1995	0	ALL	0	ALL
7	0.16	1978	0	ALL	0	ALL
8	0.05	1975	0	ALL	0	ALL
9	0.51	1990	0	ALL	0	ALL
10	0.71	1983	0	ALL	0	ALL
11	0.40	1970	0	ALL	0	ALL
12	0.53	1997	0	ALL	0	ALL
13	0.53	1962	0	ALL	0	ALL
14	0.28	1964	0	ALL	0	ALL
15	0.38	1985	0	ALL	0	ALL
16	0.29	1996	0	ALL	0	ALL
17	0.40	1987	0	ALL	0	ALL
18	0.21	2004	0	ALL	0	ALL
19	0.42	1973	0	ALL	0	ALL
20	0.35	1973	0	ALL	0	ALL
21	0.83	1987	0	ALL	0	ALL
22	0.73	1973	0	ALL	0	ALL
23	1.25	1979	0	ALL	0	ALL
24	0.35	1977	0	ALL	0	ALL
25	0.40	1991	0	ALL	0	ALL
26	0.18	1951	0	ALL	0	ALL
27	0.78	1984	0	ALL	0	ALL
28	0.23	1997	0	ALL	0	ALL
29	0.70	1984	0	ALL	0	ALL
30	0.40	1985	0	ALL	0	ALL
31	0.56	1985	0	ALL	0	ALL

Table B-8. CFA daily precipitation extremes for August.

AUGUST						
Day	Greatest Daily Precipitation (.in)	Year of Greatest Daily Precipitation	Greatest Daily Snowfall (.in)	Year of Greatest Daily Snowfall	Greatest Daily Snow Depth (.in)	Year of Greatest Daily Snow Depth
1	0.24	1952	0	ALL	0	ALL
2	0.23	2004	0	ALL	0	ALL
3	0.43	1951	0	ALL	0	ALL
4	0.41	1963	0	ALL	0	ALL
5	0.28	1951	0	ALL	0	ALL
6	0.54	1951	0	ALL	0	ALL
7	0.11	1964	0	ALL	0	ALL
8	0.41	1961	0	ALL	0	ALL
9	0.56	1982	0	ALL	0	ALL
10	0.31	1997	0	ALL	0	ALL
11	0.72	1950	0	ALL	0	ALL
12	0.23	1989	0	ALL	0	ALL
13	0.59	1968	0	ALL	0	ALL
14	0.41	1968	0	ALL	0	ALL
15	0.13	1979	0	ALL	0	ALL
16	0.31	1960	0	ALL	0	ALL
17	0.31	2004	0	ALL	0	ALL
18	0.55	1990	0	ALL	0	ALL
19	0.70	1959	0	ALL	0	ALL
20	0.74	1959	0	ALL	0	ALL
21	0.37	1968	0	ALL	0	ALL
22	0.80	1960	0	ALL	0	ALL
23	0.65	1976	0	ALL	0	ALL
24	0.18	1987	0	ALL	0	ALL
25	0.07	1977	0	ALL	0	ALL
26	0.03	1970	0	ALL	0	ALL
27	0.58	1991	0	ALL	0	ALL
28	0.08	1964	0	ALL	0	ALL
29	0.37	1971	0	ALL	0	ALL
30	0.23	1986	0	ALL	0	ALL
31	0.40	1963	0	ALL	0	ALL

Table B-9. CFA daily precipitation extremes for September.

SEPTEMBER						
Day	Greatest Daily Precipitation (.in)	Year of Greatest Daily Precipitation	Greatest Daily Snowfall (.in)	Year of Greatest Daily Snowfall	Greatest Daily Snow Depth (.in)	Year of Greatest Daily Snow Depth
1	0.36	1973	0.0	ALL	0	ALL
2	0.14	1985	0.0	ALL	0	ALL
3	0.56	1971	0.0	ALL	0	ALL
4	0.10	1992	0.0	ALL	0	ALL
5	0.12	1970	0.0	ALL	0	ALL
6	0.45	1978	0.0	ALL	0	ALL
7	0.73	1971	0.0	ALL	0	ALL
8	0.66	1980	0.0	ALL	0	ALL
9	1.09	1961	0.0	ALL	0	ALL
10	0.27	1985	0.0	ALL	0	ALL
11	0.20	1997	0.0	ALL	0	ALL
12	0.82	1976	0.0	ALL	0	ALL
13	0.44	1982	0.9	1970	0	ALL
14	0.34	1986	0.0	ALL	0	ALL
15	0.31	1959	0.0	ALL	0	ALL
16	0.39	1996	0.0	ALL	0	ALL
17	0.45	1961	0.5	1965	0	ALL
18	1.55	1961	0.0	ALL	0	ALL
19	0.27	1963	0.0	ALL	0	ALL
20	0.70	1962	0.0	ALL	0	ALL
21	0.49	1962	1.0	1961	0	ALL
22	0.08	1968	0.0	ALL	0	ALL
23	0.29	1973	0.0	ALL	0	ALL
24	0.01	1973	0.0	ALL	0	ALL
25	0.21	1960	0.0	ALL	0	ALL
26	0.20	1982	0.0	ALL	0	ALL
27	0.93	1989	0.0	ALL	0	ALL
28	0.37	1983	0.0	ALL	0	ALL
29	0.06	1971	0.0	ALL	0	ALL
30	1.10	1994	0.2	1959 1971	0	ALL

Table B-10. CFA daily precipitation extremes for October.

OCTOBER						
Day	Greatest Daily Precipitation (.in)	Year of Greatest Daily Precipitation	Greatest Daily Snowfall (.in)	Year of Greatest Daily Snowfall	Greatest Daily Snow Depth (.in)	Year of Greatest Daily Snow Depth
1	0.60	1971	4.5	1971	0	ALL
2	0.51	1976	1.5	1969	0	ALL
3	0.32	1957	0.2	1969	0	ALL
4	0.32	1994	0.0	ALL	0	ALL
5	0.25	1967	0.0	ALL	0	ALL
6	0.25	1990	0.0	ALL	0	ALL
7	0.32	1961	3.0	1961	0	ALL
8	0.58	1973	0.0	ALL	0	ALL
9	0.39	1983	0.0	ALL	0	ALL
10	0.30	1972	0.2	1985	0	ALL
11	0.20	2000	0.0	ALL	0	ALL
12	0.38	1981	0.0	ALL	0	ALL
13	0.11	1975	0.0	ALL	0	ALL
14	0.36	1993	0.8	1981	1	1981
15	0.35	1953	0.0	ALL	0	ALL
16	0.42	1980	0.2	1969	0	ALL
17	0.17	1984	0.0	ALL	0	ALL
18	0.17	1986	1.0	1984	1	1984
19	0.77	2004	0.0	ALL	0	ALL
20	0.15	2004	0.0	ALL	0	ALL
21	0.52	1975	1.5	1975	2	1975
22	0.17	1985	0.0	ALL	1	1975
23	0.35	1997	2.8	1970	1	1975 1997
24	0.30	1974	0.5	1997	0	ALL
25	0.37	1996	2.0	1996	2	1996
26	0.22	1991	0.1	1970	0	ALL
27	0.74	1956	2.0	1991	2	1991
28	0.17	1999	0.4	1991	2	1991
29	0.09	1992	0.0	ALL	2	1991
30	0.65	1964	2.0	1971	1	1991
31	0.11	1982	0.6	1956	2	1971

Table B-11. CFA daily precipitation extremes for November.

NOVEMBER						
Day	Greatest Daily Precipitation (.in)	Year of Greatest Daily Precipitation	Greatest Daily Snowfall (.in)	Year of Greatest Daily Snowfall	Greatest Daily Snow Depth (.in)	Year of Greatest Daily Snow Depth
1	0.23	1987	0.2	1991	1	1956 1971 1991
2	0.16	1987	0.2	1994	1	1956 1971 1991
3	0.60	1968	0.7	1961	1	1991
4	0.19	1963	1.8	1956	1	1956 1991
5	0.19	1973	1.0	1998	1	1956
6	0.43	1969	0.0	ALL	0	ALL
7	0.57	1969	3.0	1998	3	1998
8	0.24	2002	1.5	1986	2	1998
9	0.31	1994	3.0	1994	3	1994
10	0.20	1958	2.0	1975	2	1975 1998
11	0.38	1985	3.0	1985	3	1985
12	0.48	1973	3.1	1964	3	1985
13	0.34	1988	3.5	1988	3	1978 1985
14	0.34	1971	1.5	1957 1971	5	1988
15	0.48	1954	1.1	1971	4	1988
16	0.31	1972	2.0	1972	4	1988
17	0.51	1964	5.1	1964	6	1964
18	0.44	1996	2.0	1996	7	1988
19	0.29	1982	2.5	1979	7	1988
20	0.21	1950	1.5	1950	6	1964 1985 1988
21	0.22	1998	0.5	1983	6	1964 1985 1988
22	0.70	1977	6.0	1977	6	1964 1977 1985
23	0.36	1988	5.0	1963	6	1985
24	0.58	1981	6.5	1981	6	1981 1985
25	0.50	1984	4.0	1983	8	1985
26	0.33	1964	3.0	1964 1989 1997	8	1985
27	0.12	1991	1.0	1951	8	1985
28	0.28	1984	4.0	1975 1984	8	1985
29	0.71	1970	2.0	1970	8	1985
30	0.27	1970	2.5	1970	9	1985

Table B-12. CFA daily precipitation extremes for December.

DECEMBER

Day	Greatest Daily Precipitation (.in)	Year of Greatest Daily Precipitation	Greatest Daily Snowfall (.in)	Year of Greatest Daily Snowfall	Greatest Daily Snow Depth (.in)	Year of Greatest Daily Snow Depth
1	0.52	2005	6.5	1982	9	1985
2	0.34	2001	4.0	2001	10	1985
3	0.41	1980	5.0	1972	13	1985
4	0.44	1974	7.0	1983	12	1983
5	0.34	1966	3.4	1966	14	1983
6	0.10	1971 1972 1982	2.5	1972	14	1983
7	0.30	1950	3.6	1950	14	1983
8	0.27	1985	3.0	1963 1997	13	1985
9	0.33	1970	3.0	1970	12	1985
10	0.26	1964	2.6	1964	12	1985
11	0.16	1996	2.0	1996	12	1985
12	0.60	1995	3.0	1971 1983	13	1983
13	0.16	1974 1990	2.5	1974	13	1983
14	0.30	1977	2.0	2001	13	1983
15	0.14	1977	0.6	1957	13	1983
16	0.16	1984	2.0	1984	13	1983
17	0.23	1973	2.1	1973	13	1983
18	0.39	1967	6.0	1967	13	1983
19	0.20	1964	1.5	1964	13	1983
20	0.17	1981	1.2	1963	13	1983
21	0.62	1964	3.0	1973	13	1983
22	1.07	1964	4.5	1971	13	1983
23	0.59	1982	2.0	1979	13	1982 1983
24	0.52	1959	4.0	2003	13	1983
25	0.44	1959	3.0	1968	13	1983
26	0.24	1955	2.6	1968	13	1983
27	0.27	1964	2.7	1964	13	1983
28	0.48	2005	4.1	1972	13	1983
29	0.51	1992	8.0	1992	18	1992
30	0.29	1977	4.0	1977 1981	18	1992
31	0.37	2004	4.0	2004	18	1992

This page intentionally left blank.

APPENDIX C: NOAA INL MESONET WIND ROSES

The following are the NOAA INL Mesonet wind roses for each station and level. The top wind rose shows the day average (1200-1800 MST), middle wind rose shows the night average (0000-0600 MST), and the bottom wind rose shows the all hours average.

Note: Big Southern Butte (BIG) 15 m tower is located approximately six miles SW of the mountain on the valley floor. Big Southern Butte Summit (SUM) 6 m tower is located on the NE summit ridge.

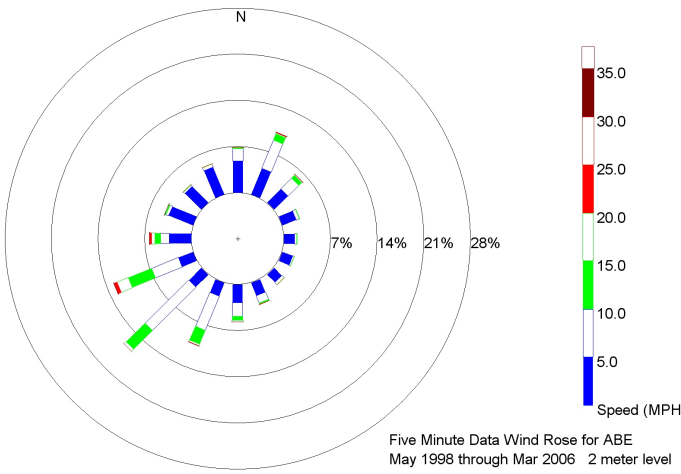
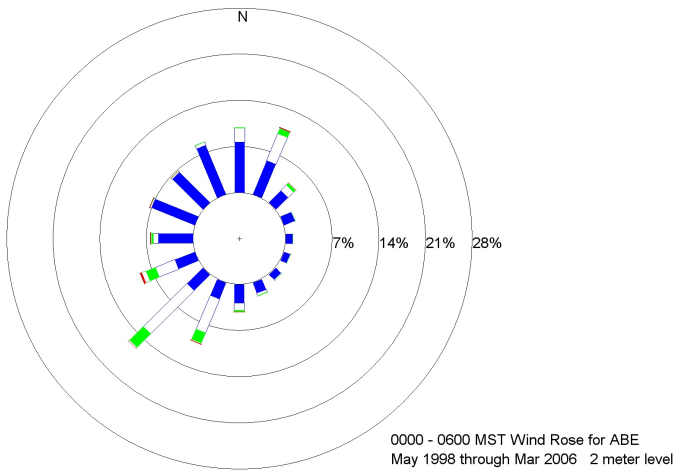
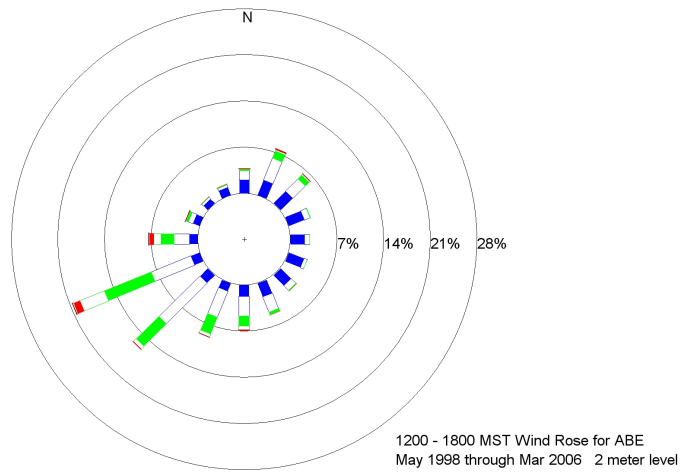


Figure C-1. Day (top), night (middle), and all hours (bottom) wind roses for the 2 meter level at ABE.

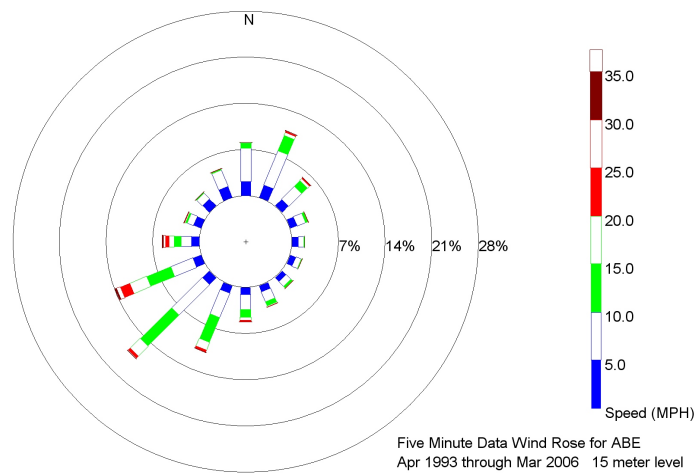
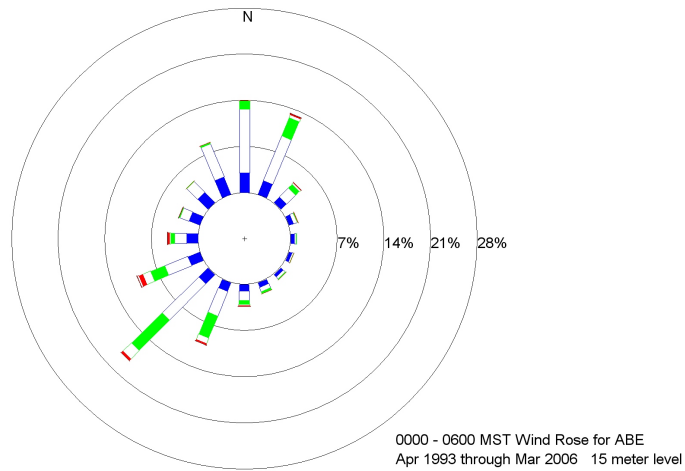
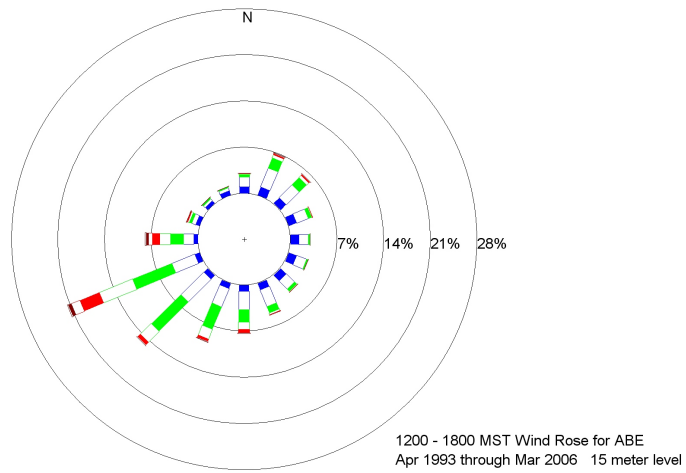


Figure C-2. Day (top), night (middle), and all hours (bottom) wind roses for the 15 meter level at ABE.

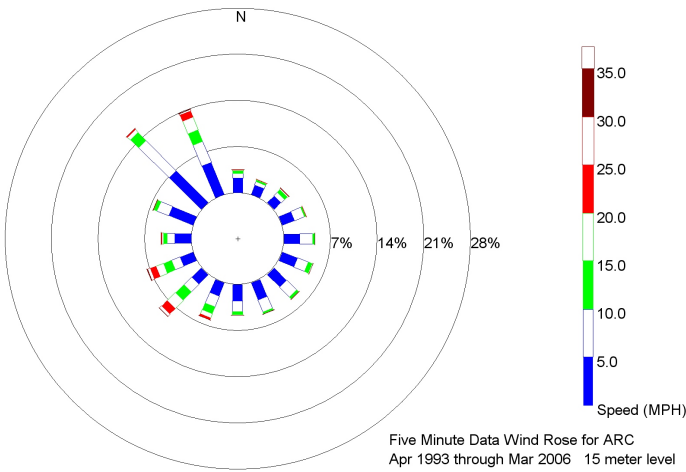
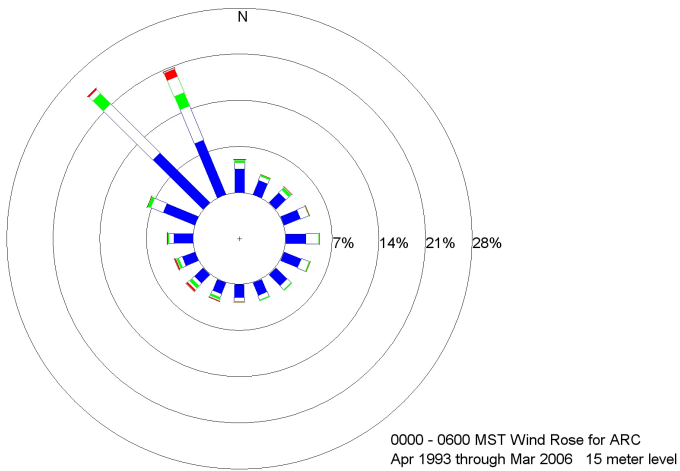
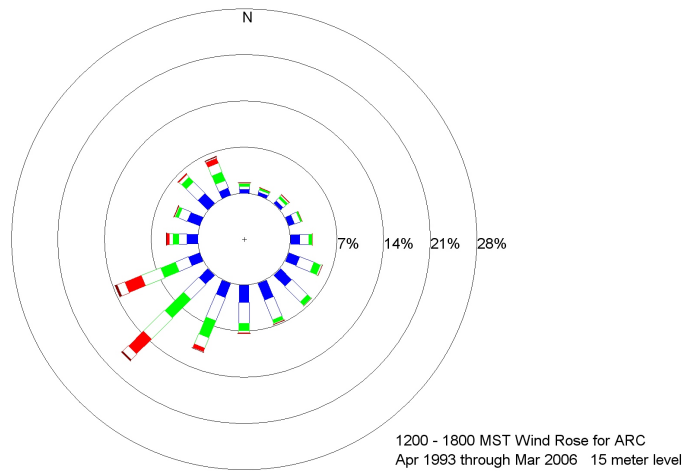


Figure C-3. Day (top), night (middle), and all hours (bottom) wind roses for the 15 meter level at ARC.

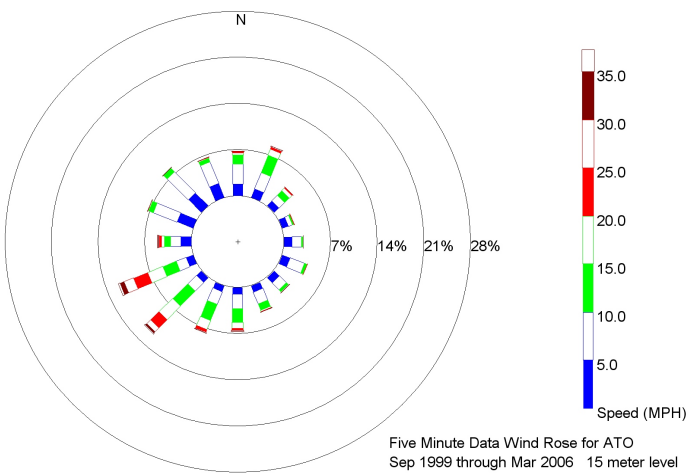
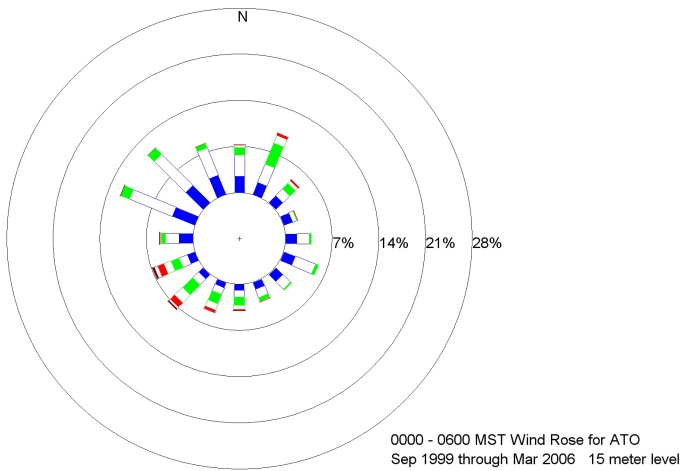
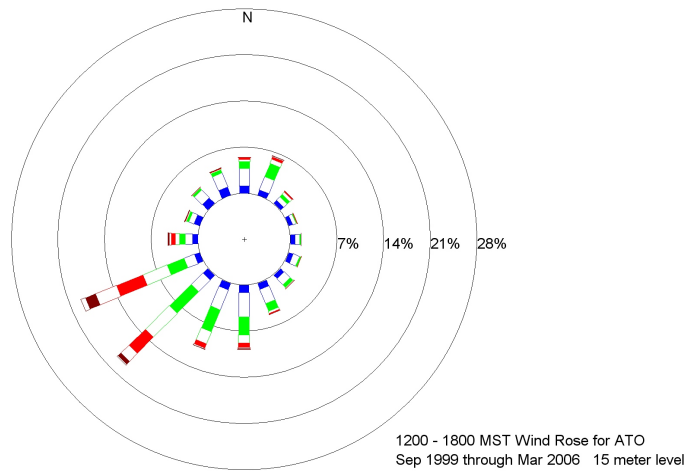


Figure C-4. Day (top), night (middle), and all hours (bottom) wind roses for the 15 meter level at ATO.

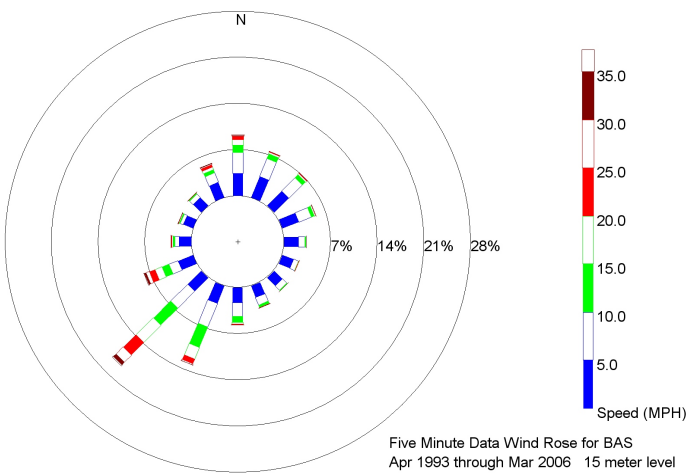
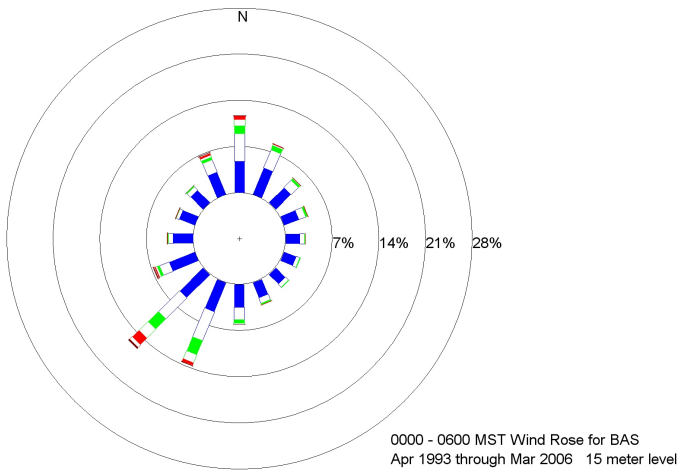
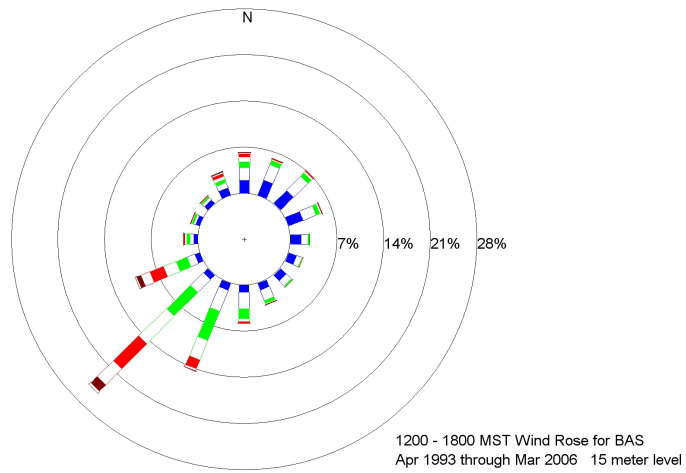


Figure C-5. Day (top), night (middle), and all hours (bottom) wind roses for the 15 meter level at BAS.

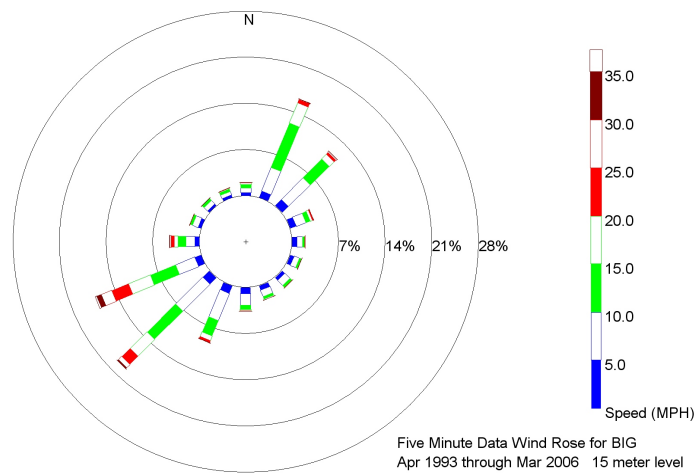
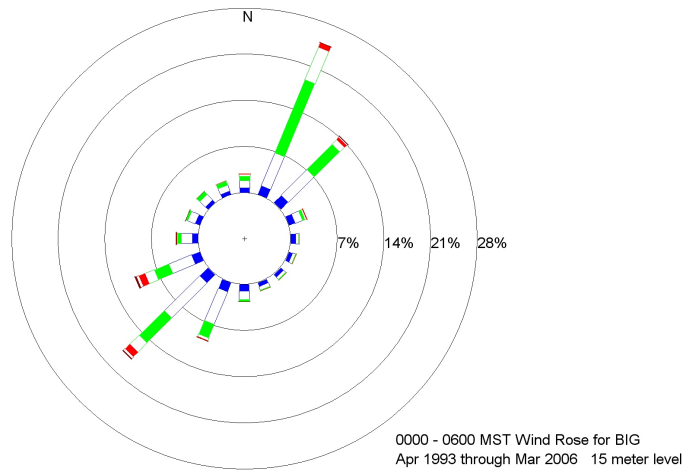
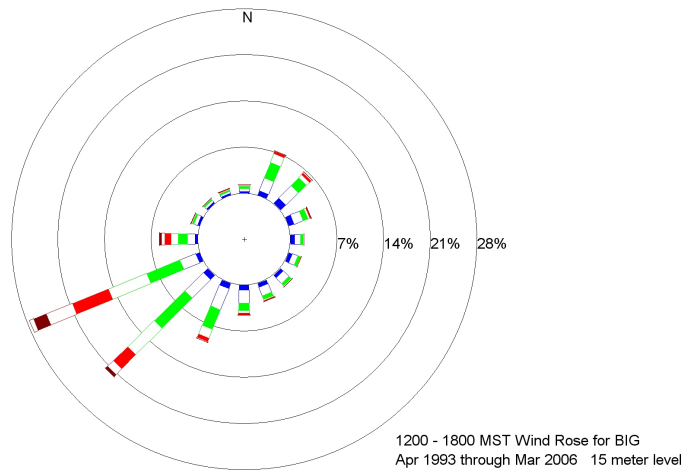


Figure C-6. Day (top), night (middle), and all hours (bottom) wind roses for the 15 meter level at BIG.

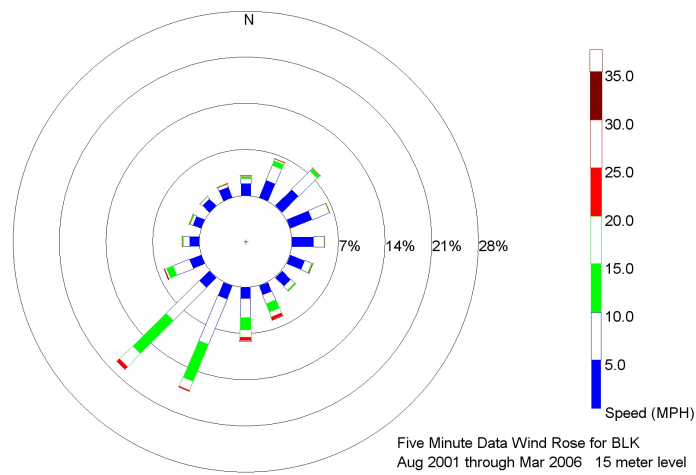
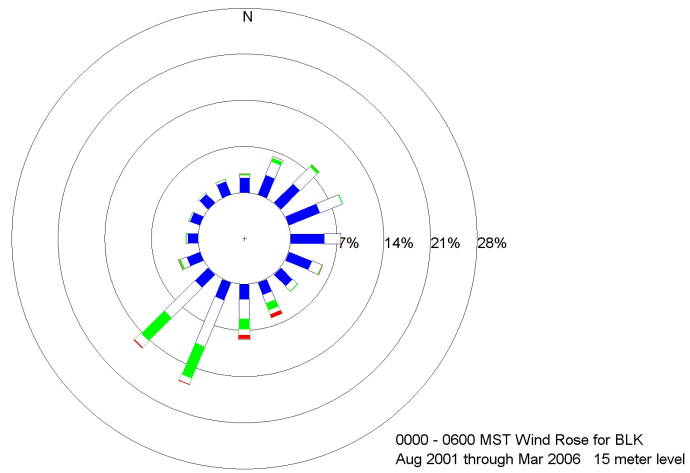
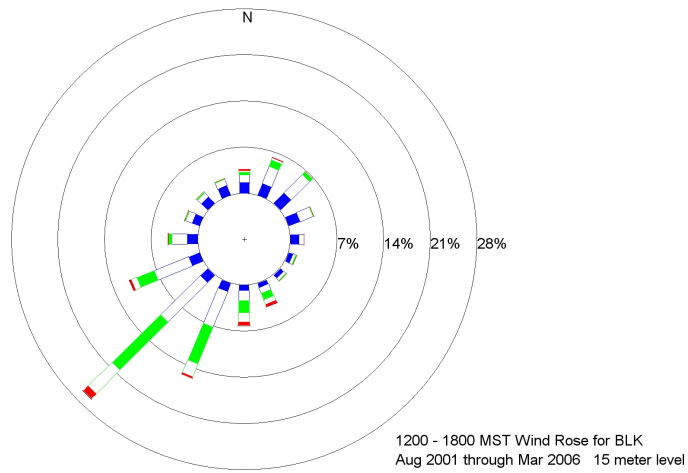


Figure C-7. Day (top), night (middle), and all hours (bottom) wind roses for the 15 meter level at BLK.

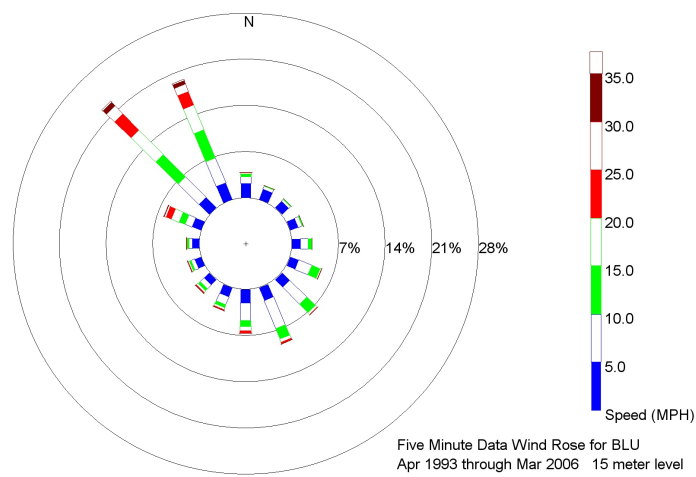
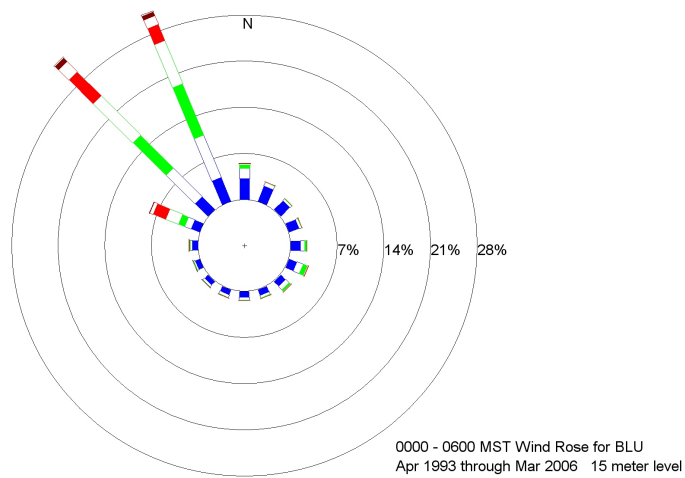
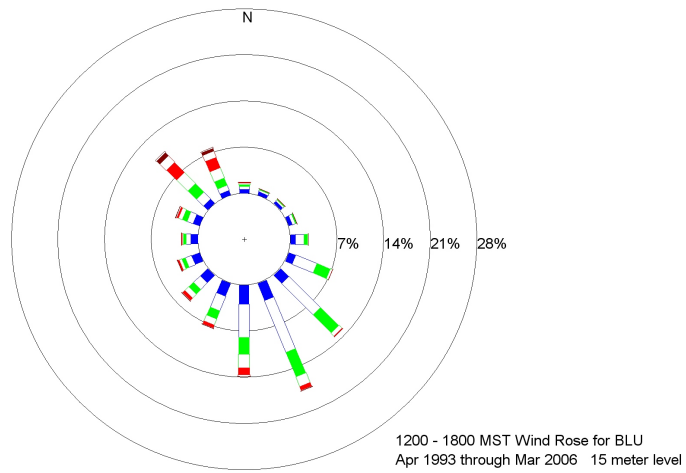


Figure C-8. Day (top), night (middle), and all hours (bottom) wind roses for the 15 meter level at BLU.

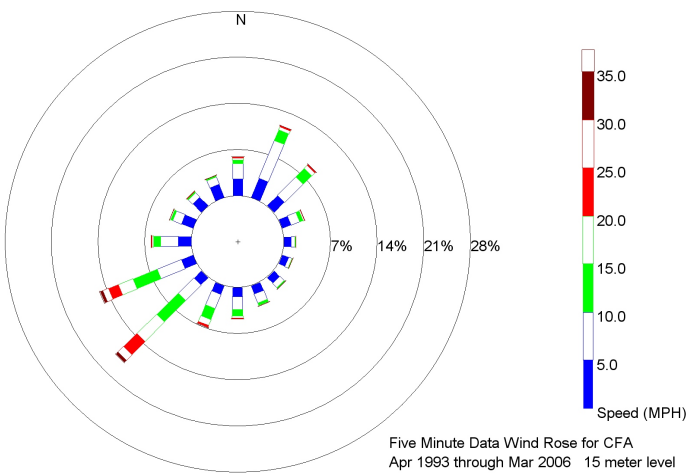
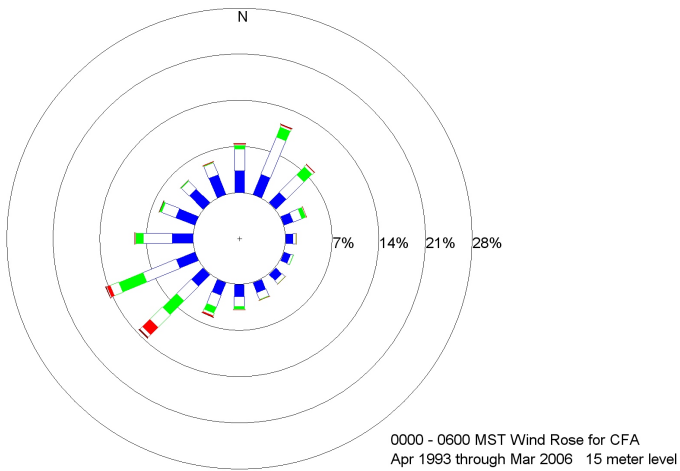
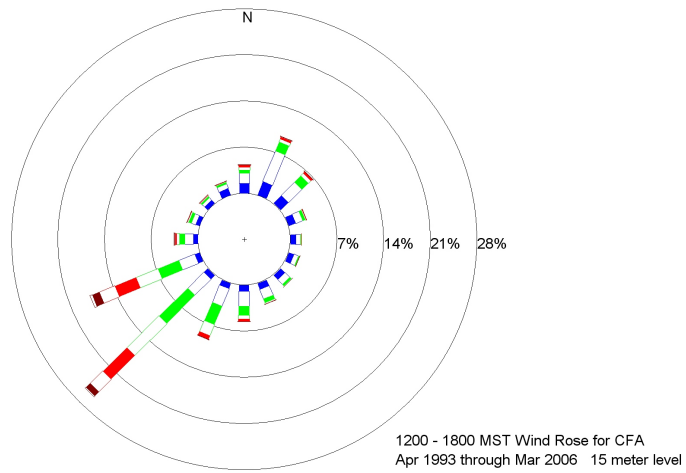


Figure C-9. Day (top), night (middle), and all hours (bottom) wind roses for the 15 meter level at CFA.

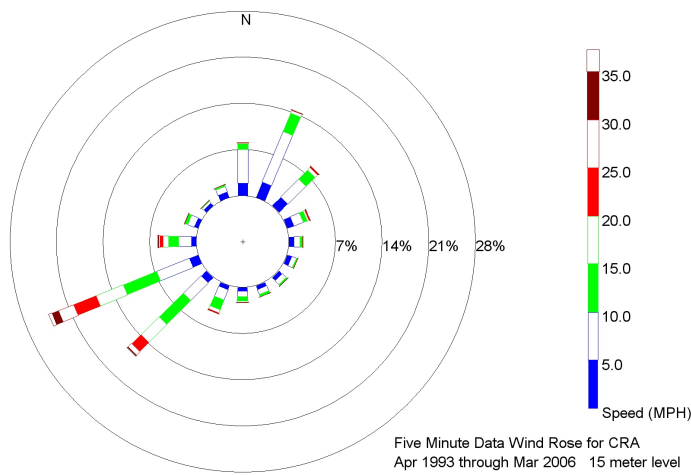
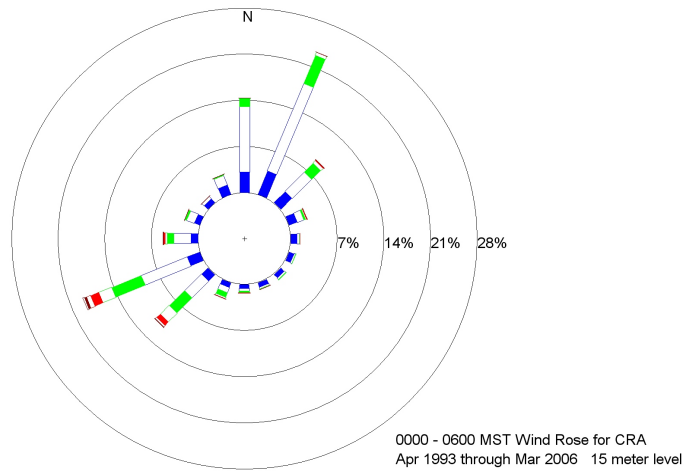
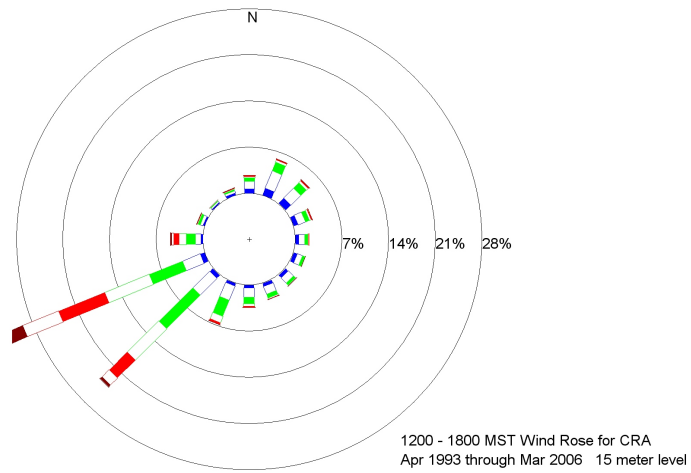


Figure C-10. Day (top), night (middle), and all hours (bottom) wind roses for the 15 meter level at CRA.

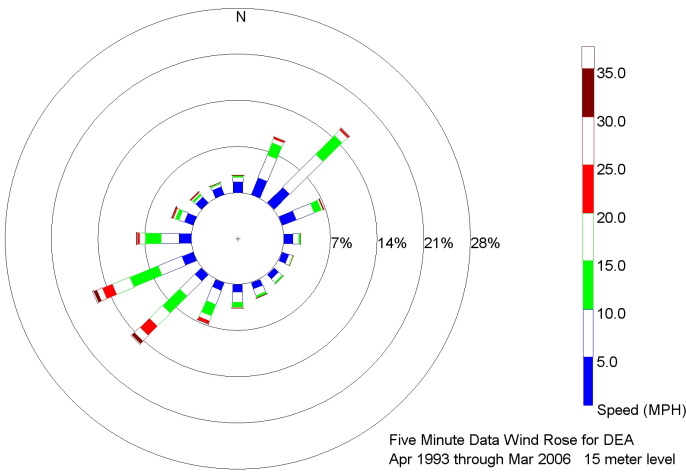
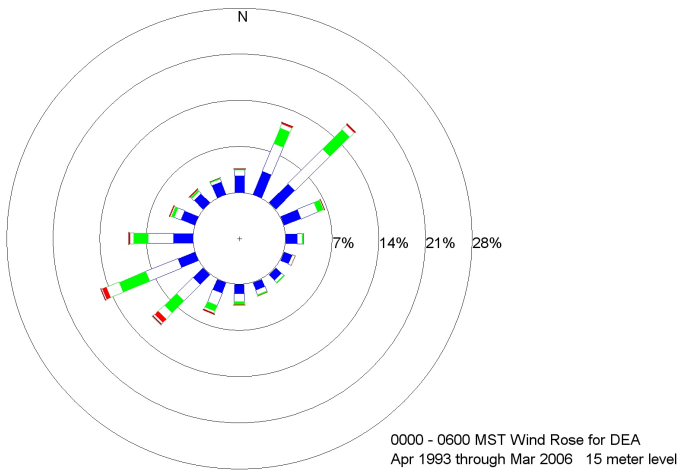
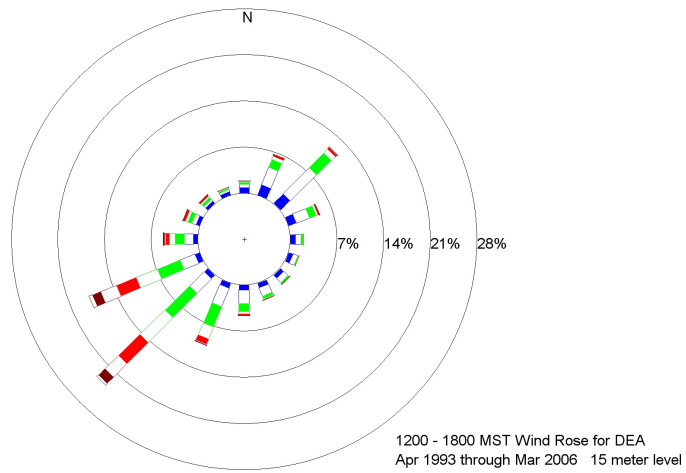


Figure C-11. Day (top), night (middle), and all hours (bottom) wind roses for the 15 meter level at DEA.

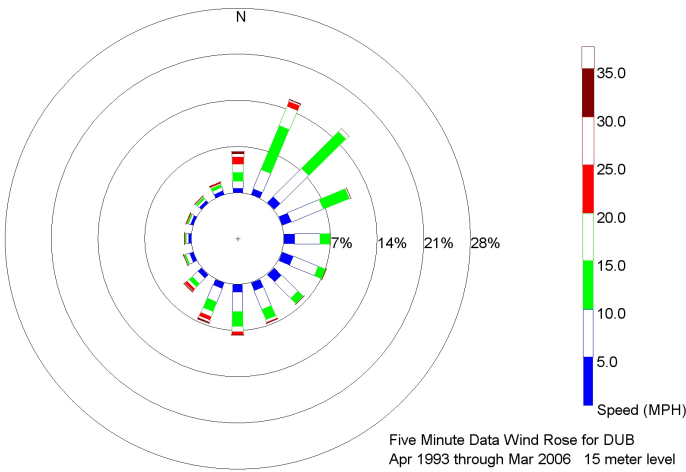
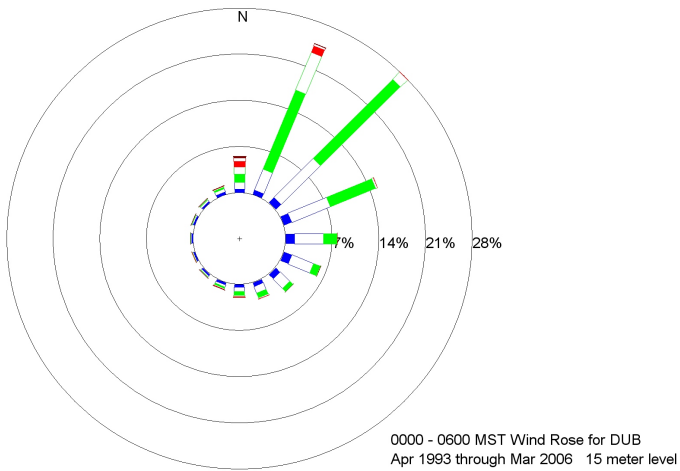
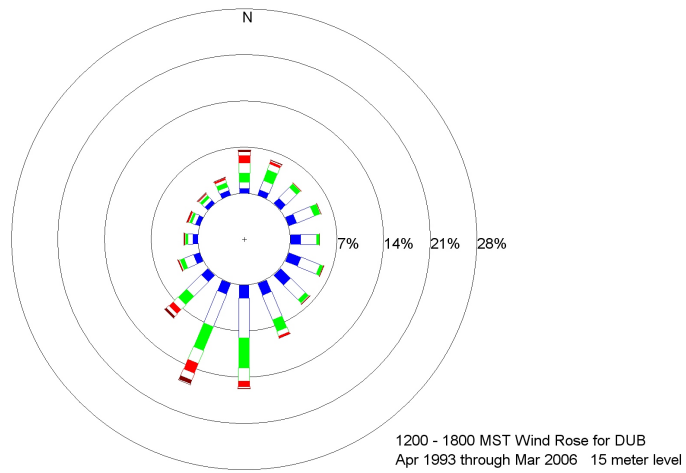


Figure C-12. Day (top), night (middle), and all hours (bottom) wind roses for the 15 meter level at DUB.

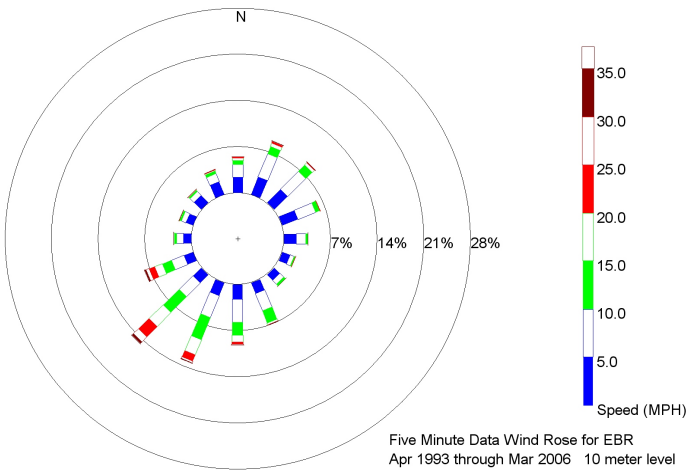
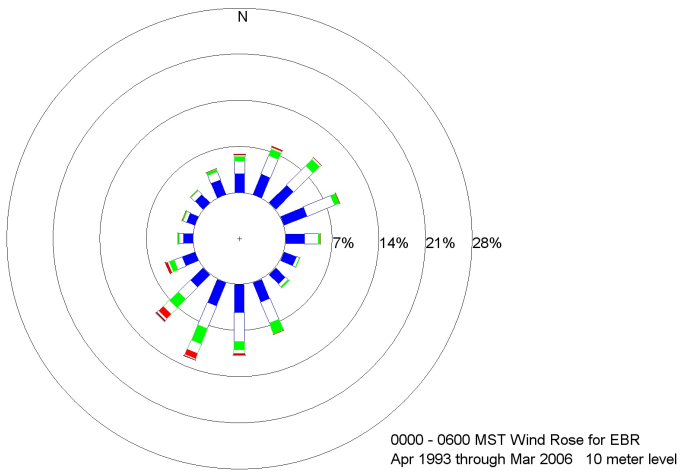
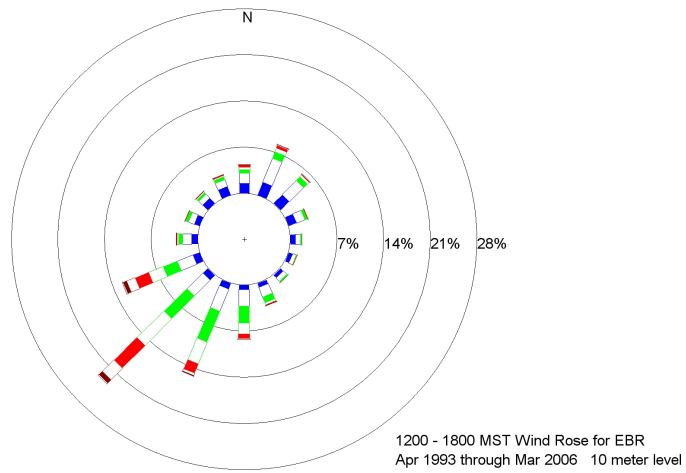


Figure C-13. Day (top), night (middle), and all hours (bottom) wind roses for the 10 meter level at EBR.

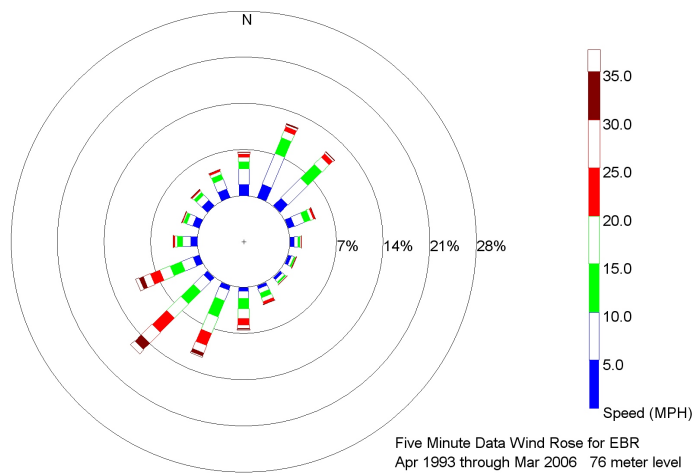
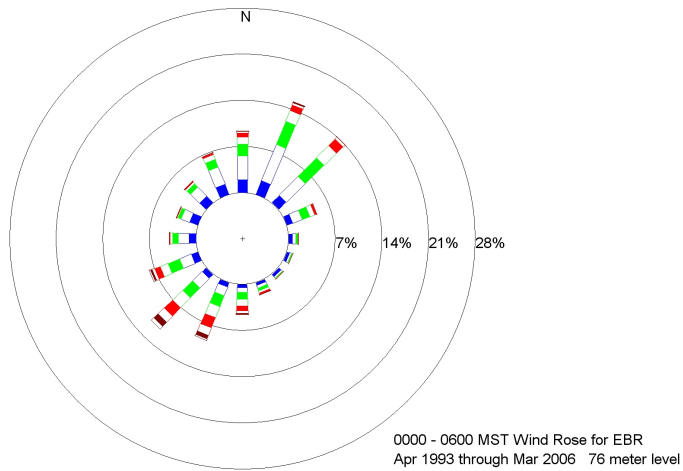
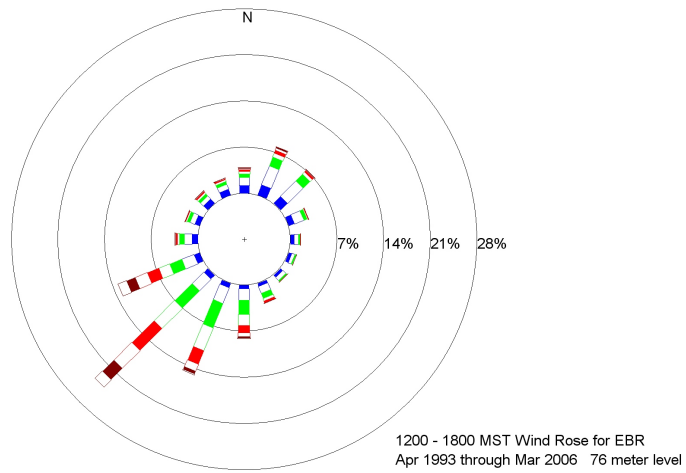


Figure C-14. Day (top), night (middle), and all hours (bottom) wind roses for the 76 meter level at EBR.

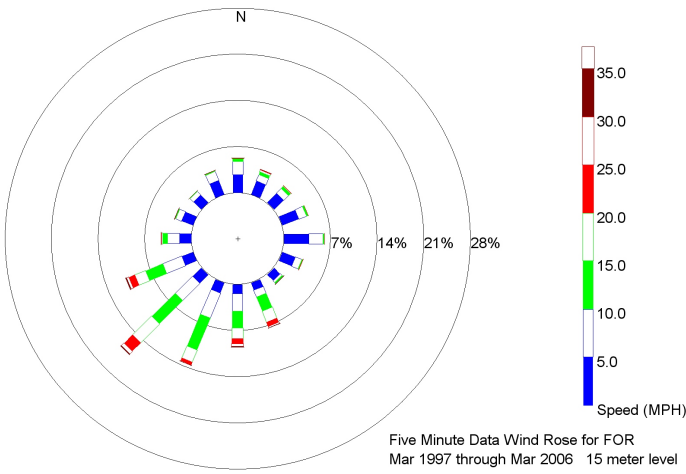
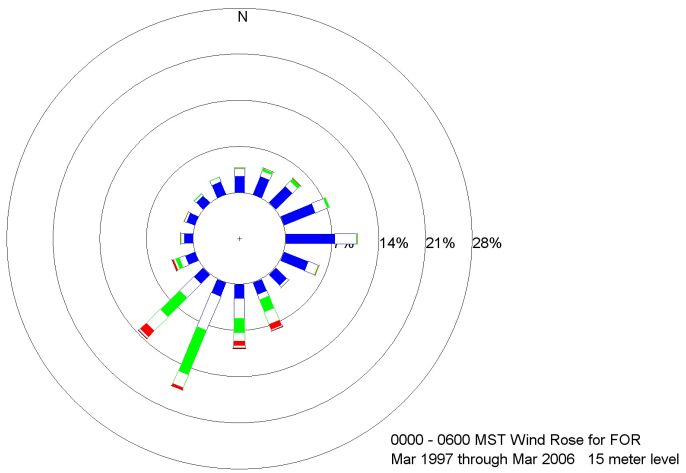
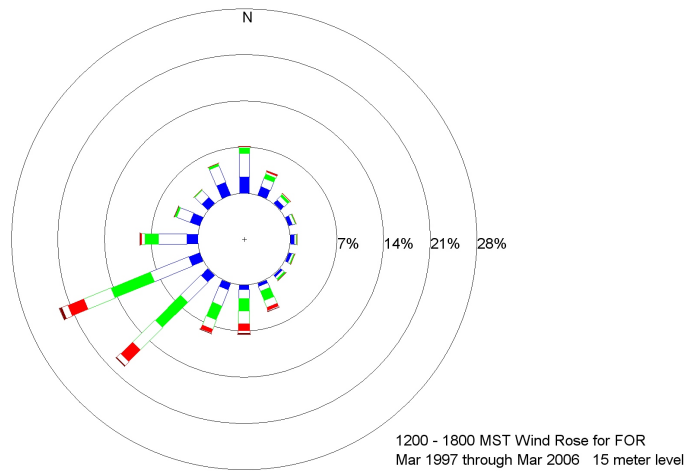


Figure C-15. Day (top), night (middle), and all hours (bottom) wind roses for the 15 meter level at FOR.

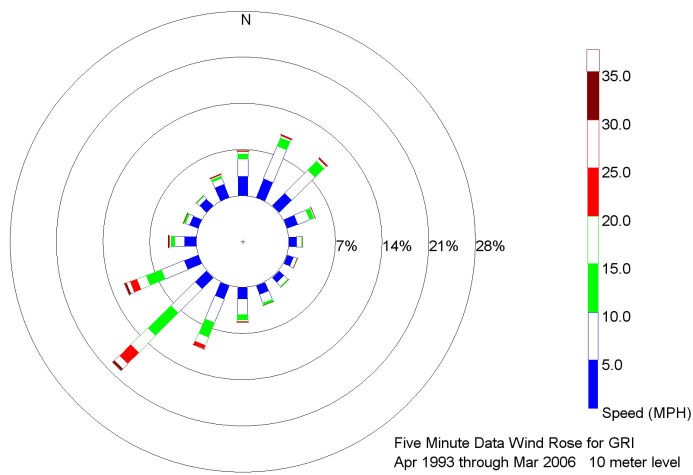
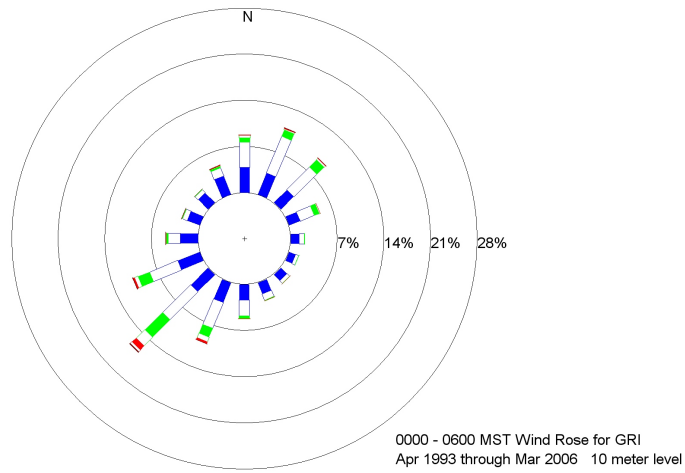
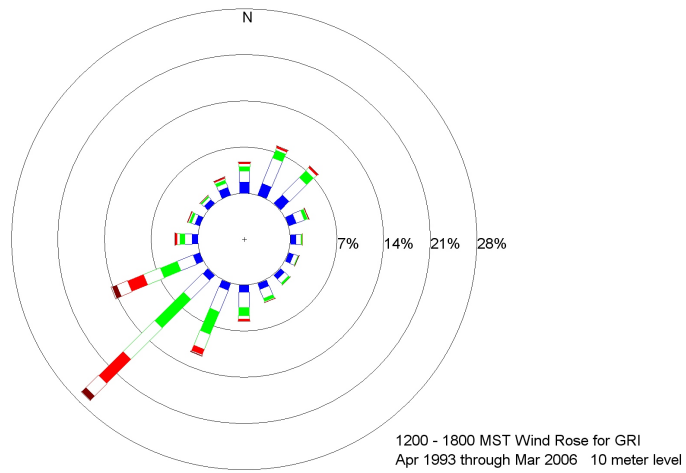


Figure C-16. Day (top), night (middle), and all hours (bottom) wind roses for the 10 meter level at Grid 3.

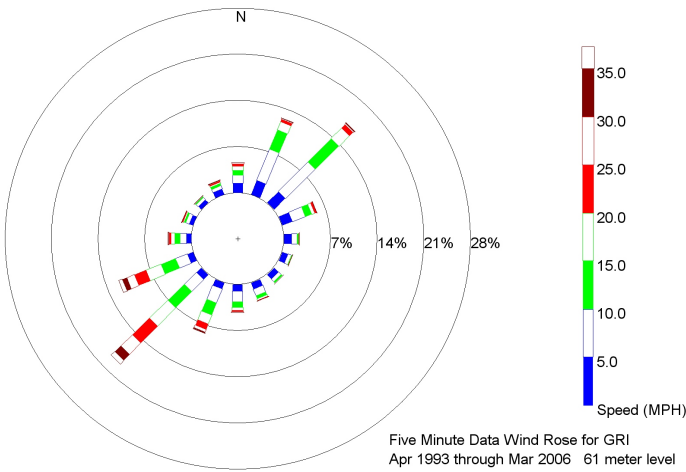
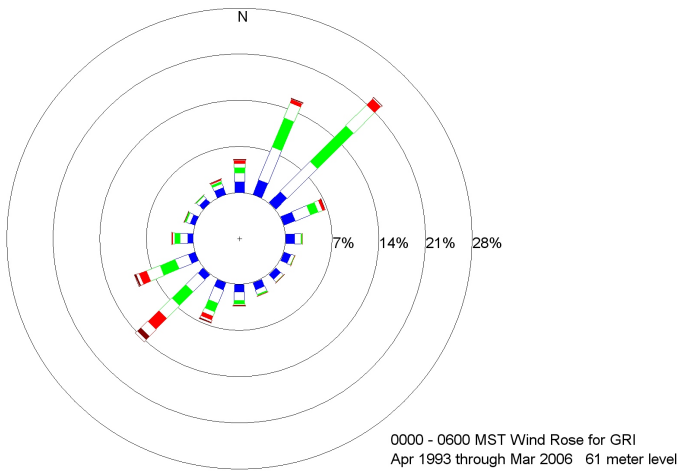
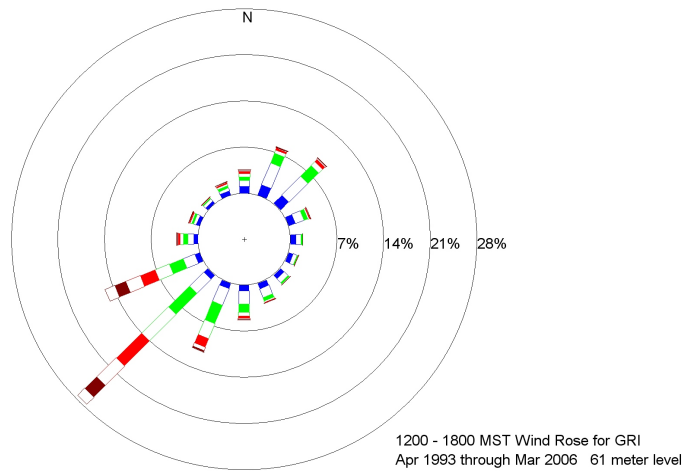


Figure C-17. Day (top), night (middle), and all hours (bottom) wind roses for the 61 meter level at Grid 3.

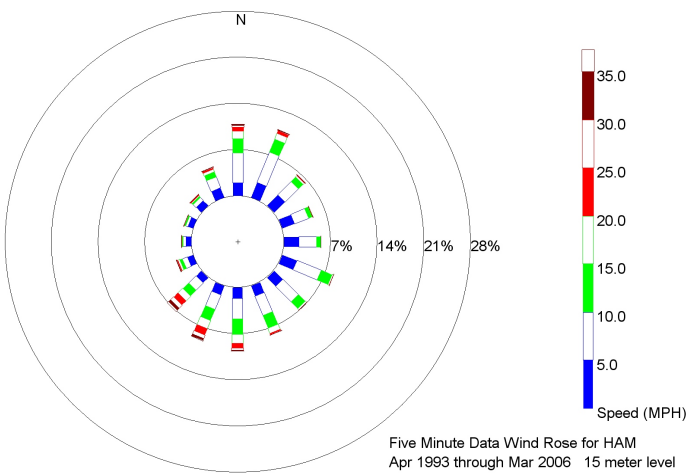
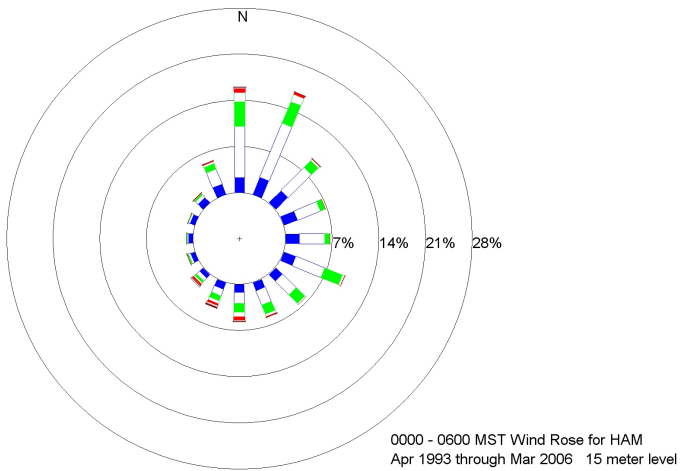
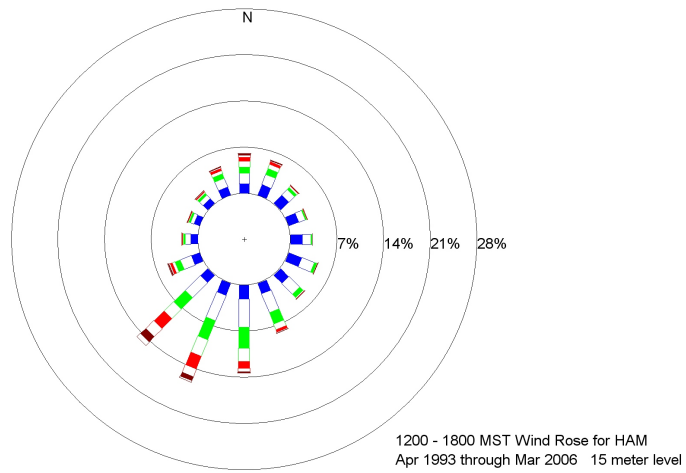


Figure C-18. Day (top), night (middle), and all hours (bottom) wind roses for the 15 meter level at HAM.

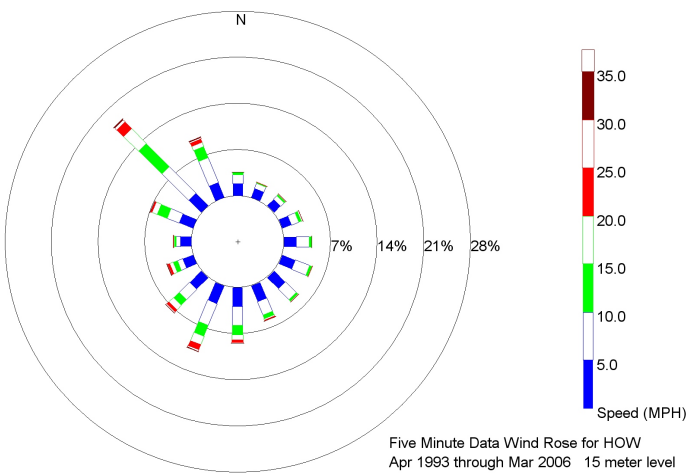
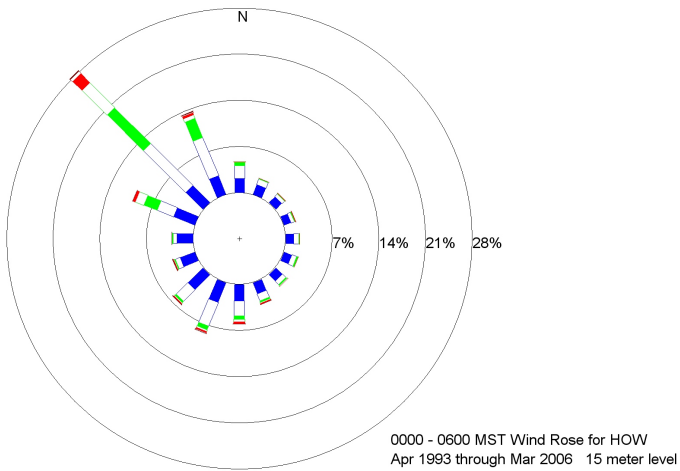
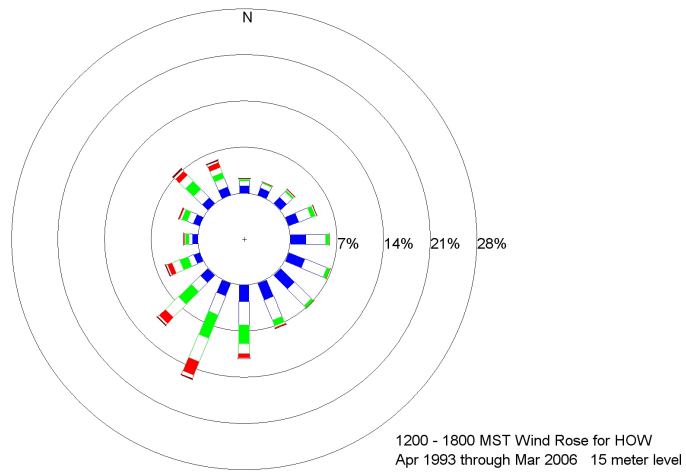


Figure C-19. Day (top), night (middle), and all hours (bottom) wind roses for the 15 meter level at HOW.

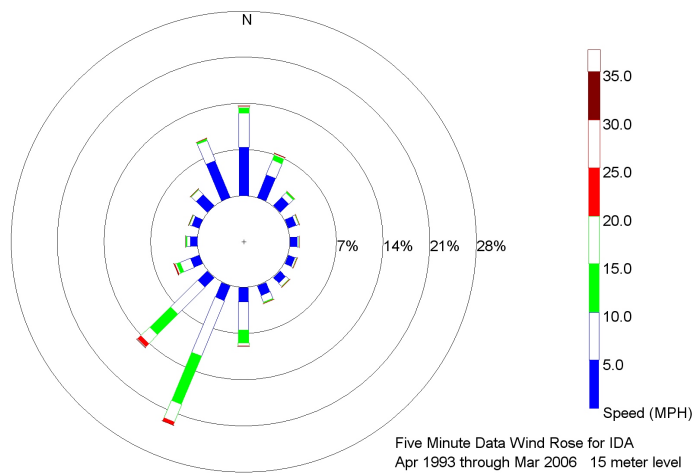
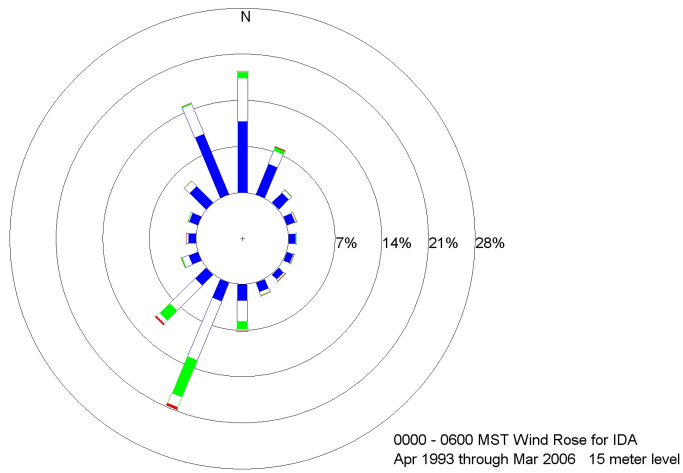
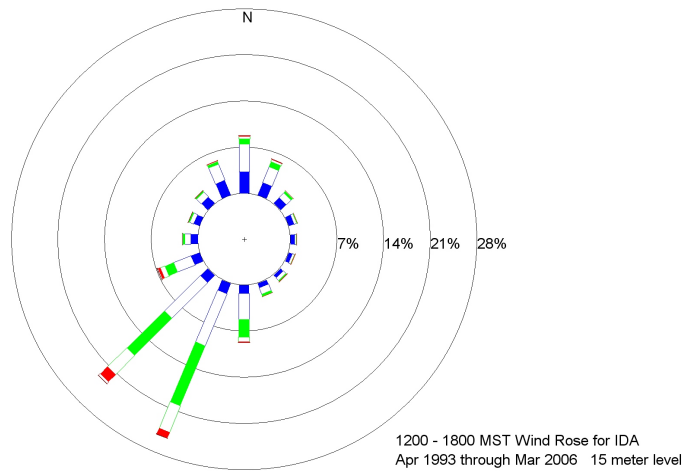


Figure C-20. Day (top), night (middle), and all hours (bottom) wind roses for the 15 meter level at IDA.

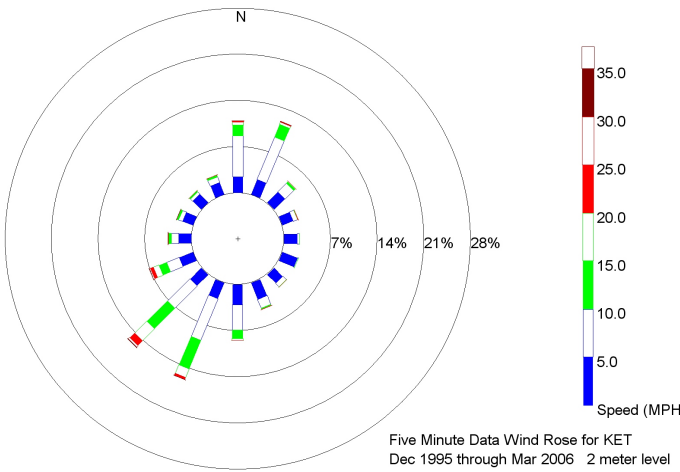
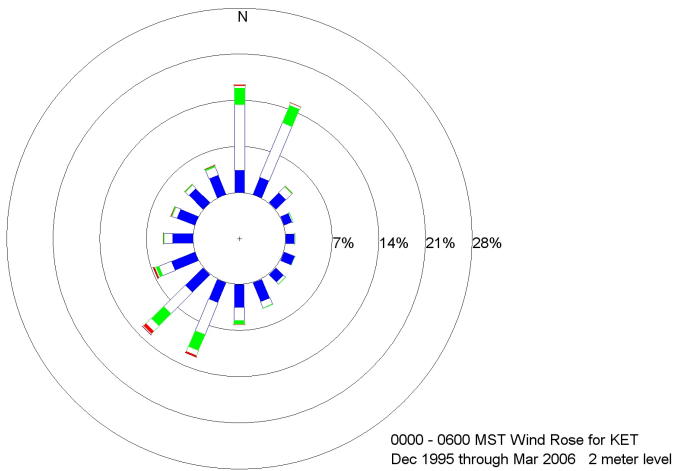
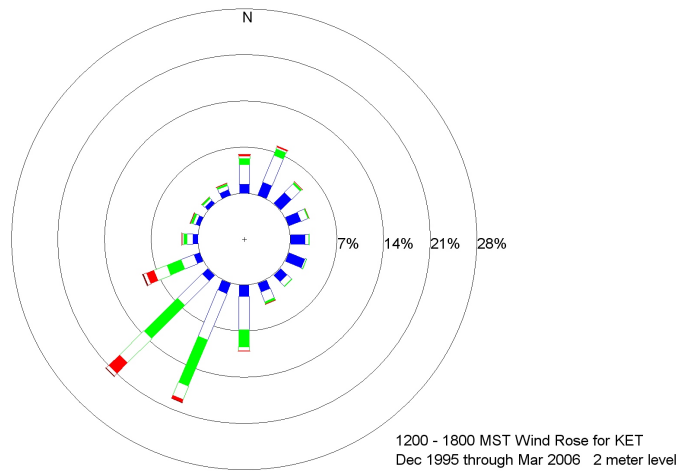


Figure C-21. Day (top), night (middle), and all hours (bottom) wind roses for the 2 meter level at KET.

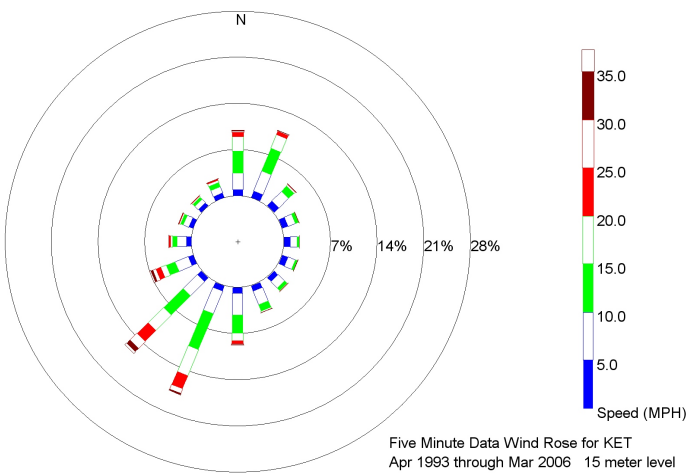
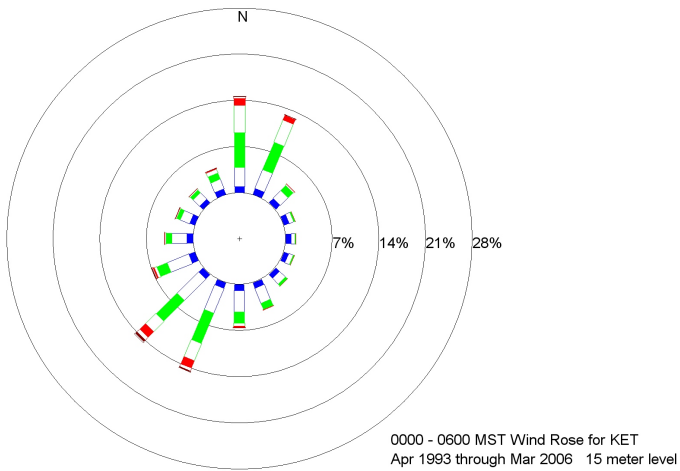
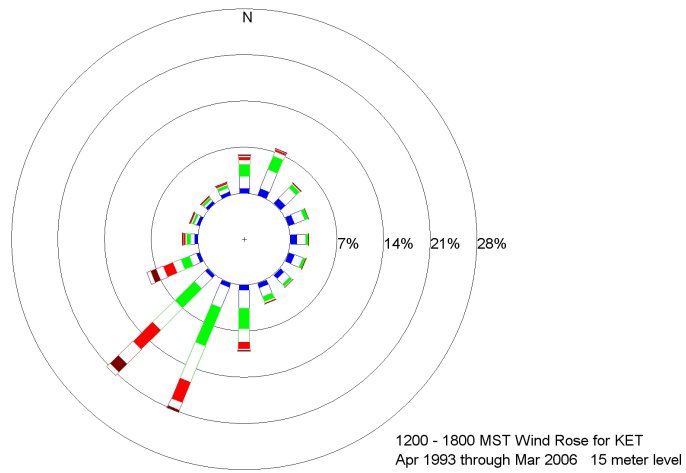


Figure C-22. Day (top), night (middle), and all hours (bottom) wind roses for the 15 meter level at KET.

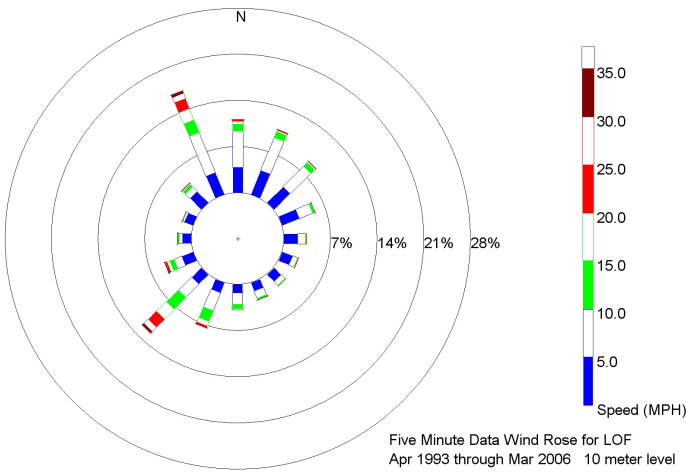
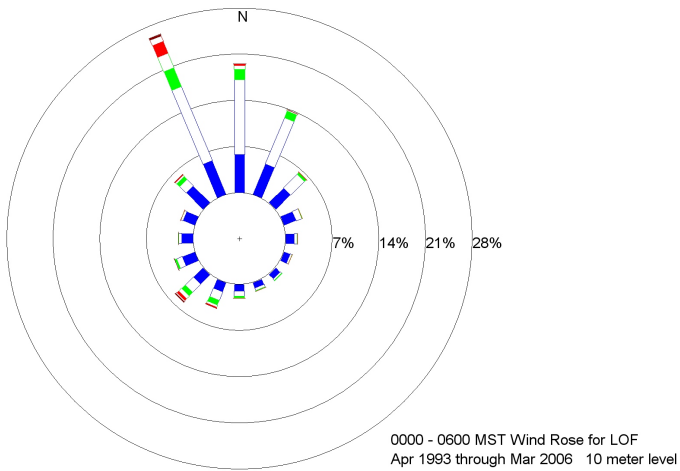
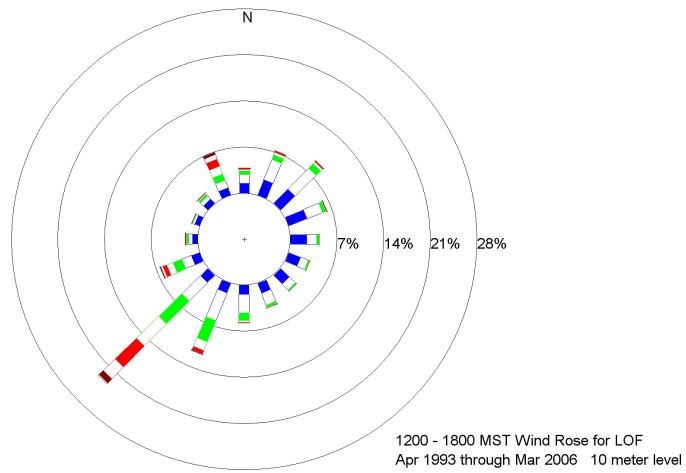


Figure C-23. Day (top), night (middle), and all hours (bottom) wind roses for the 10 meter level at LOF.

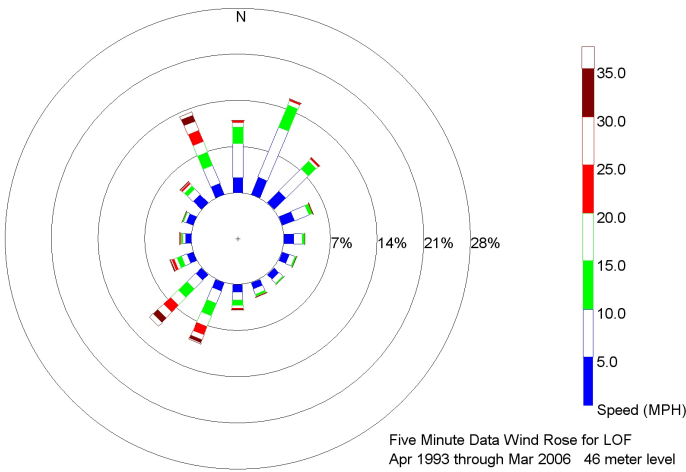
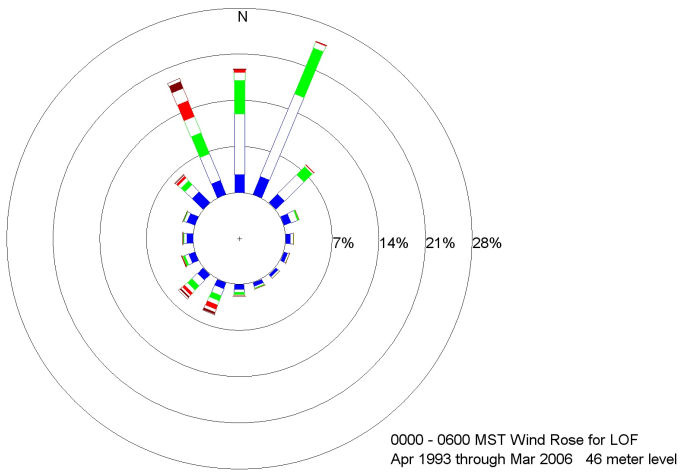
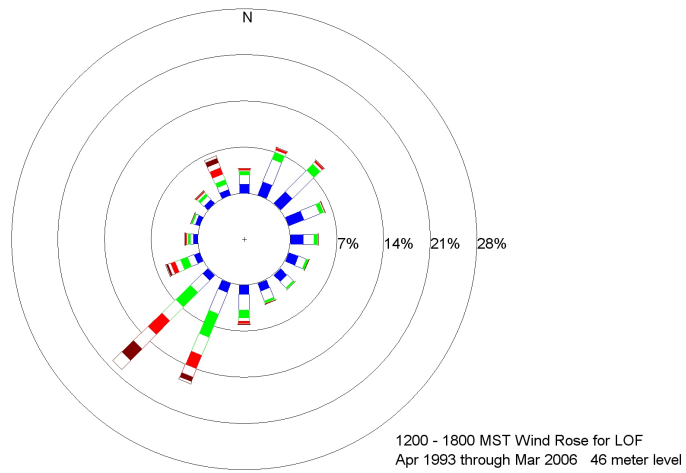


Figure C-24. Day (top), night (middle), and all hours (bottom) wind roses for the 46 meter level at LOF.

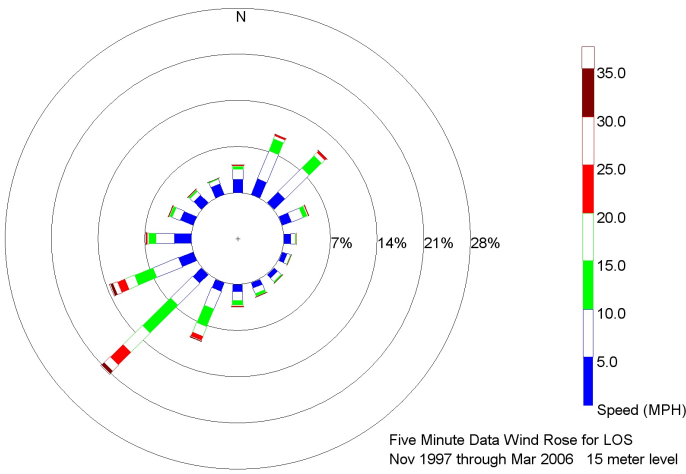
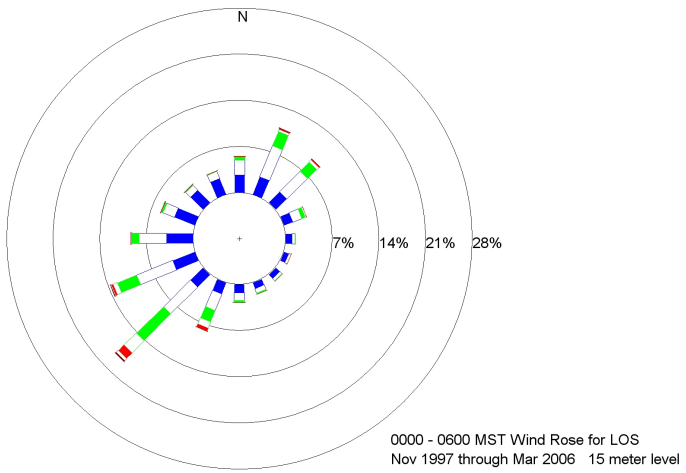
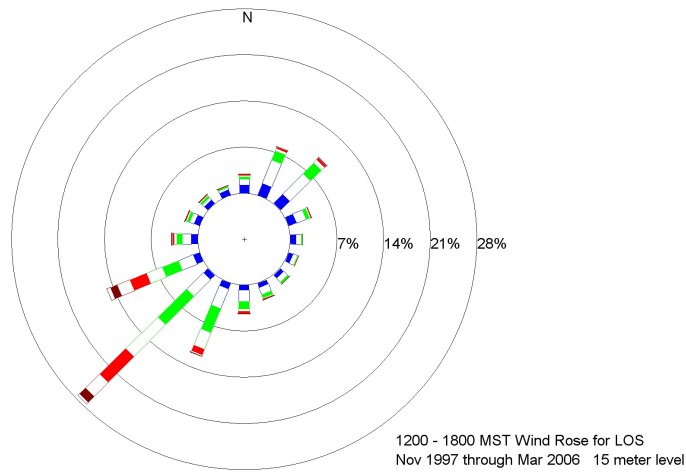


Figure C-25. Day (top), night (middle), and all hours (bottom) wind roses for the 15 meter level at LOS.

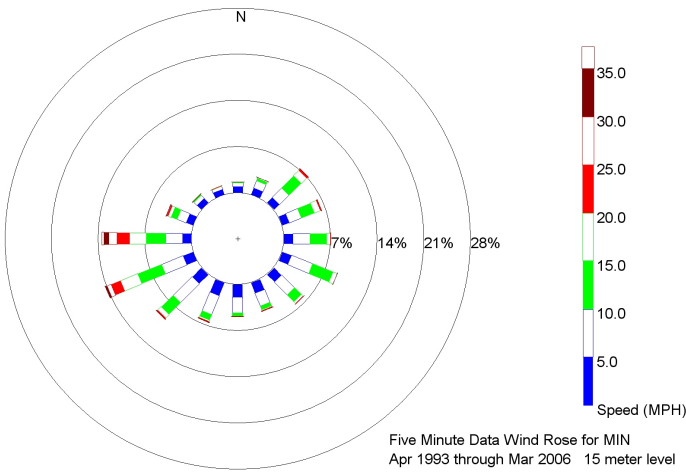
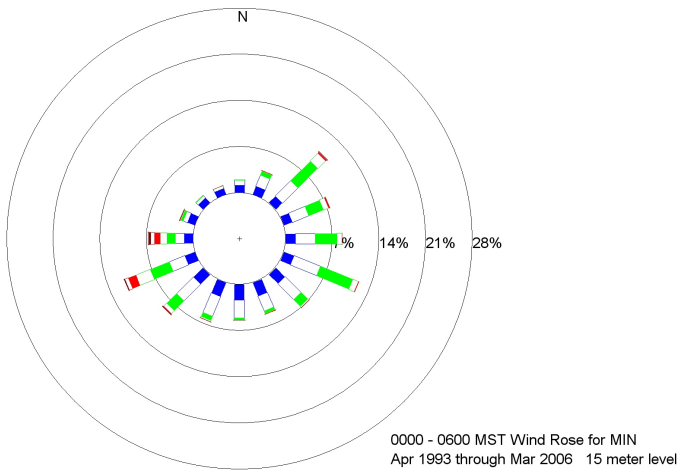
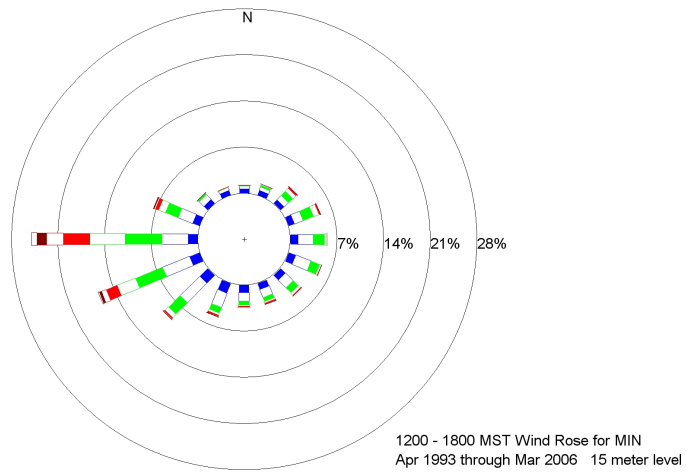


Figure C-26. Day (top), night (middle), and all hours (bottom) wind roses for the 15 meter level at MIN.

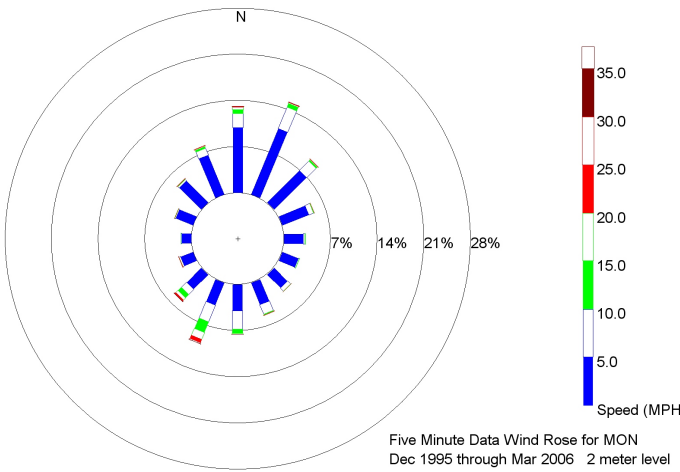
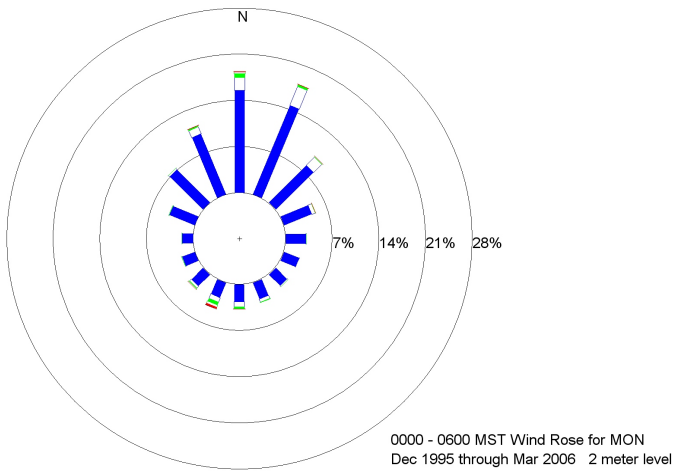
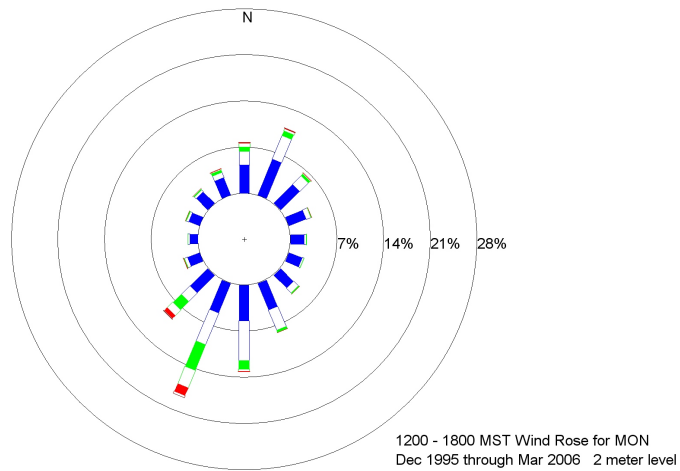


Figure C-27. Day (top), night (middle), and all hours (bottom) wind roses for the 2 meter level at MON.

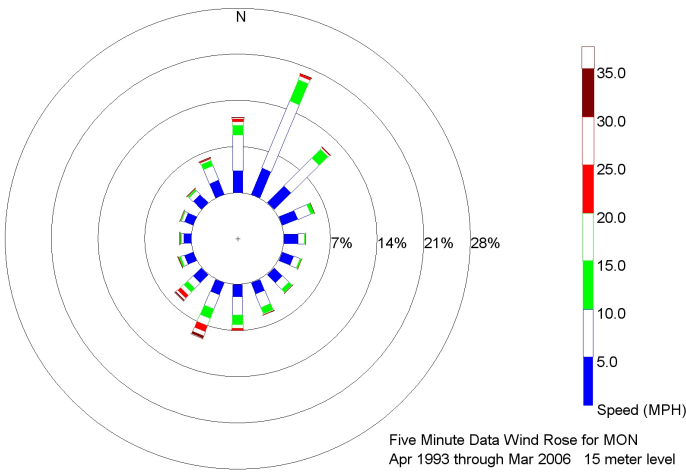
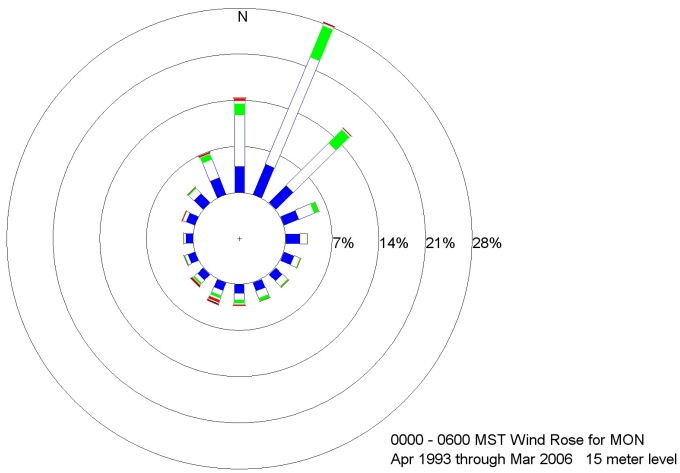
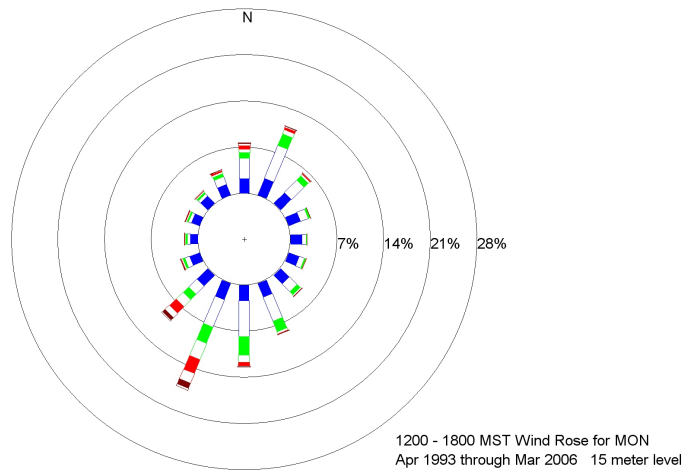


Figure C-28. Day (top), night (middle), and all hours (bottom) wind roses for the 15 meter level at MON.

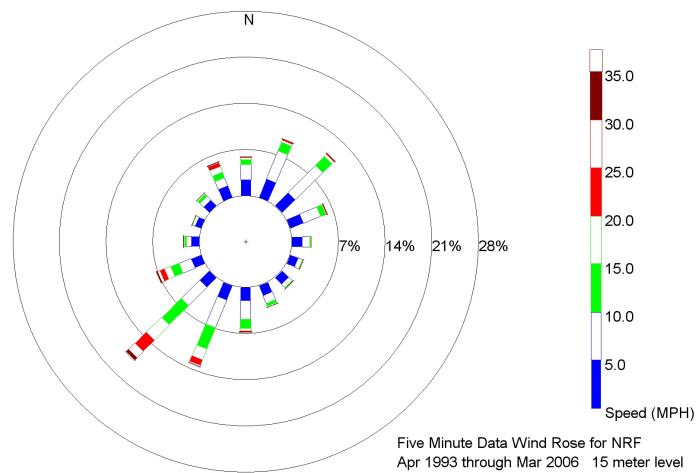
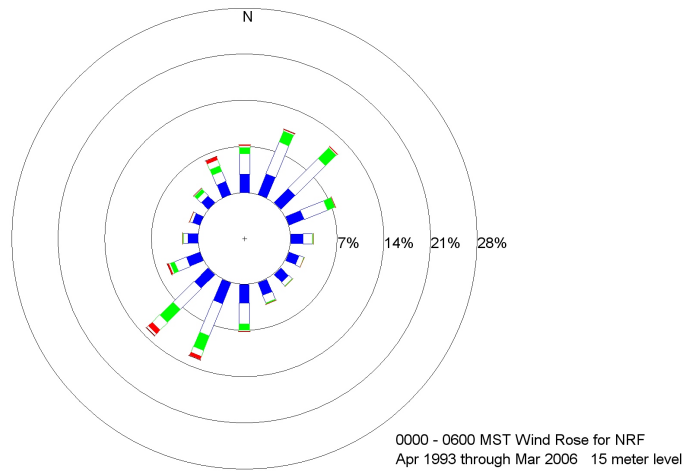
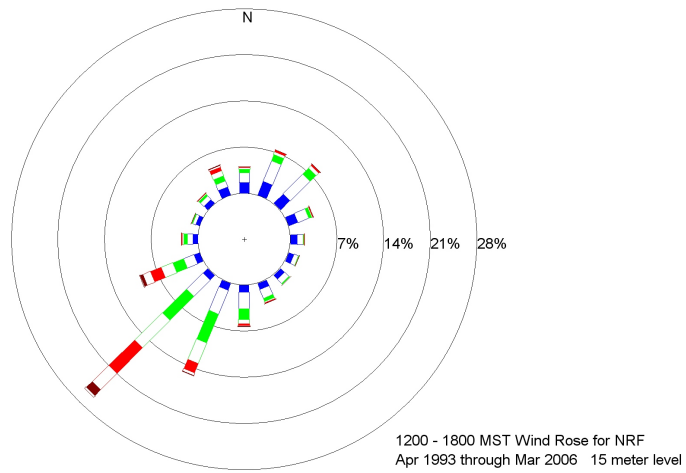


Figure C-29. Day (top), night (middle), and all hours (bottom) wind roses for the 15 meter level at NRF.

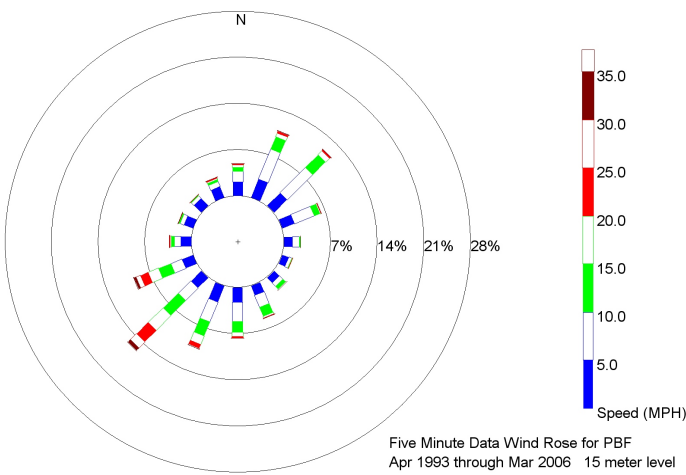
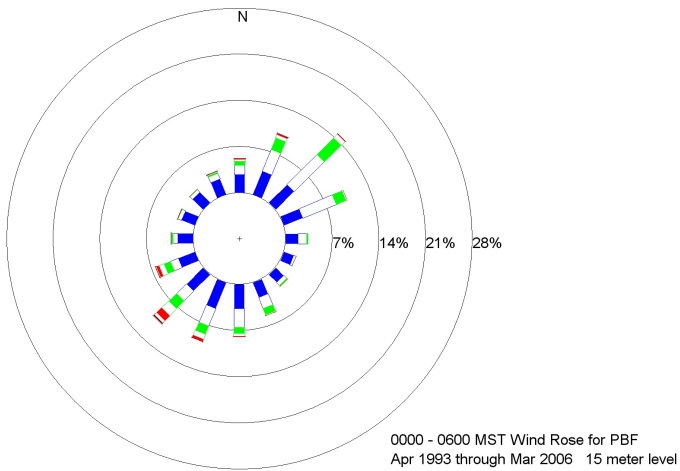
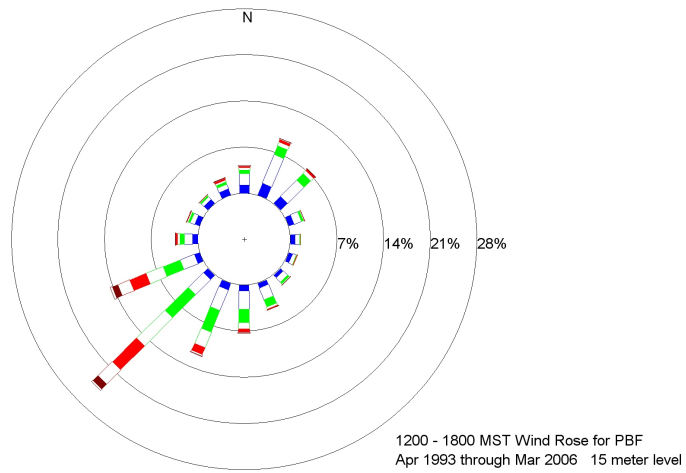


Figure C-30. Day (top), night (middle), and all hours (bottom) wind roses for the 15 meter level at PBF.

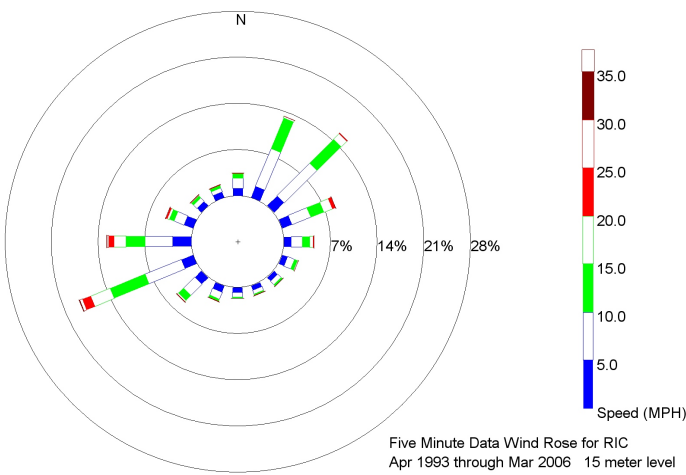
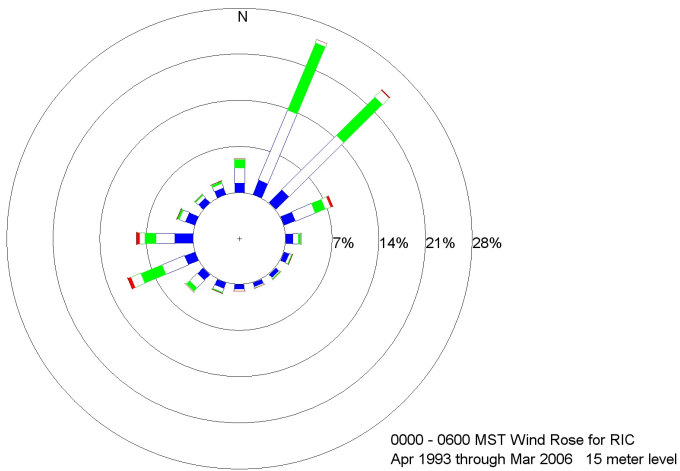
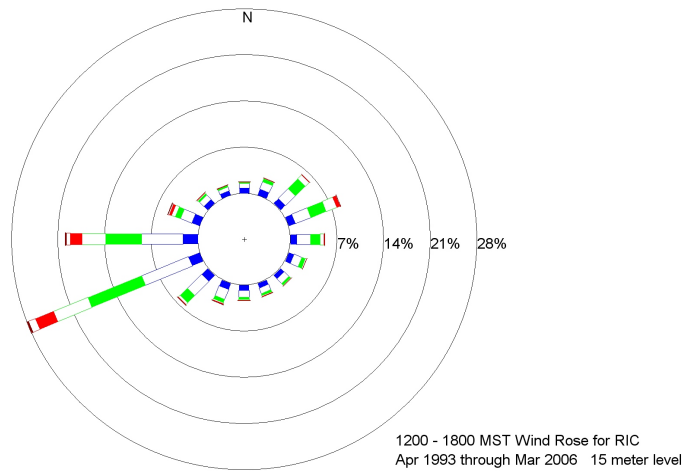


Figure C-31. Day (top), night (middle), and all hours (bottom) wind roses for the 15 meter level at RIC.

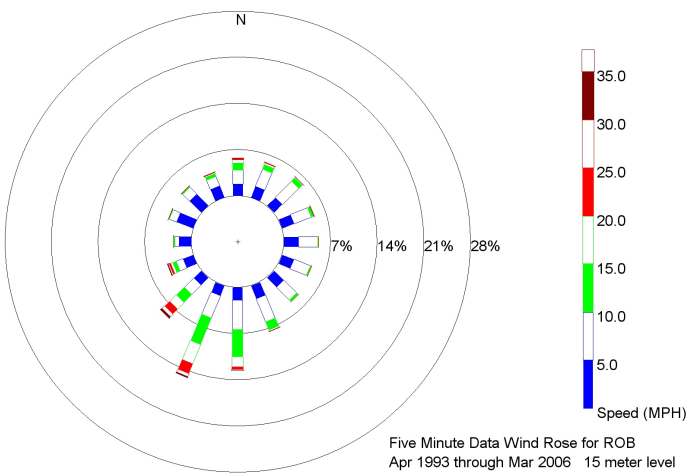
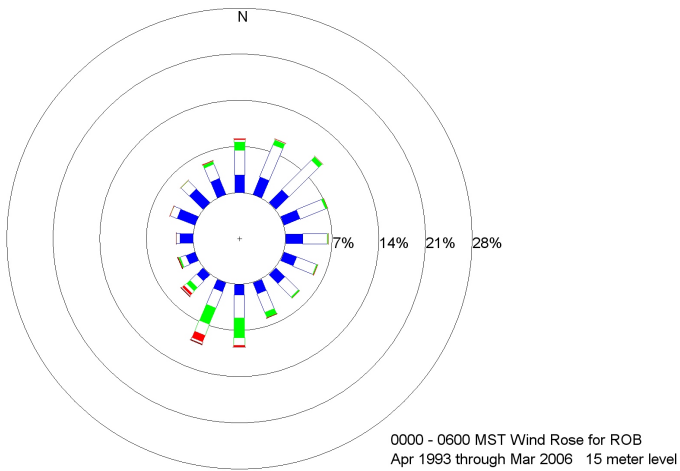
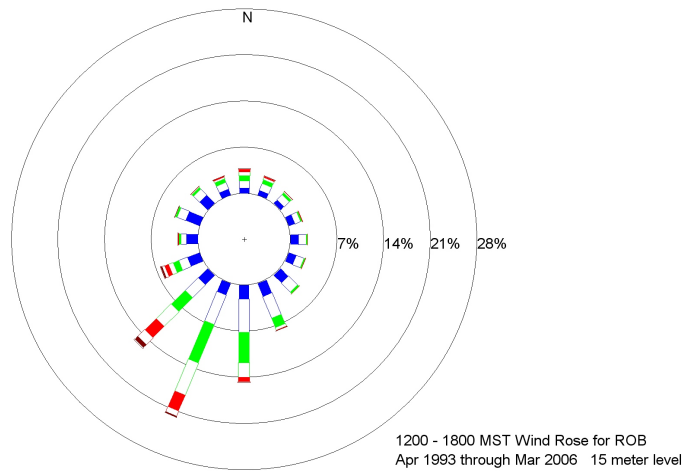


Figure C-32. Day (top), night (middle), and all hours (bottom) wind roses for the 15 meter level at ROB.

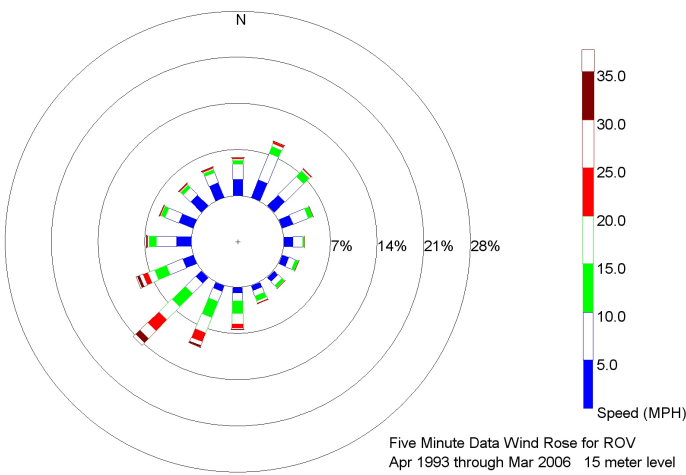
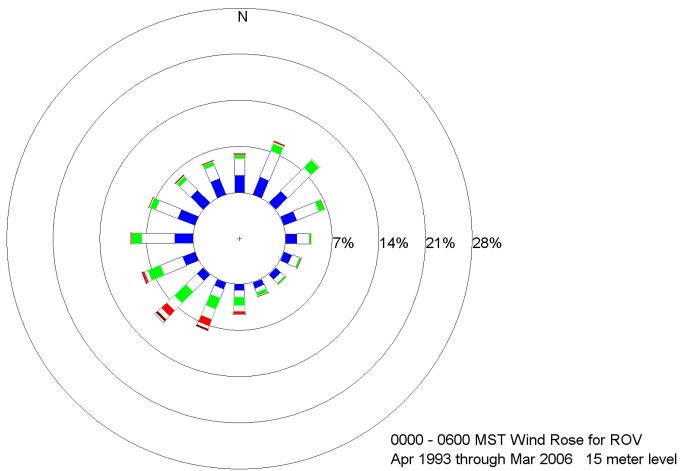
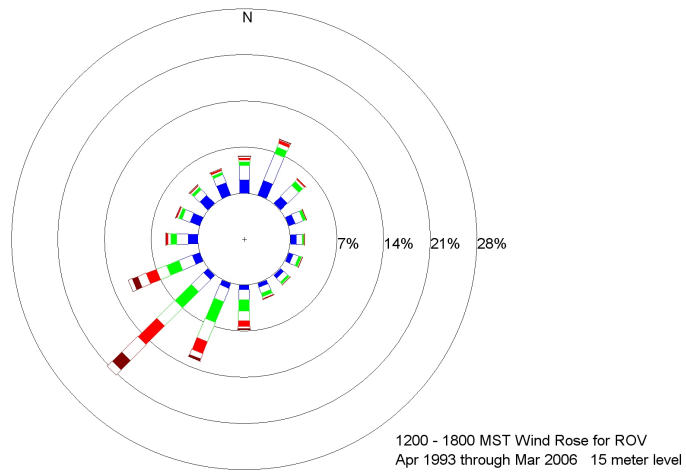


Figure C-33. Day (top), night (middle), and all hours (bottom) wind roses for the 15 meter level at ROV.

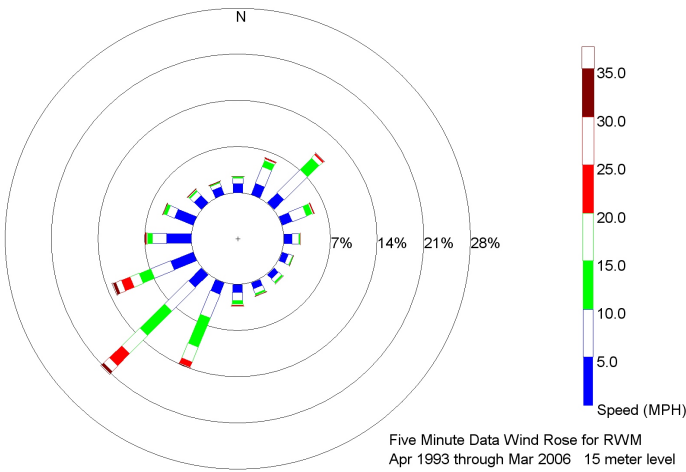
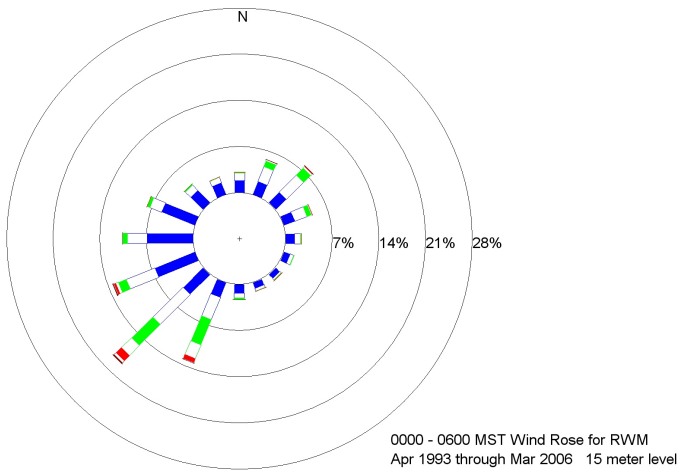
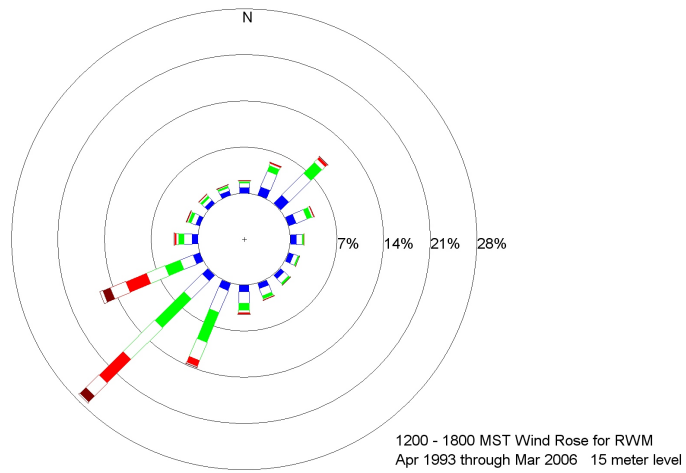


Figure C-34. Day (top), night (middle), and all hours (bottom) wind roses for the 15 meter level at RWM.

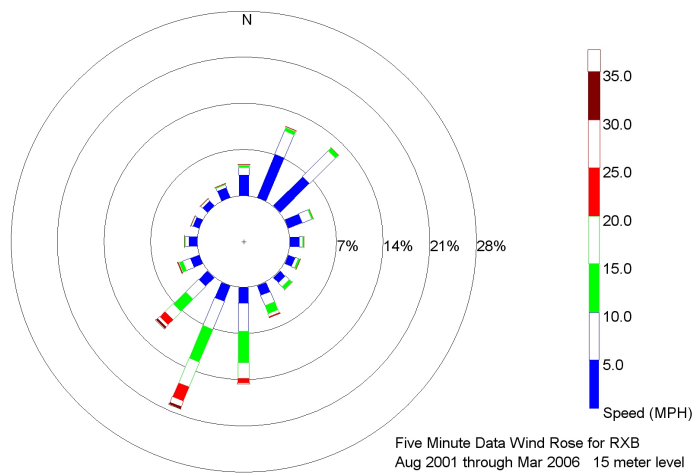
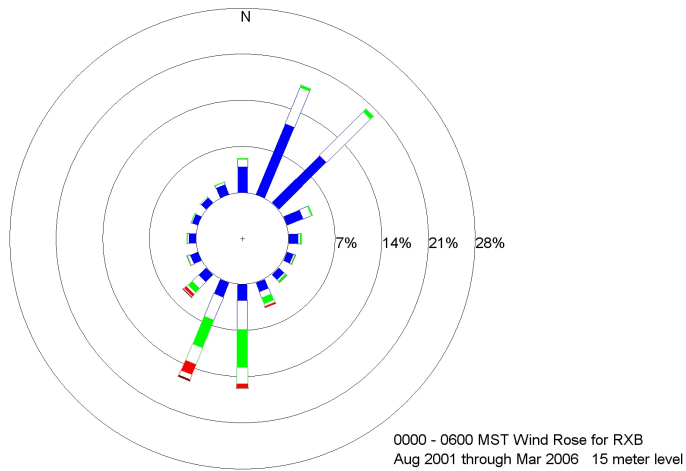
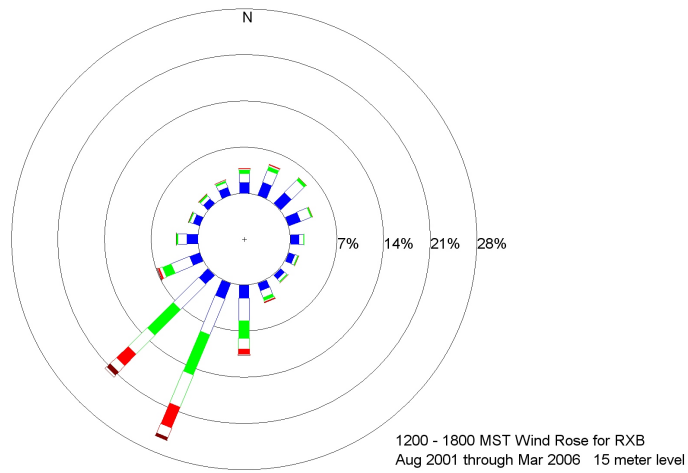


Figure C-35. Day (top), night (middle), and all hours (bottom) wind roses for the 15 meter level at RXB.

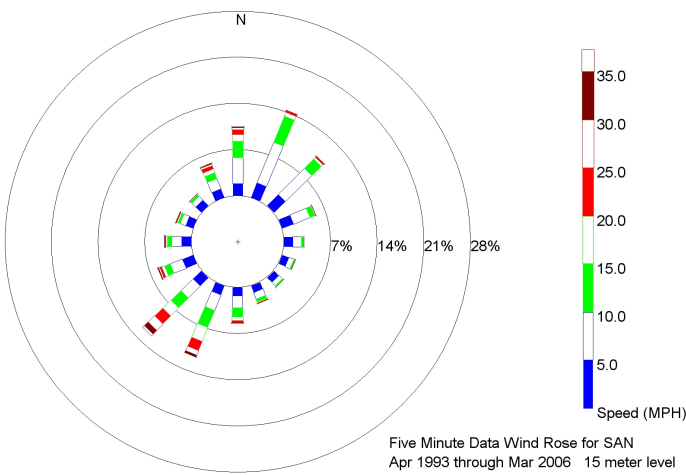
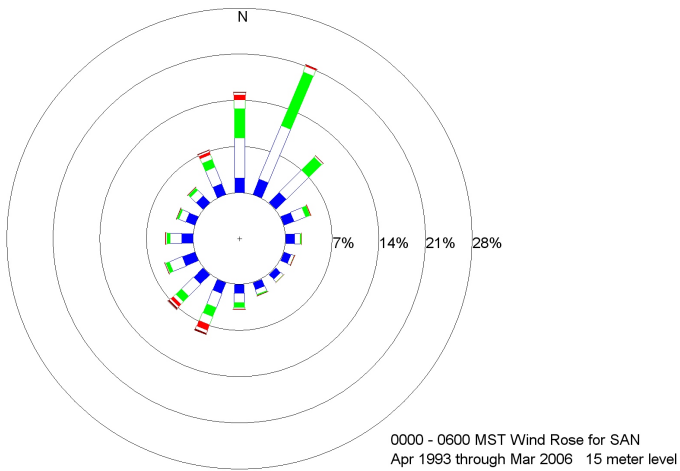
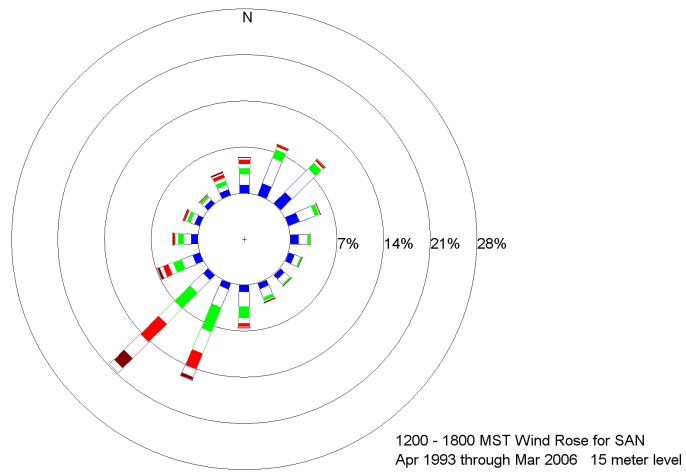


Figure C-36. Day (top), night (middle), and all hours (bottom) wind roses for the 15 meter level at SAN.

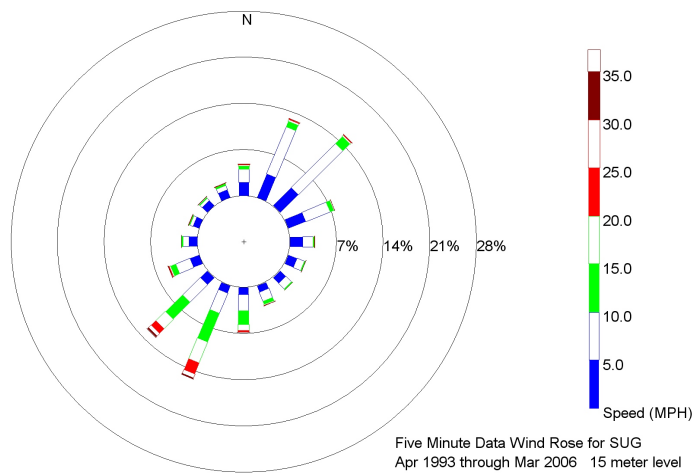
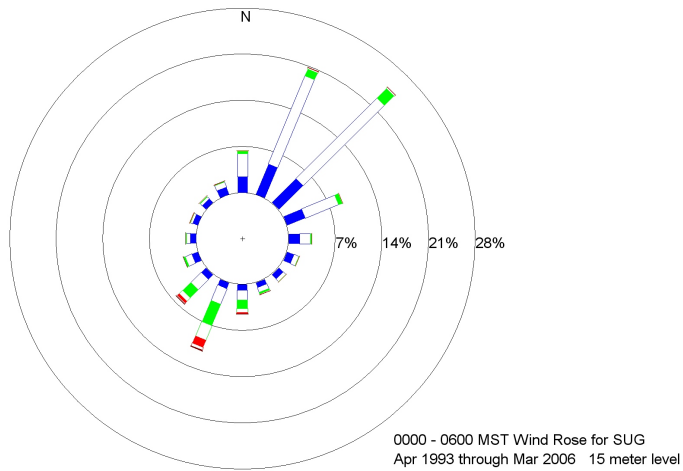
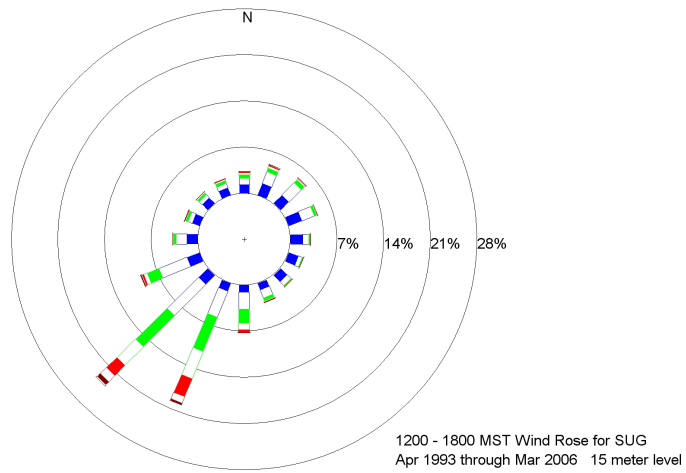


Figure C-37. Day (top), night (middle), and all hours (bottom) wind roses for the 15 meter level at SUG.

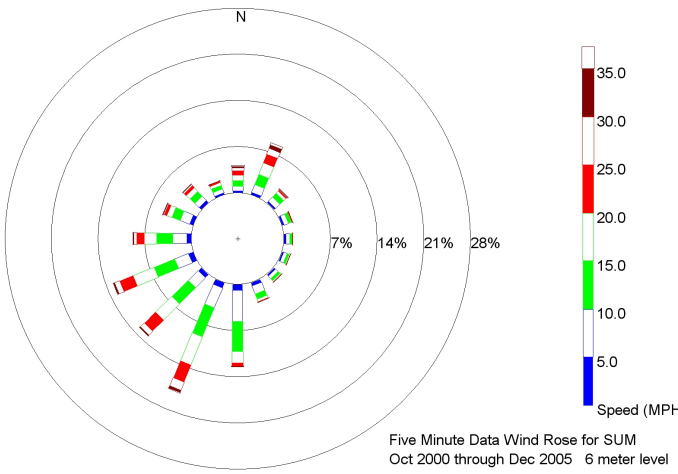
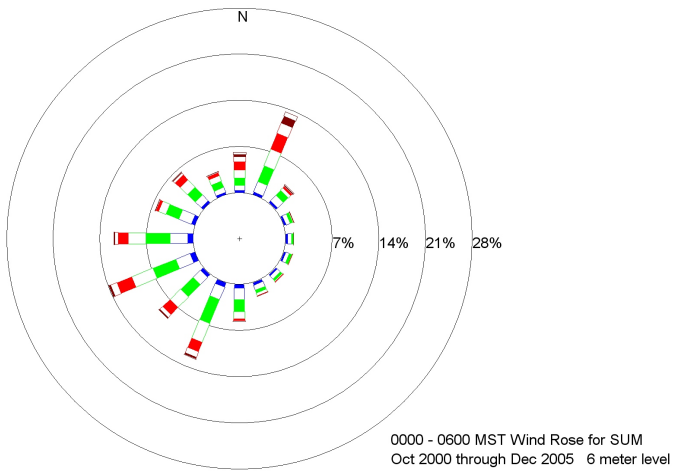
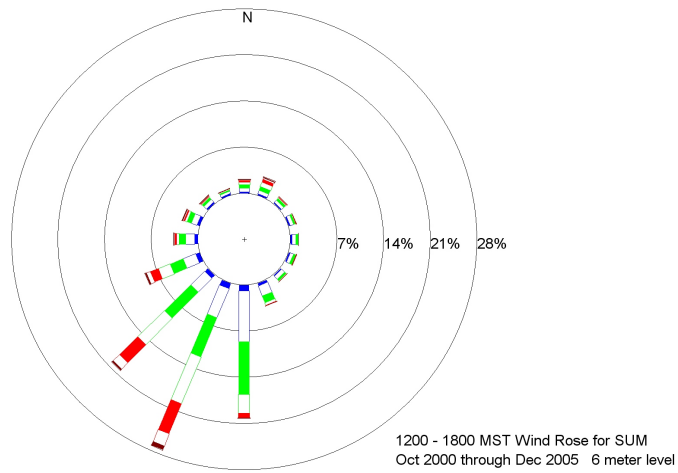


Figure C-38. Day (top), night (middle), and all hours (bottom) wind roses for the 6 meter level at SUM.

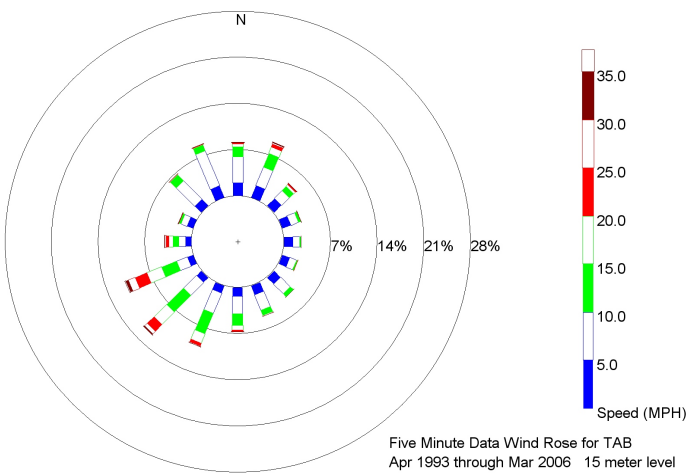
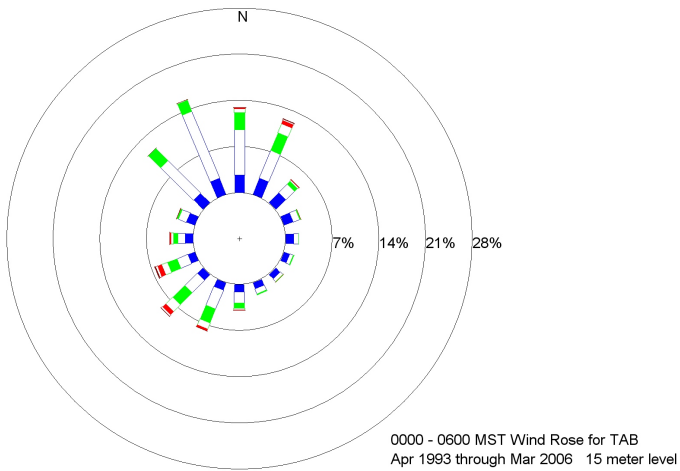
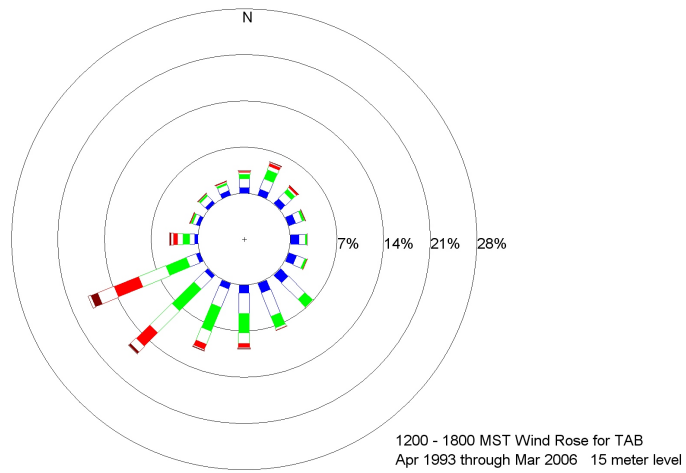


Figure C-39. Day (top), night (middle), and all hours (bottom) wind roses for the 15 meter level at TAB.

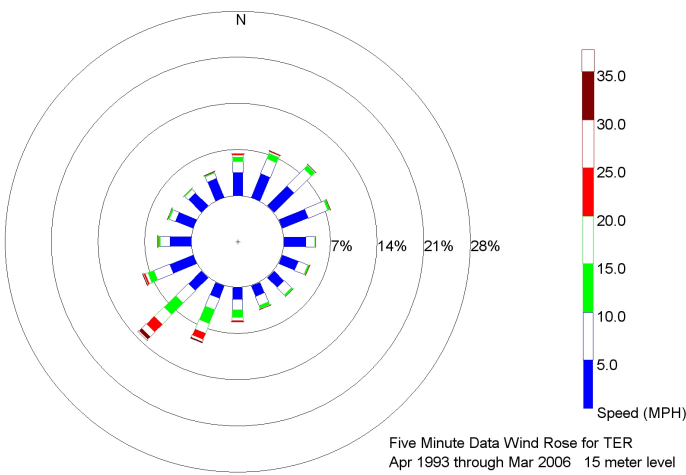
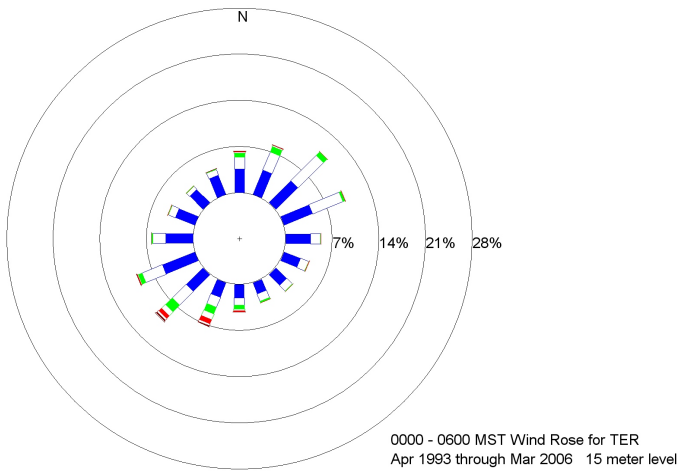
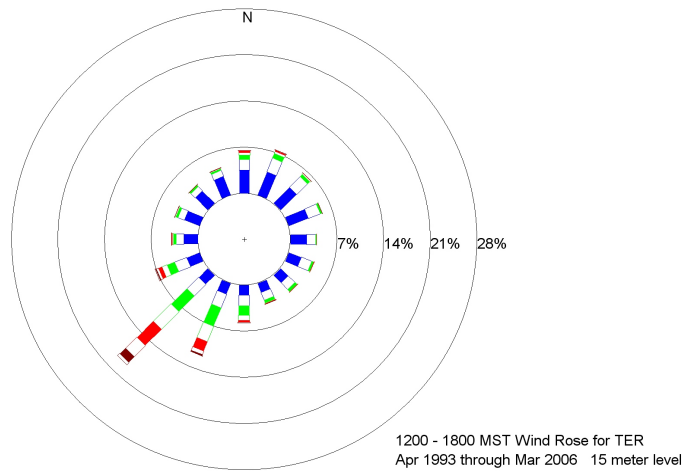


Figure C-40. Day (top), night (middle), and all hours (bottom) wind roses for the 15 meter level at TER.

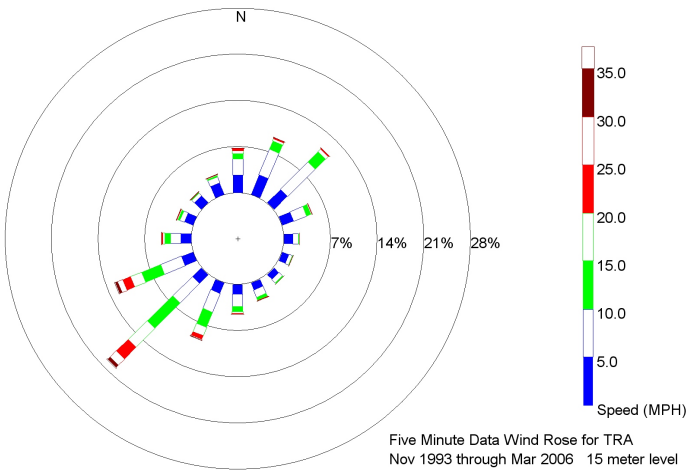
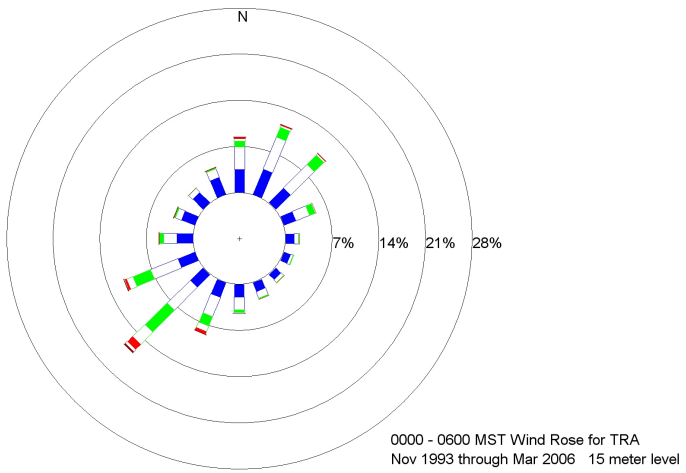
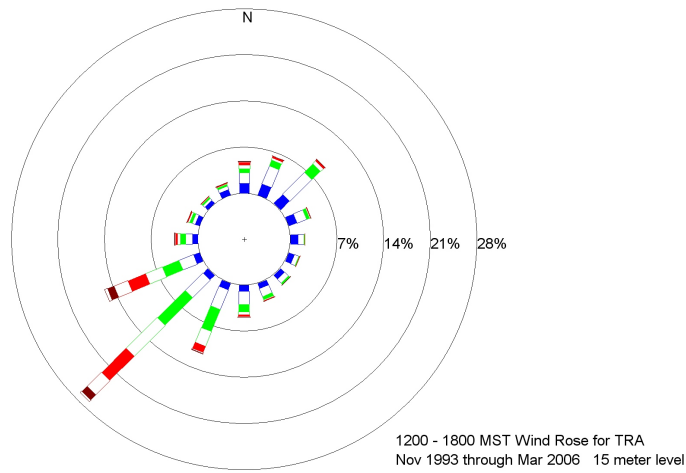


Figure C-41. Day (top), night (middle), and all hours (bottom) wind roses for the 15 meter level at TRA.

APPENDIX D

IMPLICATIONS OF HISTORICAL DATA FROM RELOCATING TOWER LOCATIONS

Researchers must use care when using data from stations that have been relocated. Relocation of a meteorological tower, even over a short distance, can have huge implications on the historical data of that station. Some features that could affect the climatology of stations relocating across the ESRP include the topography (hills and canyons), vegetation, and urban setting. Two stations, Blackfoot and Hamer, were recently relocated. This appendix compares the temperature and wind differences between the old and new locations of these two stations.

BLACKFOOT

The original Blackfoot tower was operational from April 1993 through May 2003. This tower was located approximately 5 miles NW of town at the north end of the road 500 W. The location is on flat open land with sagebrush surrounding the tower. The location is not too close from any buildings and far from the eastern hills of the Blackfoot Mountains. A second tower location was installed at the Blackfoot Middle School to become a community monitoring station in August of 2001. This second location is the current location of the NOAA INL Mesonet Blackfoot location. The tower at the middle school is located in a neighborhood in NW part of town and is somewhat sheltered with houses and trees. The new station is closer to the eastern foothills of the Blackfoot Mountain range. The data time period used in this section is from August 22, 2001 through

May 26, 2003 when both stations were operating at the same time.

Temperature

Figure D-1 and D-2 shows a colored coded diagram of average temperatures by hour and month of the old and new Blackfoot locations, respectively. Figure D-3 shows a similar diagram of the temperature difference (multiplied by 10) between the two stations. Temperatures from the old Blackfoot station were on average 1.5-3.5° F cooler than the new station in the overnight hours. The old station, being out in the open and away from the urban environment, had slightly more radiative cooling which allowed temperatures to be cooler at night than in town. Conversely, the new station temperatures were anywhere from similar to 3.4° F cooler during the daytime hours. Shade trees and green vegetation located at the school and surrounding neighborhood kept the afternoon temperatures down compared to the open, desert like area of the old station.

Winds

Figure D-4 and D-5 shows a wind rose for the old and new Blackfoot station. These wind roses showed the most common wind direction for both stations were out of the SW. However the frequency of the SW winds was slightly higher for the new station. Even though SW winds were more frequent at the new station, the overall winds speeds were much greater at the old station. The buildings,

houses and trees in the city may shelter the tower location at the middle school. The urban environment causes some turbulence in the wind flow that decreases the intensity as the winds at they move across the city.

Another feature evident by the wind roses is the NE winds that are typically found at night. The old station has a more frequent and slightly stronger NE wind component

than the new station. However, an isolated SSE wind is found at the new station and not at the old station. This is a topographic feature. The new station is receiving a down canyon or diurnal flow out of the eastern foothills at night. The old station being further out in the plain is far enough away from the eastern foothills to be affected by this microclimate feature from the Blackfoot Mountain Range.

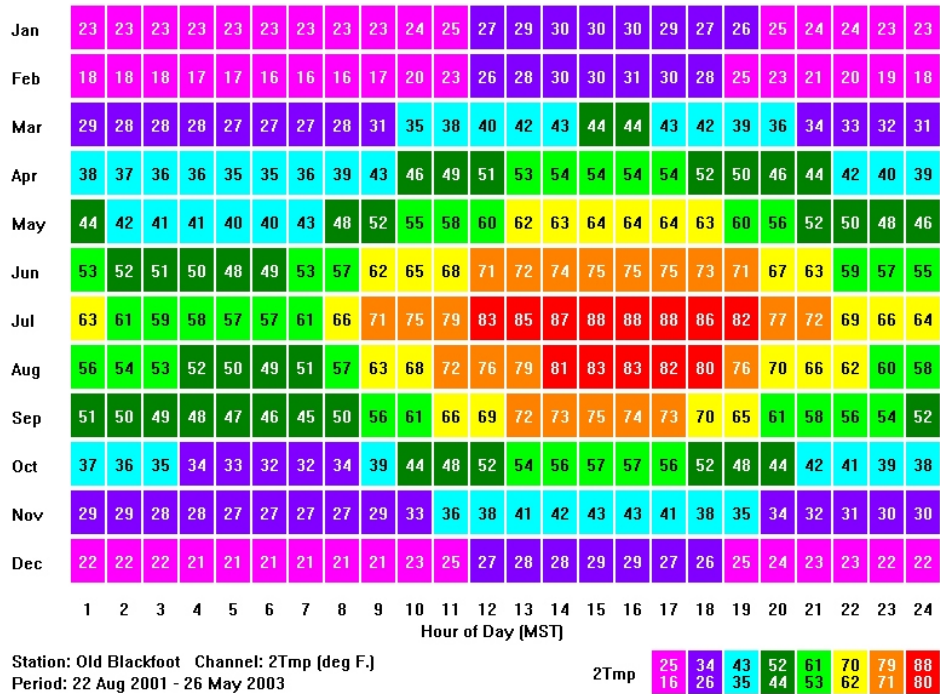


Figure D-1. Average temperatures by hour and month of the old Blackfoot Mesonet station from 22 August, 2001 through 26 May, 2003.

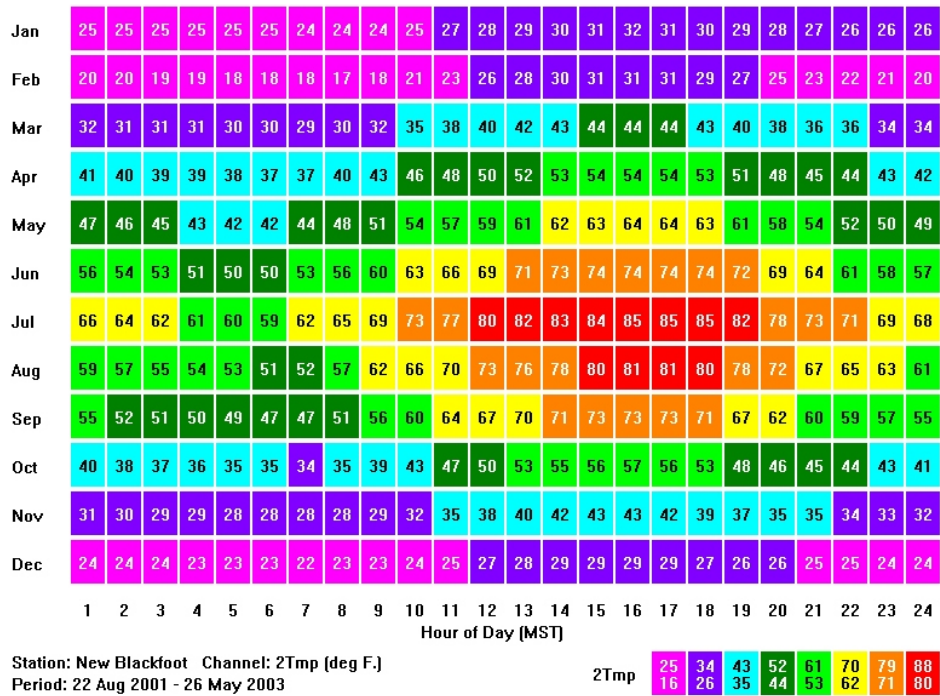


Figure D-2. Average temperatures by hour and month of the new Blackfoot Mesonet station from 22 August, 2001 through 26 May, 2003.

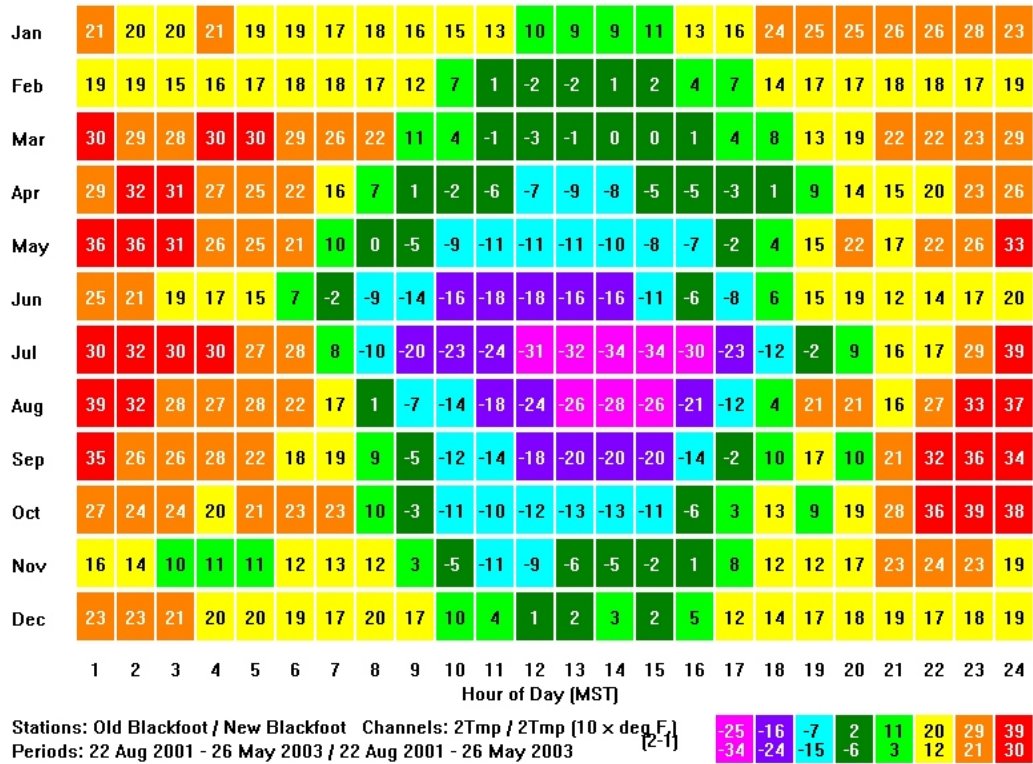


Figure D-3. Temperature difference (multiplied by 10) between the new and old Blackfoot Mesonet station between 22 August 2001 and 26 May 2003.

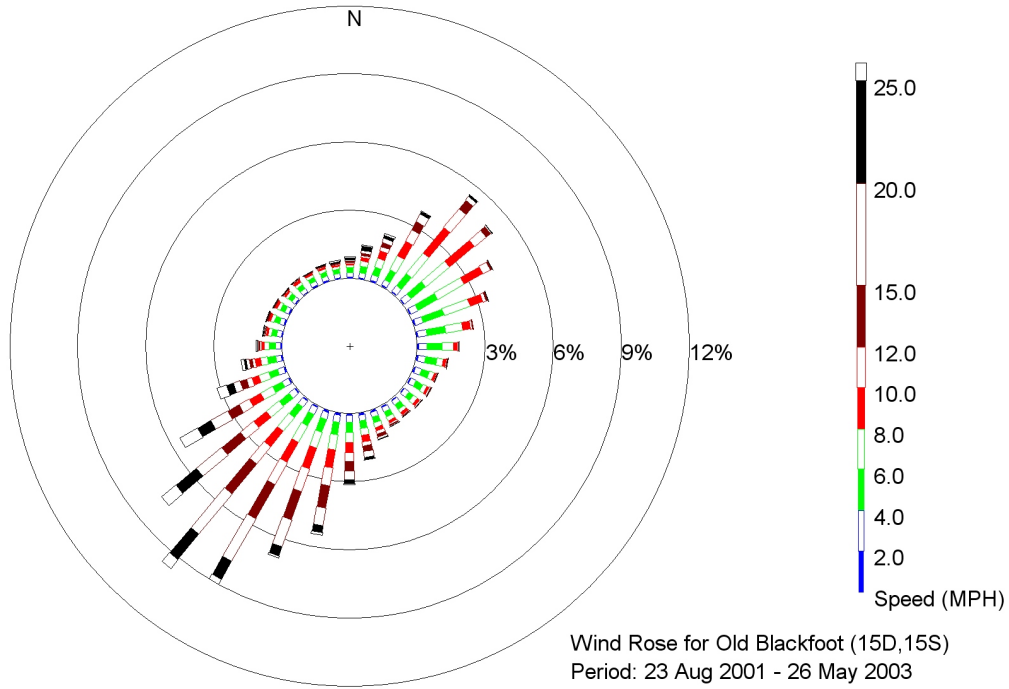


Figure D-4. Wind rose for the old Blackfoot Mesonet station from 23 August 2001 through 26 May 2003.

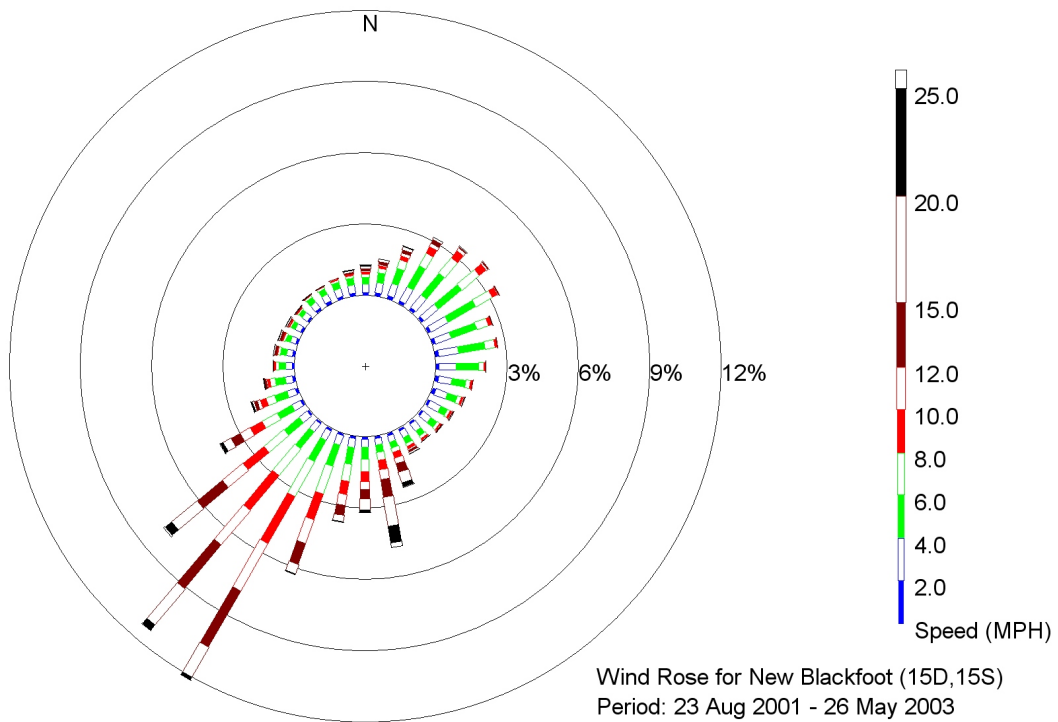


Figure D-5. Wind rose for the new Blackfoot Mesonet station from 23 August 2001 through 26 May 2003.

HAMER

The original Hamer tower was began operating in April 1993. The tower location was located on top of a small hill or butte (250 feet above valley floor) approximately 4.5 miles SE of Camas or approximately 10 miles SW of the St. Anthony Sand Hills. The location on top of the hill is open, surrounded by sagebrush and not too close to any buildings or trees. In September 1999, the landowner installed a linear sprinkling system and required that the station be relocated. This same tower was moved near Camas in January 2000 where it is operational today. The new location is in the open valley and is far away from any buildings or trees. This section compares the averages of the entire period record for each station. Since the station was moved no overlapping of data exists.

Temperature

Figure D-6 and D-7 shows a colored coded diagram on average temperatures by hour and month of the old and new Hamer locations, respectively. Figure D-8 shows a similar diagram of the temperature difference (multiplied by 10) between the two stations. Temperatures from the old Hamer station were up to 8.5° F cooler on winter mornings

than at the new station. This is due to temperature inversions in the winter, where cooler air sinks to the valley floor while the mountains including the nearby hills stay slightly warmer. Conversely, the new Hamer station temperatures were up to 7.8° F warmer during the summer months than the old station. This is also due to the elevation difference of the two stations where afternoon temperatures are usually warmer in lower elevations.

Winds

Figure D-9 and D-10 show a wind rose for the old and new Hamer station, respectively. The new Hamer wind rose showed a typical pattern of stations located in the middle of the plain. The two most frequent wind directions were either from the NNE (that usually occurs at night) or SW (usually occurs during the day) that are the typical diurnal flows of the ESRP. However, the old Hamer station has a less frequent N wind component and an ESE component of the wind that the new station does not measure. This ESE wind feature is topographic. The sand hills are close enough that the diurnal flow at night moves around the sand hills and reaches the old station from the ESE. The new Hamer station is far enough west and north to be affected by the St. Anthony sand hills.

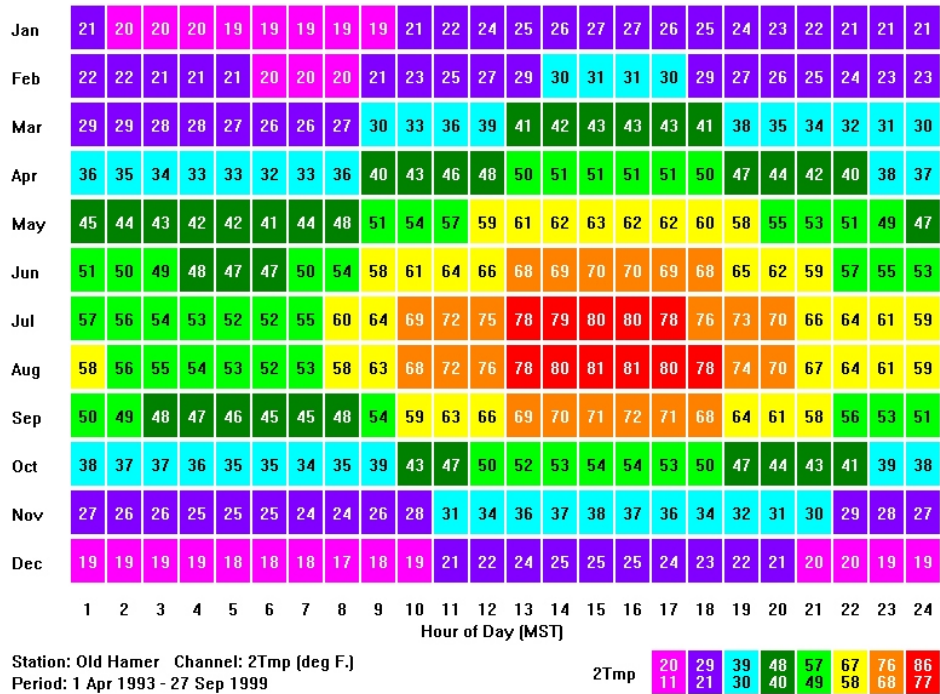


Figure D-6. Average temperatures by hour and month of the old Hamer Mesonet station from 1 April 1993 through 27 September 1999.

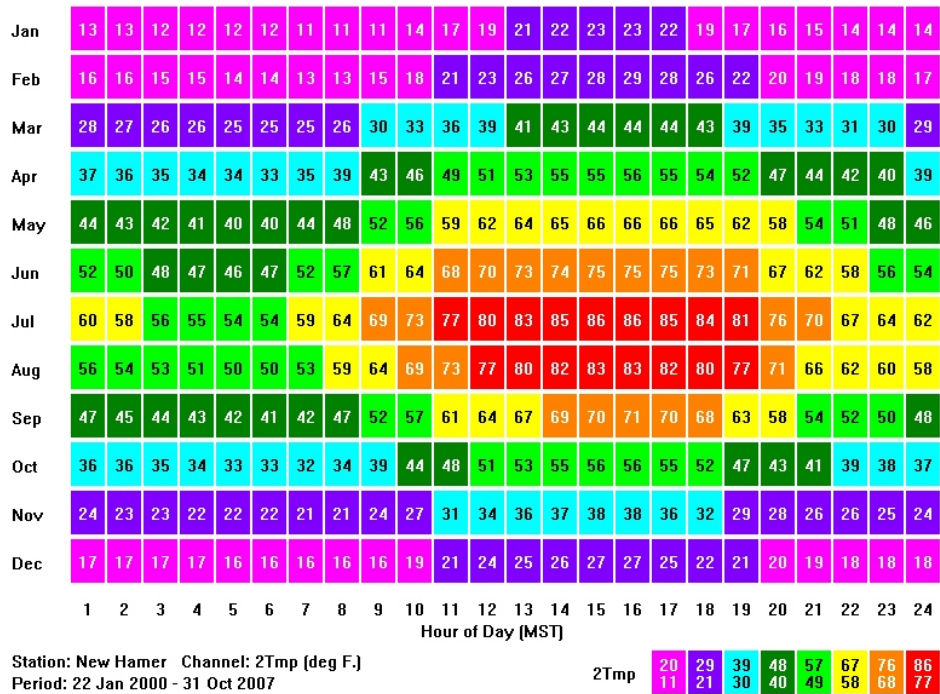


Figure D-7. Average temperatures by hour and month of the new Hamer Mesonet station from 22 January 2000 through 31 October 2007.

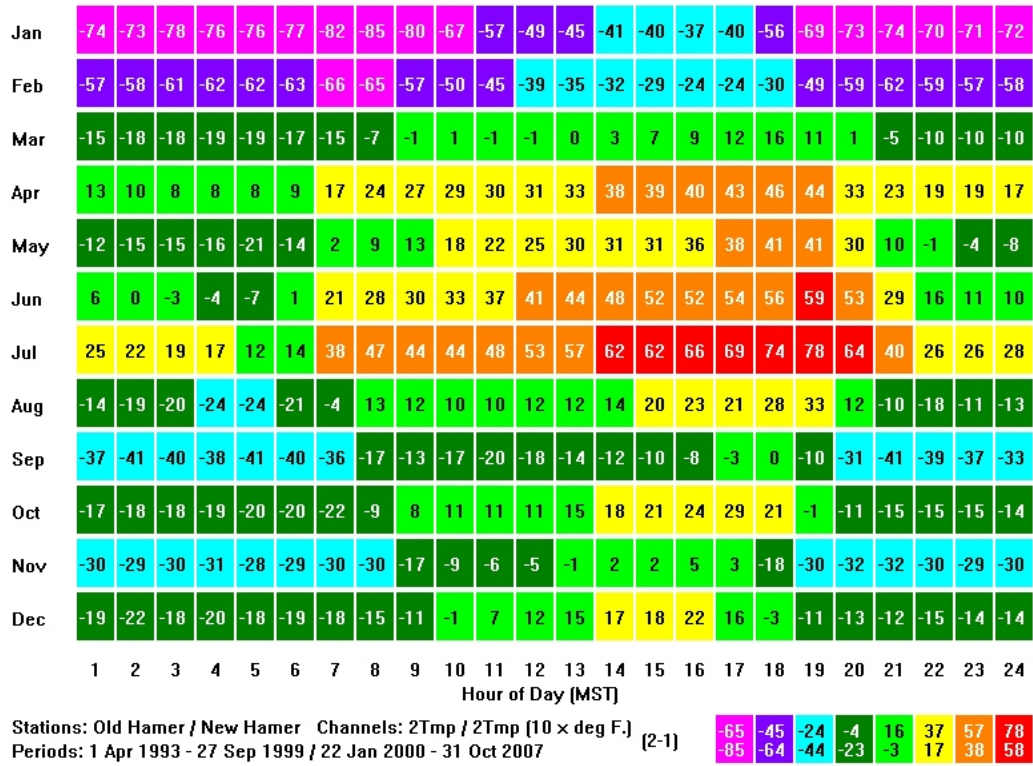


Figure D-8. Temperature difference (multiplied by 10) between the new and old Hamer Mesonet station.

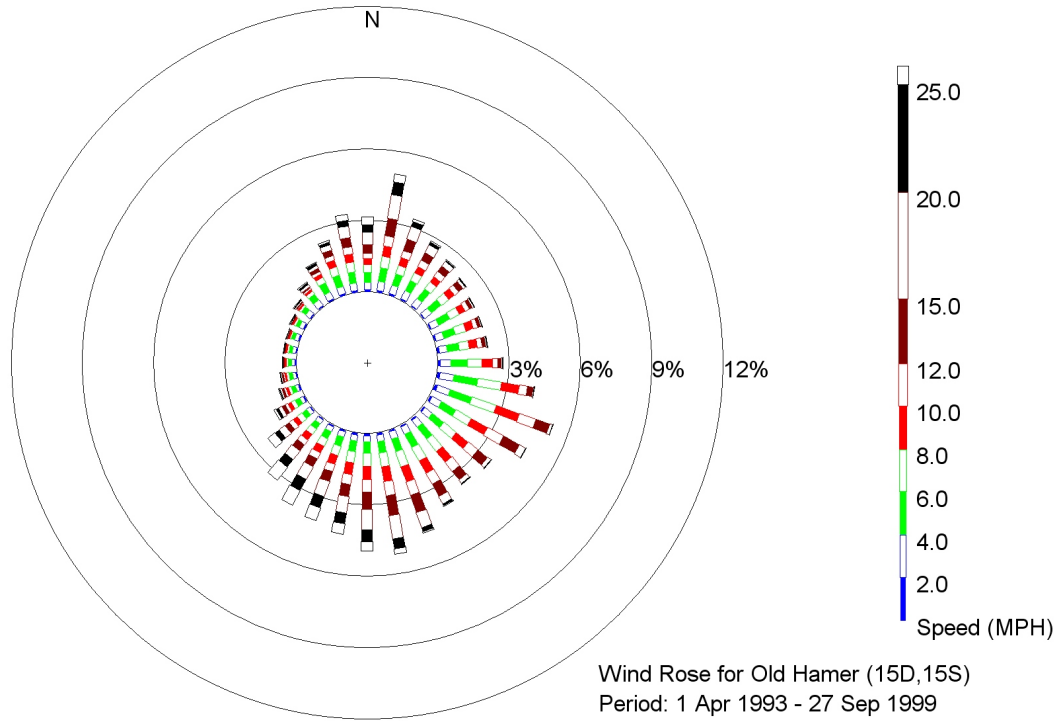


Figure D-9. Wind rose for the old Hamer Mesonet station from 1 April 1993 through 27 September 1999.

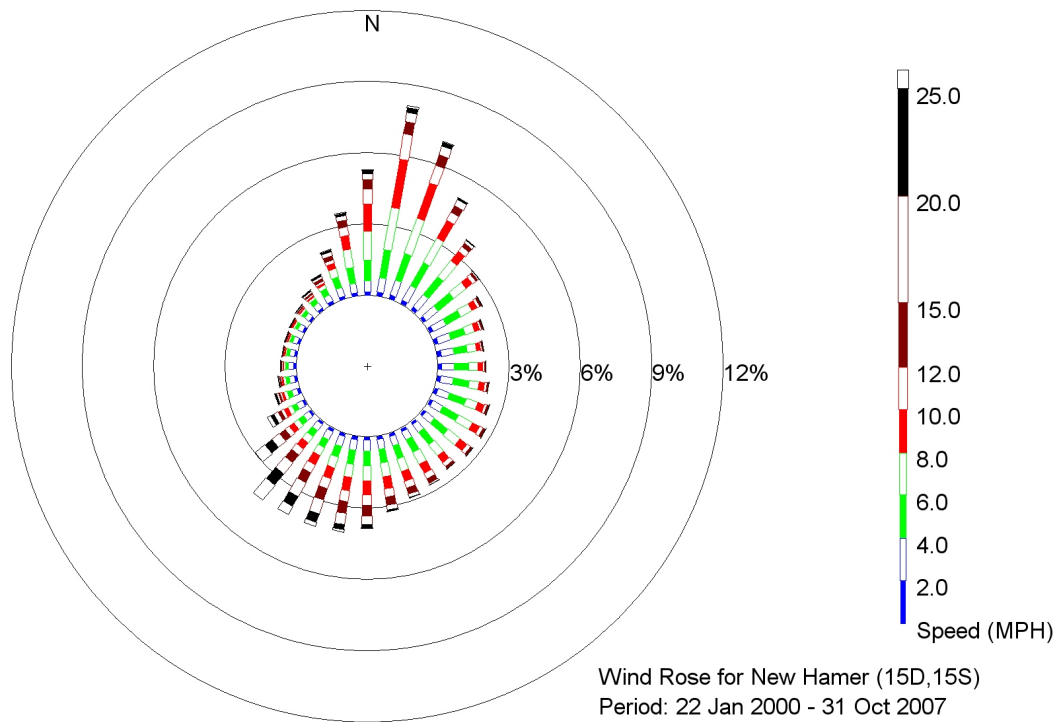


Figure D-10. Wind rose for the new Hamer Mesonet station from 22 January 2000 through 31 October 2007.

SUMMARY

Relocating the Blackfoot and Hamer Mesonet stations and comparing the data between the new and old stations showed big differences in both the speed and frequency of the winds and temperatures. Topographical

features, differences in vegetation surrounding the tower, and the urban environment can have major implications on the climate data of stations moving only 4-5 miles from each other. These examples illustrate the need for caution when working with historical data.

APPENDIX E: NOAA INL WEATHER CENTER

The Field Research Division recently developed a NOAA INL Weather Center (NIWC) web page (Fig. E-1). The new web page URL is <http://niwc.noaa.inel.gov/>. This new one-stop weather web page has been designed to simultaneously provide “INL site specific” meteorological information to both emergency and daily operations managers.

The highlight of the new weather page is the presentation of severe weather hazard information. Weather watches, warnings, and advisories issued by the National Weather Service (NWS) in Pocatello are displayed at the top of the page under the “Current INL Warnings” section. However, since the INL forecast zone covers all of the Upper Snake River Plain, some warnings may not always apply to or be relevant to the INL. Therefore, FRD issues other weather alerts and statements to give additional weather information specific to INL needs or when no watch, warning, or advisory is issued by the Pocatello NWS. These INL weather alerts and statements are also displayed under the “Current INL Warnings” section. The NWS issues watches and warnings 24 hours a day, 7 days a week while FRD-issues

weather statements or alerts only during normal FRD working hours. A list of current weather alerts and criteria can be found on the website.

Six large thumbnail images located beneath the “Current INL Warnings” section display popular INL related weather products.

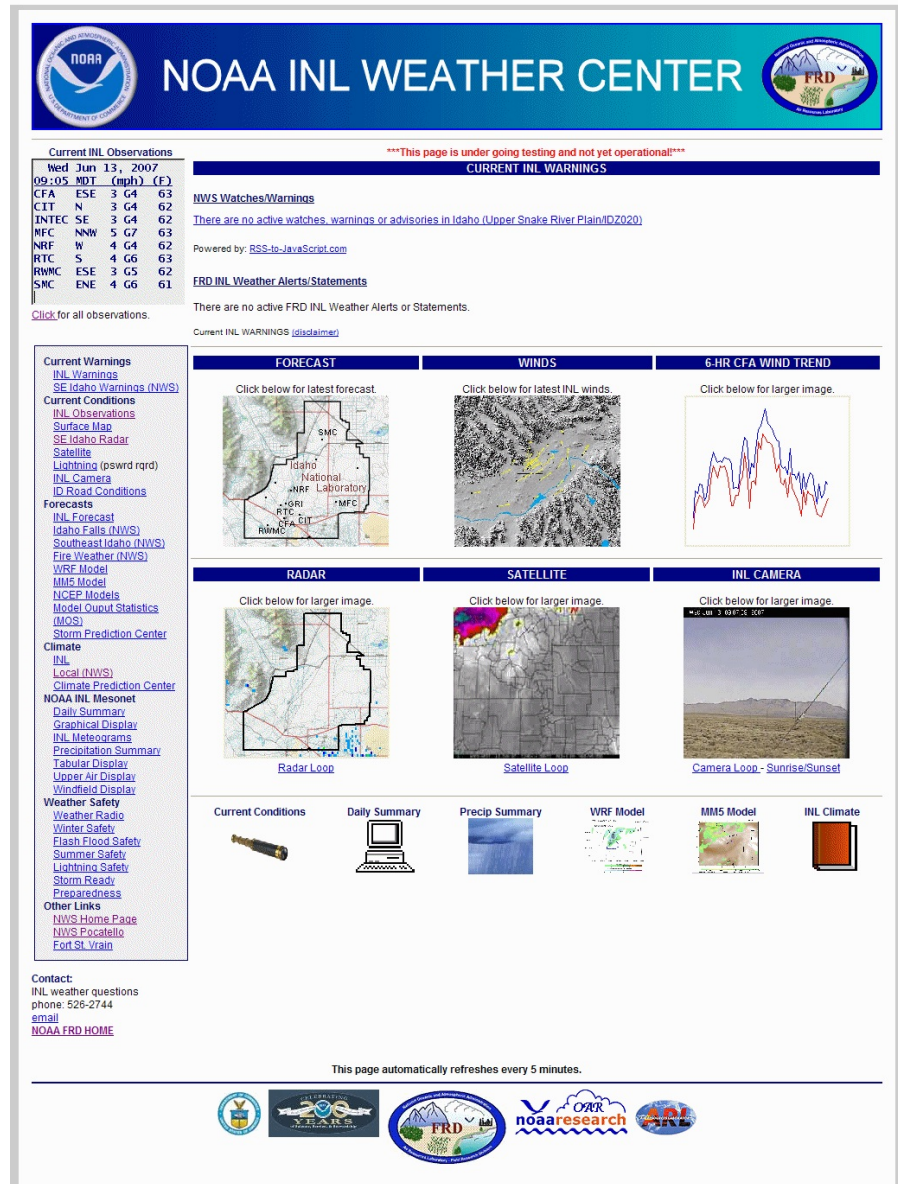


Figure E-1. Snapshot of the new NOAA INL Weather Center web page.

These thumbnails include a link to the INL weather forecast, a plot of the NOAA/INL Mesonet wind vectors, a plot of the wind speed trends for the last 6-hours, an INL site-specific weather radar image, the SE Idaho satellite image, and the current image of the INL weather camera. These thumbnail images give emergency and daily operations managers a glance of the overall weather across the site. Each of the images can be enlarged for more detail and easier viewing. The web page automatically refreshes every 5-minutes to keep weather watches, warnings, statements, alerts, and images current.

Other INL related and general weather

information is available in the menu on the left-hand side of the NIWC page and is available at the click of a mouse button. Some of these products are current observations that include a lightning map and table (only available to INL Internet users), links to NWS zone and weather forecast models, INL climate information, NOAA/INL Mesonet data, and weather safety information.

Many positive comments have been received from the INL emergency managers. The new page will continue to undergo improvements, updates, and additions over the coming months.

APPENDIX F: NOAA/INL MESONET INSTRUMENTATION



Figure F-1. Example NOAA INL Mesonet station layout, with the addition of the community monitoring station kiosk (foreground) on the Idaho Falls Greenbelt at the John's Hole Bridge and Forebay.

1. Wind Speed - Wind speed is measured using a 3-cup anemometer. Most cup anemometers consist of three (or more) hemispherical cups mounted on a vertical shaft. The difference in wind pressure from one side of a cup to the other causes the cups to spin about the shaft. The rate at which they rotate is directly proportional to the speed of the wind measured in miles per hour.

Wind speed gust - The wind gust is the highest 3-second wind speed average measured at the tower during the last five minutes.

Wind Chill - Is a measurement of how much heat is lost by your body based on the current temperature and wind speed.

2. Wind Direction - Wind direction is measured with an instrument called a wind vane. The vane always points into the wind and always gives the wind direction in compass degrees *from* which the wind is blowing.

3. Top Temperature - The temperature is measured using a thermocouple placed inside a metal housing (aspirator). This housing provides aspiration and shielding to eliminate the effects of radiative heating and cooling. The temperature is measured at two heights on the tower to provide information necessary to calculate the stability of the atmosphere.

4. Pyranometer - The pyranometer measures the electromagnetic radiation emitted by the sun or solar radiation. It is measured using solar cells that collect sunlight and converts it into electrical energy measured in watts per meter squared.

5. 6 - Foot (2 m) Temperature - The temperature is measured using a precision platinum resistance sensor placed inside a metal housing (aspirator). This housing provides aspiration and shielding to eliminate the effects of radiative heating and cooling. The temperature at 6 feet (2 m) is a true air temperature without the effects of

radiative and convective heating and cooling. The temperature is measured at two heights on the tower to provide information necessary to calculate the stability of the atmosphere.

Relative Humidity - Sensors also located inside the metal housing (aspirator) measure the amount of moisture in the air. The amount of moisture in the air versus how much the air could hold at the current temperature is called relative humidity.

Dew Point Temperature - The humidity sensor's output is used to calculate the temperature at which the current moisture in the air would condense to form dew.

6. Heated Tipping Bucket Rain Gauge - Rain and snow is collected using a heated tipping bucket rain gauge. When the amount of water equivalent to 0.01 inch of precipitation has been collected in the bucket, it tips over emptying the bucket. The accumulated precipitation in a given time period is calculated from the number of tips.

7. Weighing Rain Gauge - Rain gauge used to measure the amount of precipitation based on its weight. This rain gauge is setup temporarily only at the Idaho Falls station.

8. Pressurized Ionized Chamber (PIC) - Nuclear radiation in the form of gamma rays is measured using a high-pressurized ion chamber. The PIC is capable of measuring background levels of radiation in the environment as well as additional contributions from manmade activities. The units for the measurement of gamma radiation are micro-Roentgens (μR) per hour on the number of ionizations in the air that occur during an hour-long period. The PIC is owned and maintained by the State of Idaho.

9. Electronics Box - The electronics box, located on the tower behind the HiVol, contain the datalogger and barometric pressure sensor. The datalogger collects data from the meteorological

instrumentation and transmits it via radio back to the ARLFRD office storage computers.

Barometric Pressure - The barometric pressure is measured in inches of mercury. The values are reported in actual pressure. Local weather reports will often convert the actual pressure to adjusted sea-level measured values.

10. High Volume Air Sampler (HiVol) - An auxiliary air sampler that is capable of drawing large quantities of air through a particulate filter is placed on each monitoring tower. The high volume air sampler can be activated remotely in the unlikely event that an accidental release occurs at the INL facility. By sampling large quantities of air over a short period of time, the ability to detect low-level radioactivity in the atmosphere is increased. In essence, the larger quantity of air drawn, the lower the measurement sensitivity becomes.

11. Community Monitoring Station (CMS) kiosk- Several stations, called Community Monitoring Stations (CMS), are sited at schools and other places frequented by the public to enhance relations with the local communities. The CMS stations include a walk-up kiosk that displays current meteorological parameters and

describes each of the measured variables. These stations are located in Terreton, Big Lost River Rest Area, Fort Hall, Blackfoot, Idaho Falls, and Rexburg.

Instruments not shown

Nrad - The Nrad uses Geiger-Muller tubes to measure the total radiation present in the environment from naturally occurring cosmic and mineral sources, as well as any incidental man-made activities. The values report in microRoentgens (μR) per hour, which is proportional to the number of atoms ionized in air per hour.

Air Sampler - Particulate matter in the atmosphere is collected by an air sampler that is operated continuously around the clock. Each week the filter used to collect and retain the particulate matter is removed from the sampler and exchanged with a new filter. The used filter is sent to a laboratory where it can be analyzed for the gross or total amount of radioactivity collected from the atmosphere at this location. Air samplers are operated at several locations throughout southeast Idaho to evaluate the air quality both from the natural contributions of background sources and any manmade sources.

INSTRUMENT SPECIFICATIONS

Met One Instruments, Inc. Model 010C - Wind Speed Summary

Maximum Operating Range:	0 to 125 mph (0 to 56 m s ⁻¹)
Starting Speed:	0.6 mph (0.27 m s ⁻¹)
Calibrated Range:	0 to 100 mph (0 to 50 m s ⁻¹)
Accuracy:	±1% or 1 mph (0.45 m s ⁻¹)
Temperature Range:	-58°F to +185°F (-50° C to +85° C)
Response:	Distance Constant less than 5 feet (1.5 meters)* of the flow

* The distance traveled by the air after a sharp-edged gust has occurred for the anemometer rate to reach 63% of the new speed.

Met One Instruments, Inc. Model 020C - Wind Direction (Azimuth) Summary

Azimuth:	0 to 360°
Threshold:	0.6 mph (0.27 m s ⁻¹)
Linearity:	±0.5% of full scale
Accuracy:	±3°
Damping Ratio:	0.4 to 0.6
Delay Distance:	less than 3 ft. (0.91 m)
Temperature Range:	-58°F to +185°F (-50° C to +85° C)

Campbell Scientific Inc. Model HMP45C - Temperature and Relative Humidity Probe Summary

Temperature Sensor Specifications

Temperature and Measurement

Range:	-40°F to +140°F (-40° C to +60° C)
Temperature Accuracy:	±0.5° C

Relative Humidity Sensor Specifications

Relative Humidity Measurement

Range:	0 to 100% non-condensing
Accuracy at 20° C (68° F):	±2% RH (0 to 90% Relative Humidity) ±3% RH (90 to 100% Relative Humidity)

Temperature Dependence of

Relative Humidity Measurement:	±0.05% RH/° C
Typical Long Term Stability:	Better than 1% RH per year

Campbell Scientific Inc. Model 076B - Fan Aspirated Radiation Shield Summary

Errors Reduced: < 0.05° F (0.028° C)

LICOR Model LI200X - PYRANOMETER Summary

Range 0 to 3000 m W⁻²
Stability: <± 2% change over a 1 year period
Response Time: 10 μs
Cosine Correction: Cosine corrected up to 80° angle of incidence
Operating Temperature -40° + 149°F (-40 to +65° C)
Temperature Dependence: 0.15% per °C
Relative Humidity: 0 to 100%
Accuracy: Absolute error in natural daylight ±5% max; ±3% typical
Sensitivity: 0.2 kW⁻² mV⁻¹
Linearity: Maximum deviation of 1% up to 3000 W⁻²

Setra Systems Model 270 - Barometric Pressure Summary

Range: 800 to 1100 hPa/mb
Accuracy: ±0.05% FS or 0.55 mb

Vaisala Model PTB101B - Barometric Pressure Summary

Range: 600 to 1060 hPa/mb
Accuracy: ±0.5% FS
±6mb @ -40 to 140° F (-40 to 60° C)

Friez Engineering Company Model 7405H - Tipping Bucket Rain Gauge Summary

Accuracy: ±2% to 2" (5.08 cm) per hour
±4% to 10" (25.4 cm) per hour
Sensitivity: 0.01 inch (0.25 mm) per tip

Met One Model 385 Tipping Bucket Rain Gauge Summary

Accuracy: ±0.5% < 0.5" (1.3 cm) per hour
±2.0% < 3.0" (7.6 cm) per hour
Sensitivity: 0.01 inch (0.25 mm) per tip

Campbell Scientific Model TE525WS Tipping Bucket Rain Gauge Summary

Accuracy: ±1.0% up to 2" (5.08 cm) per hour

This page intentionally left blank.